On the Determination of Charge Carriers Density-of-States Distribution in OLED Materials

Dissertation

Von der Universität Bayreuth
zur Erlangung des Grades eines
Doktors der Naturwissenschaften (Dr. rer. nat.)
genehmigte Abhandlung

von

Andrei Stankevich

aus Brest, Weißrussland

Erste Gutachterin: Prof. Dr. Anna Köhler
Zweiter Gutachter: Dr. Andriy Kadashchuk
Dritter Gutachter: Prof. Dr. Axel Enders

Tag der Einreichung: 10.02.2025
Tag des Kolloquiums: 14.07.2025

Alice: Would you tell me, please, which way I ought to go from here?
The Cheshire Cat: That depends a good deal on where you want to get to.
Alice: I don't much care where.
The Cheshire Cat: Then it doesn't much matter which way you go.
Alice: ...So long as I get somewhere.
The Cheshire Cat: Oh, you're sure to do that, if only you walk long enough.

LEWIS CARROLL, ALICE IN WONDERLAND

Kurzzusammenfassung

Molekulare amorphe organische Halbleiter sind aufgrund der einfachen Herstellung von Bauelementen und der breiten Abstimmbarkeit der optischen und elektrischen Eigenschaften gern verwendete Materialien für Anwendungen in organischen Leuchtdioden (OLEDs). Ihre Anwendung wird jedoch häufig durch eine geringe Ladungsmobilität eingeschränkt, die zu leistungsmindernden Ladungsungleichgewichten und Ladungsansammlungen führt. Daher ist das Verständnis und die Kontrolle der Ladungstransporteigenschaften von entscheidender Bedeutung. In amorphen organischen Halbleitern bewegen sich Ladungen über eine Folge inkohärenter, thermisch aktivierter Sprünge durch die verfügbare Zustandsdichte (DOS) und bilden eine besetzte Zustandsdichte (ODOS). Der Ladungstransport in organischen Halbleitern wird durch die ODOS bestimmt, die von der Form und der Breite der DOS (σ_{DOS}) und der Temperatur beeinflusst wird. Bei Gleichgewichtsbedingungen, namentlich hohen Temperaturen und kleinen σ_{DOS}, ist die Breite der ODOS gleich der Breite der DOS. Es ist jedoch noch unklar, wie sich das Verhältnis zwischen σ_{DOS} und σ_{ODOS} unter Nicht-Gleichgewichtsbedingungen, die in vielen Bauelementen häufig vorliegen, ändert. Im Rahmen meiner Arbeit beabsichtigte ich daher, das Wissen über die DOS in organischen Halbleitern zu erweitern, wobei ich mich besonders auf die Bildung der ODOS im Nicht-Gleichgewichtszustand und die Auswirkungen von σ_{DOS} auf das Einfangen von Ladungsträgern in Fallenzuständen und die Photogeneration von Ladungen bei tiefen Temperaturen konzentriere. Trotz der weit verbreiteten Annahme, dass die Bestimmung der DOS und ODOS in organischen Halbleitern, insbesondere bei Nicht-Gleichgewichtsbedingungen, eine Herausforderung darstellt, zeige ich, dass die thermisch stimulierte Lumineszenz (TSL) effektiv zur Messung sowohl der DOS als auch der Tieftemperatur-ODOS in organischen Halbleitern erfolgreich angewendet werden kann. Bei den Messungen stellte ich zudem fest, dass die experimentell beobachtete ODOS-Breite etwa 2/3 der verfügbaren DOS-Breite in mehreren gängigen OLED-Hostmaterialien beträgt, was auf eine Art „spektrale Verengung" der ODOS bei niedrigen Temperaturen hindeutet. Um ein tieferes Verständnis über die Bildung der ODOS zu erlangen, führte ich zudem Kinetische Monte-Carlo (KMC) Simulationen durch, die meine experimentellen Beobachtungen bestätigten. Die Simulationen zeigen, dass die „spektrale Verengung" eine charakteristische Eigenschaft des Nicht-Gleichgewichts-Ladungstransports innerhalb der gaußschen DOS bei niedrigen Temperaturen ist. Außerdem fand ich, dass dieses Phänomen durch räumliche Korrelation der Energien, die in organischen Halbleitern aufgrund von Ladungs-Dipol-Wechselwirkungen entstehen, signifikant reduziert wird. Durch die systematische Charakterisierung von OLED-Hostmaterialien identifizierte ich kritische Faktoren, welche die energetische Unordnung beeinflussen, wie das permanente Dipolmoment und die molekulare Polarisierbarkeit. Insbesondere konnte ich demonstrieren, dass die energetische Unordnung in Materialien mit hoher Polarisierbarkeit von Kationen oder Anionen geringer ist. Außerdem war es mir möglich, den Ursprung der anomalen intrinsischen Photogeneration der Ladungsträger zu identifizieren, die in TSL-Experimenten beobachtet wird. Insbesondere zeigten meine Forschungen, die mit mCBP-CN als Fallstudie durchgeführt wurden, dass die intrinsische Photogeneration von geminalen Paaren durch den von Triplet-Triplet Annihilation (TTA)-induzierten Up-Conversion (UC)-Prozess dominiert wird, während der Ladungstrennungsprozess durch energetische Unordnung beeinflusst wird.

English abstract

Small molecule amorphous organic semiconductors are highly desirable materials for organic light-emitting diode (OLED) applications due to the ease of device fabrication and the wide tunability of optical and electrical properties. However, their application is often limited by low charge mobility, leading to performance-impeding charge imbalances and charge accumulation. Therefore, understanding and controlling charge transport properties is a critical concern. In amorphous organic semiconductors, charges move via a sequence of incoherent, thermally activated hops through the available Density of States (DOS), forming an occupied Density of States (ODOS). Charge transport in amorphous organic semiconductors is determined by the ODOS, which is influenced by the shape and width of the DOS (σ_{DOS}) and temperature. Under equilibrium conditions, when the temperature is high and σ_{DOS} is small, the ODOS is located at equilibrium energy, and the width of the ODOS (σ_{ODOS}) is equal to the σ_{DOS}. However, it remains unclear how ODOS behaves under non-equilibrium conditions, which are common in many devices.

Therefore, aiming to increase our understanding of charge transport in organic semiconductors, my thesis is focused on the non-equilibrium process of ODOS formation and the effect of σ_{DOS} on charge trapping and low-temperature charge photogeneration. Despite the common belief that mapping the DOS and ODOS in amorphous organic semiconductors, especially under non-equilibrium conditions, is challenging, I have demonstrated that thermally stimulated luminescence (TSL) can be effectively applied to measure both the DOS and low-temperature ODOS. I found that the experimentally observed ODOS width amounts to about 2/3 of the available DOS across several common OLED host materials, implying a kind of 'spectral-narrowing' of ODOS at low temperatures. To gain deeper insight into the ODOS formation process, I employed Kinetic Monte Carlo (KMC) simulations, which corroborated my experimental observations. The simulations revealed that 'spectral narrowing' is a genuine property of non-equilibrium charge transport within the Gaussian DOS at low temperatures. Furthermore, I found that this phenomenon is significantly reduced by spatial energetic correlations, which arise in amorphous organic semiconductors due to charge-dipole interactions. Through systematic characterization of OLED host materials, I identified critical factors affecting energetic disorder, such as permanent dipole moment and molecular polarizability. In particular, I have demonstrated that energetic disorder is reduced in materials with high cation or anion polarizability. Moreover, my research was not only confined to charge transport; I also unraveled the origin of the anomalous intrinsic charge photogeneration observed in TSL experiments. In particular, my research, conducted with mCBP-CN as a case study, showed that the intrinsic photogeneration of geminate pairs is dominated by the Triplet-Triplet Annihilation (TTA)-induced Up-Conversion (UC) process, while the charge separation process is influenced by the energetic disorder.

Part I
Introduction

1 Motivation

The semiconductor revolution of the late 1950s radically changed modern life, which is now hard to imagine without electronic devices for leisure and professional purposes[1]. The development of semiconductor technology led to a growing demand for new materials that are not only efficient and affordable but also straightforward to implement. Driven by this relentless pursuit of new, cost-effective materials [2, 3], organic semiconductors have begun to penetrate fields traditionally dominated by inorganic materials [4–7]. The application of amorphous organic semiconductors (AOSs) offers considerable benefits in optoelectronic devices, such as ambient temperature processing [8, 9], mechanical flexibility [10], and abundant raw material availability. Notably, AOSs promise cost reductions by enabling solution processing over the slower and costlier high-vacuum evaporation based methods [11–16]. Consequently, AOSs are emerging as preferred materials for electricity-to-light (e.g., organic light-emitting diodes, or OLEDs) and light-to-electricity (e.g., organic photovoltaics, or OPVs) conversion applications. The organic semiconductor market is worth \$81.5 billion in 2022 and is projected to grow at least 20% from 2023 to 2032 [5]. For example, OLED technology has become a significant player in the pixilated display market due to its high contrast ratios, wide viewing angles, luminance, and rapid response times. In addition, OLED technology is replacing monochrome LCDs in a number of industrial uses, such as measurement devices, instrumentation, benchtop apparatuses, current analyzers, and industrial handheld monitors[5].

In 1963, the first electroluminescence in organic semiconductors was demonstrated by Pope for the anthracene crystal [17]. However, active research on OLEDs was triggered in 1987 by Tang and VanSlyke [18], when they demonstrated that incorporating two thin AOS layers between an anode and a cathode enabled bright electroluminescence at sufficiently low voltages. Within the last 40 years, extensive efforts have been made to improve OLED technology [19], resulting in the development of three generations of OLED emitters [20]. The first generation employed fluorescent emitters, exhibiting up to 25 % internal quantum efficiency (IQE). The second generation uses phosphorescent emitters that can achieve IQEs up to 100%. However, their disadvantage is the use of heavy and rare metals and the lack of a stable blue emitter [21–23]. The third generation OLEDs are based on purely organic emitters with thermally activated delayed fluorescence (TADF) [24] emitters that provide 100% IQE without relying on heavy metal complexes.

However, OLED efficiency depends not only on IQE but also on the recombination probability of electrons and holes, and therefore on the charge transport process in the organic layers. [25–29]. In AOS films, charge transport occurs via thermally activated hopping through a localized state manifold. The density of states (DOS) in amorphous organic semiconductor (AOS) films is approximated by a Gaussian distribution with a standard deviation σ_{DOS}, which is the so-called energy disorder parameter [30, 31]. Energy disorder significantly impacts charge mobility in AOS films, resulting in a broad distribution of intermolecular hopping rates, hindering high charge mobility [30–33]. The width of the DOS, and consequently charge

mobility, plays a crucial role in the likelihood of electron-hole recombination in the OLED emissive layer [34, 35]. When electron and hole mobilities are well-balanced, recombination efficiency increases, resulting in higher electroluminescence efficiency and brighter OLEDs. However, unbalanced charge transport can lead to enhanced bimolecular recombination near the electrodes, thereby causing excitation quenching and a reduction in efficiency [36, 37]. This contributes to device degradation and instability in the color point of the device. Moreover, the intrinsically wide DOS poses a critical concern, as it results in charge accumulation, which in turn leads to undesirable reactions within the bulk material [38]. Trapped charge-carriers become quenching centers, triggering triplet-polaron annihilation (TPA) [39–41], which has been recognized as a major source of TADF emitter layer degradation [41, 42].

To predict device characteristics and enhance their performance, it is essential not only to accurately determine the shape and width of the DOS but also to discern the factors affecting energy disorder. These critical aspects are central to my thesis, which contributes to the understanding of charge transport in organic semiconductors, including the effects of charge-dipole interactions and spatial energy correlations.

Mapping the DOS in organic semiconductors is challenging due to excitonic transitions that obscure weak direct optical transitions between Highest Occupied Molecular Orbital (HOMO) and Lowest Unoccupied Molecular Orbital (LUMO) levels, making optical probing of the DOS impossible [30]. The results of indirect DOS measurement methods, like space-charge-limited current (SCLC) [43], time-of-flight (TOF) [44], or charge extraction by linearly increasing voltage (CELIV) [44], depend on the transport model chosen for the analysis of the experimental data. Direct methods, such as ultraviolet photoemission spectroscopy (UPS) [45] or inverse photoemission spectroscopy (IPES), have their challenges, notably significant background signals [46].

The aim of this thesis is to determine the shape of the DOS distribution, the factors that affect it, and the impact of σ_{DOS} on charge transport and photogeneration. I study the shape of the DOS distribution, in particular, σ_{DOS}, in amorphous organic semiconductor films using Thermally Stimulated Luminescence (TSL) (Papers 1–3), TSL offers several advantages as a pure optical and electrode-free technique. Firstly, TSL eliminates interface and contact effects. Secondly, it allows for DOS measurements even in systems with a large σ_{DOS}, where charge transport is highly dispersive. To broaden the research, I complemented TSL measurements with Kinetic Monte Carlo (KMC) simulations (Paper 1), which allowed me to gain deeper insight into charge dynamics and the energy landscape within organic semiconductor films. These simulations reveal the presence of spatial energy correlations, which arise from charge-dipole interactions. Continuing the investigation of charge-dipole interactions, Papers 2 and 3 focus on understanding factors that affect the width of the DOS, particularly the effect of induction interactions on charge-dipole interactions. This was achieved by corroborating the TSL data on σ_{DOS} with the results from quantum mechanics (QM) and molecular mechanics (MM) molecular dynamics simulations (Papers 2 and 3). Finally, in Paper 4, I explore the origin of charge photogeneration in neat OLED host materials at low temperatures that I observed during my TSL studies (Papers 1–3).

2 Charge transport and photogeneration in amorphous organic semiconductors

2.1 Charge transport states in AOS

2.1.1 Polarization energy

Conventional inorganic semiconductors such as Si and Ge (covalent crystals) have strong bonding between their atoms, allowing electrons to be delocalized [47]. In AOS, however, due to the weak magnitude of non-covalent intermolecular interactions, charges move in a particle-like manner [48]. As an electron navigates within an organic solid, it interacts with its surroundings, via electrostatic forces; the excess of charge polarizes the electronic orbitals, mainly the highly polarizable π orbitals, of neighboring molecules [48–50]. This interaction energy is termed the electronic polarization energy, illustrated in Figure 2.1 and represents the difference between the ionization potentials in a gas and in a solid phase [49]. Therefore, it can be determined experimentally by comparing the ionization energies (I) and electron affinity (A) of molecules in the gaseous and solid states [51], as shown in Figure 2.1a, b Polarization energy alters the energy levels of charges in organic semiconductors, typically by 1-2 electron volts (eV) [50], which affects charge transport [52], charge injection [48, 53], photoionization measurements [54], as well as charge dissociation in organic photovoltaics (OPV) devices [55, 56].

The total electrostatic energy, denoted as P_{el}, for a molecular system consisting of N molecules, after the introduction of a charge carrier into one of the molecules, can be described within the framework of lattice model, where molecules are treated as structureless vector-like sites with cubic symmetry [57]. This interaction energy is expressed as follows [57]:

$$P_{el} = Q_A \sum_{i \neq A}^{N} \frac{\vec{p_i} \cdot \hat{r}_{iA}}{r_{iA}^2} - \sum_{i}^{N} \sum_{j>i}^{N} \vec{p_i} \frac{3(\vec{p_i} \cdot \hat{r}_i)\hat{r}_i - \vec{p_i}}{r_{ij}^3} + \frac{1}{2} \sum_{i}^{N} \alpha_i F_i^2 \qquad (2.1)$$

where p_i is total dipole moment, F_i is local field, Q_i is the charge, α_i is polarizability, and r_i is position of the ith molecule. $\vec{r_{ij}} \equiv \vec{r_i} - \vec{r_j}$, and $\hat{r}_{ij}$ denotes the unit vector parallel to $\vec{r_{ij}}$. The $\vec{p_i}$ is a sum of the static and induced dipole moments of each molecule [57]:

$$\vec{p_i} = \vec{d_i} + \alpha_i \vec{F_i} \qquad (2.2)$$

where $\overrightarrow{d_i}$ is a static dipole moment. The $\overrightarrow{F_i}$ represents the sum of the contributions made to each molecule's local field by the surrounding [57]:

$$\overrightarrow{F_i} = \sum_{i \neq A}^{N} \left[\frac{Q_A \cdot \hat{r}_i}{r_{iA}^2} + \frac{3(\overrightarrow{p_i} \cdot \hat{r}_i)\hat{r}_i - \overrightarrow{p_i}}{r_{ij}^3} \right] \qquad (2.3)$$

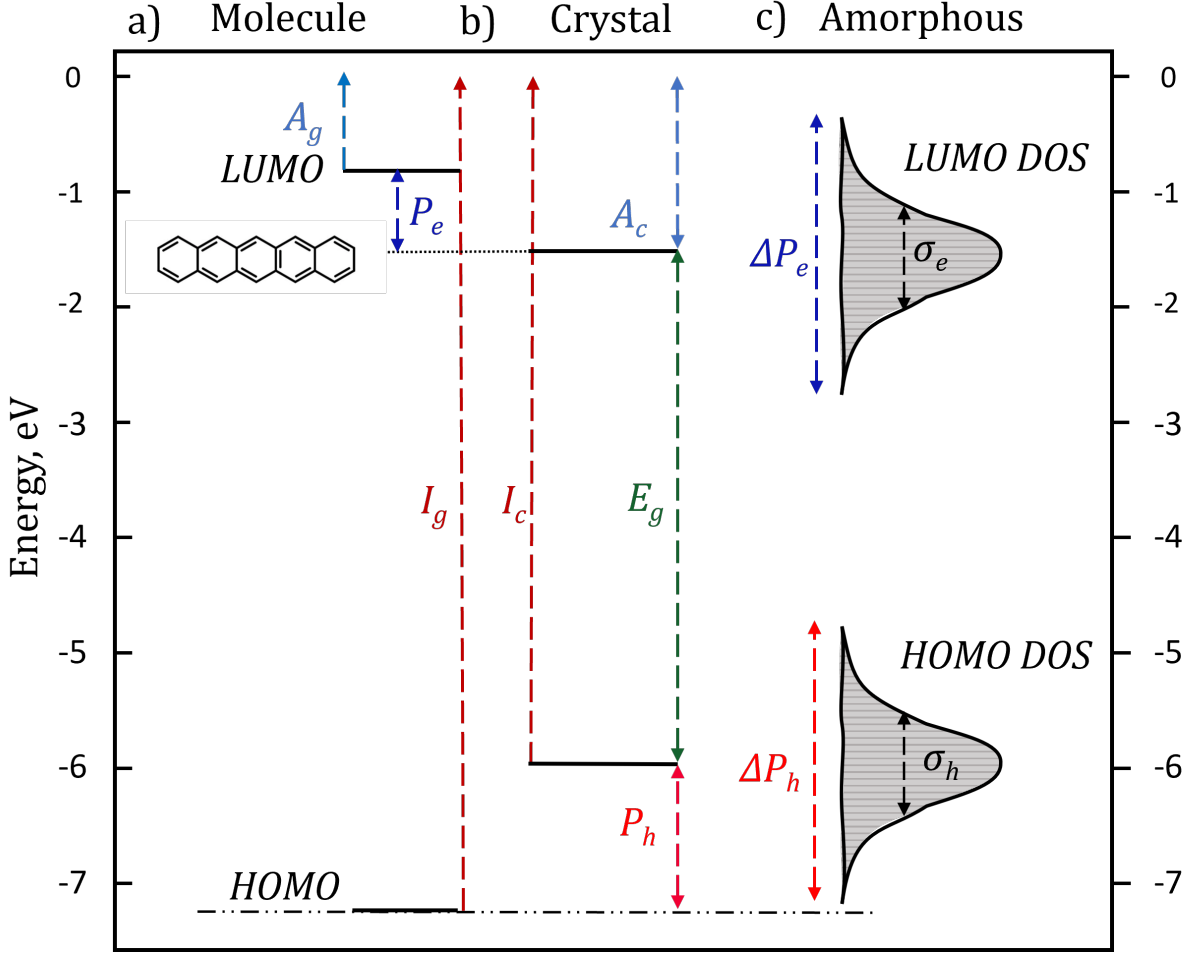Herein, I will use the term 'induction interaction' to refer to the contribution of induced dipoles.

Figure 2.1: Energetic diagram of ionized states of a) molecule, b) organic crystal and c) the DOS distribution of amorphous system: E_g – band gap, P_h and P_e – hole and electron polarization energy, A_g – vertical electron affinity of molecule, I_g – ionization energy of molecule, A_C – electron affinity of crystal, I_c – ionization energy of crystal. Adapted from [48]

2.1.2 The DOS

The number of states that a charge can occupy within organic semiconductors is denoted by the density of states distribution (DOS) $g\left(\varepsilon\right)$ [31, 58]. In a single crystal, every charge transport site would possess the same energy. However, in AOS, fluctuations in the polarization energy,

ΔP_{el}, affect the energies of the charge carriers. Specifically, in amorphous systems, the polarization energy (see Equation 2.1) for each site varies due to the random arrangement of intermolecular distances and the orientations of molecules [57, 59, 60]. Since these variations are random and independent according to the central limit theorem, the DOS follows a Gaussian distribution [57, 58, 60, 61] (Equation 2.4), as depicted in Figure 2.1c.

$$g\left(\varepsilon\right) = \frac{N}{\sqrt{2\pi\sigma_{DOS}^2}} \, exp\left[-\frac{1}{2}\left(\frac{\varepsilon - \varepsilon_0}{\sigma_{DOS}}\right)^2\right] \tag{2.4}$$

where σ_{DOS} is the energy disorder parameter that determines the state's energy distribution, ε_0– the center of the DOS. The DOS width characterizes the charge transport properties of materials.

The Gaussian distribution of the DOS is substantiated by experimental findings from Ultraviolet Photoelectron Spectroscopy (UPS) and by studying the low-temperature absorption profiles of polymers and AOS [58, 61].

The shape of DOS

The shape of the DOS might not always align with a Gaussian distribution [62, 63]. In a series of studies [64–66], the Gaussian distribution used to describe the DOS distribution was complemented with an exponential tail. This modification aimed to improve the fitting of temperature-dependent IV characteristics in certain AOS materials [64–66]. The following cumulative DOS was used to describe the Gaussian distribution with an exponential tail [64–66] :

$$g\left(\epsilon\right) = \frac{N_t}{\sqrt{2\pi\sigma_{DOS}^2}} exp\left[-\frac{1}{2}\left(\frac{\varepsilon - \varepsilon_0}{\sigma_{DOS}}\right)^2\right] + \frac{N_{trap}}{kT_0} exp\left(\frac{\varepsilon}{kT_0}\right) \tag{2.5}$$

where T_0 is the characteristic width of the exponential distribution and N_{trap} is the trap sites concentration (for energies $\varepsilon < \varepsilon_0$), σ is the Gaussian DOS width and N_t is the transport sites concentration.

Additionally, exponential tails were observed by Kelvin probe force microscopy [67, 68] and TSL studies [62]. Charge transport studies in electrochemically gated transistors also revealed exponential tails in poly(p-phenylene vinylene) (PPV) films[69]. The results confirmed that in PPV, the intrinsic Gaussian DOS is complemented by an exponential distribution of deep trap states [62, 69]

Numerous theoretical models have been proposed to explain such type of DOS distribution found in AOS materials [63, 70, 71] . May and colleagues [72] showed that when a material possesses permanent dipole moments, exponential tails can emerge if the sites—whether negatively or positively charged—are highly polarizable[62, 72]. Further, Novikov proposed that these tails could arise due to the partial alignment of either dipoles or quadrupoles [73].

2.2 Charge transport in a Gaussian DOS

The DOS is a parameter that describes the number of allowed electronic states per unit volume and energy in a material. However, knowledge of the DOS alone does not provide complete information about the macroscopic properties such as mobility or electrical conductivity. Thus, to establish a relationship between the DOS and charge mobility, it is necessary to consider charge transport hopping theories.

2.2.1 Gaussian disorder model

The charge transport mechanism in AOS differs from that in systems where the charge is delocalized [30, 31]. Being localized, charge carriers move through a solid via a sequence of thermally activated hops. The hopping rates are influenced by electronic coupling and the energy difference between hopping sites, which are distributed [30, 31]. Consequently, the width and shape of the DOS are critical parameters that govern charge transport [30, 31, 52, 74]. This thesis focuses on AOS, where disorder dominates over band and polaronic effects. The stochastic hopping model provides a reliable way to describe the movement of charge carriers and triplet excitations in materials with a Gaussian DOS. Based on several assumptions in his seminal paper [30], Prof. Bässler introduced the Gaussian Disorder Model (GDM):

1. The DOS is Gaussian

2. The Miller-Abrahams expression [75] is used to describe the rate of carrier transition between two sites, i and j

$$v_{ij} = \nu_0 \ exp\left(-2\gamma R_{ij}\right) \ exp\left[-\frac{|E_j - E_i| + (E_j - E_i)}{2k_b T}\right] \tag{2.6}$$

   where E_i and E_j are the energies of charge carriers on sites i and j, R_{ij} is the hopping distance. γ is the inverse localization radius and shows how the electronic coupling between sites decay. ν_0 is the attempt-to-hop frequency, close to an intermolecular phonon frequency $10^{12} \ s^{-1}$, T is temperature and k_b is the Boltzmann constant [75–77]. The electron hops upward or downward in energy in this approximation are characterized by absorption or emission of a single phonon, respectively, that compensates for the energy difference $E_j - E_i$ [75–77]. Miller-Abrahams equation is valid when the electron-phonon coupling is weak [52]. More recently, using complete quantum treatment of charge dynamics[78] and Monte Carlo simulations[76] in amorphous molecular semiconductors, it was demonstrated that at low temperatures, the Miller-Abrahams equation approximates charge transport remarkably well.

3. The charge transport is a memoryless stochastic process (Markovian property)

4. Charges concentration is low, specifically $n/N \ll 10^{-6}$ (n/N represents the relative charge concentration). Initially, for the charge carriers, the GDM model was validated through time-of-flight (TOF) experiments under conditions where the charge concentration is below $n/N \ll 10^{-6}$ [79–81]. Such conditions indicate that a material is approaching its intrinsic state and the behavior of the charges is not affected by electron-electron repulsion (for details, see subsubsection 2.2.2).

The GDM explains several experimental observations in AOS and relates the DOS distribution to macroscopic parameters such as mobility or the mean energy of charge carriers or triplet excitations. The latter can be easily obtained from time-resolved spectroscopy studies [82, 83]. While probing the mean energy of charge carriers, especially at low temperatures, presents significant challenges; this issue is addressed in Paper 1.

Energetic relaxation and zero-field mobility

Within a DOS distribution, charge carriers can be generated either through injection or photogeneration [31]. As these carriers move, they hop between sites, relaxing towards the tails of the DOS [31]. This continues until a dynamic equilibrium between downhill and thermally activated uphill jumps is established [30, 31]. Monte Carlo simulations [30] and effective medium approximation EMA [84] calculations show that the charge carriers stabilize in the vicinity of an equilibrium energy $\langle \varepsilon_\infty \rangle$ which is temperature-dependent.

$$\langle \varepsilon_\infty \rangle = \frac{\int_{-\infty}^{+\infty} \varepsilon g(\varepsilon) exp(-\varepsilon/k_b T)d\varepsilon}{\int_{-\infty}^{+\infty} g(\varepsilon) exp(-\varepsilon/k_b T)d\varepsilon} = -\frac{\sigma^2}{k_b T} \tag{2.7}$$

The presence of $\langle \varepsilon_\infty \rangle$ is a genuine attribute of Gaussian DOS.
In AOS, charge transport occurs through the thermal activation of charge carriers from states localized around the $\langle \varepsilon_\infty \rangle$ to a site at the transport energy (see subsubsection 2.2.1). When $\langle \varepsilon_\infty \rangle$ decreases, the activation energy increases, and vice versa [30, 31]. As a consequence, the mobility does not follow the Arrhenius law [85] and does not depend on carrier concentration (only valid when relative charge concentration is below 10^{-5} see subsubsection 2.2.2. Monte Carlo simulations within the GDM confirm the experimentally observed non-Arrhenius temperature dependence of mobility [30, 31]:

$$\mu(T) \simeq \mu_0 exp\left[-\left(C\frac{\sigma}{k_b T}\right)^2\right] \tag{2.8}$$

where C is a constant. The value of C for a three-dimensional system is approximately 2/3. The equations above are, however, only valid for zero field and equilibrium transport conditions. Charge transport properties are more difficult to study at low temperatures or when disorder is significant. My thesis addresses this issue both theoretically and experimentally Papers 1–3. The Gaussian Disorder Model also considers electric-field dependence of charge carrier mobility.

The field dependence of mobility

Electrons and holes must, in principle, move according to the electric field applied to them [30, 31]. External potential lowers the activation energy for jumps in the field direction. Consequently, equilibrium energy becomes field-dependent. Ries et al. [86] demonstrated that the applied field increases the equilibrium energy $\langle \varepsilon_\infty \rangle$, as described by the equation below.

$$< \varepsilon_\infty > = -(\sigma^2/k_b T) + (F/F_o)^{3/2} \tag{2.9}$$

where F_0, is $1.8 \cdot 10^6$ V/cm and is independent of $\sigma/k_b T$.
The experimental studies show that $\mu(F, T)$ in AOS follows the so-called Poole–Frenkel-type

field dependence $ln(\mu) \sim \sqrt{F}$[87]. Since the electric field affects $< \varepsilon_\infty >$, it should also influence the charge carrier mobility. Based on Bässler's GDM [30], the T and F dependence of charge carrier mobility is described as follows:

$$\mu(\hat{\sigma}, F) = \mu_0 \exp\left(-\frac{4\hat{\sigma}^2}{9}\right) \exp\left\{C\left(\hat{\sigma}^2 - \Sigma^2\right)\sqrt{F}\right\} \quad \text{for } \Sigma \geq 1.5,$$

$$\mu(\hat{\sigma}, F) = \mu_0 \exp\left(-\frac{4\hat{\sigma}^2}{9}\right) \exp\left\{C\left(\hat{\sigma}^2 - 2.25\right)\sqrt{F}\right\} \quad \text{for } \Sigma \leq 1.5,$$

(2.10)

Here $\hat{\sigma} = \sigma/k_b T$, and Σ represents the positional or "off-diagonal" disorder, which accounts for variations in the electronic coupling parameter $2\gamma R_{ij}$ (see Equation 3.29).

The Equation 2.10 verify a $\sqrt{F}$ dependence in AOS albeit for extremely high fields exceeding 10^6 V/cm. [30, 31]. However, experimentally this phenomenon was observed over a wider field range, lower than or of the order of 10^5 V/cm [88].

Equation 2.10 also predicts that under certain conditions, the field dependence of mobility can become negative, which is a sign of positional disorder. In weak fields, charge carriers can move against the field direction to avoid obstacles due to weak electronic coupling. However, as the field strength increases it can block these transitions, consequently leading to a reduction in mobility [30, 31]. A similar effect can be also observed due to the saturation of the drift velocity at high fields.

According to Equation 2.10, the mobility is a steep function of DOS width. An increase in energy disorder by just 10% can have a pronounced effect, resulting in a twofold decrease in mobility. This emphasizes the critical role of energy disorder in influencing device performance. Hence, in Papers 1–3, I focus on the DOS width measurements.

Transport energy

Charge carrier transport in positionally and energetically disordered hopping systems is notoriously difficult to simulate [89]. The concept of transport energy E_t simplifies the description of charge transport in disordered media by reducing the hopping problem to a more familiar multiple-trapping and release formalism with a broad energy distribution of localized states [89, 90]. Furthermore, E_t is essential for understanding the theoretical aspects of TSL. The transport energy level E_t is similar to the mobility edge in amorphous inorganic semiconductors and reflects the percolation nature of charge transport in AOS. In inorganic semiconductors, the mobility edge represents the energy level above which charge carriers can move freely and below which they remain localized [91]. Similarly, in AOS, once a carrier reaches the E_t level, it has enough energy to continue movement. To define the transport energy, one must locate the state energy E_i that satisfies the condition for maximal hopping rate. For the upward hopping rate $\nu_\uparrow$ from state i to state j one can write [89, 90]:

$$\nu_\uparrow = \nu_0 exp\left(-\frac{2R(E_i - \delta)}{\alpha} - \frac{\delta}{k_b T}\right),$$

$$R(\epsilon) \simeq \left\{(4\pi/3) \int_{-\infty}^{\epsilon} g(x)dx\right\}^{-1/3}$$

(2.11)

The condition of maximum rate $\nu_\uparrow$ is:

$$\partial \nu_\uparrow(E_i, \delta)/\partial \delta = 0 \tag{2.12}$$

where δ is $E_j - E_i$

Efficient hopping between sites is more likely to occur when the neighboring sites with the lowest energy difference (δ) are located at a reasonable distance. The left term in Equation 2.12 is a sharply decreasing function of R and hopping events predominantly occur within the first coordination shell. This implies that the transport energy level is typically situated around the center of the DOS. Notably, the position of the transport energy is not influenced by the energy of the initial state i. E_t can be found as [89, 90]:

$$E_t = \sigma \cdot x(T, N_0, \alpha, \sigma) \tag{2.13}$$

where σ is energy disorder parameter and $x(T, N_0, \alpha, \sigma)$ is the solution of the equation:

$$if\ x = (E_i - \delta)/\sigma$$
$$e^{x^2} \left(\int_x^\infty e^{-t^2} dt \right)^{4/3} = \frac{2}{3} \left(\frac{4\pi}{3} N_0 \alpha^3 \right)^{-1/3} \pi^{1/6} \cdot \frac{k_b T}{\sigma} \tag{2.14}$$

where N_0 is the number of transport sites. Equation 2.14 shows that E_t is the value determined by a specific set of system parameters: $N_0\alpha$ and $\frac{k_b T}{\sigma}$. For realistic parameters, the E_t is located a bit lower than the DOS center [90].

2.2.2 Further development of GDM

During the last decades, the GDM was significantly advanced. While the main idea remained unchanged, some of its principles have been refined to better describe the nuances of various material properties and experimental observations. These adaptations led to a more comprehensive and precise understanding of charge transport phenomena in AOS.

Charge carrier concentration effect

The GDM assumes that interactions between charge carriers are negligible. However, there are scenarios where this assumption may not be valid. For instance, when a substantial portion of the tail states in the DOS is occupied, interactions between charge carriers become pronounced, as shown in Figure 2.2 [92]. As a result, the position of the Fermi level can influence the charge-transport [31, 74]. While, the position of Fermi level ε_f in a Gaussian DOS $g(\varepsilon)$ is defined by the condition:

$$\int_{-\infty}^\infty \frac{g(\varepsilon)d\varepsilon}{1 + \exp\left[(\varepsilon - \varepsilon_F)/kT\right]} = n \tag{2.15}$$

where n is the charge carrier concentration. To understand how the position of the Fermi level can affect charge transport one can consider two scenarios. When the charge carrier concentration is significantly less than a certain critical value (n_c, see below Equation 2.17), $n \ll n_c$, the Fermi level position remains below $\langle \varepsilon_\infty \rangle$, and the carrier mobility μ remains independent of n (Figure 2.2) [92, 93]. However, as the charge carrier concentration exceeds
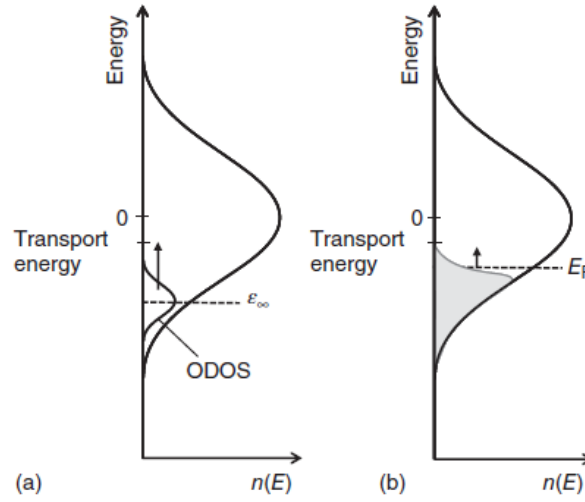
Figure 2.2: The impact of charge carrier concentration on transport in a Gaussian DOS: At negligible charge carrier concentration, carriers move through thermally activated transitions from $\langle \varepsilon_\infty \rangle$ to transport energy (a), However, when a significant portion of the tail states becomes occupied, the carriers' motion is characterized by transitions from the Fermi-energy to the transport energy (b). Adapted from "*Electronic and Optical Processes of Organic Semiconductors*" **(2015)** by Köhler, A. and Bässler, H. https://doi.org/10.1002/9783527685172.ch3. Reprinted from WILEY-VCH Verlag GmbH & Co. KGaA according to the CC BY 4.0 license.

$n \geq n_c$, upward jumps of charge carriers no longer start from a temperature-dependent quasi-equilibrium energy but rather from the Fermi level determined by the applied voltage [94, 95]. As a consequence, the carrier mobility follows the Arrhenius temperature dependence [96] :

$$\mu = \overline{\mu_0'} \exp\left[-\left(\frac{\varepsilon_t - \varepsilon_F}{kT^*}\right)\right] \tag{2.16}$$

with a prefactor $\overline{\mu_0'}$ slightly dependent on T, and ε_t is a transport energy position.
The above equation elucidates the n-dependence of mobility. As the concentration of charge carriers increases, the position of the Fermi level rises, leading to a decrease in activation energy.
The critical concentration n_c is given by [97]:

$$n_c = \frac{N}{2} \exp\left(-\frac{\sigma^2}{2(kT)^2}\right) \tag{2.17}$$

where N is the total number of localized states. For instance, when $\sigma/k_b T = 4$ the value for n_c/N is approximately 10^{-5}, which is a typical n value for OLED.

EGDM

Pasveer et al. extended GDM to account for a finite charge concentration in 2005 by introducing the extended Gaussian disorder model (EGDM) [34, 97]. EGDM predicts that at room temperature the mobility is predominantly n-dependent. However, at lower

temperatures and under high electric fields, the mobility becomes F-dependent. In EGDM mobility as a function of charge concentration n, temperature T and field F is given by:

$$\mu(T, n, E) = \mu_p(T, n) \times f(T, F) \tag{2.18}$$

The left-hand side of the mentioned expression shows the mobility's dependence on carrier concentration (p) and temperature (T), which is given by:

$$\mu(T, p) = \mu_0 C_1 \exp\left[-C_2\left(\frac{\sigma}{k_b T}\right)^2 + \frac{1}{2}\left(\left(\frac{\sigma}{k_b T}\right)^2 - \left(\frac{\sigma}{k_b T}\right)\right)(2na^3)^\delta\right] \tag{2.19}$$

where δ is given by:

$$\delta = 2 - \frac{\ln\left(\left(\frac{\sigma}{k_b T}\right)^2 - \left(\frac{\sigma}{k_b T}\right)\right) - \ln(4)}{\left(\frac{\sigma}{k_b T}\right)^2} \tag{2.20}$$

The electric field (F) dependence is described by the second term of Equation 2.18 which is defined as:

$$f(T, E) = \exp\left[0.44\left(\left(\frac{\sigma}{k_b T}\right)^{\frac{3}{2}} - 2.2\right) \times \sqrt{1 + 0.8\left(\frac{Fea}{\sigma}\right)^2} - 1\right] \tag{2.21}$$

In the aforementioned equations, the parameters are defined as follows: μ_0 mobility prefactor, e electronic charge , σ width of the DOS, $C_1 = 1.8 \times 10^{-9}$ constant, $C_2 = 0.42$ constant, k_b Boltzmann's constant, T temperature, a lattice constant. Currently, the EGDM is widely utilized to analyze the charge transport properties of polymers as well as small molecule-based organic semiconductors [65, 98, 99]. However, when using the EGDM to analyze IV curves, an inherent limitation becomes evident. The method lacks sensitivity to the tail states of DOS, as these states are occupied by charge carriers not participating in charge transport. As a result, this approach fails to capture the distribution of DOS tail states.

Correlated Disorder Model

The long-range charge-dipole [100] or charge-quadrupole [101] interactions lead to a significant spatial correlation within the energetic landscape [102].
The correlation function $C(r_{ij})$, which quantifies the degree of energy correlation between sites separated by a distance r_{ij}, expresses as follows[103]:

$$C\left(r_{ij}\right) = \frac{\langle(E_i - \langle E\rangle)(E_j - \langle E\rangle)\rangle}{\langle(E_i - \langle E\rangle)^2\rangle} \tag{2.22}$$

where E_i and E_j are the energies of the sites i and j separated by a distance r_{ij} and, $< \dots >$ represents the expectation value. If E_i and E_j are fully correlated, then $C\left(r_{ij}\right)$ is unity, while if they are uncorrelated, then $C\left(r_{ij}\right))$ is 0.

In organic polar materials, the correlation between sites decreases with distance as $1/r$[100] and in non-polar materials, the correlation decays as $1/r^3$[101]. Notably, the DOS even in

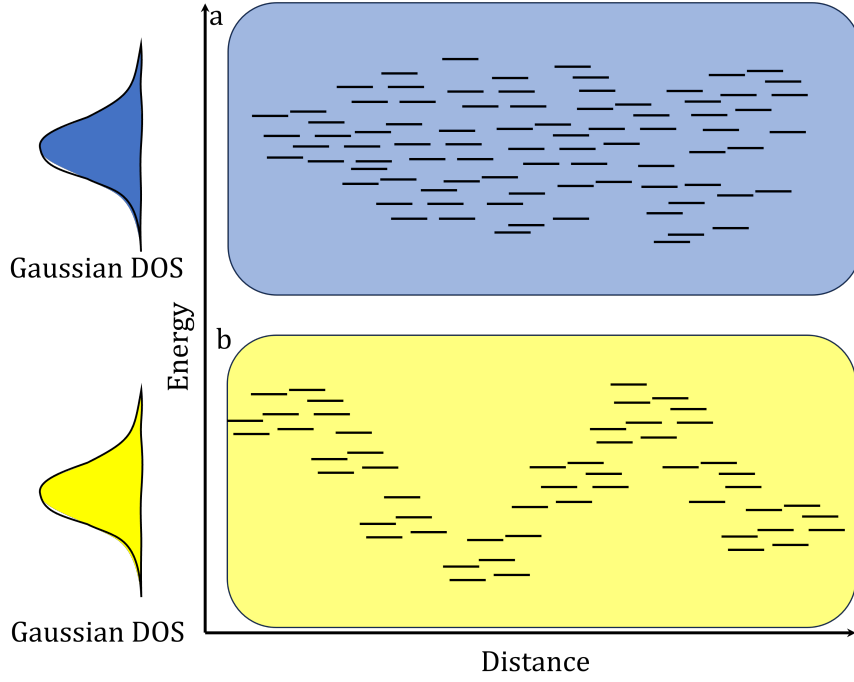correlated landscapes exhibits a Gaussian shape (see Figure 2.3).

Figure 2.3: The figure illustrates the spatial distribution of sites for 1D random (a) and correlated disorder (b).

The Correlated Disorder Model (CDM) provides a more accurate description of transport in disordered organic polar materials[88, 99, 100, 104]. For instance, experimental findings frequently show the Poole-Frenkel-like field dependence for electron or hole mobility, described as $Ln(\mu) \propto \sqrt{F}$. While the GDM captures this behavior, its prediction is confined to a high-field range (above 10^6 V/cm). Incorporating spatial energy correlations allows for the extension of the Poole-Frenkel-like dependence to a wider field range (lower than or of the order of 10^5 V/cm) [88].

In general, the field dependence of mobility originates from reduced charge escape times from critical traps[105] in the presence of an external field. In uncorrelated disorder systems, critical traps are isolated sites. In correlated dipolar disorder, the width of these critical traps is influenced by a balance among trap depth, width, and the reduction in potential barrier due to the applied field [105]. This balance in turn leads to a more distinct field dependence as illustrated in Figure 2.4.
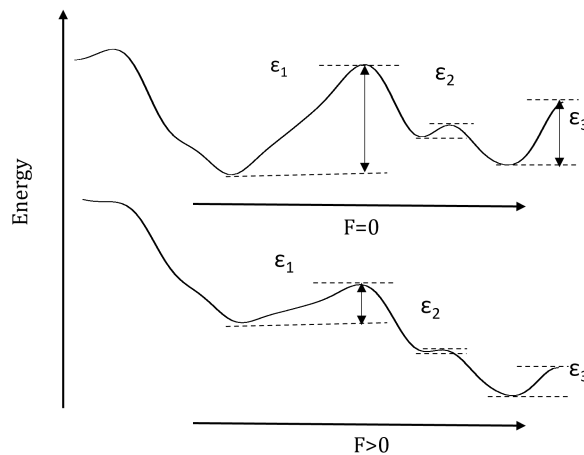
Figure 2.4: Figure illustrates the effects of an applied field on a correlated random potential. In the scenario without an applied field (as shown at the top), the widest wells are also the deepest. However, when a field is applied (as depicted at the bottom), the widest potential wells experience a tilt, leading to a significant reduction in their barriers.

2.3 Trap states in AOS

Due to charge localization and the hopping nature of charge transport, it is challenging to distinguish trap states from regular transport states in AOS [106]. Trap states can, however, be defined using the concept of transport energy. Any state in the DOS with an energy level below the transport energy level is considered as a trap state despite all states being localized [106–109]. Therefore, even in neat films, tail states of DOS act as traps[77] (Figure 2.5). It should be noted, however, that the transport energy is temperature-dependent. It is possible for a state that initially acts as a trap state at room temperature to turn into a transport state at low temperature[89, 90, 106]. Along with intrinsic traps formed by the tail states of the intrinsic DOS, there may also be extrinsic traps at discrete energy levels or with arbitrary energy distributions within the energy gap below the transport energy. An extrinsic trap can be introduced in several ways, including exposure to oxygen and water [110–112], electromagnetic radiation, dopants [108, 113, 114], and interactions with other substances of interest such as metals or dielectrics [26].

Extrinsic traps can substantially change the energetic landscape of AOS. However, in some cases, it merely leads to a broadening of the DOS, resulting in the experimental observation of the so-called effective σ_{eff}. Borsenberger and Bässler [115–117], from the analysis of TOF current transients, showed that for extrinsic traps, if the difference in HOMO or LUMO levels between the trap and host molecules E_{t}, is less than $3\sigma_{\mathrm{DOS}}$ (see Figure 2.6 for clarity), then the cumulative density of states will have a tail with an effective width:

$$\left(\sigma_{\mathrm{eff}}/\sigma_{\mathrm{DOS}}\right)^2 = 1 + \left(3k_bT/2\sigma_{\mathrm{DOS}}\right)^2 \left(E_{\mathrm{t}}/k_bT + \ln c\right) \tag{2.23}$$

This effect can be easily illustrated, I plotted the cumulative DOS distribution of a system with 1% trap molecules, varying the trap depths (see Figure 2.6). When $E_{\mathrm{t}} < 3\sigma_{\mathrm{DOS}}$ the cumulative DOS can be approximated as a single Gaussian. However, as the trap depth increases, the cumulative DOS starts to deviate from the Gaussian distribution, and
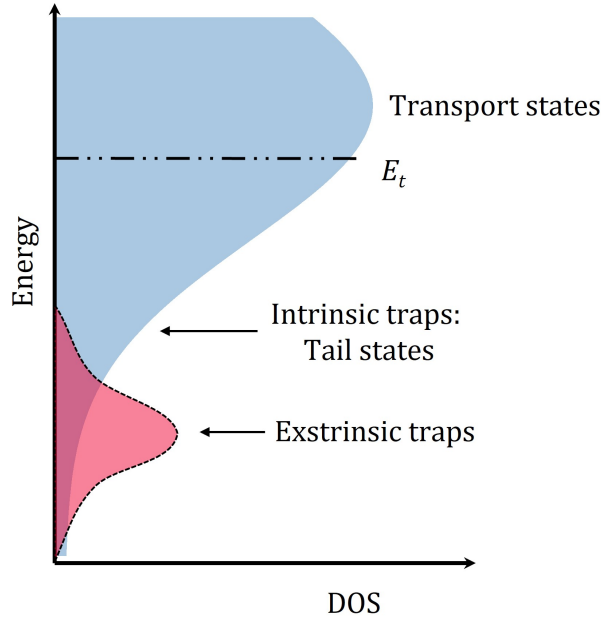
Figure 2.5: Trap states in AOS, illustrating the DOS distribution. The figure shows intrinsic traps, represented by the tail states of the DOS, and extrinsic traps, which arise from impurities. The transport energy level indicates the energy required for a charge to transition from the trap states to the conduction pathways.

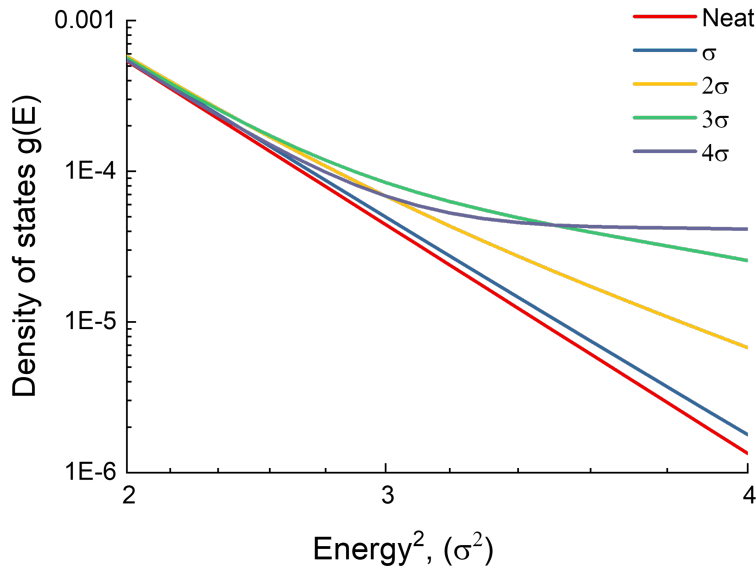for deep traps ($E_{\mathrm{t}} > 3\sigma_{\mathrm{DOS}}$), the guest molecules act like separate traps. Consequently,

Figure 2.6: The cumulative DOS distribution, plotted as $Log_{10}(E) vs E^2$, of the host-guest system of form: $g(E) = \frac{N_{\mathrm{host}}}{\sqrt{2\pi}\sigma} \exp\left(-\frac{E^2}{2\sigma^2}\right) + \frac{N_{\mathrm{trap}}}{\sqrt{2\pi}\sigma} \exp\left(-\frac{(E-E_t)^2}{2\sigma^2}\right)$, where the trap concentration N_{trap} is 1% mol and host concentration N_{host} is 99%.

even a small amount of impurity can significantly broaden the DOS distribution, making

it challenging to determine whether the measurement reflects the intrinsic DOS or the trap-affected DOS distribution. Therefore, many of my TSL measurements, especially where significant intrinsic energetic disorder is observed, are complemented with Quantum Mechanics/Molecular Mechanics calculations of the energetic disorder to confirm the intrinsic nature of the broad DOS distribution [62, 118].

2.4 Charge photogeneration in single component AOS

This section discusses the mechanisms of intrinsic photogeneration in AOS. When a molecule absorbs a photon, it generates excited states. This excited state comprises a bound electron-hole pair, known as an exciton or, more strictly, an excitation. After formation, the excitation can either decay radiatively or non-radiatively [31, 48, 49]. It can also diffuse through the organic semiconductor or participate in second-order processes such as TTA or singlet fission. Alternatively, the excitation may decay by dissociating into a pair of opposite charges [31]. Figure 2.7 illustrates such charge photogeneration process within an organic semiconductor crystal. The energy needed to break this excitation apart is termed exciton binding energy E_b. To find E_b we need to know the energy of the first singlet excited state, S_1, that defines the optical gap, $E_o = S_1$. The difference between the electrical E_e and optical gaps is the exciton binding energy, $E_b = E_e - E_o$. While E_e for AOS films is a gap between the ionization energy (IE) and the electron affinity (EA). The difference between the electrical and optical gaps arises from the hole–electron Coulomb interaction. In AOS, photogeneration of charge carriers upon photoexcitation in the lowest absorption band (S_1 transition) is restricted due to the high exciton binding energy [31, 48, 49]. Therefore, for neat AOS to produce geminate pairs, excitation binding energy must be overcome [31, 48, 49].
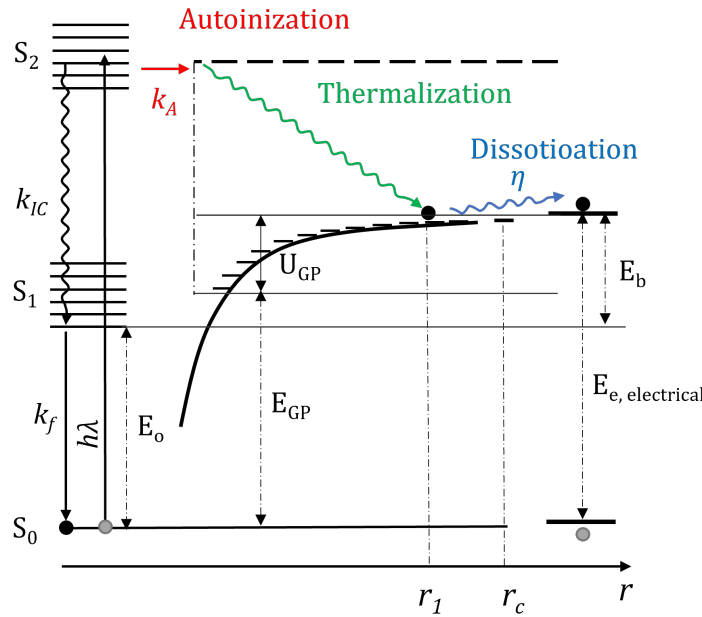

Figure 2.7: The photogeneration process within an organic semiconductor crystal is a sequence of events. Firstly, a neutral excitation is generated. Afterward, it undergoes autoionization and thermalization, leading to the formation of a geminate pair (GP). This GP, as a result of thermal and field-assisted dissociation, eventually separates into charge-separated states (CS): k_A – autoionization rate constant, k_{IC} – the internal relaxation rate constant, k_F – the exciton relaxation rate constant, S_0 – the ground state of the exciton, S_1 – the first excited singlet state of the exciton, U_{GP} – the Coulombic energy of the GP, E_{GP} – the energy of the GP, η – dissociation probability of the GP r_1 – the average thermalization length, E_e – the bandgap, E_b – the exciton binding energy , r_c – the critical Coulombic capture radius.

Free charge carriers are typically photogenerated in two main stages. Initially, charge transfer (CT) states or geminate pairs (GP) (synonyms in certain contexts) bound by the Coulomb interaction emerge either from autoionization or from the interfacial charge separation. These GP then dissociate into free charge carriers, sometimes referred as charge-separated states (CS) [31, 48, 49].

Usually, the dissociation of photogenerated geminate pairs (GP) is described by Onsager's diffusion theory. This was corroborated by research on the spectral dependencies of activation energy and the field dependencies of intrinsic photogeneration [119–121]. However, there are certain cases where the scenario above may not hold [122–124]. First, conjugated polymers may display a unique GP dissociation behavior. In MeLPPP [125], for instance, intrinsic photogeneration remains unaffected by temperature. Second, for donor-acceptor systems, the Onsager-Braun model [126, 127] is favored over the Onsager model. The key reason is its consideration for the finite lifetime of a GP, a factor the Onsager model does not account for [126, 127].

To dissociate the GP, a specific activation energy, E_A, is required [119–121]. Thus, the total quantum yield of photogeneration of free charges is dependent on the photon energy $h\lambda$, the strength of the external electric field F, and temperature T. The total quantum yield can be represented as the product of two probabilities: the autoionization probability η_0 and the dissociation probability Ω.

$$\eta(h\upsilon, F, T) = \eta_0(h\upsilon) \times \Omega\left[r_{th}(h\upsilon, F, T), F, T\right] \tag{2.24}$$

where r_{th} is the average thermalization length, defined as the distance between the electron and hole. r_{th} plays a crucial role in the efficiency of photovoltaic devices, affecting charge separation and collection efficiency. Using F and T as parameters, the Onsager theory describes the efficiency of dissociation of the GP at some value of r_{th}

$$\Omega\left(r_{\text{th}}, \text{F}, T\right) = \frac{1}{2\gamma < r_{\text{th}} >} \exp\left[-\frac{r_{\text{c}}}{< r_{\text{th}} >}\right] \sum_{m=0}^{\infty} \frac{(r_{\text{c}}/ < r_{\text{th}} >)^m}{m!} \times$$
$$\times \sum_{n=0}^{\infty} \left[1 - \exp\left(-2\gamma < r_{\text{th}} >\right) \sum_{k=0}^{m+n} \frac{(2\gamma < r_{\text{th}} >)^k}{k!}\right] \tag{2.25}$$

where r_c is the critical radius of GP (the Onasager radius) and γ one given by :

$$r_{\text{c}} = \frac{e^2}{4\pi\varepsilon\varepsilon_0 kT}$$
$$\gamma = \frac{e\mathbf{E}}{2kT} \tag{2.26}$$

For the simplest case of the delta-function distribution of GP distances $-g(r_{th})$

$$g(r_{th}) = \left(4\pi r_{th}^2\right)^{-1} \delta\left(r - r_0\right) \tag{2.27}$$

The r_{th} can be estimated as

$$\langle r_{th} \rangle \equiv e^2/4\pi\epsilon\epsilon_0 E_a^t \tag{2.28}$$

where $\langle...\rangle$ denotes mean value.

The thermalization length is affected by various factors, such as photon energy, temperature, as well as field strength, and can be described by exponential [128], Gaussian and double Gaussian distributions [129, 130].

As indicated in Equation 2.24, η_0 is influenced by the photoexcitation energy. In various applications, especially when describing photogeneration in organic and inorganic solids with low carrier mobility η_0 is often treated as either a constant or a weak function of $h\upsilon$ [131]. According to [132], $\eta_0 = \eta_0(h\upsilon)$ follows:

$$\eta_0(h\upsilon) = \frac{k_{\mathrm{A}}(h\upsilon)}{k_{\mathrm{A}}(h\upsilon) + \sum_i k_i(h\upsilon)} \tag{2.29}$$

$k_{\mathrm{A}}(h\upsilon)$ is the autoionization rate constant, and $k_i(h\upsilon)$ are the intramolecular (radiative and radiationless) energy dissipation rate constants [132]. Moreover, several processes can affect autoionization. It is possible for triplet-excited states with a long lifetime to undergo triplet-triplet annihilation (TTA) and generate high-energy states capable of autoionization [133]. In a classical case, however, photon energy mainly determines r_{th}. Conversely, electrical field F and temperature T can influence the photogeneration of free charge carriers at all stages. Additionally, it should be noted that autoionization occurs at some specific energy level, such as S_2 or S_3, which is reflected in a stepwise activation energy dependence on an excitation wavelength [134].

Nevertheless, it is important to note that the generation of geminate pairs is not solely reliant on the autoionization process [135, 136]. Defects or impurities possessing a higher electron affinity or lower ionization energy than the bulk materials can also affect the photogeneration process. Experimental findings have provided evidence that chemical acceptors can sensitize exciton dissociation [137]. Sensitization generates ionized donor-acceptor pairs that can subsequently undergo dissociation into free charges, albeit with a low probability[138]. Moreover, the dissociation of excitons on injected holes originating from the ITO interface can exhibit exceptional efficiency [139, 140]. Therefore, unintentional hole injections should be avoided when measuring the intrinsic photocurrent since it can affect excitation dissociation. The dissociation process of the GP is substantially affected by energy disorder. Depending on the conditions, both intrinsic and extrinsic trap states may facilitate or hinder GP state dissociation [141–143]. For instance, the Monte-Carlo simulations conducted by Albrecht and Bässler[144] (Figure 2.8), and subsequently confirmed by numerical simulations Bässler and Emelianova [145], demonstrated a strong correlation between the energetic disorder and GP dissociation efficiency. Dissociation efficiency increased significantly when the disorder parameter was increased. The strong field dependence and weak temperature dependence of the GP dissociation yield are generic signatures of energetically random systems [142, 144, 145]. Rubel[143] showed that disordered systems exhibit smoother field dependence than ordered systems, indicating that disorder facilitates GP states dissociation at low fields and impedes it at high fields.
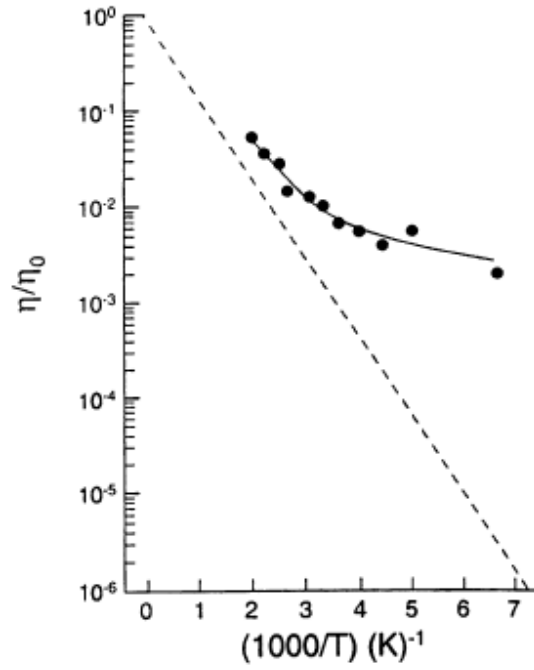
Figure 2.8: The figure displays the temperature dependence of the dissociation probability for GP with $r_{th} = 24A$ in a Gaussian DOS where $\sigma = 0.10$ eV. The Monte Carlo simulation, representing disorder-assisted dissociation, is shown as a solid line. The Onsager model, which doesn't account for disorder, is depicted as a dashed line. The experimental data points are denoted by dots. Adapted from *"Yield of geminate pair dissociation in an energetically random hopping system"* by Albrecht U., Bässler H., Chem. Phys. Lett., 235 (3-4), **1995**, p. 389, https://doi.org/10.1016/0009-2614(95)00121-J [144]. Reprinted from Elsevier according to the CC BY 4.0 license.

3 Methods

Subsection 3.1.1 of this chapter provides details on the materials and sample preparation routine. Following this, Subsection 3.1.2 describes the common techniques used for AOS film characterization. Chapter 3.2 will provide a comprehensive theoretical description of the Thermally Stimulated Luminescence (TSL) method, which is central to this thesis.

3.1 Experimental details

3.1.1 Materials and samples preparation

Figure 3.1 depicts the molecular structures of the organic materials I studied. I used most of the materials as received without further purification. TCTA, Spiro-TAD, and NPB samples were received as evaporated films from Max-Planck-Institut for Polymer Research Mainz (Paul Blom group). The mCP-CN was received as evaporated films from Durham University, UK (Andrew Monkman group). The DMAC-pz-TRZ was received as a powder from St Andrews University, UK (Zysman-Colman group). Some mCBP-CN samples were received from Augsburg University (Wolfgang Brüting Group).

Thin films of AOS were fabricated by vacuum thermal evaporation or spin-coating onto quartz substrates and crystalline silicon wafers. For specific applications, I used metallic substrates like aluminum foil to prepare the samples. During the deposition process, surface preparation is a quality-determining step; therefore, prior to coating, the substrates were cleaned using the following procedure:

- Pre-cleaning with water and soap

- Ultrasonic bath for 15 min in deionized water with soap

- Ultrasonic bath for 5 min in deionized water

- Ultrasonic bath for 5 min in acetone

- Ultrasonic bath for 5 min in isopropanol.

- UV-ozone cleaning for 20 minutes

Samples deposition   A typical sample for TSL measurements is shown in Figure 3.2. Spin-coating is a common method for thin film deposition and is well-suited for most of the molecules discussed in this thesis. In the initial step, a solution of the organic compound is cast onto the substrate and placed in the center of the spin-coater. The centripetal force and the surface tension uniformly spread the liquid across the substrate. Subsequently, during the spinning process, the solvent evaporates, which usually results in a uniform amorphous
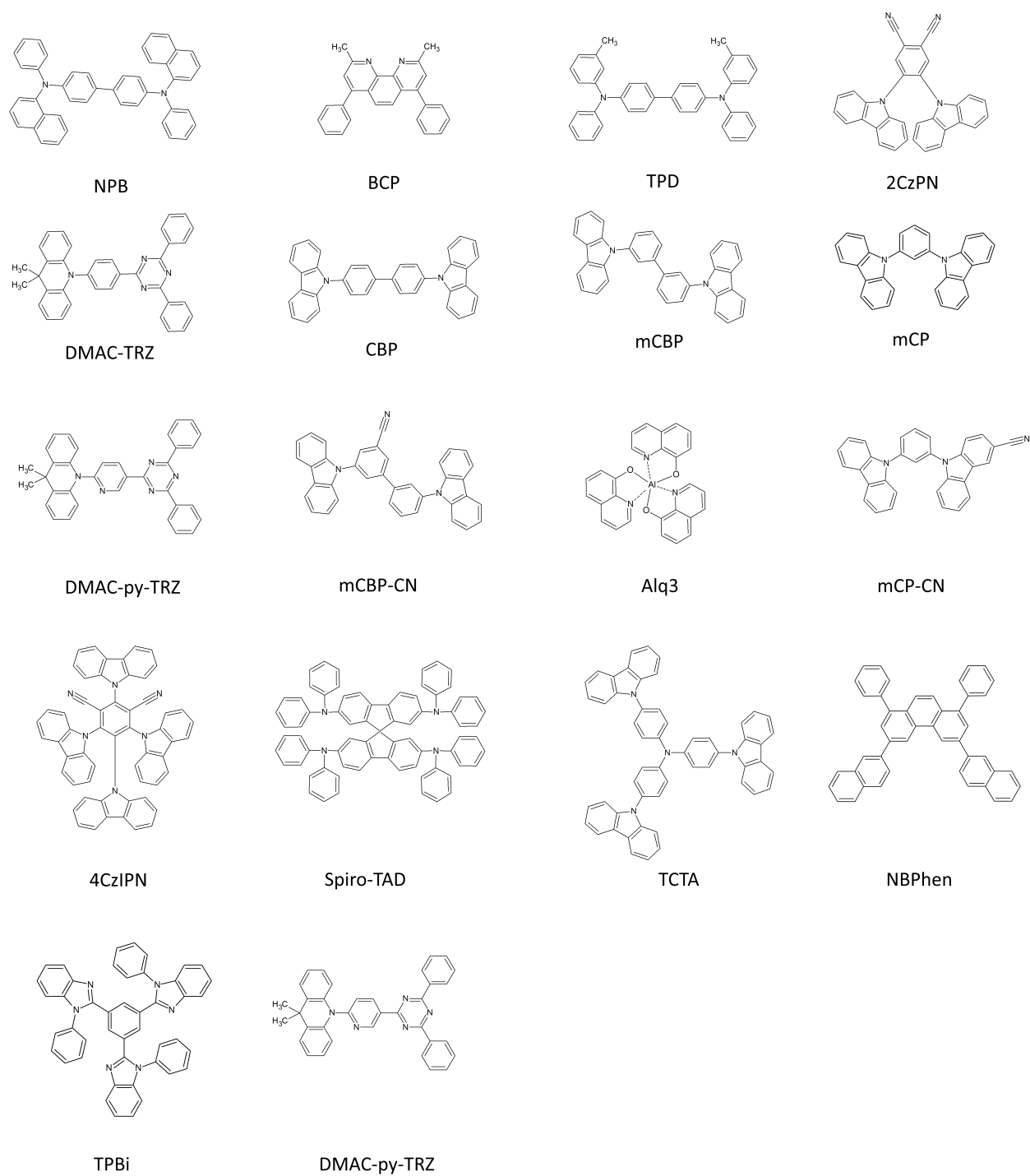
NPB

BCP

TPD

2CzPN

DMAC-TRZ

CBP

mCBP

mCP

DMAC-py-TRZ

mCBP-CN

Alq3

mCP-CN

4CzIPN

Spiro-TAD

TCTA

NBPhen

TPBi

DMAC-py-TRZ

Figure 3.1: The molecular structures of the organic materials studied in this dissertation

film of the organic material. The thickness of this film depends on different factors: viscosity, concentration of molecules, solvent boiling point, and rotation speed.
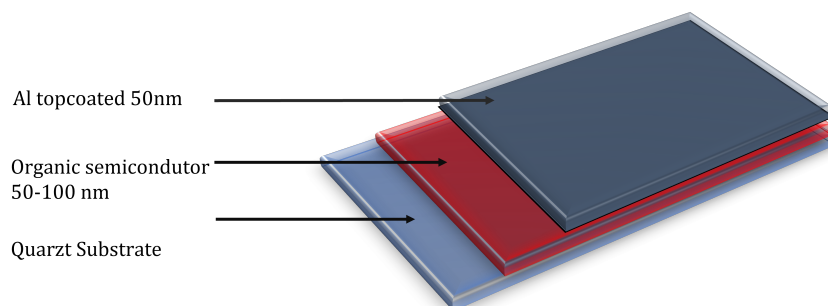

Figure 3.2: Structure of the sample for TSL measurements

The typical sample thickness for TSL measurements is 50 nm, obtaining uniform films thicker than 50 nm is difficult for small molecules. To obtain films, the material was first dissolved in chloroform at a concentration of 10 mg/ml. The solution was then spin-coated onto a quartz substrate (unless otherwise specified) at 1000 rpm. The substrate was first dried on a hot plate at 40 °C for 10 minutes, followed by a vacuum treatment for 1 hour to completely remove any residual solvent.

When organic molecules are not readily soluble or if multilayered devices are required, the thermal vacuum evaporation method was employed. In a typical experiment, substrates were placed into a glovebox filled with N_2 and subsequently transferred to a vacuum chamber. The active layers of 50 nm thickness were deposited by thermal evaporation under a vacuum of 5×10^{-7} Torr at a deposition rate of 0.1-0.2 Å s^{-1}. Finally, if necessary, top-contact aluminum or gold electrodes (50-nm thick) were thermally deposited under a vacuum of 1×10^{-5} Torr at a deposition rate of 0.3-1 Å s^{-1}.

3.1.2 Common experimental techniques

Steady state absorption Steady-state absorption and photoluminescence are widely used spectroscopical methods to study the excited states of molecules. Absorption measurements were performed using the Cary 5000 UV-Vis-NIR spectrophotometer, with a two-channel scheme. A quartz substrate or cuvette filled with a neat solvent was utilized as a reference. The transmittance T at a specific wavelength (λ) is expressed as:

$$T(\lambda) = \frac{I_{\text{sam}}(\lambda)}{I_{\text{ref}}(\lambda)} \tag{3.1}$$

where $(I_{\text{sam}}(\lambda))$ and $(I_{\text{ref}}(\lambda))$ are the intensity of light transmitted through the reference and sample channels, respectively.
The optical density (OD) is described by:

$$\alpha(\lambda) = \log_{10}\left(\frac{I_{\text{sam}}(\lambda)}{I_{\text{ref}}(\lambda)}\right) \tag{3.2}$$

Photoluminescence   I conducted both photoluminescence and phosphorescence measurements using the Jasco FP-8600 spectrofluorometer. Steady-state photoluminescence spectra were collected at room temperature (RT) and 77 K using spectrally selected CW excitation. For phosphorescence emission measurements at 77 K, a chopper was utilized to control the delay between excitation and signal collection. Both these methods provide a straightforward approach for probing the first singlet and triplet excited states of molecules. For measurements at 77 K, the film or cuvette was placed in a liquid nitrogen bath cryostat. For photoluminescence measurements beyond the 77 K range, I used a separate time-resolved setup, equipped with an integrated helium cryostat, as depicted in Figure 3.3.

Time-resolved photoluminescence measurements   I employed time-resolved photoluminescence (TRPL) to study the radiative relaxation dynamics of excitations in organic semiconductors. TRPL captures the emission spectrum at different time intervals after the laser pulse excitation. This allows me to study prompt fluorescence, delayed fluorescence, or phosphorescence. Prompt emission originates from the radiative decay of singlet excitations, while delayed fluorescence can arise from triplet-triplet annihilation (TTA), reverse intersystem crossing (RISC), or geminate pair recombination. The effect of laser intensity on these emissions was investigated using a set of neutral-density filters.

The time-resolved photoluminescence (TRPL) setup (see Figure 3.3) utilizes a Q-switched Nd-YAG laser source. The laser emits third harmonic light pulses at 355 nm with a bandwidth of 5 nm and a repetition rate ranging between 20 and 1 kHz. A spectrograph coupled with an IStar A-DH334T-18F-03 iCCD camera was used to collect the light emitted from the sample. The iCCD camera supports gated detection with a temporal resolution ranging from 1 nanosecond up to 50 milliseconds. Before taking measurements, the temperature of the samples was stabilized for 10 minutes in a helium atmosphere.
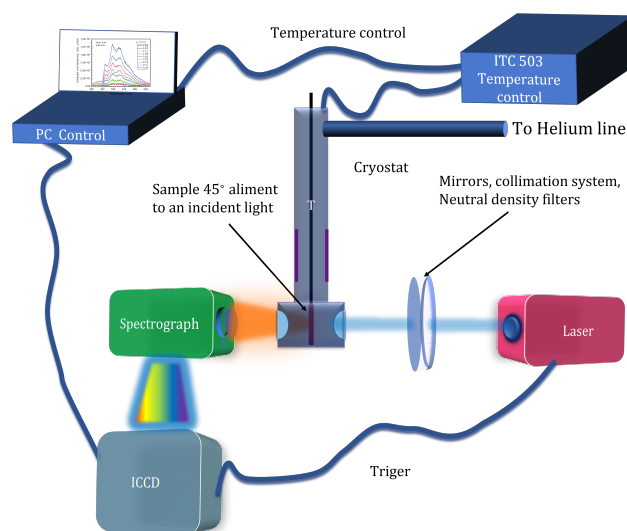

Figure 3.3: Schematic illustration of a measurement setup for time-resolved photoluminescence.

Photocurrent spectroscopy Photocurrent spectroscopy (PC) is: "A type of spectroscopy where light energy absorbed by the sample results in the production of a current (the 'photocurrent') which is measured at different spectral intervals" [146]. I measured photocurrent in the AOS-based Schottky diode as a function of wavelength and temperature.

Details of the photocurrent spectroscopy can be found in Paper 4. As a light source for photocurrent spectroscopy, I used a 1200 W Xe arc lamp (LOT LS1200Xe) with double monochromator (LOT MSH-300). The light was focused by two parabolic mirrors onto the cryostat's entrance window. I used a Keithley 6430 Source/Measure Unit to apply a fixed bias and measure the PC. To calculate the PC I subtracted the dark current from the current under excitation. To measure the excitation intensity dependence of PC, I employed an appropriate set of neutral density filters. Wavelength-dependent measurements were conducted using a lock-in amplifier (SR830) and a chopper to modulate the frequency. To ensure that the PC had stabilized and was representative, I took several averages and advanced in small wavelength steps. The PC action spectrum was then corrected to account for the effective absorption spectrum of the AOS film embedded in the device. I calculated the effective absorption spectrum using a transfer matrix approach implemented by Bukhard et al. [147]. The real and imaginary part of the refractive index, n and k, for mCBP-CN were measured by Prakhar Sahay (Augsburg University) using Sentec SE 850 Spectroscopic Ellipsometry along with SpectraRay software for the fitting. For other materials, I used the values provided in [147].

3.2 Thermally Stimulated Luminescence

Thermally Stimulated Luminescence (TSL) is an emission in a solid that occurs after the removal of excitation (in this case, UV light) when the temperature increases[148–150]. Details of the TSL measurements can be found in Papers 1–3. TSL measurements are carried out over a temperature range from 4.2 to 300 K using an optical temperature-regulating liquid-helium cryostat with a temperature control unit. The experimental setup is presented in Figure 3.4. In the cryostat, the sample is attached to the end of a sample holder and is suspended in a helium heat-transfer gas environment inside the inner sample chamber.
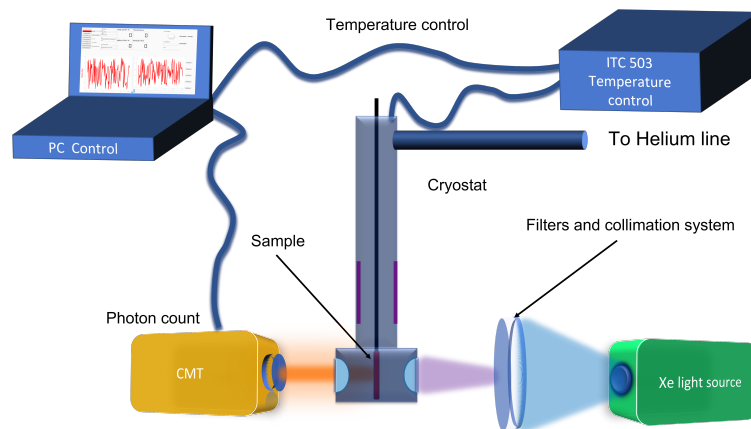

Figure 3.4: Thermally stimulated emission experimental setup

The typical TSL procedure is shown in Figure 3.5. Samples are firstly cooled to 4.2 K and then irradiated for 3 min with light (cw-excitation) selected by appropriate sets of cut-off filters from a 100W high-pressure Hg lamp. No sample heating occurs during UV-light illumination. The studied organic films do not exhibit any notable photodegradation during the measurements. After ceasing the photoexcitation, samples remain in the dark at a constant temperature, for a specified dwell time (typically 10 minutes). This allows all isothermal emission processes, such as phosphorescence and the isothermal recombination of short-range geminate charge-carrier pairs, to decay to negligible levels [62, 77, 118]. Then TSL is detected upon heating the sample, and the thermally stimulated emission is collected using a curved photomultiplier tube (CMT) (C193YE Proxyvision), which is positioned adjacent to the cryostat window. This CMT demonstrates a typical dark count rate < 10 cps and operates in photon-counting mode.
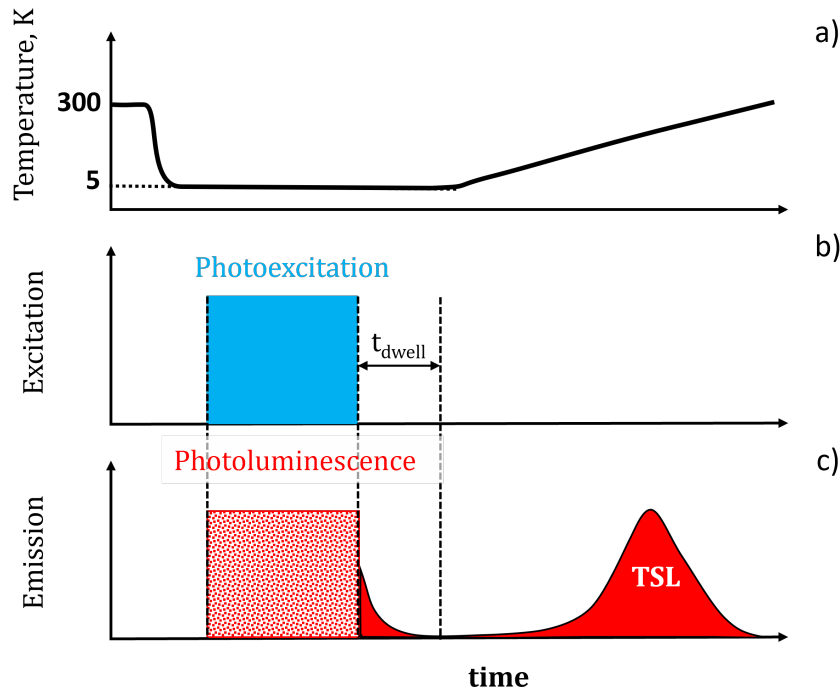
Figure 3.5: Schematic representation of the TSL experiment procedure, illustrating the relationship between temperature (a), excitation (b), and emission (c) over time.

Since the TSL technique is an *"exotic technique"*, I will now provide a brief description of the physical processes underlying the TSL process, beginning with the simplest case of thermally assisted release from a monoenergetic trap

3.2.1 Thermally assisted release from a monoenergetic trap

The simplest case of TSL is the thermally assisted release of a charge carrier from a monoenergetic trap (Figure 3.6). This process is illustrated schematically in Figure 3.6 for a single crystalline material with monoenergetic hole (E_{t,h^+}) and electron (E_{t,e^-}) traps, where $E_{t,h^+} >$

E_{t,e^-}. The probability of thermal release from a trap of depth $E_{trap} is described by Boltzmann distributio$
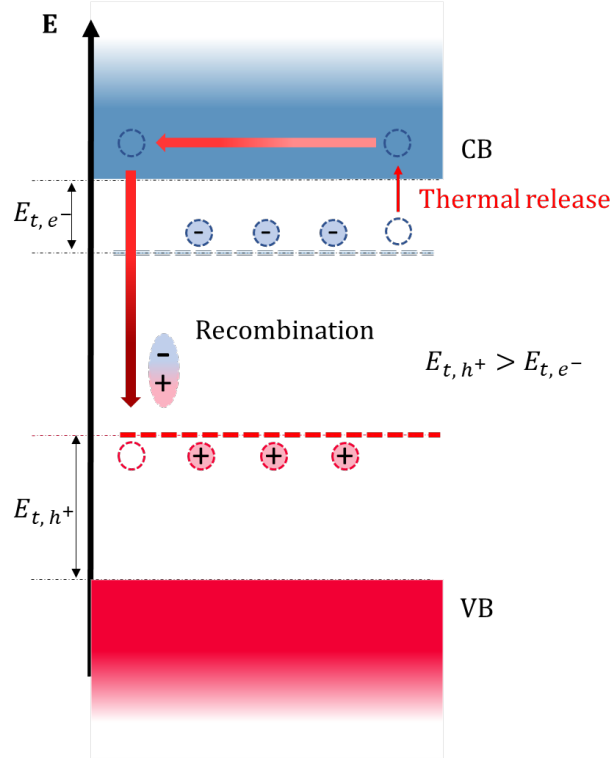

Figure 3.6: Energetic diagram of a single crystal with discrete trap levels. As the temperature rises, a carrier is thermally liberated from the trap state e^-. Following its release, the electron moves through a conduction band and then reaches the recombination center h^+, where the carrier subsequently undergoes radiative recombination

152] : $p = s \cdot exp(-\frac{E_{trap}}{k_b T})$ (3.3) where s is the *frequency factor*, k_b is Boltzmann constant If one considers the trap as a potential box, then s will represent the product of the frequency at which the electron strikes the box's sides and the reflection coefficient [150–152]. Therefore, it is reasonable to suppose s to be of an order less than that of the vibrational frequency, $\sim 10^{12} \ s^{-1}$.

Assuming first-order kinetics, and given that the total number of trapped charge carriers at time t is n, the release rate is:

$$\frac{\partial n}{\partial t} = -n \cdot s \cdot exp(-\frac{E_{trap}}{k_b T}) \tag{3.4}$$

When a charge carrier is released from the trap, it reaches – either the Conduction Band (CB) or Valence Band (VB) (for crystalline materials). It subsequently advances to the deeply trapped countercharge (recombination center) without being re-trapped and undergoes radiative recombination. The TSL intensity I_{TSL} is proportional to the release rate and can be described as[152]:

$$I_{TSL} = -I_0 \frac{\partial n}{\partial t} = -I_0 \cdot s \cdot n \cdot exp(-\frac{E_{trap}}{k_b T}) \tag{3.5}$$

where I_0 is the TSL process constant.

Considering that $dT = \beta \cdot dt$, where β is the heating rate, One can integrate Equation 3.4 over time t and substitute the result into Equation 3.5 which yields:

$$I_{TSL} = I_0 \cdot n0 \cdot s \cdot exp(-\frac{Etrap}{k_b T}) \times exp\left[-\int_0^T \cdot \frac{1}{\beta} \cdot s \cdot exp(-\frac{E_{trap}}{k_b \hat{T}})d\hat{T}\right] \qquad (3.6)$$

Here n_0 denotes the initial number of charge carriers. Figure 3.7a shows the numerical solution of Equation 3.6 for different E_{trap}. The calculated TSL curves feature wide peaks, indicative of the stochastic nature of the thermal release. As the trap depth increases, the TSL peak progressively shifts towards higher temperatures and broadens.
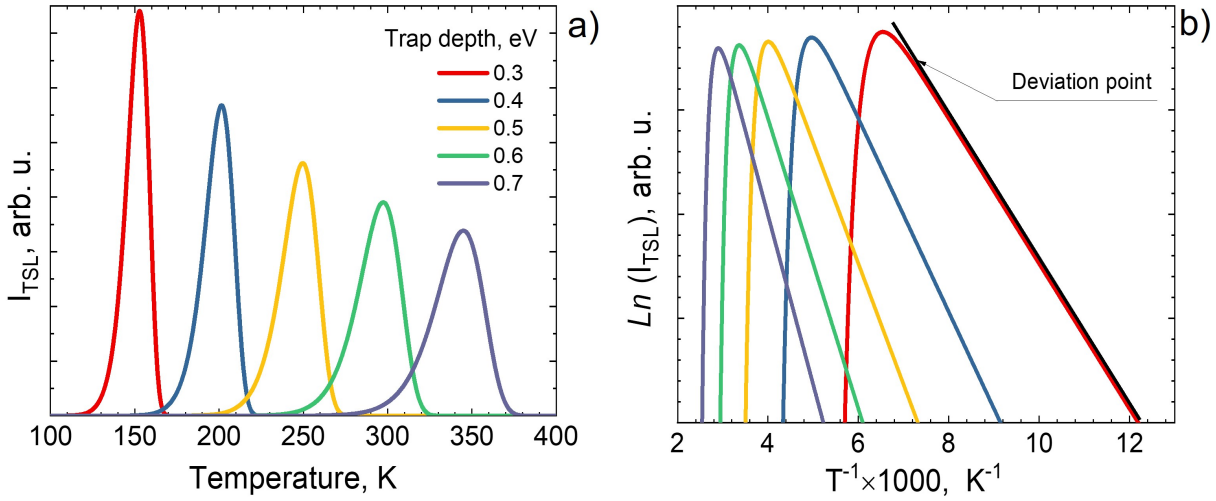
Figure 3.7: Calculated TSL curves (a) for the different trap depths, $s_0 = 2.8 \cdot 10^9$, The linear fit of the calculated TSL curves in Arrhenius coordinates is shown in (b). The "Initial rise method" is utilized, and the black line highlights the region where the TSL curve aligns with Equation 3.7.

3.2.2 The initial rise method

To estimate the trap depth, one can use the Initial Rise method. This is a simple and versatile approach, particularly effective for monoenergetic and well-separated traps[152, 153]. Using the initial rise method the trap depth can be determined by analyzing the low-temperature region of the TSL curve, specifically where the TSL signal begins to increase (initial rise). A detailed theoretical justification for this method is presented below. Equation 3.6 can be simplified. The exponent on the right-hand side of Equation 3.6 is a sharp function of T, approaching unity when $k_b T << E_{trap}$. Thus, under "low-temperature conditions" where $k_b T << E_{trap}$ holds, I_{TSL} depends only on the left-hand side of Equation 3.6. Consequently, the equation can be reduced to:

$$I_{TSL} \propto I_0 \cdot n_0 \cdot s \cdot exp(-\frac{E_{trap}}{k_b T}) \qquad (3.7)$$

Equation 3.7 is used for the trap depth estimation and involves plotting the logarithm of the TSL curve's low-temperature part against reciprocal temperature i.e., in the Arrhenius representation. As seen in Figure 3.7b, the low-temperature part of the TSL curves aligns with a straight line. Notably, the slope of the TSL curves becomes steeper as the trap depth increases.

Unfortunately, the initial rise method can not be applied to systems with a distribution of trap states' energies. For a systems with a trap distribution $\rho(E_{trap})$, the total TSL curve I_{TSL} is determined by $I_{TSL} = \sum_0^n I_{TSL}(E_i)$ where $E_i \in \rho(E)$.

In the case of quasi-continuous conditions, one can replace the sum with an integral, assuming a constant transport level position for all E_i:

$$I_{TSL} = \int_{-\infty}^{+\infty} \rho(\hat{E}) \cdot I_0 \cdot s \cdot \exp(-\frac{\hat{E}}{kT}) \times \exp\left[-\int_0^T \cdot \frac{1}{\beta} \cdot s \cdot \exp(-\frac{\hat{E}}{k_B \hat{T}}) d\hat{T}\right] d\hat{E} \qquad (3.8)$$

where $\rho(E)$ is the trap density distribution. Fitting TSL curves with equation (3.8) is not feasible, which motivates an alternative approach.

For systems with a distribution of trap states' energies, for accurate estimation of trap depth, it is necessary to utilize the fractional thermally stimulated luminescence technique.

3.2.3 Fractional TSL

Fractional heating of TSL is widely used to quantify the energies of the trapping states in solids. The TSL glow curves, $I_{TSL}(T)$ of AOS are typically broad and unstructured due to overlapping contributions from localized states and traps with different energy levels. Therefore, to determine the trap energetics and their distribution, it is necessary to perform fractional TSL measurements [154]. Fractional (or partial) TSL [154] is an extension of the "initial rise method," where small heating and cooling cycles are superimposed on a constant heating ramp[77]. This approach allows for the partial release of trapped charges and enables the accurate determination of the corresponding activation energies ($\langle E_a(T) \rangle$) of the traps. This technique is particularly effective for studying AOS with a continuous trap distribution [77].

In the fractional TSL technique, each heating-cooling cycle i begins by heating the sample from an initial temperature $T_{initial,i} = T_0 + (i-1)\Delta T_{step}$, $(T_0 = 5K, \Delta T_{step} = 3....5K)$ to the final temperature $T_{final,i} = T_{initial,i} + \Delta T_{depth}$ $(\Delta T_{depth} = 10...30K)$ at a constant heating rate β, as illustrated in Figure 3.8.
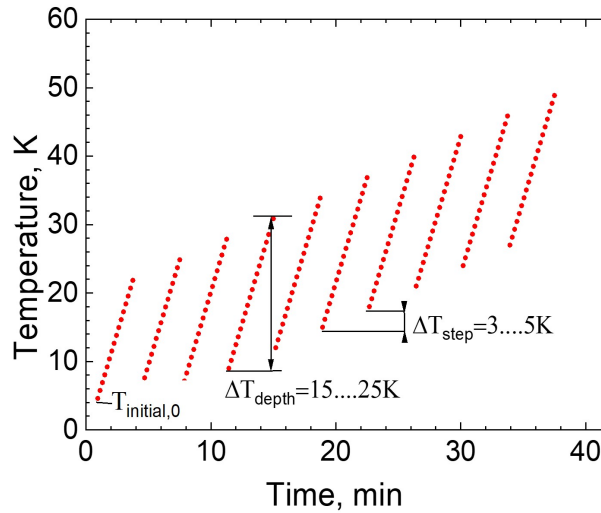

Figure 3.8: Schematic illustration of heating/cooling cycles used in fractional TSL method

Here T_{step} is the temperature differences between heating-cooling cycles and ΔT_{depth} is the amplitude that defines the upper-temperature limit of the heating-cooling cycle.

During the heating cycle, I record the thermally stimulated emission $I_{TSL}(T)$, as shown in Figure 3.9a. Then, I cool the sample down to the next temperature point $T_{initial,i}$. In the subsequent heating-cooling cycle, charges are released from deeper and deeper states. Thus, for each cycle, I can estimate the corresponding activation energy $\langle E_a(T)1 \rangle$ using an Arrhenius analysis (Figure 3.9b)[77]:

$$\langle E_a \rangle i = \frac{\partial Ln(I_{TSL}(T))}{\partial(1/k_B T)} \ \ at \ \ \beta = const \tag{3.9}$$

where $I_{TSL}(T)$ is the intensity of the TSL, T is the temperature, k_B is the Boltzmann

constant.

By gradually increasing T_{final}, I scan the entire spectrum of activation energies corresponding to the TSL curve and plot the calculated activation energies $\langle E_a \rangle$ against the mean temperature of the heating-cooling cycle[154]. Thus, I obtain the $\langle E_a(T) \rangle$ dependence, which is the main result of the fractional TSL measurements (Figure 3.10a). All organic compounds studied in this thesis exhibit a $\langle E_a(T) \rangle$ that increases linearly with temperature and can be approximated by the following empirical relation[77]:

$$\langle E_a(T) \rangle = 0.0032 \times T - 0.091 \ in \ eV \tag{3.10}$$

I further use this empirical equation, Equation 3.10 to convert the temperature scale to a
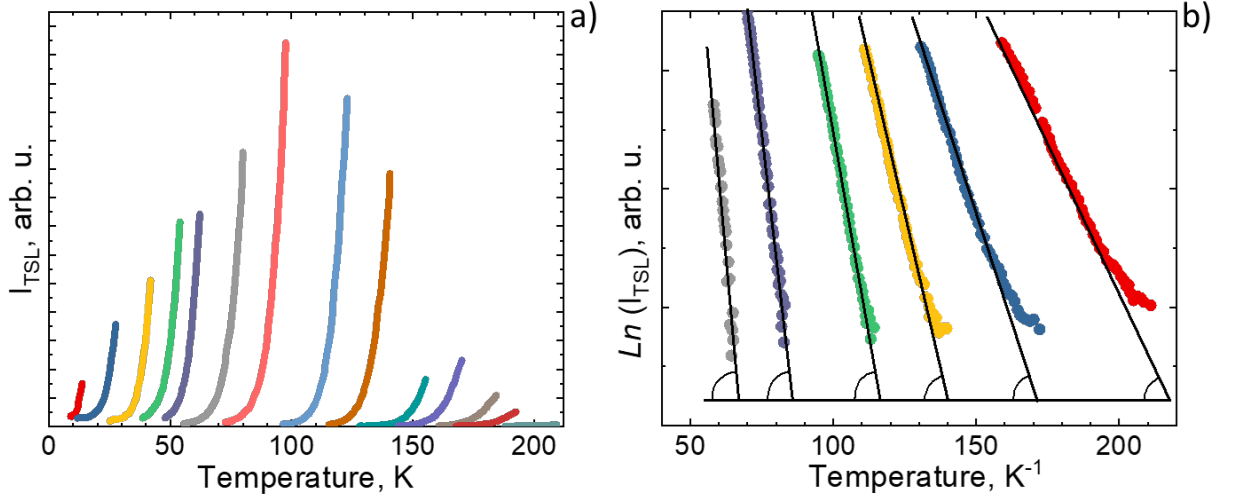
Figure 3.9: TSL intensity (I_{TSL}) measured during heating cycles, and b) Arrhenius plots ($ln(I_{TSL})$ vs.$1/T$) illustrated for different heating cycles to calculate activation energy ($\langle E_a \rangle$) during each heating cycle.

trap energy scale for the analysis. A trap distribution function, $\rho(E)$, is then determined in arbitrary units as follows[77]:

$$\rho(E) \propto \frac{I(\langle E_a(T) \rangle)}{d \langle E_a(T) \rangle / dT} \tag{3.11}$$

where $I(\langle E_a(T) \rangle)$ represents the TSL curve after converting the temperature scale to the energy scale using Equation 3.10. It is worth nothing that for a monoenergetic trap $\frac{I(E)}{dE/dT} \rightarrow \infty$ as $dE/dT \rightarrow 0$. This implies observing a plateau in the temperature dependence of $\langle E_a(T) \rangle$, indicating the mean activation energy remains constant.

In the fractional heating mode, if $\rho(E)$ is distributed in a quasi-continuous manner, $\langle E_a(T) \rangle$ is mainly determined by the frequency factor s. The latter is defined as follows [155]:

$$s = \nu_0 \ exp\left(-2\gamma a\right) \tag{3.12}$$

In general, the parameter $2\gamma a$ in Equation 3.12, where γ is inverse localization radius and a is hoping distance, is expected to maintain relatively constant across studied materials. This

is because both a and γ, are not expected to differ significantly for the low-molecular-weight materials considered herein. My experimental findings support this assumption, as illustrated in Figure 3.10a. The data indicates that variations in temperature-dependent activation energy among the materials are negligible

According to Equation 3.12 [156], increasing the distance between charge-transporting molecules, for example by diluting the system in an amorphous matrix, increase γa. This, in turn, will lead to a decrease in the temperature dependence of activation energy $\langle E_a(T) \rangle$ (Figure 3.10b). It is anticipated that higher temperatures will be required to release charge carriers from traps if the frequency factor decreases. The frequency factor in Equation 3.12
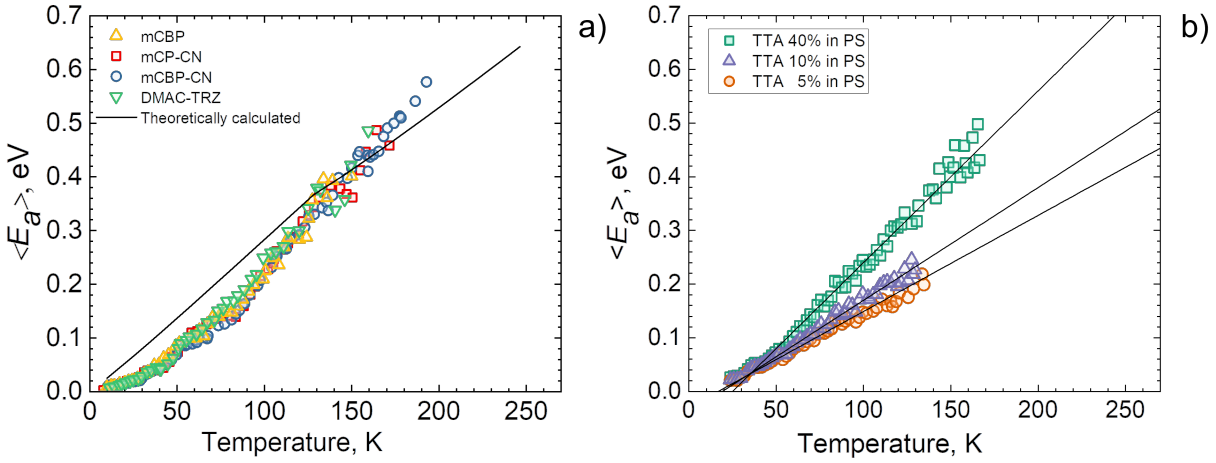
Figure 3.10: Temperature dependence of $\langle E_a(T) \rangle$ in mCBP, mCP-CN, mCBP-CN, and DMAC-TRZ films as well as theoretically calculated value according to Arkhipov [157] (a), the effect of dopant dilution on $\langle E_a(T) \rangle$, the activation energies are measured for different tri-p-tolylamine(TpTA) concentration in an amorphous matrix (b) from [155].

can be determined experimentally. At the maximum of the TSL peak, s is defined by the following equation [156]:

$$\langle s \rangle = \frac{\beta \langle E_m \rangle}{k T_m^2} \times exp \left(\frac{\langle E_m \rangle}{k T_m} \right) \tag{3.13}$$

where T_m and E_m are the temperature and the activation energy of the maximum of the TSL peak, respectively. Equation 3.13 have been used to estimate inverse localization radius values for molecularly doped polymers [156].

3.2.4 TSL in AOS

The following section is a summary of *Chem. Phys.*, 2001, 266(1), 97-108 [157]. To capture the charge transport features of AOS, Arkhipov, and co-workers have developed a hopping-transport model for the TSL process [157]. This model is based on the concept of a thermally stimulated random walk of a charge carrier within a positionally and energetically random system of hopping sites. It was utilized for analyzing TSL in disordered organic materials

and effectively captures the key characteristics of the TSL process observed in molecularly doped polymers [157, 158].

ODOS formation via low-temperature energy relaxation

In TSL experiments, low energy sites of DOS distribution are populated by photogenerated charges at low temperatures, leading to the formation of the occupied DOS (ODOS) distribution. Unlike crystals, the charge relaxation in AOS is characterized by downward hopping within a Gaussian DOS:

$$g(E) = \frac{N_t}{\sqrt{2\pi}\sigma} \cdot \exp\left(-\frac{\varepsilon^2}{2\sigma^2}\right) \tag{3.14}$$

where N_t is the total number of states.
Since low-energy sites act as traps TSL can be observed in neat films of AOS. At 4.2K, the typical temperature for the DOS population in TSL experiments, charges predominantly undergo energetically downward hops due to a lack of thermal activation. According to the Miller-Abrahams Equation 3.29 the downward hopping rate to the state E_i is :

$$\nu_\downarrow = \nu_0 exp\left(-\frac{2R(E_i)}{\alpha}\right) \tag{3.15}$$

Where, the average distance to the hopping neighbor with energy less than E_i is given by:

$$R(E_i) \simeq \left\{(4\pi/3)\int_{-\infty}^{E_i} g(x)dx\right\}^{-1/3} \tag{3.16}$$

The above equation indicates that the distance between available sites for the downward hopping in a Gaussian DOS increases significantly as energy decreases. For instance $R(E_i)$ in a Gaussian DOS for states below 3σ is $58a$, 4σ is $2500a$, 5σ is $2.75 \cdot 10^5 a$, where a represents the lattice constant. Consequently, the $\nu_\downarrow$ decelerates as the charge undergoes a series of downhill hops. As a result, the charges in the center DOS distribution exhibit a much faster $\nu_\downarrow$ compared to those located at the tail of the DOS.
Arkhipov [157, 158] rationalized the above concept and showed that the ODOS $\rho(E,t)$ as a function of DOS and time, is given by [157]:

$$\rho(E,t) \cong \frac{\pi}{6\gamma^3} \cdot \frac{[ln(\nu_0 t)]^3}{1 - exp\left[-(\frac{\pi N t}{6\gamma^3})[Ln(\nu_0 t)]^3\right]} \, g(E)\times$$

$$\times exp\left[-\frac{\pi}{6\gamma^3} \cdot [ln(\nu_0 t)]^3 \cdot \int E^\infty dE \cdot g(E)\right] \tag{3.17}$$

where γ is the inverse localization radius, t is a dwell time before heating run begins and $g(E)$ is the Gaussian DOS distribution, ν_0 is the attempt-to-escape frequency.
In Figure 3.11a the numerical solution of Equation 3.17 demonstrates that with increasing time, the ODOS shifts toward lower energy and narrows. Notably, (Figure 3.11b) shows, that
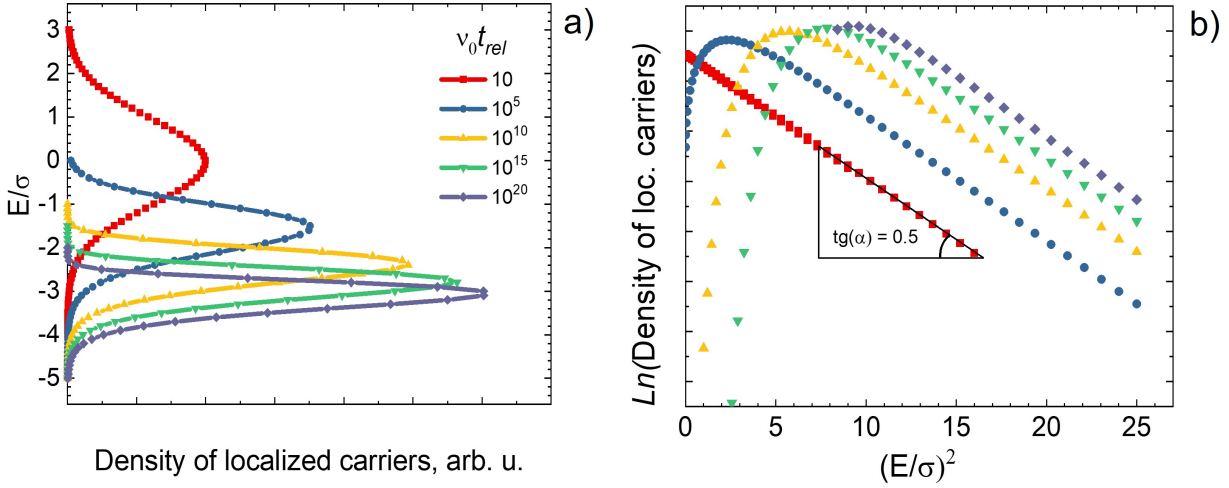
Figure 3.11: Time dependence of ODOS in a random hopping system with a Gaussian DOS distribution at zero temperature (a), the numerical solution of Equation 3.17 [157]. "Gaussian analysis" of *ODOS*(a) – The low energy tail of the ODOS always follows the DOS function (b)

the low-energy part of the ODOS retains a constant slope over time, indicating that DOS defines the low-energy part of ODOS. [157].

During downward hopping, a carrier occupies a particular localized state at time t after photogeneration if the probability of hopping into a deeper state is low. A time-dependent energy level, referred to as the demarcation energy $E_{d(t)}$ (subsection 2.2.1), can then be defined. This energy level separates charge carriers into two groups based on their likelihood of undergoing further relaxation within a time interval t. Carriers located at sites above $E_{d(t)}$ are more likely to find hopping neighbors and proceed with relaxation. In contrast, charges positioned below the demarcation energy tend to stay in local minima (currently deep traps), for an extended period (t) and therefore follow the low energy part of the DOS. [157].

As a consequence, the most reliable information about the DOS distribution can be derived from the low-energy part of ODOS. Considering that charges are liberated from the deepest traps at higher temperatures, one can infer that the high-temperature wing of TSL curves is an exact replica of the deeper portion of the DOS distribution and yields the effective DOS width σ_{DOS} [157].

More strictly, for the charges located below $E_{d(t)}$ the right-hand side of Equation 3.17 equals to *1* then ODOS becomes only the function of DOS $g(E)$. In our scenario, Equation 3.17 follows a Gaussian distribution [157]:

$$\rho(E,t) \cong \frac{\pi}{6\gamma^3} \frac{[\ln(v_0 t)]^3}{1 - \exp\left\{-(\pi N_t/6\gamma^3)[\ln(v_0 t)]^3\right\}} g(E)$$

$$E < E_d(t)$$

(3.18)

Whereas $E_{d(t)}$ is defined by [157]:

$$E_\mathrm{d}(t) \approx \sigma \sqrt{2 \ln \left\{ \frac{N_\mathrm{t}}{12\sqrt{2\pi}\gamma^3} \left[\ln\left(v_0 t\right)\right]^3 \right\}} \tag{3.19}$$

The dwell time t_{rel} after photoexcitation during the TSL experiment, falls within the range from 10^2 to 10^5 s. Given that $\nu_0 = 10^{13} s^{-1}$ the product $\nu_0 t_{rel}$ is in the range of 10^{15} to 10^{18}. From Figure 3.11a, one can see that the TSL signal has a minimal dependence on the dwell time within this specified range. Specifically, the average energy of the carrier distribution shifts by less than 7 % of σ_{DOS}. Consequently, the TSL signal remains unaffected by the dwell time after photoexcitation (in the range from 10^2 to 10^5 s). Then for energies below the demarcation level, one can write that [157]:

$$\rho(E, t) \approx \rho_0(E_\mathrm{d}(T)) \tag{3.20}$$

This implies that ODOS is time-independent.

Hopping model of TSL

In a similar manner to inorganic materials, the rate-limiting step in the TSL of AOS (Equation 3.23) is the thermal activation of charges from ODOS to transport energy level (see Figure 3.12). The differences between demarcation energy and transport energy level determine the activation energy required for charges to be released from traps (Equation 3.23). Once a charge carrier reaches the transport energy level, it is assumed to have enough energy to continue hopping toward a deeply trapped countercharge and form an exciton. [157]. At sufficiently high temperatures the demarcation energy is obtained as [157]:

$$E_\mathrm{d}(T) = kT \left[\ln\left(\frac{v_0 T}{\beta}\right) - \left(\frac{6}{\pi}\right)^{1/3} \frac{\gamma}{N_\mathrm{t}^{1/3}} \right] \tag{3.21}$$

The transport energy is obtained as [157]:

$$E_\mathrm{tr} = -\left(\frac{6}{\pi}\right)^{\frac{1}{3}} \frac{\gamma}{N_t^{\frac{1}{3}}} kT \tag{3.22}$$

The activation energy measured in TSL by definition is just differences between $E_\mathrm{d} - E_\mathrm{tr} = \langle E_a(T) \rangle$. A distinctive feature of the demarcation energy is its independence from DOS [157]. Indeed, according to the Equation 3.21 the demarcation energy is influenced by the attempt-to-hop frequency and the ratio $\gamma/N_t^{1/3}$. While v_0 remains relatively constant across different materials, the $\gamma/N_t^{1/3}$ ratio varies depending on the concentration of transport molecules. In the materials I studied, the concentration of transport molecules is anticipated to remain relatively constant. This is evidenced by minor variations in $\langle E_a(T) \rangle$ for mCBP-CN, mCP-CN, and DMAC-TRZ, as shown in Figure 3.10a. Given E_tr and $E_\mathrm{d}(T)$ the TSL intensity
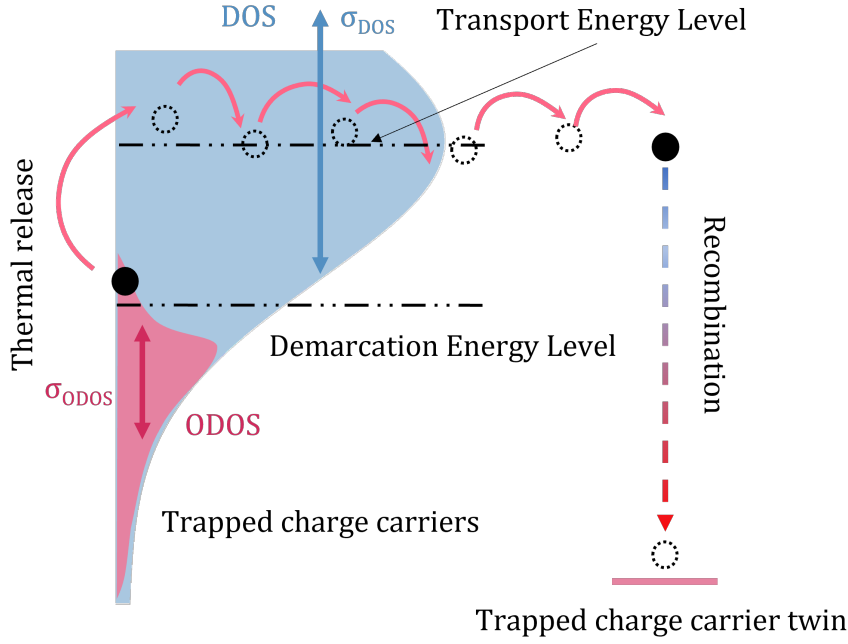
Figure 3.12: The TSL process in AOS. This figure depicts the thermally activated hopping process. Upon heating, charge hops from the ODOS to the transport energy level, forming an exciton with a deeply trapped counthercharge, which then undergoes radiative recombination.

can be expressed as [157]:

$$
I(TSL) \propto v_0 kT \rho_0 \left[E_{\mathrm{d}}(T)\right] \exp\left[-\frac{E_{\mathrm{d}}(T) - E_{\mathrm{tr}}(T)}{kT}\right]
$$
$$
\approx k\beta \rho_0 \left[E_{\mathrm{d}}(T)\right]
$$

(3.23)

Equation 3.23 explicitly attributes the ODOS with the TSL curve. One can theoretically justify the direct extraction of the energy disorder parameter from *TSL* using Equation 3.18 According to Equation 3.18 and Equation 3.20, the high-temperature part of I_{TSL} is a function of the DOS only. The σ_{DOS} then can be extracted through the so-called Gaussian analysis by plotting the logarithm of intensity versus the square of energy (see equation Equation 3.24), as shown in Figure 3.11(b).

The high-temperature part of the TSL curve follows [62, 77]. :

$$
I_{TSL} \propto \exp\left(-\frac{\langle E_a(T)\rangle^2}{2\sigma^2}\right) \Rightarrow ln(I_{TSL}) \propto -\frac{\langle E_a(T)\rangle^2}{2\sigma^2}
$$

(3.24)

where $\langle E_a(T)\rangle$ is $Ed - E_{tr}$.

The energetic disorder derived from TSL typically reveals the DOS of shallower trapped charges type (electron or hole). Thermally released charges recombine with their more deeply trapped counterparts [118]. Since TSL is an electrode-free technique, the number of electrons and holes within the film remains constant, ensuring material neutrality throughout the entire TSL process. As a result, by the time the temperature is high enough to release the deeper carriers, they have already recombined [118]. Details of the analysis of *TSL* curves of

the AOS is discussed in (Papers 1 and 2), while the chapter should give the main idea of a TSL phenomenon.

3.3 Kinetic Monte Carlo simulations of charge carrier relaxation processes

Charge carrier relaxation in a lattice can be analyzed using the master equation. At any point in time, the probability $P_i(t)$ for being in state i obeys the Master Equation (ME) [159]:

$$\frac{\partial}{\partial t} P_i(t) = -\sum_{j \neq i} k_{ij} P_i(t) + \sum_{j \neq i} k_{ji} P_j(t) \tag{3.25}$$

From a mathematical standpoint, Equation 3.25 is a system of coupled differential rate equations. Unfortunately, the explicit solution of Equation 3.25 becomes unfeasible as the number of states involved in the charge transport increases. Kinetic Monte Carlo modeling can be used to solve the above equation [160, 161]. The problem then falls into the category of time-continuous Markov processes in discrete space, where the system evolves through a sequence of states $P_{t,i} \in X$ from a state space X, which depends on a model at transition times $t_0 < t_1 < ... < t_i < ...$ [160, 161]. It should be noted that the likelihood of the hop is intended to be based solely on the transition probabilities from the current state: charges have no memory – the Markovian process's condition.

I used the following methodology to study a charge distribution. I did the KMC simulations by employing an isotropic three-dimensional (3D) cubic lattice ($100 \times 100 \times 100$ lattice sites) with a lattice constant of 1.0 nm. I considered both random- *(GDM)* and spatially correlated energetic disorder *(CDM)* [77]. The site energies for the random disorder were selected from a Gaussian distribution $g(\varepsilon)$ Equation 3.26 with a standard deviation σ_{DOS} centred at zero energy:

$$g(\varepsilon) = \frac{N}{\sqrt{2\pi}\sigma} exp\left[-\frac{1}{2}\left(\frac{\varepsilon}{\sigma_{DOS}}\right)^2\right] \tag{3.26}$$

For systems with a correlated disorder, I calculated the cite energies using the dipolar disorder model [77, 162]. For that, a cubic lattice was populated with randomly aligned dipoles separated by a distance a. I chose a dipole moment whose magnitude produces a disorder strength of 50 meV using the equation $\sigma_{DOS} \approx 2.35 \frac{e \cdot d}{\varepsilon \cdot \varepsilon_0 \cdot a^2}$ and kept it constant for all calculations [77, 162]. By Ewald's summation [163], the on-site energy E due to charge-dipole interactions was determined as [77, 162]:

$$E_i = -\sum_{j \neq i} \frac{e\boldsymbol{d}_j \cdot (\boldsymbol{r}_j - \boldsymbol{r}_i)}{\varepsilon_0 \varepsilon_r |\boldsymbol{r}_j - \boldsymbol{r}_i|^3} \tag{3.27}$$

where j is the number of sites within a cube size of 30 lattice sites around site i, e the unit charge, ε_0 the vacuum permittivity, and ε_r the relative permittivity of the material. Figure 3.13c and d, respectively. The resulting DOS adheres to a Gaussian distribution, with a width σ_{DOS} proportional to d.

As illustrated in Figure 3.13a and b, charge-dipole interactions have a significant effect on the energy landscape within an arbitrary slice (2D cross-section) of the lattice [77]. The energy

of sites for random disordered (Figure 3.13a) is uncorrelated. Conversely, in a system with the correlated disorder (Figure 3.13a), it is more likely that sites with the same energy will be found in close proximity. One can calculate the correlation between sites separated by a distance r_{ij} by the spatial correlation function $C(r_{ij})$ [77]. This function is defined as follows [103]:

$$C\left(r_{ij}\right) = \frac{\langle(E_i - \langle E \rangle)(E_j - \langle E \rangle)\rangle}{\langle(E_i - \langle E \rangle)^2\rangle} \tag{3.28}$$

where E_i and E_j are the energies of the sites i and j separated by a distance r_{ij} and, $< \ldots >$ represents the expectation value.

If E_i and E_j are fully correlated, then $C\left(r_{ij}\right)$ is unity, while if they are uncorrelated, then $C\left(r_{ij}\right))$ is 0. The spatial correlation functions evaluated for CDM and GDM are shown in Figure 3.13c and d, respectively. Unlike random disorder, where the correlation function is zero, $C\left(r_{ij}\right)$ exhibits a $\dfrac{1}{r_{ij}}$ dependence on distance for correlated energetic disorder. As anticipated, for long-range charge-dipole electrostatic interactions.

The hopping rate between an initial site of energy E_i and a final site of energy E_j is determined by the Miller-Abrahams rate [75]:

$$k_{ij} = k_0 \; exp\left[-\frac{|E_j - E_i| + (E_j - E_i)}{2k_B T}\right]$$
$$k_0 = \nu_0 \; exp\left(-2\gamma R_{ij}\right) \tag{3.29}$$

where k_0, the MA rate prefactor, is determined by the hopping distance Rij. The inverse localization radius γ relates to the electronic coupling matrix element between the adjacent sites. ν_0 is the attempt-to-escape frequency usually being close to an intermolecular phonon frequency, k_B is the Boltzmann constant, and T is temperature [75–77]. The parameter γ was isotropic in all directions. I performed the KMC simulations considering the hopping contributions to the two nearest hopping sites, within the variable range hopping (VRH) regime. To calculate the charges distribution I used the constant time step KMC (*ct-KMC*) approach, implementing the following algorithm:

1. Randomly generate the charge on site i.

2. Uniformly sample a transition from state i to a state j $(i \neq j)$ among the 124 two-nearest neighbors N_i.

3. Calculate the corresponding transition rate k_{ij} using the MA equation Equation 3.29.

4. Accept or reject the transition event: the event is accepted if $f_{ij} = \frac{k_{ij}}{v_0} > U$, where U is a uniform random number from the interval $(0, 1]$, and v_0 is the isoenergetic hopping rate to the nearest neighbor.

5. *If* the event is accepted, execute the transition $i \rightarrow j$ and update the charge coordinates. *Else*, the charge carrier continues to occupy the current site i.

6. Update the simulation time with Δt, which is a random number following an exponential distribution: $\Delta t = \frac{1}{v_0 N_{tot}} \ln\left(\frac{1}{U}\right)$, where U is a random number drawn from the uniform

distribution $U \in (0, 1]$.

7. *If* the simulation time is less than the required time, go to step 2.
   Else, terminate the simulation.

The *ct-KMC* method is utilized to gain insight into charge carrier relaxation in both short and intermediate-time regimes [77]. As charges relax within the DOS, the hopping rates k_{ij} (and k_T) decrease rapidly by several orders of magnitude, leading to a significant increase in computation time [77].
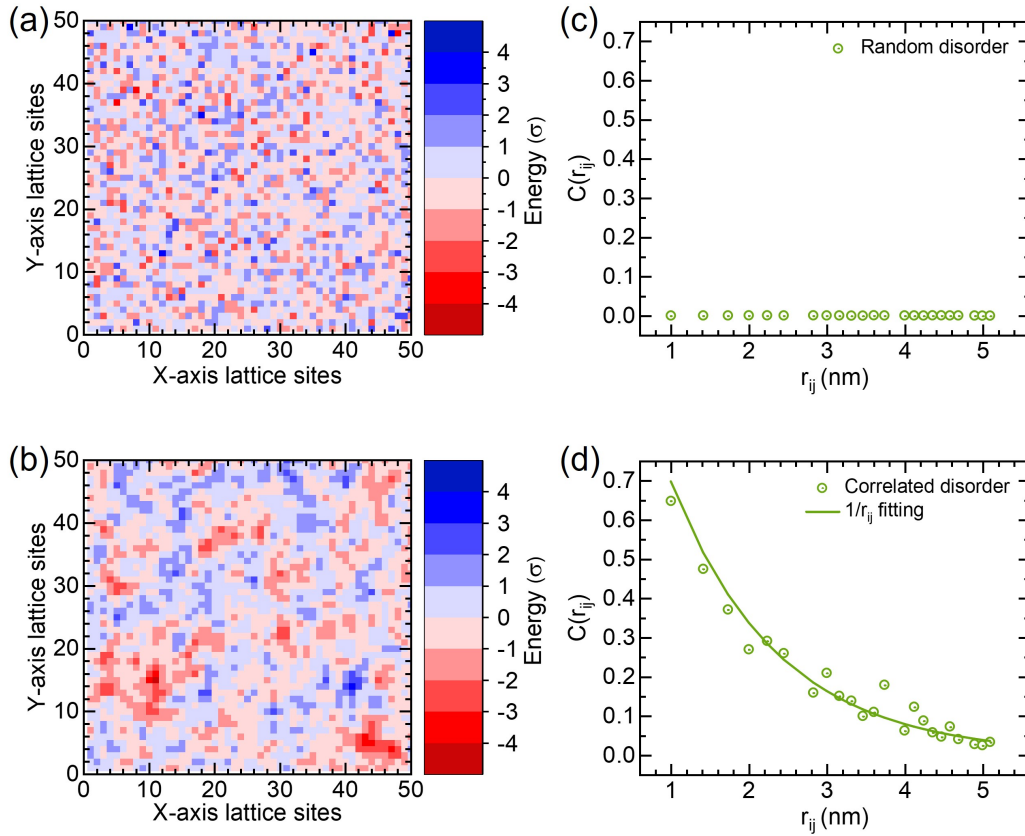

Figure 3.13: Heatmap of the energetic landscape for a system with a) random disorder and b) correlated disorder. The variation of the spatial energy correlation function, $C(r_{ij})$ (see Equation 3.28) with distance for c) random disorder system and d) correlated disorder system. Adapted from "*Monitoring the Charge-Carrier-Occupied Density of States in Disordered Organic Semiconductors under Nonequilibrium Conditions Using Thermally Stimulated Luminescence Spectroscopy*" by A.Stankevych, R. Saxena, A. Vakhnin et. al., Phys. Rev. Applied, 19(5), **2023**, p. 054007, https://doi.org/10.1103/PhysRevApplied.19.054007 [77]. Reprinted from American Physical Society according to the CC BY license.

4 State-of-the-Art

4.1 Introduction

According to the Gaussian Disorder Model (GDM), the charge mobility in amorphous organic semiconductors (AOS) depends on the half-width of the DOS, commonly referred to as energetic disorder. [30]. The Gaussian shape of the DOS naturally arises from the central limit theorem [30] and is the most frequently used approximation for the DOS [30, 31, 52, 74]. Since the introduction of GDM [30], the exact shape of the DOS has been a subject of ongoing investigation and debate. While the Gaussian shape accurately describes the central region of the DOS, experimental and theoretical evidence suggests that in the tail states—the low-energy regions where charge transport predominantly occurs—an exponential distribution can emerge. This phenomenon has been supported by various studies [64–66, 72, 164–166], which emphasize that the DOS distribution in the tail states can exhibit a complex structure, underscoring the critical role these tail states play in governing charge transport. Characterization of the localized states in AOS, which include both spatial and energetic distributions, presents a significant challenge. Unfortunately, charge DOS is not directly amenable to probing by absorption spectroscopy because the optical spectra of molecular solids are governed by excitonic transitions, unlike the valence band to conduction band transitions in inorganic semiconductors [30]. Recognizing the issue, substantial progress was achieved in characterizing the DOS distribution. Various known methods can be grouped into categories: charge transport measurements, optical and thermally activated spectroscopy, scanning probe methods, as well as theoretical studies.

The following section is not intended to provide a comprehensive review of all possible DOS measurement techniques but instead aims to highlight the techniques that have significantly influenced this research field, offering a brief overview of their advantages, disadvantages, and disparities.

4.2 Charge transport measurements.

The determination of the DOS through charge transport measurements typically involves modeling the temperature and electric field-dependent mobility using theoretical frameworks such as the Gaussian Disorder Model (GDM) or the Extended Gaussian Disorder Model (EGDM) [167]. To obtain corresponding charge mobilities, space-charge-limited current (SCLC) measurements are typically employed [168, 169].

SCLC

SCLC measurements are conducted using electron- or hole-only devices that consist of a semiconductor sandwiched between two electrodes[168, 169]. The injection of charges from the electrode creates a charged layer, known as space charge, which electrostatically limits the flow of current in the device. The current-voltage relationship for SCLC was first established by Mott and Gurney [170]:

$$J_{SCLC} = \frac{9}{8}\mu\epsilon_0\epsilon_s\frac{V^2}{L^3} \tag{4.1}$$

where: J_{SCLC} is the current density, ϵ_0 is the vacuum permittivity, ϵ_s is the relative permittivity of the material, μ is the charge mobility, V is the applied voltage, and L is the thickness of the sample.

The quadratic dependency of current on voltage is indicative of trap-free SCLC. To ensure the SCLC regime, the current must exhibit the cubic thickness dependence, i.e. $J_{SCLC} \propto L^{-3}$ [170]. The SCLC method has a set of disadvantages. As mentioned earlier, in SCLC, high charge carrier concentrations are often observed, frequently exceeding $n/N > 10^{-5}$, where n/N represents the relative charge carrier concentration, which in turn can affect the DOS width measurements. For an accurate representation of the IV curves in the SCLC measurements, it is crucial to account for the effect of charge density on mobility.

Thus, it is not surprising that the choice of the fitting model has a profound impact on the extracted σ_{DOS} values, thereby complicating its determination. Analysis of IV curves using EGDM[171] yields higher DOS width values than those from GDM[43]. For instance, for the OC1C10-PPV, the sigma DOS values determined by EGDM and GDM were 0.14 eV [171] and 0.112 eV[43], respectively. However, both models give reasonably good IV-fits as shown in Figure 4.1. The SCLC method has gained popularity due to the growing interest in evaluating device characteristics under operando conditions. Since organic semiconductors are typically used in a diode configuration, it is practical to conduct DOS measurements within these devices. In contrast, during TOF measurements, the device operates as a capacitor.

It is also important to highlight that achieving trap-free conditions, essential for the SCLC regime, is not a straightforward task. Often, IV curves display charge-trapping behavior for either electrons or holes[172, 173], which complicates the interpretation of SCLC results. Additionally, for SCLC measurements, it is essential to ensure effective charge injection[174]. This task becomes particularly challenging due to the exponential relationship between injection current and barrier height. Moreover, given that some OLED materials possess work functions extending up to 6.1 eV, careful electrode selection is crucial to ensure accurate SCLC measurements[174, 175].

In recent years, the IV characteristics of devices are commonly fitted directly using GDM or EGDM models [167], as well as through KMC modeling [97, 99, 162].
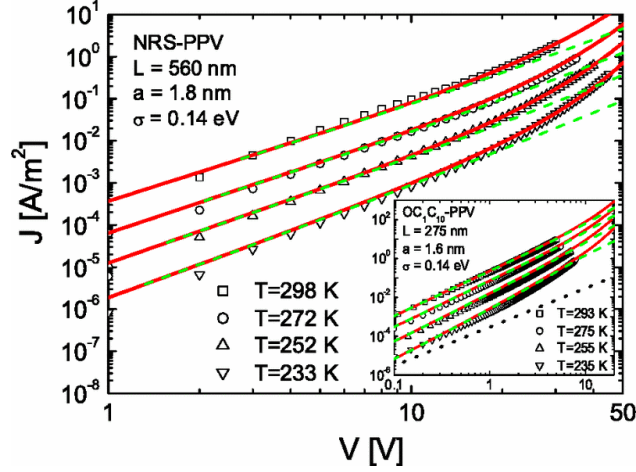
Figure 4.1: Experimental (symbols) and theoretical (lines) current-density vs voltage results for polymer layers of NRS-PPV (main panel) and OC1C10-PPV (inset). Full line: solution of SCLC via EGDM with the T-, n-, and F-dependent mobility. Dashed line: SCLC result without F dependence. Dotted line: SCLC results without n- or F- dependence (shown only in the inset, for $T = 235\ K$). Adapted from "*Unified Description of Charge-Carrier Mobilities in Disordered Semiconducting Polymers*" by Pasveer, W. F. and Cottaar, J., Tanase, C. et. al., Phys. Rev. Lett., 94 (20), **2005**, p. 206601, https://link.aps.org/doi/10.1103/PhysRevLett.94.206601 [171]. Reprinted from American Physical Society according to the CC BY license.

Time-of-Flight

Time-of-flight (TOF) is another method for measuring charge mobility. The TOF method is based on measuring the transit time τ of a packet of photogenerated charges as they travel through an organic film sandwiched between two electrodes. One can estimate the charge mobility using the following equation:

$$\mu = \frac{d^2}{V\tau} \tag{4.2}$$

where μ is mobility, d is the sample thickness, and V is the voltage applied between two electrodes. To accurately determine the DOS width via the TOF method, photogenerated charges are expected to reach the thermal equilibrium prior to being extracted [30, 31, 101, 176]. This condition can only be achieved in a non-dispersive transport regime [101, 176]. The transition from a non-dispersive to a dispersive transport regime was empirically found to occur at a critical disorder parameter $\left(\sigma_{DOS}/k_B T\right)_{cr}$ that depends on the length L of the sample according to $\left(\sigma_{DOS}/k_B T\right)_{cr}^2 = 44.8 + 6.7 \cdot \log_{10} L$, with L being given in cm [176]. That leads in turn to the main TOF limitation namely the requirement for thick films, often above $1\mu m$. Deposition of thick films is impractical, especially for small molecules during material screening phases when only limited quantities of a material are available. For TOF it is also essential for the absorption depth to be sufficiently short so that the photogenerated carriers are densely concentrated within a layer that is much smaller than the film thickness d [31, 176, 177]. This condition can be expressed as $d \gg \frac{\ln 10}{\alpha}$ suggesting that approximately 90 % of the photogenerated carriers are confined within a layer of thickness of $ln(10)/\alpha$. For example, a $10\mu m$ thick sample demands an optical density of 10. Conversely, the standard sample thickness for SCLC measurements is typically a few hundred nanometers[178, 179].

In general, it is expected that TOF measurements are more accurate in determining DOS widths compared to SCLC. The TOF signal remains unaffected by high carrier concentration, ensuring that the DOS is not distorted. Thus, the mobility values derived from TOF and SCLC methods might differ. Both types of measurements are characterized by different charge carrier densities. For example, σ_{DOS} value extracted from SCLC measurements for rr-P3HT are approximately 0.054 eV [180]. In contrast, TOF measurements conducted by the same group indicated that the energetic disorder in rr-P3HT is 0.069 eV[181]. For NPB and Spiro-TAD measurements, the energy disorder parameter determined by TOF was found to be 0.075 eV, as reported in [182], and 0.08 eV, according to [183], respectively. While, SCLC studies of NPB and Spiro-TAD indicated an energy disorder of approximately 0.09 eV for both compounds, as detailed in [98].

Here I want to emphasize that the measured σ_{DOS} values are significantly influenced by film morphology, which can cause variations across different studies. For instance, in SCLC studies of NPB and Alq3, the σ_{DOS} values vary based on film thickness, ranging from 0.080 to 0.106 eV for NPB and from 0.130 to 0.140 eV for Alq3, as shown in [184]. In that study, authors suggest that the DOS is affected not only by the interfacial trap states but also by the molecular arrangement on the surface [184].

The charge extraction by linearly increasing voltage

The charge extraction by linearly increasing voltage (CELIV) technique offers an alternative method for determining σ_{DOS} [185–189]. In CELIV measurement a linearly increasing voltage (triangular pulse) extracts thermally generated carriers from the semiconductor film [190]. The mobility can be estimated from:

$$\mu = \frac{2d^2}{3At^2}\frac{1}{1 + 0.36\frac{\Delta J}{J_0}} \tag{4.3}$$

where A is the ramp rate (V/s), d is the device thickness, $\Delta J/J_0$ is the ratio between the average conduction current of the active layer and the average displacement current due to the film capacitance, and t is the time of the current transient maximum[190]. Unlike the TOF technique, which requires thick samples, CELIV measurements can be conducted on relatively thin samples, typically spin-coated films that are only a few hundred nanometers thick [185, 190]. In the CELIV method, the extracted charges are intrinsic and assumed to be in thermal equilibrium [190, 191]. In contrast, in the TOF method, charges are generated through photoexcitation and subsequently undergo thermally assisted energetic relaxation.

In CELIV experiments, for materials that are devoid of intrinsic charges, a laser pulse or an electrode-based injection can be utilized to introduce them. Once these carriers are generated and following a designated delay, they can be extracted from the film. These modified approaches are typically referred to as photo-CELIV[192] and (metal insulator semiconductor) MIS-CELIV[193].

CELIV can complement the TOF technique, examining charge mobility at lower fields and providing a more comprehensive understanding of charge carrier dynamics in wider field range[44]. For instance, in the case of P3HT (as shown in Table 4.1), the values of σ align well between CELIV[44] and TOF measurements[44]. TOF and CELIV measurements likely have comparable charge concentrations[44]. However, this premise may not necessarily apply to

Table 4.1: Determined values of μ_0 (prefactor mobility), σ (energetic disorder), C (fit constant), and Σ (positional disorder parameter) of the disorder formalism obtained by CELIV and time-of-flight (TOF) techniques for P3HT. From [44].

Material/Sample	Method	μ_0 (cm^2 V^{-1} s^{-1})	σ (eV)	C [(cm V^{-2})$^{1/2}$]	Σ
1/1	CELIV	4×10^{-3}	0.063	3.6×10^{-4}	3
1/2	CELIV	4×10^{-3}	0.061	3.6×10^{-4}	3.15
1/1	TOF[a]	1×10^{-2}	0.070	1.5×10^{-4}	3.4
1/2	TOF[a]	5×10^{-2}	0.074	2.1×10^{-4}	3.9

[a]Calculated between 310–180 K temperature region.

MIS-CELIV measurements. In such case, injected charge carriers might create a charge sheet on the insulator surface, and consequently form a Fermi level. Unfortunately in all CELIV modifications, the main challenge is to observe the extraction peak in current transients, which in many cases is not discernible [194]. This obscures the analysis and sometimes makes it unfeasible. Moreover, the field dependence of mobility needed to obtain zero-field mobility can only be recorded within a limited field range, while the electric field changes continuously during the extraction[195].

4.3 Electrochemical impedance spectroscopy

Energy Resolved EIS (ER-EIS) is a relatively new electrochemical method for DOS characterisation[196]. Unlike the previously discussed methods, the ER-EIS method has a significant advantage, as it allows for the direct observation of the positions of the HOMO and LUMO levels, as well as the shape of the DOS. The ER-EIS is conducted in an electrochemical cell, which consists of a working electrode coated with the material of interest, a reference electrode to measure the potential, and a supporting (auxiliary) electrode to polarize the working electrode against the reference electrode (Figure 4.2). The ER-EIS detects the redox reaction at the liquid-solid interface (Figure 4.2). This redox reaction only takes place when an external potential (U) adjusts the AOS film's Fermi level to align with its HOMO or LUMO levels.
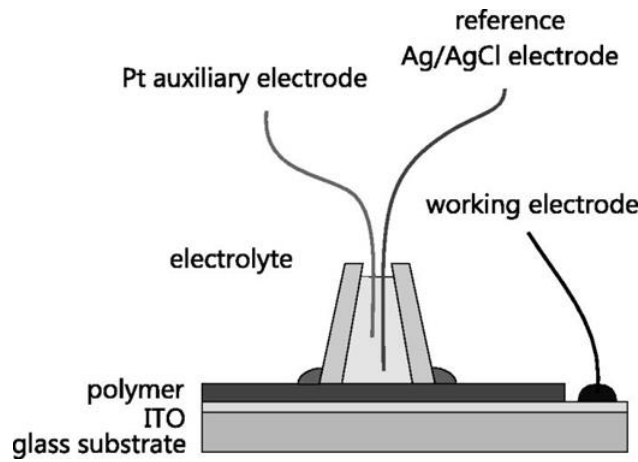
Figure 4.2: The scheme of the ER-EIS microcell. Adapted from "*Energy resolved electrochemical impedance spectroscopy for electronic structure mapping in organic semiconductors*". By Nádaždy V., Schauer F., Gmucová K., Appl. Phys. Lett. **2014**; 105 (14): p 142109. https://doi.org/10.1063/1.4898068 [197]. Reprinted from American Institute of Physics according to the CC BY 4.0 license

To conduct ER-EIS, for each given potential (U), a corresponding output current is measured at a given frequency [198]. Analysis of the obtained data using a suitable equivalent circuit provides information about the electrochemical system, including solution resistance, double layer capacitance, and charge transfer resistance. The DOS as a function of the Fermi energy, $g(E_F)$, can be related to the charge transfer resistance, $R_{ct}(U)$, measured under an applied voltage U[198]. This relationship is given by:

$$g(E_F = eU) = \frac{dn_s}{d(eU)} = -\frac{1}{ek_{et}[A]S}\frac{dj(S)}{dU} = -\frac{1}{ek_{et}[A]SR_{ct}} \tag{4.4}$$

here electron concentration n_s in semiconductor surface and $[A]$ the concentration of the redox (donor/acceptor) pair, e is the elementary charge and k_{et} is the charge-transfer coefficient, S is the sample surface area [198].

One can draw comparisons between ER-EIS and traditional charge transport DOS measurements. For instance, the ER-EIS value of σ for P3HT is 0.067 eV[198], aligning closely with the 0.069 eV the TOF value reported in [199]. However, discrepancies can also arise. The

analysis of the temperature dependence of the MDMO-PPV hole mobility within the EGDM reveals the value of $\sigma_{HOMO} = 0.100$ eV as outlined in [200], whereas the ER-EIS results indicate the value of $\sigma_{HOMO} = 0.173$ eV [196, 198].

ER-EIS effectively captures the exponential dependence of DOS tail states[198] it is worth noting that handling such tails through charge transport measurements can be notably challenging and it requires the ansatz solution of the drift-diffusion equations.

Utilizing the ER-EIS method to evaluate the DOS in organic semiconductors poses several challenges. Firstly, the AOS film must be conductive to prevent undesirable ohmic voltage drops that could distort the observed potential. This effect is particularly pronounced in organic solvents[201]. Moreover, the accurate determination of the absolute potential in solutions is not straightforward; hence, an internal standard like Ferrocene is typically used to calibrate to the absolute energy scale[202]. It is also essential that the oxidation-reduction reaction is reversible to avoid film degradation[202]. The solvent's thermodynamic stability window limits the measurement of HOMO and LUMO levels[202]. For wide-bandgap semiconductors, often only one level, either HOMO or LUMO, is accessible. It is essential to ensure that the semiconductor films are insoluble; otherwise, the solvent might modify or dissolve the film. Therefore, ER-EIS is predominantly utilized to measure DOS in polymeric organic semiconductors[196, 198, 203].

4.4 The Kelvin probe

The Kelvin probe (KP) method, also referred as the Kelvin Probe Force Microscopy (KPFM) or Surface Potential Microscopy, is an extension of the non-contact atomic force microscopy (AFM) technique[204]. In KPFM, the contact potential difference (CPD) between the tip and the sample is determined. The CPD measured in KPFM directly relates to the amount of injected charge, into the surface layer of the sample[204]. Due to band bending and nonuniform distribution of charges, the relationship between CPD and Fermi level is complex[205]. The degree of band bending has been demonstrated to be dependent on energetic disorder. Specifically, the charge transfer across an interface is influenced by the relative energy difference between molecules on opposing sides[71, 204]. Consequently, the width of the DOS also affects the band bending[71, 206]. The DOS values are then derived by fitting the potential as a function of distance from the interface using numerical modeling or available software[206].

In Figure 4.3, one can see the work function fit for PTB7-Th and MEH-PPV films at different thicknesses [71]. In [71] for MEH-PPV, charge transport measurements revealed $\sigma = 0.124 \pm 0.010$ eV and KPFM indicated $\sigma = 0.130 \pm 0.025$ eV. These values are comparable with other studies where the DOS width varies from 0.067 to 0.120 eV, contingent upon the coating conditions[207]. The Gussian DOS width for P3HT determined through KPFM, was 0.08eV[206], aligns with the results from transport measurements.
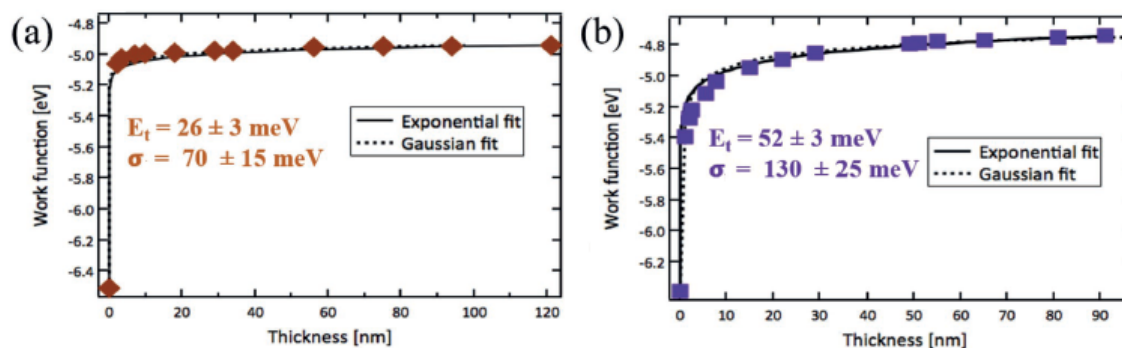
Figure 4.3: Band-bending profiles of a) PTB7-Th and b) MEH-PPV films cast on 70 nm thick MoO_3 layer. Adapted from "*Unifying Energetic Disorder from Charge Transport and Band Bending in Organic Semiconductors*" by A. Karki, G.-J. A. H. Wetzelaer, G. N. M. Reddy et. al. T.-Q. Nguyen, Adv. Funct. Mater. **2019**, 29, p 1901109. https://doi.org/10.1002/adfm.201901109 [71]. Reprinted from WILEY-VCH Verlag GmbH & Co. KGaA according to the CC BY 4.0 license

A significant limitation of the KPFM is that it is only sensitive to tail states. Consequently, it is challenging to differentiate between a Gaussian DOS and an exponential DOS solely based on this analysis [71, 204]. As a result, while the method can provide estimates for the disorder parameters σ in the Gaussian model and E_T in the exponential model, it does not discern one over the other [71, 204].

4.5 Ultraviolet photoemission spectroscopy

Ultraviolet photoemission spectroscopy (UPS) is a commonly used technique for direct probing of the DOS distribution[45, 208–210]. The UPS measures the energy of photoelectrons emitted due to ultraviolet excitation. The energy of the emitted photoelectrons, according to Einstein's photoelectric law, is given by:

$$E_k = h\nu - I \tag{4.5}$$

where E_k is the kinetic energy, $h\nu$ is the photon energy, I is the ionization energy. For molecular semiconductors that have low electrical conductivity, the application of UPS is limited to thin films with a thickness on the order of tens of nanometres[46]. This limitation arises due to the charging of the samples during the measurement process. In a classical UPS experiment, the kinetic energy spectra of photoelectrons, emitted by molecules upon absorption of ultraviolet photons, are measured[46]. In principle, UPS offers direct DOS probing, for example, photoelectrons that are emitted from the HOMO upon UV-irradiation represent DOS for holes. However, quantitative evaluation of the DOS value (eV^{-1} cm^{-3}) using UPS presents challenges. At a given photon's flux, photoelectron intensity is affected by a variety of factors beyond DOS. These factors include the wave function of the electronic state, molecular orientation, photon energy, its polarization direction[46]. UPS primarily studies the central part of the DOS that remains unoccupied in devices, and transport typically occurs at much lower energies that are currently unreachable by UPS [211]. For instance, HOMO DOS values derived from UPS measurements tend to be higher than those expected from transport and impedance measurements. In the case of Y6, Kroh et al. observed the σ value of 0.072 eV using EIS [196], whereas UPS measurements indicated a σ value of 0.188 eV[45]. Such a disparity is unlikely to be solely attributed to variations in morphology or coating conditions. A similar scenario is observed for P3HT, where the identified σ value of 0.245 eV[45] significantly exceeds the reasonable values of DOS width, a conclusion corroborated by multiple charge transport studies – 0.060-0.070 eV.

4.6 Theoretical calculations

The width of the DOS can be calculated using several theoretical models [62, 72, 78, 212–218]. The advancement in computational capabilities has enabled the microscopic modeling of DOS in organic semiconductors. However, even now, such calculations are limited to relatively small systems, encompassing up to 10^4 molecules [62, 219]. A typical computational workflow involves determining various molecular properties using first-principles calculations [62, 219]. For DOS calculations first, for each type of molecule, various properties such as the potential energy surface, reorganization energy, ionization potential, and electron affinity are determined [62, 219]. Additionally, distributed multipoles and polarizabilities are calculated. The derived parameters are then utilized to set up a classical (polarizable) force field, which is subsequently used to simulate amorphous morphologies [62, 219]. The polarizable force field is further employed in a perturbative manner to calculate the electrostatic and induction interactions between a localized charge and its surroundings. [62, 219].The energies of the sites then are derived from the sum of the individual energy contributions and their interactions with the polarisable environment. The long-range Coulomb interaction energy is evaluated using the Ewald summation technique, and the induction interaction energy can be derived

using the Thole model [62, 219].

Achieving realistic morphologies is important for such calculations [62, 219]. Organic materials often exhibit polymorphism or a certain degree of order[220], which often causes drastic changes in energetic landscape within films[221–223]. In amorphous materials, the situation is somewhat simpler, however, many studies have confirmed the presence of short-range order even in amorphous films[224]. Another challenge in microscopic modeling is incorporating the formation of dimeric states. For example, the dimerization of carbazole-based compounds has been identified as a primary source of charge and exciton trapping[225–227]. However, a comprehensive microscopic treatment capturing these effects has not been yet undertaken.

Lattice model

Among different theoretical models a simplified lattice model was particularly useful for understanding the DOS properties in amorphous materials [228, 229]. The lattice model is a mathematical representation of a finite physical system arranged on a lattice. For organic semiconductors this model was developed based on a uniform lattice cubic lattice where sites are occupied by randomly oriented multipoles [228]. Lattice model can reveal the effect of multipoles [72], on charge transport dynamics namely: Coulomb interactions [162] , charge carrier density [171], spatial correlations [57, 73, 100].

Currently, there is a trend to parametrize lattice models using electronic properties of individual molecules [72]. This approach suggests the prediction of the DOS from quantum mechanically calculated properties like charge distributions within the molecule, polarizabilities, and ionization potentials. Andrienko and co-authors showed that the impact of multipole moments on the DOS within a lattice model can be approximated by[72]:

$$\sigma_{l^|,l} = \frac{k_{l^|,l}\Delta q_{l^|}q_l\sqrt{c}}{a^{l^|+l+1}\epsilon_{l^|}^{eff}(\alpha)} \quad l^| = 0,1...,l = 1,2... \tag{4.6}$$

$\Delta q_{l^|}$ is the rotationally averaged change of the multipole moment of the carrier site upon charging, and q_l is the rotationally averaged moment of the surrounding neutral molecules, a is the lattice spacing, $k_{l^|,l}$ is a constant of order one which accounts for the topology of the lattice, $\epsilon_{l^|}^{eff} \geq 1$ incorporates the effective screening parameterized as a function of the polarizability of the (surrounding) neutral molecules, α, and c accounts for a possible fractional filling of the lattice.

The mentioned model can be simplified, particularly when considering materials with equivalent polarizabilities, such as homologous rows or isomers [62]. Thus, by considering only dipolar σ_d or quadripolar σ_q contributions, and treating other effects as constants. As a result, the complete DOS is a composition of σ_d or/and σ_q contributions, complemented by the consistent effects from so-called van der Waals interactions (σ_{vdW}), which account for all other potential sources of disorder. This approach was widely employed for the analysis of energy disorder in molecularly doped polymers by Borsenberger and Bässler using Monte-Carlo simulations [229–232] . The DOS can be deconvoluted into various components, each representing a distinct physical contribution [229–232]:

$$\sigma = \left(\sigma_d^2 + \sigma_{\text{vdW}}^2\right)^{1/2} \tag{4.7}$$

Dipolar disorder is typically regarded as the primary contributor to the energy disorder [229–233]. As a function of dipole moment, the magnitude of the dipolar disorder can be described as follows[162]:

$$\sigma_d \approx 2.35 \frac{e \cdot d}{\varepsilon \cdot \varepsilon_0 \cdot a^2} \tag{4.8}$$

where ε_0 the vacuum permittivity, ε the relative dielectric constant of the organic material, a lattice constant, d static dipole moment. According to Equation 4.8, to minimize dipolar disorder, one should utilize materials with high dielectric permittivity and a low dipole moment. However, in several scenarios, a high dipole moment of molecules is required. For instance, in OLED host materials, the electric field of the dipole can tune the energy of the excited state of the emitter, subsequently affecting the device's EQE. This necessitates the study of factors that can influence DOS, which will be further discussed in the results chapter

4.7 Conclusion

The experimental determination of the DOS width and shape in AOS is quite challenging. In inorganic semiconductors, this task can be tackled using optical measurements, but in AOS, direct optical transitions between HOMO and LUMO levels are weak. As a result, the DOS is often estimated through charge transport measurements, which can be heavily influenced by device quality and the theoretical models used. Additionally, many organic materials exhibit energetic disorder exceeding 100 meV, leading to non-equilibrium charge transport, whereas most models are developed for equilibrium charge transport conditions. For example, many TOF measurements suffer from indistinguishable arrival times, leading to significant uncertainty in the estimated energetic disorder. Multi-parametric fitting of IV curves often introduces substantial variability in the extracted σ_{DOS} values. Direct probing techniques, such as UPS, also fall short of providing a completely conclusive picture due to their limited resolution for tail states.

All the aforementioned problems motivate me to find an alternative approach for measuring DOS width and shape. I tackled this issue using the TSL technique, which, of course, also comes with its own set of advantages and limitations.

Part II

Results

5 Thesis Summary

5.1 General overview – thesis structure

One of the key parameters governing charge transport in amorphous organic semiconductors is the half-width of the density of states (DOS) distribution, commonly referred to as the energetic disorder (σ_{DOS}). All four papers presented in this thesis focus on the DOS distribution, using thermally stimulated luminescence (TSL) as a tool to investigate not only energetic disorder but also charge photogeneration in amorphous organic semiconductors (AOS).

In general, this thesis aims to provide a deeper understanding of charge transport in AOS by examining the effects of energetic disorder on low-temperature charge trapping and the non-equilibrium process of occupied density of states (ODOS) formation. Additionally, I explored the role of energetic disorder in charge photogeneration at low temperatures. My dissertation covers these topics in four chapters. Figure 5.1 illustrates the thesis structure.

Papers 1–3 focus on the DOS distribution in AOS, as its shape and width (σ_{DOS}) significantly impact charge transport. As part of Papers 1-2, I demonstrated that TSL is a versatile and straightforward technique to probe the width and shape of the DOS distribution. This, in Paper 1, allows a systematic study of energy disorder in popular OLED materials. According to Paper 1, the DOS of the studied organic materials adheres to a Gaussian distribution and is intrinsically large. However, a closer examination in Paper 2 shows that the DOS distribution in AOS is not always strictly Gaussian. In some AOS, the intrinsic Gaussian profile is complemented by exponentially decaying tails. To study the ODOS width, in Paper 1, I further extended the 'Classic TSL' to 'IR-Cleaned TSL', using additional IR irradiaton. By comparing DOS and ODOS distributions for charge carriers, I revealed previously unreported ODOS narrowing effect at low temperatures. Specifically, I found a universal ratio between DOS and ODOS widths of 2/3 in all studied OLED materials. Further, in Paper 1, to elucidate the origin of this phenomenon, I performed kinetic Monte Carlo (KMC) simulations, which verified that the spectral narrowing is an inherent feature of nonequilibrium charge transport within a Gaussian DOS. According to my KMC simulations, charge carrier relaxation in the tail of the DOS distribution are slower than in the center of the DOS. Thus, at very low temperatures such as 4.2 K, when charge transport occurs purely through downward hopping, charge carrier package gradually narrows over time.

Among the noteworthy findings of this thesis is that in most OLED materials $\sigma_{\mathrm{DOS}} > 100$ meV, implying that charge carrier transport remains nonequilibrium and dispersive even at room temperature. This will most likely be reflected in the low mobility and subsequent charge accumulation during OLED operation. Therefore, it is important to explore and discern factors influencing σ_{DOS}. I addressed this issue in Paper 2 and Paper 3, by comparing TSL data with theoretical results derived from quantum mechanics (QM) and molecular mechanics (MM) simulations conducted by Denis Andrienko at the MPIP, Mainz. Specifically,

I demonstrated in Paper 2 that the energetic disorder is not simply determined by the static dipole moment, but also by the polarizability of charged molecules (cations or anions). Consequently, findings in Paper 3 confirm that the broad DOS distributions observed in Papers 1–3 are due to intrinsic disorder rather than extrinsic traps.

The TSL studies in Papers 1–3 led to an unexpected observation: low-temperature charge carrier photogeneration upon excitation at the absorption edge in a set of OLED materiasls. This observation motivated the investigation presented in Paper 4. This paper aims to address the question: "How is the singlet exciton binding energy, approximately 1 eV for small-molecule AOS, overcome, allowing the exciton to separate into free charges at such low temperatures?". My investigation of the intrinsic photogeneration in mCBP-CN revealed that the process originated from a Triplet-Triplet Annihilation (TTA) up-conversion (UC) even at very low continuous-wave (cw) excitation intensities. Furthermore, Paper 4 highlights the effect of the energy disorder on each stage of the intrinsic photogeneration process, thereby connecting it to the research landscape of this thesis.
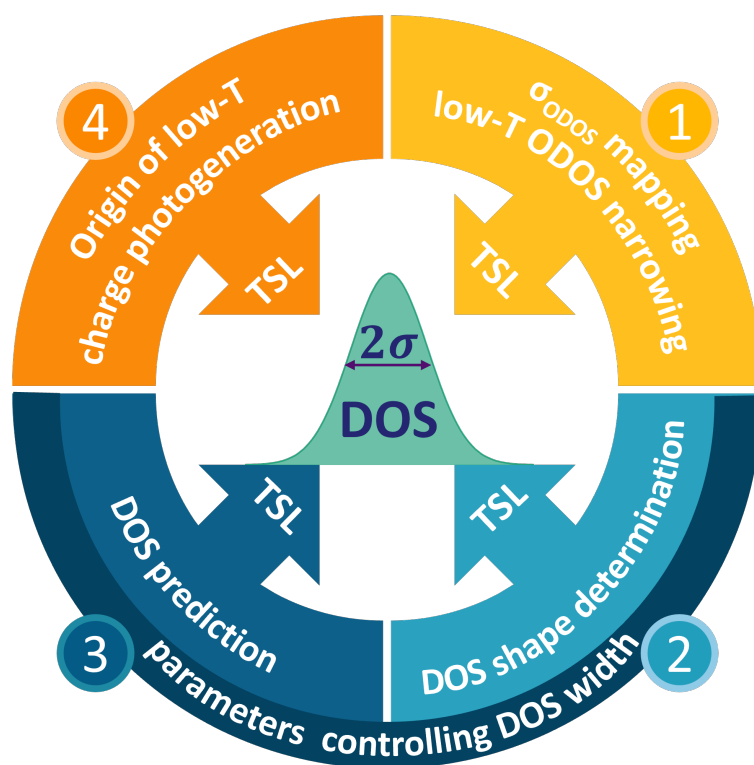
Figure 5.1: Schematic overview of the contributions of each paper to the overall research question. Paper 1 Monitoring the Charge-Carrier-Occupied Density of States in Disordered Organic Semiconductors under Nonequilibrium Conditions Using Thermally Stimulated Luminescence Spectroscopy. Paper 2 Density of States of OLED Host Materials from Thermally Stimulated Luminescence. Paper 3 Molecular library of OLED host materials—Evaluating the multiscale simulation workflow. Paper 4 Charge-carrier photogeneration in single-component organic carbazole-based semiconductors via low excitation power triplet-triplet annihilation.

5.2 Individual publications and their contribution to the thesis aim

5.2.1 Charge-Carrier-Occupied Density of States in Disordered Organic Semiconductors under Nonequilibrium Conditions Using Thermally Stimulated Luminescence Spectroscopy

Paper 1 presents a theoretical and experimental investigation of low-temperature charge trapping phenomena, specifically the nonequilibrium process of ODOS formation in neat AOS. The experimental determination of the width and shape of DOS is not straightforward (for details see Chapter 4). In contrast to inorganic semiconductors, optical studies of the DOS in neat AOS are hindered by strong excitonic transitions that overlap with the weak direct transitions between the HOMO and LUMO levels. However, Paper 1 demonstrated that DOS and ODOS distributions can be experimentally probed using a purely optical technique – thermally stimulated luminescence (TSL). Consequently, interface/contact effects are eliminated, and DOS measurements can be performed in materials with low charge carrier mobilities.

Firstly, the paper describes DOS width measurements and the low-temperature ODOS formation process. Charge carriers photogenerated at low temperatures in TSL experiments are expected to form long-range geminate pairs [234]. In AOS, the distances between charges in geminate pairs vary as a result of energetic and positional disorder. Short-range geminate pairs are inherently unstable and rapidly recombine (most charges recombine within 10 minutes at 5K). In contrast, long-range geminate pairs can evade recombination by undergoing energetic relaxation into the tail states of the DOS distribution. These charges remain trapped in intrinsic states until they are thermally released during heating. This relaxation process shapes the energy distribution of localized carriers, commonly referred to as the occupied DOS (ODOS) distribution. Thus, the TSL glow curves provide a qualitative view of the ODOS distribution.

Typical TSL glow curves and σ_{DOS} values are shown in Figure 5.2a. The DOS width can be determined from the TSL glow curves (Figure 5.2a), as was discussed in introduction part (see. page 38). Specifically, the high-temperature wing of the TSL glow curve always follows the DOS distribution[157] and thus yields the effective DOS width (schematically illustrated in Figure 5.2c red and green curves. Therefore, the DOS width (σ_{DOS}) can be determined from the high-temperature wing of the TSL curve using Gaussian analysis [62]. This procedure will be referred to as "Classical TSL" and used to evaluate σ_{DOS} parameter. "Classical TSL" has been widely used to study DOS widths [62, 109, 156–158, 234–237]. My study found that in most OLED materials σ_{DOS}>100 meV, implying that charge carrier transport remains nonequilibrium and dispersive even at room temperature. This will lead to low charge mobility and subsequent charge accumulation during OLED operation. Although the TSL signal reflects low-temperature ODOS, the presence of kinetically trapped geminate pairs with intermediate distances between countercharges complicates the analysis of the entire band profile of the TSL glow curve. As shown in Figure 5.2a, these pairs with reduced activation energy often create an additional peak on the TSL curve, typically near 40-50 K, obstructing the determination of the ODOS width.
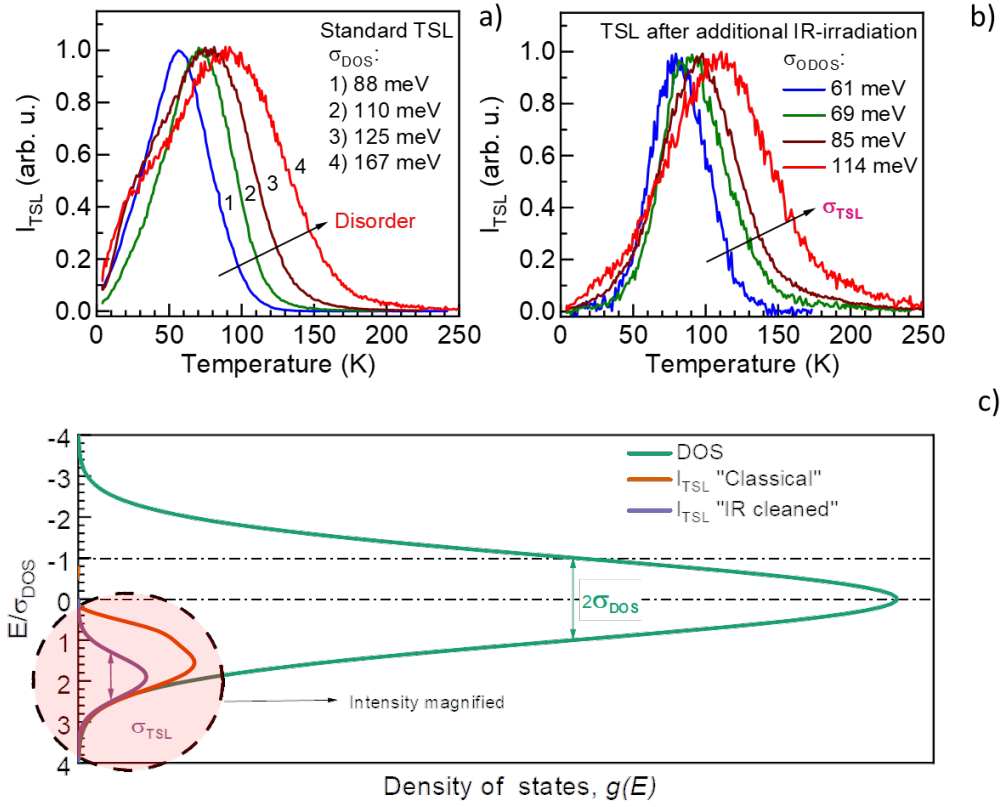
Figure 5.2: a) Normalized TSL intensity (I_{TSL}) curves measured in NPB, TPD, mCBP, and NBPhen films (curve 1, 2, 3, and 4, respectively). Inset shows σ_{DOS} values obtained by TSL; b) Effect of **"IR-cleansing"** on the TSL curve profile of NPB, CBP, mCBP and NBPhen (curve 1, 2, 3, 4 respectively). The inset shows the width of the TSL band, σ_{ODOS}, determined for these compounds. c) Schematic illustration of the available DOS distribution (green curve), the classical TSL band formed after low-temperature energy relaxation (red curve), and the TSL band formed after **"IR-cleansing"** (purple curve). Note that the intensity of the TSL signal, proportional to the occupied density of states, is strongly enlarged for ease of illustration. Reproduced from Paper 1.

However, I found that this low-temperature TSL feature can be effectively eliminated by exposing the UV-excited samples to additional infrared (IR) irradiation at 5 K for typically several minutes (Figure 5.2b). Such an IR irradiation stimulates charges trapped in intermediate local minima to advance further in the relaxation process, thus accelerating the relaxation process at cryogenic temperatures. TSL curves after "IR-cleansing" become relatively symmetrical and represent the ODOS distribution of the charge carriers, as illustrated by the purple curve in Figure 5.2c. To estimate the width of the $ODOS$ (σ_{ODOS}), I fitted the **"IR-cleansed"** TSL curves (Figure 5.3), obtained after converting temperature scale to the energy scale using Equation 3.10, with the following Gaussian function:

$$I_{TSL}(E) \sim exp\left[-\frac{(E - E_m)^2}{2\sigma_{ODOS}^2}\right] \tag{5.1}$$

where E_m is the activation energy at the TSL peak maximum.
Using this approach, I investigated the low-temperature ODOS of 18 common low-molecular-

weight OLED materials. Figure 5.3 presents the results of ODOS fitting using Equation 5.1. A striking observation was revealed when comparing σ_{ODOS} values estimated from the **"IR-cleansed TSL"** and the σ_{DOS} parameters obtained from the **"classical TSL analysis"**.
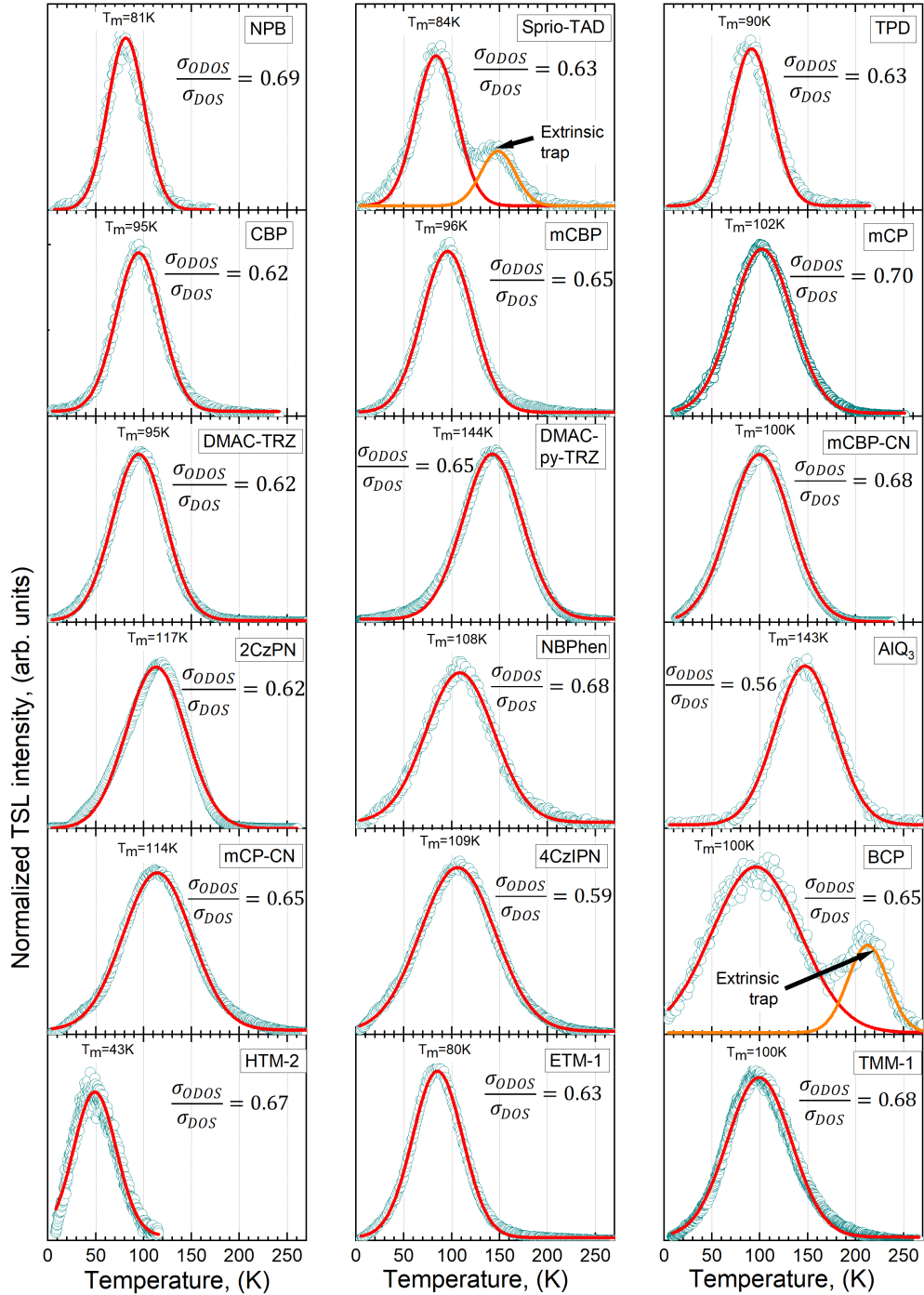
Figure 5.3: The TSL curves of different organic semiconductor films obtained after **"IR-cleansing"**. Symbols show experimental data, and the solid lines are the fitted Gaussians. Reproduced from Paper 1.

I found that σ_{ODOS} is narrower than σ_{DOS}. The phenomenon is common to all amorphous organic semiconductor films I have measured so far, with a mean value of $\sigma_{ODOS}/\sigma_{DOS} = 0.64 \pm 0,04$. Fundamentally, the measured ratio suggests a "spectral narrowing" of the charge-$ODOS$ at low temperatures. I further conducted ct-KMC simulations to provide further insight into the mechanisms behind the spectral narrowing observed in my TSL studies.

Previous KMC studies [238] have manifested that, for equilibrium charge transport, σ_{ODOS} equals σ_{DOS}. Building upon this established knowledge and the TSL results, my KMC studies investigate both equilibrium and nonequilibrium ODOS formation process.

The Figure 5.4a demonstrates the dynamics of the energetic distribution of charge carriers in the regime of equilibrium transport $\hat{\sigma} = \frac{\sigma}{k_B T} = 1.93$[238] ($\sigma$=50meV and T=300K).
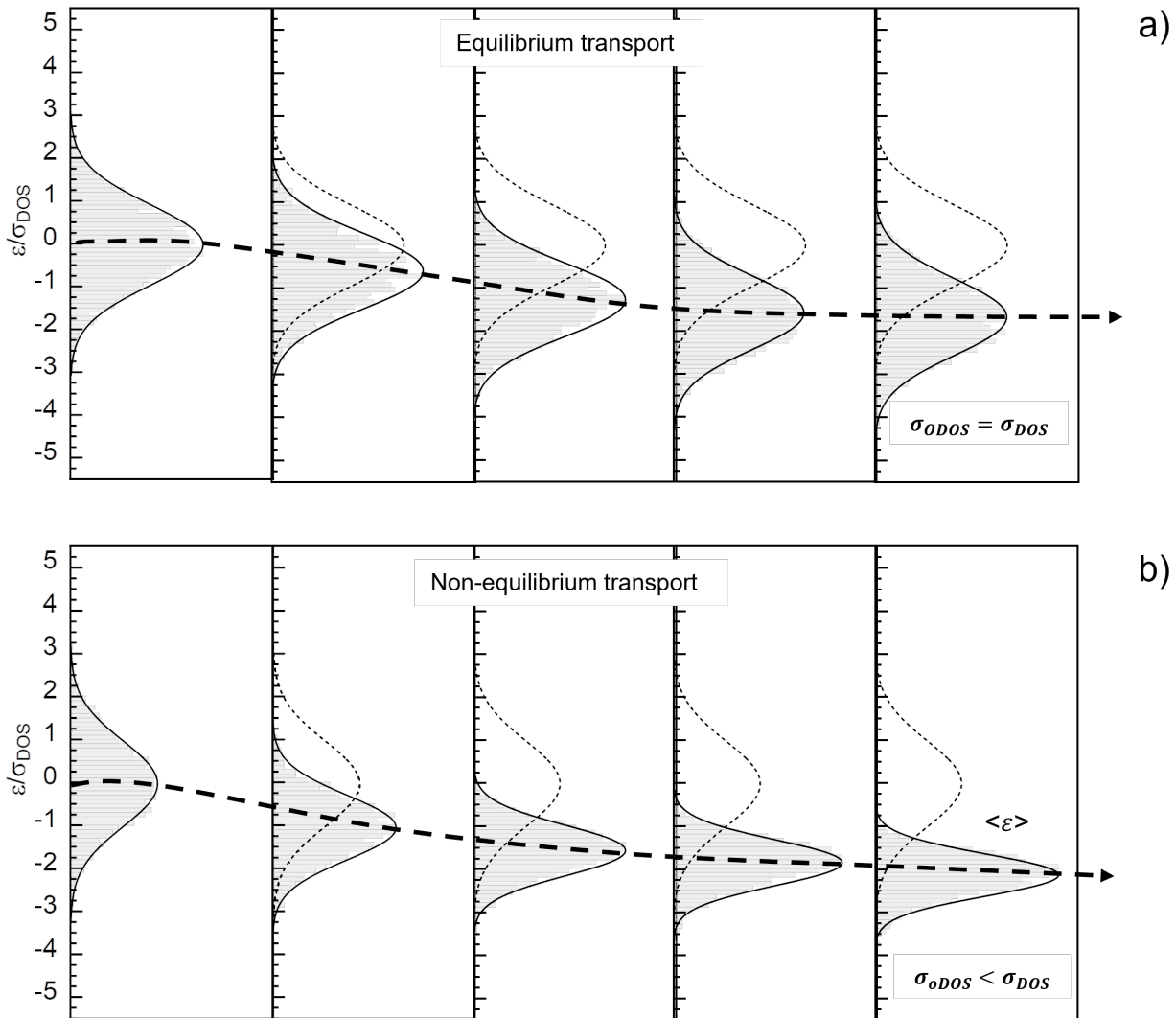
Figure 5.4: Schematic representation of the temporal evolution of the charge carrier ensemble for a) equilibrium transport and b) non-equilibrium transport for selected time intervals. The initial distribution is indicted throughout by the dotted line for reference. Reproduced from Paper 1.

Initially at (t=0) lattice is populated uniformly with charge carriers, implying $\Delta\varepsilon = 0$ and $\sigma_{DOS} = \sigma_{ODOS}$. As can be seen in the Figure 5.4a, after initial ODOS narrowing due to the prevalence of downward hopping, ODOS begins to broaden over time. And once thermal equilibrium with the lattice is established, implying that the average energy $\langle\varepsilon\rangle\,(t \to \infty) = -\frac{\sigma^2}{k_B T}$, σ_{ODOS} becomes equal to σ_{DOS}.

However, at low temperatures, which are typical of TSL photogeneration process, charge carriers fail to reach thermal equilibrium with the environment. As a result, the charges continuously relax in energy toward DOS tail states. In a Gaussian DOS, the number of available hopping sites for such relaxation decreases very steeply. Therefore, charge carriers at relatively higher energy sites, having more available hopping neighbors, relax faster than those at lower energy. Consequently, σ_{ODOS} of the charge-carrier ensemble narrows over time (Figure 5.4b). My ct-KMC studies captured both equilibrium and nonequilibrium charge transport scenarios (Figure 5.4), reinforcing the idea that nonequilibrium transport leads to the ODOS narrowing.

The experimental and theoretical observation of the spectral narrowing is one of the major findings of this thesis. The observation of the ODOS narrowing offers new practical insights into charge transport mechanisms in disordered organic semiconductors.

5.2.2 Density of States of OLED Host Materials from Thermally Stimulated Luminescence

In Paper 2, I focus on understanding the charge transport properties of OLED materials, with a specific emphasis on two key aspects of the density of states (DOS): the precise shape of the DOS and the material parameters that influence energetic disorder, such as polarizability and dipole moment. Dipolar disorder has traditionally been considered to be the main source of energetic disorder in materials with high static dipole moment [239, 240]. Dipolar disorder arises from interactions between charge carriers and randomly aligned dipoles. It is complemented by consistent contribution from "so-called" van der Waals disorder (σ_{vdW}), which accounts for other potential sources of disorder [239, 240].

The exact shape of the DOS is another crucial factor in determining charge transport properties. While the DOS in AOS is typically described by a Gaussian distribution, the shape of the DOS—especially in the tail states, where charge transport predominantly occurs—remains a subject of ongoing debate. For instance, there are experimental evidence [64–66] that in some cases, Gaussian distribution is complemented by an exponential distribution in the tail states.

To address these issues, I conducted a series of TSL studies, corroborated by theoretical calculations. My TSL studies focused on two series of OLED host materials: (i) carbazole-biphenyl derivatives, CBP, mCBP, and mCBP-CN, and phenyl derivatives mCP and mCP-CN (for structural formula see Figure 3.1). Both CBP and CP derivatives share similar cores but differ in polarity (from 0 to 6 D), thus providing a system to investigate the impact of dipole moment on the DOS shape and to establish a structure-property relationship.

mCP and CBP derivatives (see Figure 5.5a and Figure 5.6a) exhibited strong TSL signals, allowing for the identification of the DOS shape in the tail state region.
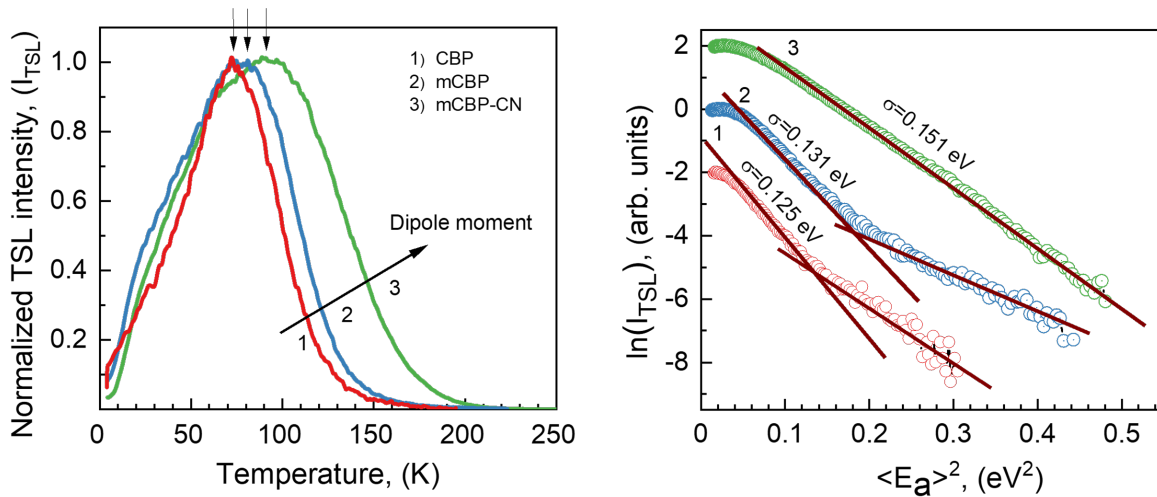
Figure 5.5: Normalized TSL glow curves measured in CBP, mCBP and mCBP-CN films (curve 1, 2, 3, respectively) (a); Gaussian analysis of high-temperature wings of TSL curves shown in (a) (see Papers 1 and 2 for details). Curves are shifted with respect to each other for clarity (b). Reproduced from Paper 2.

To estimate DOS width, the high-temperature wing of the TSL curves was analyzed using

Gaussian analysis, as described in my Papers 1 and 2 and on page 38. According to the Gaussian analysis (see Figure 5.5b and Figure 5.6b), the intrinsic DOS of CP and CBP derivatives exhibited a Gaussian DOS profile, with deep exponential tails observed in CBP and mCBP films. To quantify these tails, I used an exponential distribution $g(\epsilon) \propto \exp(\frac{-\epsilon}{kT_0})$, where T_0 is the width of the exponential distribution (for energies $\epsilon < 0$). By fitting the slower-decaying tails, I determined T_0 values of 716 K for CBP films and 673 K for mCBP films. While according to Figure 5.6b CP derivatives exhibit an exclusively Gaussian profile of the DOS.

Further, I address the effect of dipole moment on DOS in CBP derivatives. For CBP derivatives, the DOS broadens with increasing dipole moment, ranging from 0.125 eV for non-polar CBP ($p \cong 0$ D) to 0.131 eV for mCBP ($p = 2.15$ D) and 0.151 eV for mCBP-CN ($p = 4.6$ D) (see Figure 5.5b). Results of the TSL studies are summarized in (Table 5.1). Furthermore, the same correlation was revealed between the magnitude of the dipole moments and the energetic disorder for the mCP derivatives (Figure 5.6a). The values of σ_{DOS} increases from 0.140 eV in moderately polar mCP ($p=1.35$ D) to 0.177 eV in strongly polar mCP-CN ($p=6$ D). Interestingly, mCBP, with a higher dipole moment ($p=2.15$ D), exhibits lower energetic disorder than mCP ($p=1.35$ D), suggesting that CP derivatives are inherently more disordered. Analysis of energetic disorder within the dipolar disorder model [232, 233,

Table 5.1: Dipole moment (D), polarizability of neutral molecule (α_{neutr}), polarizability of cation (α_{cation}), width of Gaussian DOS (σ_{DOS}^{exp}) evaluated by TSL and (σ_{DOS}^{calc}) by computer simulations, dipolar disorder component (σ_{DIP}^{exp}), and width of superimposed exponential low-energy tail (T_0 K). σ_{DOS}^{exp}, σ_{DIP}^{exp} and T_0 K were measured by me. α_{neutr}, α_{cation}, σ_{DOS}^{calc} were calculated by Dr. Denis Andrienko, MPI für Polymerforschung Mainz.

Material	Dipole moment p (D)	α_{neutr} ($Bohr^3$)	α_{cation} ($Bohr^3$)	σ_{DOS}^{exp} (eV)	σ_{DIP}^{exp} (eV)	T_0 (K)	σ_{DOS}^{calc} (eV)
CBP	0.04	670	3200	0.125	0	716 K	0.10
mCBP	2.15	600	3000	0.131	0.039	673 K	0.12
mCBP-CN	4.6	600	3000	0.151	0.085	-	0.20
mCP	1.35	450	1500	0.140	0.024	-	0.16
mCP-CN	6	540	1500	0.177	0.111	-	0.24

239–241] revealed that CP derivatives exhibit $\sigma_{vdW} = 0.138$ eV, which is significantly larger than the $\sigma_{vdW} = 0.125$ eV determined for the CBP-derivatives.

To gain a deeper insight into the origin of the intrinsically larger non-dipolar disorder component in CP derivatives, Dr. Denis Andrienko from the Max Planck Institute for Polymer Research in Mainz performed computer simulations of the energetic disorder. The calculations confirmed that the energetic disorder increases with the dipole moment due to stronger charge-dipole interactions, which contribute to a larger electrostatic component of the disorder. However, it was also demonstrated that in materials with high polarizability of cations or anions, induced dipoles screen the charge more effectively than in materials with smaller polarizability. Since energetic disorder arises from variations in the local electric field near a localized charge, the lower interaction energy with neighboring molecules due to such screening results in a narrower DOS. Therefore, the differences in σ_{vdW} between CP and CBP derivatives are attributed to variations in the screening of electrostatic disorder between

the derivatives. For instance, mCP has a significantly smaller cation polarizability but higher disorder ($\sim$1500 ($Bohr^3$) and 160 meV) compared to mCBP ($\sim$3000 ($Bohr^3$) and 120 meV), see Table 5.1).

The main results of this study are, firstly, that the effect of dipole moment on the DOS in OLED host materials is well captured by the dipolar disorder model, albeit only for materials that possess similar polarizability of cations and neutral molecules. In addition, I observe the deep exponential tails in the CBP and mCBP films.
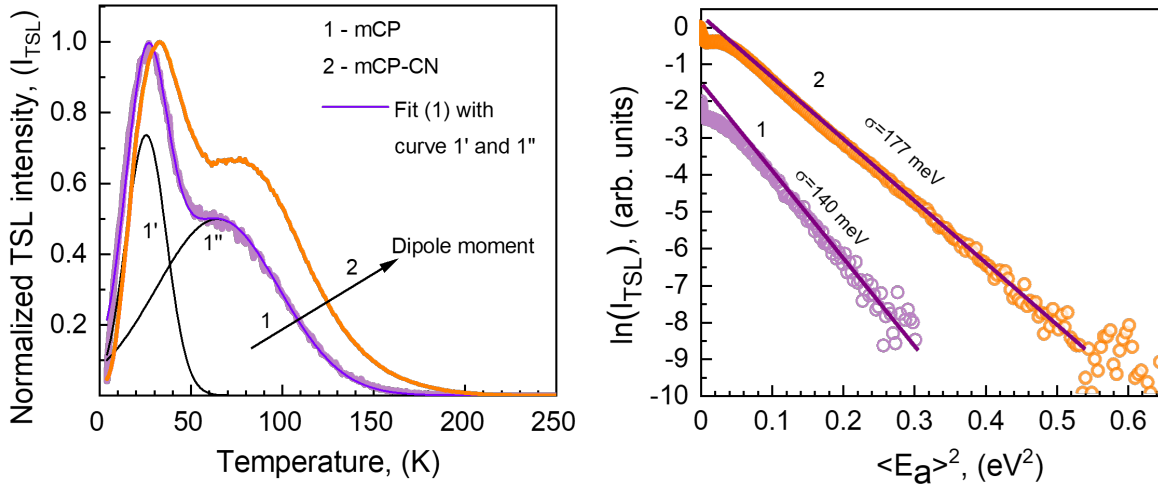
Figure 5.6: Normalized TSL glow curve measured in mCB and mCP-CN film (curve 1 and 2, respectively) (a). Curves 1' and 1" represent deconvolution of the TSL curve of mCP (curve 1) into two Gaussian peaks; Gaussian analysis of high temperature wing of the corresponding TSL curves(b) shown in (a). Reproduced from Paper 2.

5.2.3 Molecular Library of OLED Host Materials—Evaluating the Multiscale Simulation workflow

Paper 3 centred around predictive calculations of the bulk properties of AOS, such as DOS distribution and charge mobility. In this paper Dr. Denis Andreinko introduced a multiscale simulation workflow that combines Quantum Mechanical and Molecular Mechanics calculations to predict the properties of AOS. This workflow was used to estimate the charge mobility in a set of popular OLED materials.

According to the simulation results, despite variations in reorganization energies and electronic coupling elements that affect the simulated mobility, energetic disorder remains the most critical parameter that governs charge transport. Therefore, the accurate determination of the DOS width was a central focus of this thesis. Paper 3 provides deeper insight into the material parameters that influence the DOS and contributes to the research topic of this thesis. Specifically, it establishes a connection between the molecular structure (a microscopic parameter) and the DOS width (a macroscopic parameter). The calculated DOS values independently validate the results of TSL studies on the DOS.

As I pointed out in Chapter 2.3, shallow trap states can significantly broaden the DOS distribution even with a small amount of impurity. It is thus challenging to distinguish whether the TSL measurement reflects the intrinsic DOS or the trap-affected DOS distribution. For instance, DOS width scales linearly with static dipole moment. However, certain TSL results were surprising. Notably, despite having a lower dipole moment of 2.91D [118], BCP exhibited a larger energy disorder ($\sigma_{DOS} = 0.226\ eV$) than mCBP-CN, which has a dipole moment of 4.5D [118] and an energy disorder of $\sigma_{DOS} = 0.155\ eV$. Nevertheless, the DOS widths obtained using TSL techniques align well with computational predictions, as shown in Table 5.2. For instance, TSL DOS for above mentioned BCP agrees well with the calculated value of 0.19 eV (Table 5.2. This underscores the intrinsic nature of the broad DOS widths observed experimentally in most OLED materials, which range from $\sigma_{DOS} = 0.088$ to 0.226 meV, as detailed in Table 5.2. Implying that TSL characterizes the intrinsic DOS, i.e., the DOS of a chemically pure disordered material, rather than impurity-related traps.

Measured materials can still have some extrinsic trapping. As it was recently discovered that for molecules within the trap-free window, when ionization energies (IEs) exceed 6.0 eV and electron affinities (EAs) are below 3.6 eV, one could anticipate the absence of water and oxygen-induced traps [112]. Notably, the ionization energies of most of the materials measured in this study are less than, or around 6 eV [62, 77, 118]. This suggests that their hole DOS might remain unaffected by extrinsic traps since their IE values are within this trap-free window. Conversely, materials with ionization energies surpassing 6 eV are likely to experience trap-limited hole transport [112]. Similarly, an electron affinity under 3.6 eV can result in electron trapping, which in turn limits electron transport. The electron affinities of the materials in this study are significantly below 3.6 eV (Table 5.2), which suggests that electron transport in these systems may be hindered by electron traps (as oxygen-related traps) [112]. Considering that all samples were exposed to air before TSL measurements, resulting in relatively deep electron traps, the TSL measurements probe the hole DOS of these materials [62, 77, 118]. The IE of both CBP and mCBP slightly exceeds the 6 eV threshold of the trap-free window [62]. Therefore, some extrinsic hole trapping may be present. This phenomenon may account for the larger energetic disorder parameters indicated by the TSL measurements for these materials compared to the values obtained from QM/MM

calculations. The presence of water-induced traps can also explain the deviation between the experimental and theoretical energetic disorder observed for BCP. The ionization energy (IE) of BCP is 6.52 eV, which significantly exceeds the trap-free window, indicating that the hole trapping is likely [62].

Table 5.2: Comparison of QM/MD calculated energetic disorder for hole and electron transport with experimental values (in eV) obtained from SCLC (space charge limited current) and TSL methods. Note: Data pertains to selected materials where both TSL and Ea results are available. The data I measured are the TSL DOS values; all other values are from the literature. Comprises data from (a) [118], (b) [62], (c) [77]

System	Electrons		Holes				
	$\sigma_{Electron}^{calc}$	Ea_{tot}^{calc}	σ_{Hole}^{calc}	σ_{Hole}^{exp} TSL/SCLC	IE_{tot}^{calc}	IE_{tot}^{exp} PESA/UPS
NPB[a]	0.098	0.83	0.087	0.088/0.09	5.28	5.47/5.4
Spiro-TAD[a]	0.102	1.05	0.09	0.110/0.09	5.28	5.50/–
TCTA[a]	0.109	1.90	0.122	0.110/0.10	5.62	5.71/5.7
CBP[a]	0.118	1.37	0.096	0.125/0.10	6.37	6.07/6.1
mCP[b]	0.145	0.61	0.127	0.14/–	6.14	5.98/5.9
mCBP[b]	0.151	1.21	0.122	0.131/–	6.34	6.07/6.1
BCP[c]	0.192	1.14	0.19	0.226/–	6.31	6.52/6.5
NBPhen[c]	0.2	1.58	0.194	0.167/–	5.86	–/5.80

Paper 4 also compares σ_{DOS} values determined by the SCLC and the TSL techniques. According to SCLC measurements yield a shallower DOS than TSL measurements. However, the values obtained by both methods remain within the same range. These small discrepancies in the DOS width are expected, as both types of measurements have different charge carrier densities. In SCLC measurements, the injected charges partially fill the tail states of the DOS, which can lead to an underestimation of the energetic disorder.

In light of my research, Paper 3 verified that the TSL measurement characterizes the intrinsic DOS by comparing the σ_{DOS} values obtained by TSL measurements with data derived from QM/MD calculationsand theDOS widthextractedfrom SCLCmeasurements.

5.2.4 Charge-Carrier Photogeneration in Single-Component Organic Carbazole-based Semiconductors via Low Excitation Power Triplet-Triplet Annihilation

In my TSL studies of OLED materials, I observed an unusual phenomenon: low-temperature intrinsic charge photogeneration when a sample was excited at the absorption edge. This behavior contrasts with the conventional understanding of the photogeneration process, where exciton dissociation typically requires overcoming the exciton binding energy (approximately 1 eV for small molecules) [242]. Notably, this "anomalous charge photogeneration" was observed only in phosphorescent materials . This observation served as the motivation for the investigation presented in Paper 4.

To explore this phenomenon further, I compared the photogeneration in two materials: the phosphorescent mCBP-CN (see Figure 5.7a) and the non-phosphorescent P3HT (see Figure 5.7b). According to the TSL action spectra and photocurrent (PC) action spectra of
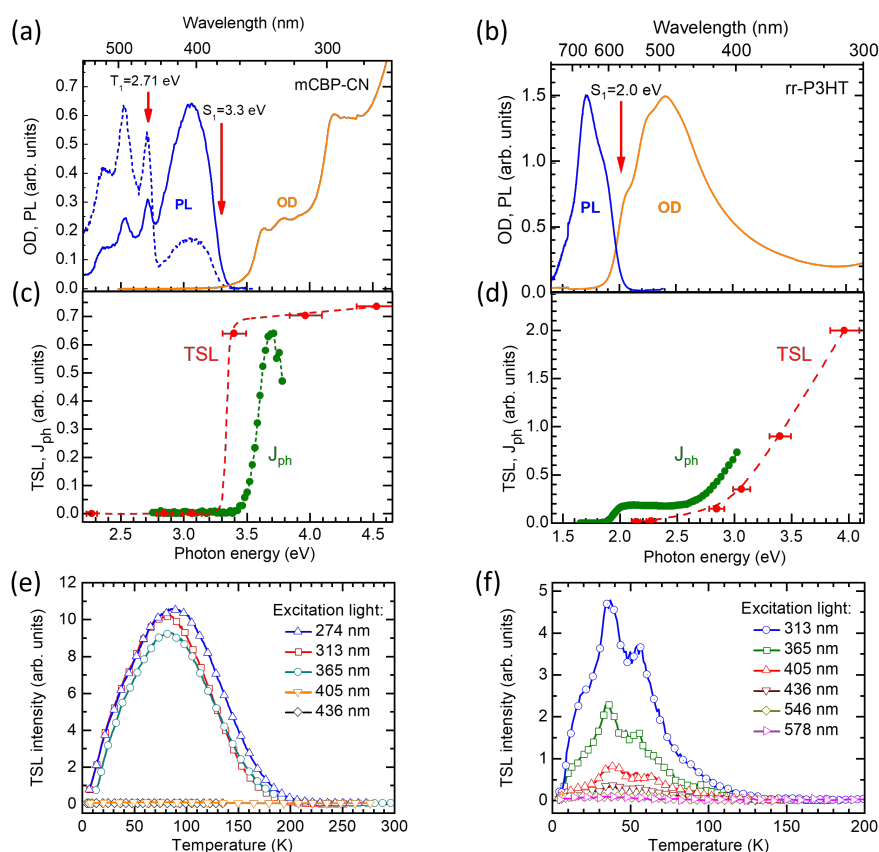
Figure 5.7: (a) Absorption (orange solid line), low-temperature steady-state PL (blue solid line) and delayed emission (blue dashed line) of a mCBP-CN film measured at 77K; (b) Absorption (orange solid line) and steady-state PL measured at 77 K (blue solid line) of a rr-P3HT film; (c) Dependence of the integral TSL intensity upon the photon energy of excitation (red symbols) and photocurrent (PC) action spectra (green symbols) of a mCBP-CN film. (d) Action spectrum of TSL (red symbols) and PC (green circles) of rr-P3HT film. (e) TSL glow curves of mCBP-CN film and of (f) a rr-P3HT film, both measured after excitation at 5 K with different photon energies. Reproduced from Paper 4.

rr-P3HT exhibited distinct behavior compared to mCBP-CN. As one can see on Figure 5.7 d, f both the TSL and PC for P3HT shifted toward higher energies by 0.6–0.7 eV relative to the 0-0 S_1 transition (Figure 5.7b). It should be noted that the process of the charge photogeneration in P3HT follows the generally accepted model, where it is necessary to overcome the exciton binding energy in order to generate charges. In contrast, mCBP-CN's TSL intensity and PC increased sharply as the excitation wavelength reaches the absorbtion band (see Figure 5.7c and f). These differences in photogeneration are unambiguously linked to triplet excitations, which on contrast to mCBP-CN, do not observed in rr-P3HT films, as shown in Figure 5.7a and b.

To demonstrate that triplet excitations are responsible for the generation of highly excited states, I first examined the influence of excitation intensity I_{exc} on phosphorescence (Ph) and delayed fluorescence (DF). According to Figure 5.8a, the delayed fluorescence intensity has a quadratic dependence on the phosphorescence intensity ($I_{\text{DF}} \sim I_{\text{Ph}}^2$), showing that triplet-triplet annihilation (TTA) is the main channel for triplet reservoir depletion in neat mCBP-CN films. Therefore, delayed fluorescence (DF) at low temperatures is only caused by triplet excitation decay via TTA. To further establish the connection between TTA and photogeneration, I measured the temperature dependence of cw-PC and DF. The correlation between the temperature dependence of the PC J_{ph} and delayed fluorescence (I_{DF}) (see Figure 5.8b) provides compelling evidence that the charge photogeneration is dominated by the triplet-triplet annihilation upconversion (TTA-UC) process. Additionally, the bimolecular process of photogeneration was confirmed by the supralinear dependence of photocurrent PC (J_{ph}) on cw-excitation power (see Figure 5.8c). Specifically, $J_{\text{ph}} \propto I_{\text{exc}}^m$, where $m = 1.5$ as measured in the range $0.016 < I_{\text{exc}} < 0.54\,\text{mW/cm}^2$.

Building on these findings, I propose a mechanism for charge-carrier generation via triplet-triplet annihilation upconversion (TTA-UC) as show in Figure 5.8 d. Following S_1 photoexcitation and efficient intersystem crossing (ISC), T_1 triplet states are populated. The high energy of T_1 ensures long enough lifetimes, sustaining a high population of the triplet reservoir. This facilitates an efficient TTA process, generating states with energies up to 5.42 eV — sufficient to overcome the exciton binding energy. These highly excited states further undergo autoionization and charge separation, producing charge-separated pairs.

Clarification of the photogeneration process in the neat mCBP-CN at low temperatures is the main result of Paper 4. Remarkably, both the TTA and charge dissociation processes are strongly influenced by energetic disorder. TTA is enhanced by excitonic energetic disorder due to the increased encounter probability of triplet states, while energetic disorder for charges enables geminate-pairs dissociation at low temperatures.
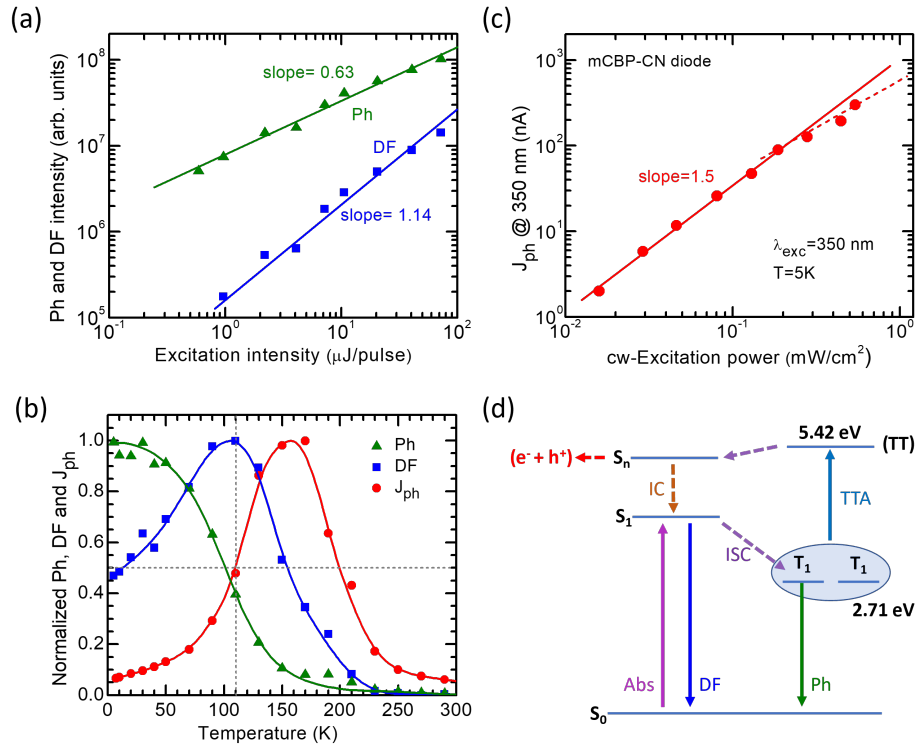
Figure 5.8: (a) Dependence of spectrally integrated phosphorescence (Ph) and delayed fluorescence (DF) intensity on laser pump intensity at 5 K; (b) Intensity of spectrally integrated Ph, DF, and photocurrent versus temperature. (c) Double-logarithmic plot of the photocurrent (J_{ph}) *vs.* cw-excitation intensity. (d) Proposed mechanism of the charge photogeneration. Reproduced from Paper 4.

5.3 Conclusions

My thesis focuses on charge transport in AOS. Variations in reorganization energies and electronic coupling elements influence the charge transport in AOS, but the simulation results presented in Paper 2 indicate that the energetic disorder, commonly referred to as σ, is the most critical factor governing charge transport. Therefore this thesis places emphasis on the density of states (DOS) distribution in AOS. Specifically, it explores the non-equilibrium processes of occupational density of states (ODOS) formation and the effect of σ_{DOS} on charge trapping and low-temperature charge photogeneration. I addressed these issues both experimentally and theoretically, enabling a deeper insight into the spatial and energetic distribution of charge transport states, along with the material parameters governing the DOS width.

In Papers 1–3, I showed that TSL is a versatile and straightforward technique for exploring the DOS in AOS. This subsequently allows for a systematic study of energetic disorder in a set of popular OLED materials. I concluded that the DOS of the studied organic materials follows a Gaussian distribution and is intrinsically large. To advance the TSL technique, In Paper 1, I introduced an infrared push-pulse method called "IR-cleansing". This method enables simultaneous optical probing of both σ_{ODOS} and σ_{DOS} of charge carriers. Through this, I captured a previously overlooked phenomenon of ODOS narrowing at low temperatures, a feature that was shown to be generic across all studied materials. In particular, I identified a linear relationship between σ_{ODOS} and σ_{DOS} that is 2/3. According to my in-depth KMC studies, such "ODOS narrowing" is an unambiguous signature of non-equilibrium charge transport in the Gaussian DOS, as described in Paper 1. I further emphasized the role of spatial energetic correlations in corroboration of the experimentally observed ratio between σ_{ODOS} and σ_{DOS}. The insights gained from Paper 1 reveals the presence of spatial energy correlations even in non-polar materials, contrary to the usual expectation.

While Paper 1 focuses on the DOS shape and the dispersive charge transport, In Papers 2 and 3, I quantified the material parameters that affect energy disorder. Using comprehensive TSL studies, complemented by multiscale computer simulations, I explored the impact of the static dipole moment and the polarizability of charged molecules on the energetic disorder. The insights obtained suggest that despite the linear relationship between σ_{DOS} and the static dipole moment, the energetic disorder is reduced in materials with high cation or anion polarizability. This high polarizability leads to a reduction in charge-dipole interactions, and consequently reduces energy disorder.

In Paper 4, I employed a combination of TSL, time-resolved spectroscopy, and photocurrent spectroscopy measurement to unveil the origin of the anomalous intrinsic charge photogeneration process under excitation at the absorption edge. By performing a case study of mCBP-CN, I identified that this process originated from a Triplet-Triplet Annihilation (TTA) up-conversion (UC). I demonstrated that, the TTA results in the formation of "hot"-excited states with energies exceeding 5eV, which consequently autoionize. Additionally, **Paper 4** highlights the role of energetic disorder in the charge photogeneration process: for charges at low temperatures, it enhances the charge separation, while for triplets, it facilitates the TTA. In light of the studies presented in Paper 1, it would be intriguing to extend the DOS and ODOS TSL studies not only to neat OLED materials but also host-guest systems with more sophisticated energy landscapes, as well as to inorganic amorphous semiconductors and hybrid organic-inorganic perovskites. Papers 2 and 3 shows that the DOS width can be

tuned by choosing materials with highly polarizable cations or anions. This insight enables the design of materials with high static dipole moments without sacrificing charge transport properties. Beyond focusing solely on molecular structure, attention can also be directed toward the film structure; for instance, local dipole ordering can significantly affect the DOS width. This approach could allow the use of established materials with high dipole moments while preserving the charge transport properties of their non-polar counterparts.

References

[1] E. Braun and S. MacDonald (1982). *Revolution in miniature: The history and impact of semiconductor electronics*. Cambridge University Press.

[2] H. Spanggaard and F. C. Krebs (2004). A brief history of the development of organic and polymeric photovoltaics. *Solar Energy Materials and Solar Cells* **83** (2-3), 125–146.

[3] C. Wang, H. Dong, L. Jiang, and W. Hu (2018). Organic semiconductor crystals. *Chemical Society Reviews* **47** (2), 422–500.

[4] *Organic Semiconductor Market Forecast 2023 - 2031*. Accessed: 2023-11-10. (2023). URL: https://www.consegicbusinessintelligence.com/press-release/organic-semiconductor-market.

[5] *Organic Semiconductor Market to Hit US$ 712.76 Billion By 2031: Updated Insights Analysis*. Accessed: 2023-11-10. (2023). URL: https://www.globenewswire.com/news-release/2023/10/13/2760023/0/en/Organic-Semiconductor-Market-to-Hit-US-712-7 6-Billion-By-2031-Updated-Insights-Analysis.html.

[6] *Organic Semiconductor Market Report*. Accessed: 2023-11-10. (2023). URL: https://www.businessresearchinsights.com/market-reports/organic-semiconductor-market-102957.

[7] *Global Organic Semiconductor Market Report*. Accessed: 2023-11-10. (2023). URL: https://www.maximizemarketresearch.com/market-report/global-organic-semiconductor-market/64258/.

[8] D. Taylor (2015). Vacuum-thermal-evaporation: the route for roll-to-roll production of large-area organic electronic circuits. *Semiconductor Science and Technology* **30** (5), 054002.

[9] R. Laudise, C. Kloc, P. Simpkins, and T Siegrist (1998). Physical vapor growth of organic semiconductors. *Journal of crystal growth* **187** (3-4), 449–454.

[10] S. E. Root, S. Savagatrup, A. D. Printz, D. Rodriquez, and D. J. Lipomi (2017). Mechanical properties of organic semiconductors for stretchable, highly flexible, and mechanically robust electronics. *Chemical Reviews* **117** (9), 6467–6499.

[11] Y. Diao, B. C. Tee, G. Giri, J. Xu, D. H. Kim, H. A. Becerril, R. M. Stoltenberg, T. H. Lee, G. Xue, S. C. Mannsfeld, et al. (2013). Solution coating of large-area organic semiconductor thin films with aligned single-crystalline domains. *Nature Materials* **12** (7), 665–671.

[12] T. Someya, T. Sekitani, S. Iba, Y. Kato, H. Kawaguchi, and T. Sakurai (2004). A large-area, flexible pressure sensor matrix with organic field-effect transistors for artificial skin applications. *Proceedings of the National Academy of Sciences* **101** (27), 9966–9970.

[13] C. D. Dimitrakopoulos and P. R. Malenfant (2002). Organic thin film transistors for large area electronics. *Advanced materials* **14** (2), 99–117.

[14] I. McCulloch, M. Heeney, M. L. Chabinyc, D. DeLongchamp, R. J. Kline, M. Cölle, W. Duffy, D. Fischer, D. Gundlach, B. Hamadani, et al. (2009). Semiconducting thienothiophene copolymers: design, synthesis, morphology, and performance in thin-film organic transistors. *Advanced Materials* **21** (10-11), 1091–1109.

[15] R. R. Søndergaard, M. Hösel, and F. C. Krebs (2013). Roll-to-Roll fabrication of large area functional organic materials. *Journal of Polymer Science Part B: Polymer Physics* **51** (1), 16–34.

[16] S. Khan, L. Lorenzelli, and R. S. Dahiya (2015). Technologies for Printing Sensors and Electronics Over Large Flexible Substrates: A Review. *IEEE Sensors Journal* **15** (6), 3164–3185.

[17] M. Pope, H. P. Kallmann, and P. Magnante (1963). Electroluminescence in organic crystals. *The Journal of Chemical Physics* **38** (8), 2042–2043.

[18] C. W. Tang and S. A. VanSlyke (1987). Organic electroluminescent diodes. *Applied Physics Letters* **51** (12), 913–915.

[19] B. Geffroy, P. Le Roy, and C. Prat (2006). Organic light-emitting diode (OLED) technology: materials, devices and display technologies. *Polymer international* **55** (6), 572–582.

[20] G. Hong, X. Gan, C. Leonhardt, Z. Zhang, J. Seibert, J. M. Busch, and S. Bräse (2021). A brief history of OLEDs—emitter development and industry milestones. *Advanced Materials* **33** (9), 2005630.

[21] J. Sun, H. Ahn, S. Kang, S.-B. Ko, D. Song, H. A. Um, S. Kim, Y. Lee, P. Jeon, S.-H. Hwang, et al. (2022). Exceptionally stable blue phosphorescent organic light-emitting diodes. *Nature Photonics* **16** (3), 212–218.

[22] J.-H. Lee, C.-H. Chen, P.-H. Lee, H.-Y. Lin, M.-k. Leung, T.-L. Chiu, and C.-F. Lin (2019). Blue organic light-emitting diodes: current status, challenges, and future outlook. *Journal of Materials Chemistry C* **7** (20), 5874–5888.

[23] J. Park, K. J. Kim, J. Lim, T. Kim, and J. Y. Lee (2022). High Efficiency of over 25% and Long Device Lifetime of over 500 h at 1000 nit in Blue Fluorescent Organic Light-Emitting Diodes. *Advanced Materials* **34** (21), 2108581.

[24] C. Adachi (2014). Third-generation organic electroluminescence materials. *Japanese Journal of Applied Physics* **53** (6), 060101.

[25] K. Walzer, B Maennig, M Pfeiffer, and K Leo (2007). Highly efficient organic devices based on electrically doped transport layers. *Chemical reviews* **107** (4), 1233–1271.

[26] H. F. Haneef, A. M. Zeidell, and O. D. Jurchescu (2020). Charge carrier traps in organic semiconductors: a review on the underlying physics and impact on electronic devices. *Journal of Materials Chemistry C* **8** (3), 759–787.

[27] A. P. Kulkarni, C. J. Tonzola, A. Babel, and S. A. Jenekhe (2004). Electron transport materials for organic light-emitting diodes. *Chemistry of materials* **16** (23), 4556–4573.

[28] J. Lee, N. Chopra, S.-H. Eom, Y. Zheng, J. Xue, F. So, and J. Shi (2008). Effects of triplet energies and transporting properties of carrier transporting materials on blue phosphorescent organic light emitting devices. *Applied Physics Letters* **93** (12).

[29] P. Burrows, Z Shen, V Bulovic, D. McCarty, S. Forrest, J. Cronin, and M. Thompson (1996). Relationship between electroluminescence and current transport in organic heterojunction light-emitting devices. *Journal of Applied Physics* **79** (10), 7991–8006.

[30] H. Bässler (1993). Charge Transport in Disordered Organic Photoconductors a Monte Carlo Simulation Study. *Physica Status Solidi (b)* **175** (1), 15–56.

[31] A. Köhler and H. Bässler (2015). *Electronic Processes in Organic Semiconductors: An Introduction.* Weinheim, Germany: Wiley-VCH Verlag GmbH & Co. KGaA.

[32] R. Noriega, J. Rivnay, K. Vandewal, F. P. Koch, N. Stingelin, P. Smith, M. F. Toney, and A. Salleo (2013). A general relationship between disorder, aggregation and charge transport in conjugated polymers. *Nature Materials* **12** (11), 1038–1044.

[33] P. Kordt, J. J. Van Der Holst, M. Al Helwi, W. Kowalsky, F. May, A. Badinski, C. Lennartz, and D. Andrienko (2015). Modeling of organic light emitting diodes: From molecular to device properties. *Advanced Functional Materials* **25** (13), 1955–1971.

[34] R. Coehoorn and P. A. Bobbert (2012). Effects of Gaussian disorder on charge carrier transport and recombination in organic semiconductors. *Physica Status Solidi (a)* **209** (12), 2354–2377.

[35] R. Coehoorn, H. Van Eersel, P. Bobbert, and R. Janssen (2015). Kinetic Monte Carlo study of the sensitivity of OLED efficiency and lifetime to materials parameters. *Advanced Functional Materials* **25** (13), 2024–2037.

[36] W. Brütting, J. Frischeisen, T. D. Schmidt, B. J. Scholz, and C. Mayr (2013). Device efficiency of organic light-emitting diodes: Progress by improved light outcoupling. *Physica Status Solidi (a)* **210** (1), 44–65.

[37] M. Tanaka, H. Noda, H. Nakanotani, and C. Adachi (2019). Effect of Carrier Balance on Device Degradation of Organic Light-Emitting Diodes Based on Thermally Activated Delayed Fluorescence Emitters. *Advanced Electronic Materials* **5** (5), 1800708.

[38] D. Y. Kondakov (2008). Role of chemical reactions of arylamine hole transport materials in operational degradation of organic light-emitting diodes. *Journal of Applied Physics* **104** (8).

[39] V Ern, H Bouchriha, J Fourny, and G Delacote (1971). Triplet exciton—trapped hole interaction in anthracene crystals. *Solid State Communications* **9** (14), 1201–1203.

[40] S. Reineke, K. Walzer, and K. Leo (2007). Triplet-exciton quenching in organic phosphorescent light-emitting diodes with Ir-based emitters. *Physical Review B* **75**, 125328.

[41] B. van der Zee, Y. Li, G.-J. A. Wetzelaer, and P. W. Blom (2022). Triplet-Polaron-Annihilation-Induced Degradation of Organic Light-Emitting Diodes Based on Thermally Activated Delayed Fluorescence. *Physical Review Applied* **18**, 064002.

[42] M. Hasan, S. Saggar, A. Shukla, F. Bencheikh, J. Sobus, S. K. McGregor, C. Adachi, S.-C. Lo, and E. B. Namdas (2022). Probing polaron-induced exciton quenching in TADF based organic light-emitting diodes. *Nature communications* **13** (1), 254.

[43] H. C. F. Martens, P. W. M. Blom, and H. F. M. Schoo (2000). Comparative study of hole transport in poly(p-phenylene vinylene) derivatives. *Physical Review B* **61**, 7489–7493.

[44] A. J. Mozer, N. S. Sariciftci, A. Pivrikas, R. Österbacka, L. Brassat, and H. Bässler (2005). Charge carrier mobility in regioregular poly(3-hexylthiophene) probed by transient conductivity techniques: A comparative study. *Physical Review B* **71**, 035214.

[45] K. Nakano, Y. Kaji, and K. Tajima (2021). Highly sensitive evaluation of density of states in molecular semiconductors by photoelectron yield spectroscopy in air. *ACS Applied Materials & Interfaces* **13** (24), 28574–28582.

[46] J.-P. Yang, F. Bussolotti, S. Kera, and N. Ueno (2017). Origin and role of gap states in organic semiconductor studied by UPS: As the nature of organic molecular crystals. *Journal of Physics D: Applied Physics* **50** (42), 423002.

[47] C. Kittel (2004). *Introduction to Solid State Physics*. 8th ed. Vol. 71. Wiley, 035214.

[48] E Silins and V. Capek (1994). *Organic molecular crystals: interaction, localization, and transport phenomena*. Vol. 71. American Physical Society, 035214.

[49] M. Pope and C. E. Swenberg (1982). *Electronic Processes in Organic Crystals*. Vol. 71. Oxford: Clarendon Press, 035214.

[50] G. D'Avino, L. Muccioli, F. Castet, C. Poelking, D. Andrienko, Z. G. Soos, J. Cornil, and D. Beljonne (2016). Electrostatic phenomena in organic semiconductors: fundamentals and implications for photovoltaics. *Journal of Physics: Condensed Matter* **28** (43), 433002.

[51] N. Sato, K. Seki, and H. Inokuchi (1981). Polarization energies of organic solids determined by ultraviolet photoelectron spectroscopy. *Journal of the Chemical Society, Faraday Transactions 2: Molecular and Chemical Physics* **77** (9), 1621–1633.

[52] V. Coropceanu, J. Cornil, D. A. DA Silva Filho, Y. Olivier, R. Silbey, and J.-L. Brédas (2007). Charge transport in organic semiconductors. *Chemical reviews* **107** (4), 926–952.

[53] J. Hwang, A. Wan, and A. Kahn (2009). Energetics of metal–organic interfaces: New experiments and assessment of the field. *Materials Science and Engineering: R: Reports* **64** (1-2), 1–31.

[54] S. Duhm, G. Heimel, I. Salzmann, H. Glowatzki, R. L. Johnson, A. Vollmer, J. P. Rabe, and N. Koch (2008). Orientation-dependent ionization energies and interface dipoles in ordered molecular assemblies. *Nature Materials* **7** (4), 326–332.

[55] T. M. Clarke and J. R. Durrant (2010). Charge photogeneration in organic solar cells. *Chemical reviews* **110** (11), 6736–6767.

[56] G. D'Avino, L. Muccioli, Y. Olivier, and D. Beljonne (2016). Charge separation and recombination at polymer–fullerene heterojunctions: Delocalization and hybridization effects. *The Journal of Physical Chemistry Letters* **7** (3), 536–540.

[57] C. Madigan and V. Bulović (2006). Charge carrier energy disorder in polar amorphous organic thin films. *Physical review letters* **97** (21), 216402.

[58] H Bässler (1981). Localized states and electronic transport in single component organic solids with diagonal disorder. *Physica Status Solidi (b)* **107** (1), 9–54.

[59] R. H. Young, T.-M. Kung, J. A. Sinicropi, N. G. Rule, J. J. Fitzgerald, J. E. Eilers, C. H. Chen, and N. W. Boaz (1996). Effect of group and net dipole moments on electron transport in molecularly doped polymers. *The Journal of Physical Chemistry* **100** (45), 17923–17930.

[60] A. Eilmes and R. Munn (2004). Microscopic calculation of the energetics of charged states in amorphous polyethylene. *The Journal of Chemical Physics* **120** (16), 7779–7783.

[61] B Hartenstein and H Bässler (1995). Transport energy for hopping in a Gaussian density of states distribution. *Journal of non-crystalline solids* **190** (1-2), 112–116.

[62] A. Stankevych, A. Vakhnin, D. Andrienko, L. Paterson, J. Genoe, I. Fishchuk, H. Bässler, A. Köhler, and A. Kadashchuk (2021). Density of states of OLED host materials from thermally stimulated luminescence. *Physical Review Applied* **15** (4), 044050.

[63] J. O. Oelerich, D. Huemmer, and S. D. Baranovskii (2012). How to Find Out the Density of States in Disordered Organic Semiconductors. *Physical Review Letters* **108**, 226403.

[64] S. Van Mensfoort, J. Billen, S. Vulto, R. Janssen, and R Coehoorn (2009). Electron transport in polyfluorene-based sandwich-type devices: Quantitative analysis of the effects of disorder and electron traps. *Physical Review B* **80** (3), 033202.

[65] S. Van Mensfoort, R. De Vries, V Shabro, H. Loebl, R. Janssen, and R Coehoorn (2010). Electron transport in the organic small-molecule material BAlq—the role of correlated disorder and traps. *Organic Electronics* **11** (8), 1408–1413.

[66] S. Van Mensfoort and R. Coehoorn (2008). Effect of Gaussian disorder on the voltage dependence of the current density in sandwich-type devices based on organic semiconductors. *Physical Review B* **78**, 085207.

[67] O. Tal, Y Rosenwaks, Y Preezant, N Tessler, C. Chan, and A. Kahn (2005). Direct determination of the hole density of states in undoped and doped amorphous organic films with high lateral resolution. *Physical review letters* **95** (25), 256405.

[68] K Celebi, P. Jadhav, K. Milaninia, M Bora, and M. Baldo (2008). The density of states in thin film copper phthalocyanine measured by Kelvin probe force microscopy. *Applied Physics Letters* **93** (8), 035214.

[69] I. Hulea, H. Brom, A. Houtepen, D Vanmaekelbergh, J. Kelly, and E. Meulenkamp (2004). Wide energy-window view on the density of states and hole mobility in poly (p-phenylene vinylene). *Physical review letters* **93** (16), 166601.

[70] X.-H. Shi, J.-X. Sun, C.-H. Xiong, and L. Sun (2016). Exponential-type density of states with clearly cutting tail for organic semiconductors. *Organic Electronics* **30**, 60–66.

[71] A. Karki, G.-J. A. Wetzelaer, G. N. M. Reddy, V. Nádaždy, M. Seifrid, F. Schauer, G. C. Bazan, B. F. Chmelka, P. W. Blom, and T.-Q. Nguyen (2019). Unifying energetic disorder from charge transport and band bending in organic semiconductors. *Advanced Functional Materials* **29** (20), 1901109.

[72] F. May, B. Baumeier, C. Lennartz, and D. Andrienko (2012). Can lattice models predict the density of states of amorphous organic semiconductors? *Physical Review Letters* **109** (13), 136401.

[73] S. Novikov (2021). Density of states in locally ordered amorphous organic semiconductors: Emergence of the exponential tails. *The Journal of Chemical Physics* **154** (12), 035214.

[74] H. Bässler and A. Köhler (2012). Charge transport in organic semiconductors. *Unimolecular and Supramolecular Electronics I: Chemistry and Physics Meet at Metal-Molecule Interfaces* **71**, 1–65.

[75] A. Miller and E. Abrahams (1960). Impurity conduction at low concentrations. *Physical Review* **120** (3), 745.

[76] R. Saxena, V. Nikitenko, I. Fishchuk, Y. V. Burdakov, Y. V. Metel, J. Genoe, H. Bässler, A. Köhler, and A Kadashchuk (2021). Role of the reorganization energy for charge transport in disordered organic semiconductors. *Physical Review B* **103** (16), 165202.

[77] A. Stankevych, R. Saxena, A. Vakhnin, F. May, N. Kinaret, D. Andrienko, J. Genoe, H. Bässler, A. Köhler, and A. Kadashchuk (2023). Monitoring the charge-carrier-occupied density of states in disordered organic semiconductors under nonequilibrium conditions using thermally stimulated luminescence spectroscopy. *Physical Review Applied* **19** (5), 054007.

[78] X. De Vries, P. Friederich, W. Wenzel, R. Coehoorn, and P. A. Bobbert (2018). Full quantum treatment of charge dynamics in amorphous molecular semiconductors. *Physical Review B* **97** (7), 075203.

[79] P. M. Borsenberger, L. T. Pautmeier, and H. Bässler (1993). Scaling behavior of nondispersive charge transport in disordered molecular solids. *Physical Review B* **48**, 3066–3073.

[80] P. M. Borsenberger, L. Pautmeier, R. Richert, and H. Bässler (1991). Hole transport in 1,1-bis(di-4-tolylaminophenyl)cyclohexane. *The Journal of Chemical Physics* **94** (12), 8276–8281.

[81] P. Borsenberger, R Richert, and H Bässler (1993). Dispersive and nondispersive charge transport in a molecularly doped polymer with superimposed energetic and positional disorder. *Physical Review B* **47** (8), 4289.

[82] F.-J. Kahle, A. Rudnick, S. Wedler, R. Saxena, R. Ammenhäuser, U. Scherf, S. Bagnich, H. Bässler, and A. Köhler (2022). Static and dynamic disorder of charge transfer states probed by optical spectroscopy. *Advanced Energy Materials* **12** (15), 2103063.

[83] R Richert and H. Bässler (1986). Dispersive triplet excitation transport in organic glasses. *The Journal of Chemical Physics* **84** (6), 3567–3572.

[84] B. Movaghar, M. Grünewald, B. Ries, H. Bassler, and D. Würtz (1986). Diffusion and relaxation of energy in disordered organic and inorganic materials. *Physical Review B* **33**, 5545–5554.

[85] S Heun and P. Borsenberger (1995). A comparative study of hole transport in vapor-deposited molecular glasses of N, N, N , N -tetrakis (4-methylphenyl)-(1, 1'-biphenyl)-4, 4'-diamine and N, N'-diphenyl-N, N'-bis (3-methylphenyl)-(1, 1'-biphenyl)-4, 4'-diamine. *Chemical physics* **200** (1-2), 245–255.

[86] B. Ries, H. Bässler, M. Grünewald, and B. Movaghar (1988). Monte Carlo study of relaxation and diffusion in glassy systems. *Physical Review B* **37**, 5508–5517.

[87] W. Gill (1972). Drift mobilities in amorphous charge-transfer complexes of trinitrofluorenone and poly-n-vinylcarbazole. *Journal of Applied Physics* **43** (12), 5033–5040.

[88] Y. Gartstein and E. Conwell (1995). High-field hopping mobility in molecular systems with spatially correlated energetic disorder. *Chemical Physics Letters* **245** (4), 351–358.

[89] S. D. Baranovskii (2014). Theoretical description of charge transport in disordered organic semiconductors. *Physica Status Solidi (b)* **251** (3), 487–525.

[90] S. D. Baranovskii, T Faber, F Hensel, and P Thomas (1997). The applicability of the transport-energy concept to various disordered materials. *Journal of Physics: Condensed Matter* **9** (13), 2699–2706.

[91] N Mott (1987). The mobility edge since 1967. *Journal of Physics C: Solid State Physics* **20** (21), 3075–3102.

[92] V. Arkhipov, P. Heremans, E. Emelianova, G. Adriaenssens, and H Bässler (2002). Weak-field carrier hopping in disordered organic semiconductors: the effects of deep traps and partly filled density-of-states distribution. *Journal of Physics: Condensed Matter* **14** (42), 9899.

[93] R. Schmechel (2002). Gaussian disorder model for high carrier densities: Theoretical aspects and application to experiments. *Physical Review B* **66** (23), 235206.

[94] S. Alesi, G. Brancolini, I. Viola, M. L. Capobianco, A. Venturini, N. Camaioni, G. Gigli, M. Melucci, and G. Barbarella (2009). Self-Organization, Optical, and Electrical Properties of α-Quinquethiophene–Dinucleotide Conjugates. *Chemistry–A European Journal* **15** (8), 1876–1885.

[95] C Tanase, E. Meijer, P. Blom, and D. De Leeuw (2003). Unification of the hole transport in polymeric field-effect transistors and light-emitting diodes. *Physical review letters* **91** (21), 216601.

[96] A. Nenashev, J. Oelerich, and S. Baranovskii (2015). Theoretical tools for the description of charge transport in disordered organic semiconductors. *Journal of Physics: Condensed Matter* **27** (9), 093201.

[97] R. Coehoorn, W. F. Pasveer, P. A. Bobbert, and M. A. J. Michels (2005). Charge-carrier concentration dependence of the hopping mobility in organic materials with Gaussian disorder. *Physical Review B* **72**, 155206.

[98] N. B. Kotadiya, A. Mondal, S. Xiong, P. W. Blom, D. Andrienko, and G.-J. A. Wetzelaer (2018). Rigorous characterization and predictive modeling of hole transport in amorphous organic semiconductors. *Advanced Electronic Materials* **4** (12), 1800366.

[99] M Bouhassoune, S. Van Mensfoort, P. Bobbert, and R. Coehoorn (2009). Carrier-density and field-dependent charge-carrier mobility in organic semiconductors with correlated Gaussian disorder. *Organic Electronics* **10** (3), 437–445.

[100] S. V. Novikov and A. V. Vannikov (1995). Cluster structure in the distribution of the electrostatic potential in a lattice of randomly oriented dipoles. *The Journal of Physical Chemistry* **99** (40), 14573–14576.

[101] S. Novikov and A. Vannikov (2009). Hopping charge transport in disordered organic materials: where is the disorder? *The Journal of Physical Chemistry C* **113** (6), 2532–2540.

[102] P. Kordt and D. Andrienko (2016). Modeling of spatially correlated energetic disorder in organic semiconductors. *Journal of chemical theory and computation* **12** (1), 36–40.

[103] V. Ruhle, A. Lukyanov, F. May, M. Schrader, T. Vehoff, J. Kirkpatrick, B. Baumeier, and D. Andrienko (2011). Microscopic simulations of charge transport in disordered organic semiconductors. *Journal of chemical theory and computation* **7** (10), 3335–3345.

[104] P. E. Parris, D. H. Dunlap, and V. M. Kenkre (2000). Energetic Disorder, Spatial Correlations, and the High-Field Mobility of Injected Charge Carriers in Organic Solids. *Physica Status Solidi (b)* **218** (1), 47–53.

[105] D. H. Dunlap, V. M. Kenkre, and P. E. Parris (1999). What is Behind the E? *Journal of Imaging Science and Technology* **43** (5), 437–443.

[106] R. Schmechel and H. Von Seggern (2004). Electronic traps in organic transport layers. *Physica Status Solidi (a)* **201** (6), 1215–1235.

[107] J Steiger, R Schmechel, and H Von Seggern (2002). Energetic trap distributions in organic semiconductors. *Synthetic metals* **129** (1), 1–7.

[108] I. Fishchuk, A. Kadashchuk, A Vakhnin, Y. Korosko, H Bässler, B Souharce, and U Scherf (2006). Transition from trap-controlled to trap-to-trap hopping transport in disordered organic semiconductors. *Physical Review B* **73** (11), 115210.

[109] A Kadashchuk, D. Weiss, P. Borsenberger, N Ostapenko, V Zaika, and Y. Skryshevski (2000). Effect of extrinsic traps on thermally stimulated luminescence in molecularly doped polymers. *Synthetic metals* **109** (1-3), 177–180.

[110] G. Zuo, M. Linares, T. Upreti, and M. Kemerink (2019). General rule for the energy of water-induced traps in organic semiconductors. *Nature Materials* **18** (6), 588–593.

[111] H. T. Nicolai, M Kuik, G. Wetzelaer, B De Boer, C Campbell, C Risko, J. Brédas, and P. Blom (2012). Unification of trap-limited electron transport in semiconducting polymers. *Nature Materials* **11** (10), 882–887.

[112] N. B. Kotadiya, A. Mondal, P. W. Blom, D. Andrienko, and G.-J. A. Wetzelaer (2019). A window to trap-free charge transport in organic semiconducting thin films. *Nature Materials* **18** (11), 1182–1186.

[113] P. W. Anderson (1958). Absence of diffusion in certain random lattices. *Physical review* **109** (5), 1492.

[114] V. I. Arkhipov, P. Heremans, E. V. Emelianova, and H. Bässler (2005). Effect of doping on the density-of-states distribution and carrier hopping in disordered organic semiconductors. *Physical Review B* **71**, 045214.

[115] U Wolf, H Bässler, P. Borsenberger, and W. Gruenbaum (1997). Hole trapping in molecularly doped polymers. *Chemical physics* **222** (2-3), 259–267.

[116] P. Borsenberger, W. Gruenbaum, U Wolf, and H Bässler (1998). Hole trapping in tri-p-tolylamine-doped poly (styrene). *Chemical physics* **234** (1-3), 277–284.

[117] P. Borsenberger, W. Gruenbaum, E. Magin, S. Visser, and D. Schildkraut (1999). Hole trapping in molecularly doped polymers. *Journal of Polymer Science Part B: Polymer Physics* **37** (4), 349–356.

[118] A. Mondal, L. Paterson, J. Cho, K.-H. Lin, B. van der Zee, G.-J. A. Wetzelaer, A. Stankevych, A. Vakhnin, J.-J. Kim, A. Kadashchuk, et al. (2021). Molecular library of OLED host materials—Evaluating the multiscale simulation workflow. *Chemical Physics Reviews* **2** (3), 035214.

[119] L. Lyons and K. Milne (1976). One-photon intrinsic photogeneration in anthracene crystals. *The Journal of Chemical Physics* **65** (4), 1474–1484.

[120] R. Chance and C. Braun (1976). Temperature dependence of intrinsic carrier generation in anthracene single crystals. *The Journal of Chemical Physics* **64** (9), 3573–3581.

[121] E. Silinsh, V. Kolesnikov, I. Muzikante, and D. Balode (1982). On charge carrier photogeneration mechanisms in organic molecular crystals. *Physica Status Solidi (b)* **113** (1), 379–393.

[122] C Im, E. Emelianova, H Bässler, H Spreitzer, and H Becker (2002). Intrinsic and extrinsic charge carrier photogeneration in phenyl-substituted polyphenylenevinylene-trinitrofluorenone blend systems. *The Journal of Chemical Physics* **117** (6), 2961–2967.

[123] V. Arkhipov, E. Emelianova, S Barth, and H Bässler (2000). Ultrafast on-chain dissociation of hot excitons in conjugated polymers. *Physical Review B* **61** (12), 8207.

[124] H. Bässler and A. Köhler (2015). "Hot or cold": how do charge transfer states at the donor–acceptor interface of an organic solar cell dissociate? *Physical Chemistry Chemical Physics* **17** (43), 28451–28462.

[125] V. Arkhipov, E. Emelianova, and H Bässler (1999). Hot exciton dissociation in a conjugated polymer. *Physical review letters* **82** (6), 1321.

[126] C. L. Braun (1984). Electric field assisted dissociation of charge transfer states as a mechanism of photocarrier production. *The Journal of Chemical Physics* **80** (9), 4157–4161.

[127] C. Deibel, T. Strobel, and V. Dyakonov (2010). Role of the charge transfer state in organic donor–acceptor solar cells. *Advanced materials* **22** (37), 4097–4111.

[128] V. A. Rassolov and A Mozumder (2001). Monte Carlo simulation of electron thermalization distribution in liquid hydrocarbons: effects of inverse collisions and of an external electric field. *The Journal of Physical Chemistry B* **105** (7), 1430–1437.

[129] A. J. Barker, K. Chen, and J. M. Hodgkiss (2014). Distance distributions of photogenerated charge pairs in organic photovoltaic cells. *Journal of the American Chemical Society* **136** (34), 12018–12026.

[130] Y. Hirata and N. Mataga (1991). Direct observation of electron-cation geminate pair produced by picosecond laser pulse excitation in nonpolar solvent: excitation wavelength dependence of the electron thermalization length. *The Journal of Physical Chemistry* **95** (4), 1640–1644.

[131] K. Kato and C. Braun (1980). The photoconduction threshold in anthracene single crystals. *The Journal of Chemical Physics* **72** (1), 172–176.

[132] E. A. Silinsh (2012). *Organic molecular crystals: their electronic states*. Vol. 16. Springer Science & Business Media, 035214.

[133] M. B. Price, P. A. Hume, A. Ilina, I. Wagner, R. R. Tamming, K. E. Thorn, W. Jiao, A. Goldingay, P. J. Conaghan, G. Lakhwani, et al. (2022). Free charge photogeneration in a single component high photovoltaic efficiency organic semiconductor. *Nature Communications* **13** (1), 2827.

[134] R. Batt, C. L. Braun, and J. Hornig (1968). Electric-Field and Temperature Dependence of Photoconductivity. *The Journal of Chemical Physics* **49** (4), 1967–1968.

[135] V. I. Arkhipov, P. Heremans, and H. Bässler (2003). Why is exciton dissociation so efficient at the interface between a conjugated polymer and an electron acceptor? *Applied Physics Letters* **82** (25), 4605–4607.

[136] V. I. Arkhipov, P. Heremans, E. V. Emelianova, and H. Bässler (2003). Exciton dissociation in doped conjugated polymers. *MRS Online Proceedings Library (OPL)* **771**, 035214.

[137] C. Im, J. Lupton, P Schouwink, S Heun, H Becker, and H Bässler (2002). Fluorescence dynamics of phenyl-substituted polyphenylenevinylene–trinitrofluorenone blend systems. *The Journal of Chemical Physics* **117** (3), 1395–1402.

[138] V. Arkhipov and H Bässler (2004). Exciton dissociation and charge photogeneration in pristine and doped conjugated polymers. *Physica Status Solidi (a)* **201** (6), 1152–1187.

[139] S Barth and H Bässler (1997). Intrinsic photoconduction in PPV-type conjugated polymers. *Physical Review Letters* **79** (22), 4445.

[140] S Barth, H Bässler, H Rost, and H. Hörhold (1997). Extrinsic and intrinsic dc photoconductivity in a conjugated polymer. *Physical Review B* **56** (7), 3844.

[141] C. Groves, J. C. Blakesley, and N. C. Greenham (2010). Effect of charge trapping on geminate recombination and polymer solar cell performance. *Nano letters* **10** (3), 1063–1069.

[142] E. V. Emelianova, M. van der Auweraer, and H. Bässler (2008). Hopping approach towards exciton dissociation in conjugated polymers. *The Journal of Chemical Physics* **128** (22), 224709.

[143] O Rubel, S. Baranovskii, W Stolz, and F Gebhard (2008). Exact solution for hopping dissociation of geminate electron-hole pairs in a disordered chain. *Physical review letters* **100** (19), 196602.

[144] U. Albrecht and H. Bässler (1995). Yield of geminate pair dissociation in an energetically random hopping system. *Chemical Physics Letters* **235** (3-4), 389–393.

[145] H Bässler and E. Emelianova (2010). Steady-state photoconduction in amorphous organic solids. *Organic Electronics* **71**, 259–300.

[146] Royal Society of Chemistry (2023). *Intensity-modulated photocurrent spectroscopy.* https://www.rsc.org/publishing/journals/prospect/ontology.asp?id=CMO:0002603&MSID=B915345D. Accessed: 2023-11-16.

[147] G. F. Burkhard, E. T. Hoke, and M. D. McGehee (2010). Accounting for interference, scattering, and electrode absorption to make accurate internal quantum efficiency measurements in organic and other thin solar cells. *Advanced Materials* **22** (30), 3293–3297.

[148] A. J. Bos (2017). Thermoluminescence as a research tool to investigate luminescence mechanisms. *Materials* **10** (12), 1357.

[149] F. Daniels, C. A. Boyd, and D. F. Saunders (1953). Thermoluminescence as a research tool. *Science* **117** (3040), 343–349.

[150] G. Garlick and A. Gibson (1948). The electron trap mechanism of luminescence in sulphide and silicate phosphors. *Proceedings of the physical society* **60** (6), 574.

[151] P Bräunlich (1967). Comment on the initial-rise method for determining trap depths. *Journal of Applied Physics* **38** (6), 2516–2519.

[152] J. T. Randall and M. H. F. Wilkins (1945). Phosphorescence and electron traps-I. The study of trap distributions. *Proceedings of the Royal Society of London. Series A. Mathematical and Physical Sciences* **184** (999), 365–389.

[153] P. Kelly and P. Bräunlich (1970). I. Phenomenological theory of thermoluminescence. *Physical Review B* **1** (4), 1587.

[154] I. Tale (1981). Trap spectroscopy by the fractional glow technique. *Physica Status Solidi (a)* **66** (1), 65–75.

[155] A Kadashchuk, D. Weiss, P. Borsenberger, S Nešpurek, N Ostapenko, and V Zaika (1999). The origin of thermally stimulated luminescence in neat and molecularly doped charge transport polymer systems. *Chemical physics* **247** (2), 307–319.

[156] A Kadashchuk, N Ostapenko, V Zaika, and P. Borsenberger (1999). Thermally stimulated luminescence in molecularly doped polymers. *Journal of Imaging Science and Technology* **43** (3), 213–219.

[157] V. Arkhipov, E. Emelianova, A Kadashchuk, and H Bässler (2001). Hopping model of thermally stimulated photoluminescence in disordered organic materials. *Chemical Physics* **266** (1), 97–108.

[158] A Kadashchuk, Y. Skryshevski, Y. Piryatinski, A Vakhnin, E. Emelianova, V. Arkhipov, H Bässler, and J Shinar (2002). Thermally stimulated photoluminescence in poly (2, 5-dioctoxy p-phenylene vinylene). *Journal of Applied Physics* **91** (8), 5016–5023.

[159] I. Oppenheim, K. E. Shuler, and G. H. Weiss (1977). Stochastic processes in chemical physics: The master equation. *Stochastic processes in chemical physics: the master equation* **71**, 035214.

[160] H. Cuppen, L. Karssemeijer, and T Lamberts (2013). The kinetic Monte Carlo method as a way to solve the master equation for interstellar grain chemistry. *Chemical reviews* **113** (12), 8840–8871.

[161] M. Andersen, C. Panosetti, and K. Reuter (2019). A practical guide to surface kinetic Monte Carlo simulations. *Frontiers in chemistry* **7**, 202.

[162] J. J. M. van der Holst, F. W. A. van Oost, R. Coehoorn, and P. A. Bobbert (2011). Monte Carlo study of charge transport in organic sandwich-type single-carrier devices: Effects of Coulomb interactions. *Physical Review B* **83**, 085206.

[163] A. Y. Toukmaji and J. A. Board Jr (1996). Ewald summation techniques in perspective: a survey. *Computer physics communications* **95** (2-3), 73–92.

[164] S. V. Novikov (2015). Far tails of the density of states in amorphous organic semiconductors. *The Journal of Chemical Physics* **143** (16), 164510.

[165] K. Celebi, P. J. Jadhav, K. M. Milaninia, M. Bora, and M. A. Baldo (2008). The density of states in thin film copper phthalocyanine measured by Kelvin probe force microscopy. *Applied Physics Letters* **93** (8), 083308.

[166] O. Tal, Y. Rosenwaks, Y. Preezant, N. Tessler, C. K. Chan, and A. Kahn (2005). Direct Determination of the Hole Density of States in Undoped and Doped Amorphous Organic Films with High Lateral Resolution. *Physical Review Letters* **95**, 256405.

[167] N. Felekidis, A. Melianas, and M. Kemerink (2018). Automated open-source software for charge transport analysis in single-carrier organic semiconductor diodes. *Organic Electronics* **61**, 318–328.

[168] Z. B. Wang, M. G. Helander, M. T. Greiner, J. Qiu, and Z. H. Lu (2010). Carrier mobility of organic semiconductors based on current-voltage characteristics. *Journal of Applied Physics* **107** (3), 035214.

[169] J. A. Rohr, D. Moia, S. A. Haque, T. Kirchartz, and J. Nelson (2018). Exploring the validity and limitations of the Mott-Gurney law for charge-carrier mobility determination of semiconducting thin-films. *Journal of Physics-Condensed Matter* **30** (10), 035214.

[170] N. F. N. F. Mott and R. W. R. W. Gurney (1940). *Electronic processes in ionic crystals.* Vol. 71. The international series of monographs on physics. Oxford: Clarendon Press, 035214.

[171] W. F. Pasveer, J. Cottaar, C. Tanase, R. Coehoorn, P. A. Bobbert, P. W. M. Blom, D. M. de Leeuw, and M. A. J. Michels (2005). Unified Description of Charge-Carrier Mobilities in Disordered Semiconducting Polymers. *Physical Review Letters* **94**, 206601.

[172] M. Mandoc, B De Boer, G Paasch, and P. Blom (2007). Trap-limited electron transport in disordered semiconducting polymers. *Physical Review B* **75** (19), 193202.

[173] J. Dacuña and A. Salleo (2011). Modeling space-charge-limited currents in organic semiconductors: Extracting trap density and mobility. *Physical Review B* **84** (19), 195209.

[174] N. B. Kotadiya, H. Lu, A. Mondal, Y. Ie, D. Andrienko, P. W. Blom, and G.-J. A. Wetzelaer (2018). Universal strategy for Ohmic hole injection into organic semiconductors with high ionization energies. *Nature Materials* **17** (4), 329–334.

[175] M Kröger, S Hamwi, J Meyer, T Riedl, W Kowalsky, and A. Kahn (2009). Role of the deep-lying electronic states of MoO3 in the enhancement of hole-injection in organic thin films. *Applied Physics Letters* **95** (12), 035214.

[176] P. Borsenberger, L. T. Pautmeier, and H Bässler (1992). Nondispersive-to-dispersive charge-transport transition in disordered molecular solids. *Physical Review B* **46** (19), 12145.

[177] M. Redecker, D. D. Bradley, M. Inbasekaran, W. W. Wu, and E. P. Woo (1999). High mobility hole transport fluorene-triarylamine copolymers. *Advanced Materials* **11** (3), 241–246.

[178] P. W. Blom, M. De Jong, and J. Vleggaar (1996). Electron and hole transport in poly (p-phenylene vinylene) devices. *Applied Physics Letters* **68** (23), 3308–3310.

[179] M. Zubair, Y. S. Ang, and L. K. Ang (2018). Thickness dependence of space-charge-limited current in spatially disordered organic semiconductors. *IEEE Transactions on Electron Devices* **65** (8), 3421–3429.

[180] Z. Chiguvare and V. Dyakonov (2004). Trap-limited hole mobility in semiconducting poly(3-hexylthiophene). *Physical Review B* **70**, 235207.

[181] J. Lorrmann, M. Ruf, D. Vocke, V. Dyakonov, and C. Deibel (2014). Distribution of charge carrier transport properties in organic semiconductors with Gaussian disorder. *Journal of Applied Physics* **115** (18), 183702.

[182] K. Tsung and S. So (2009). High temperature carrier mobility as an intrinsic transport parameter of an organic semiconductor. *Organic Electronics* **10** (4), 661–665.

[183] U. Bach, K. De Cloedt, H. Spreitzer, and M. Grätzel (2000). Characterization of Hole Transport in a New Class of Spiro-Linked Oligotriphenylamine Compounds. *Advanced Materials* **12** (14), 1060–1063.

[184] T.-Y. Chu and O.-K. Song (2008). Apparent thickness dependence of mobility in organic thin films analyzed by Gaussian disorder model. *Journal of Applied Physics* **104** (2), 023711.

[185] G Juška, K Arlauskas, M Viliūnas, and J Kočka (2000). Extraction current transients: new method of study of charge transport in microcrystalline silicon. *Physical review letters* **84** (21), 4946.

[186] V Kažukauskas, M Pranaitis, V Čyras, L Sicot, and F Kajzar (2008). Negative mobility dependence on electric field in poly (3-alkylthiophenes) evidenced by the charge extraction by linearly increasing voltage method. *Thin Solid Films* **516** (24), 8988–8992.

[187] W. Kim, Y. Nishikawa, Y. Nakayama, A. Fujii, and M. Ozaki (2021). Alkyl chain length dependence of carrier transport in solution-processed phthalocyanine thin films evaluated via MIS-CELIV method. *Japanese Journal of Applied Physics* **60** (3), 031004.

[188] W. Tang, V. Chellappan, M. Liu, Z.-K. Chen, and L. Ke (2009). Hole transport in poly [2, 7-(9, 9-dihexylfluorene)-alt-bithiophene] and high-efficiency polymer solar cells from its blends with PCBM. *ACS Applied Materials & Interfaces* **1** (7), 1467–1473.

[189] L. M. Andersson, W. Osikowicz, F. L. Jakobsson, M. Berggren, L. Lindgren, M. R. Andersson, and O. Inganäs (2008). Intrinsic and extrinsic influences on the temperature dependence of mobility in conjugated polymers. *Organic electronics* **9** (5), 569–574.

[190] O. Grynko, G. Juška, and A. Reznik (2022). Charge Extraction by Linearly Increasing Voltage (CELIV) Method for Investigation of Charge Carrier Transport and Recombination in Disordered Materials. In: *Photoconductivity and Photoconductive Materials*. Vol. 71. John Wiley and Sons, Ltd. Chap. 8, 339–368.

[191] A. J. Mozer, N. S. Sariciftci, A. Pivrikas, R. Österbacka, G. Juška, L. Brassat, and H. Bässler (2005). Charge carrier mobility in regioregular poly (3-hexylthiophene) probed by transient conductivity techniques: A comparative study. *Physical Review B* **71** (3), 035214.

[192] M. Stephen, K. Genevičius, G. Juška, K. Arlauskas, and R. C. Hiorns (2017). Charge transport and its characterization using photo-CELIV in bulk heterojunction solar cells. *Polymer International* **66** (1), 13–25.

[193] O. Grynko, G. Juška, and A. Reznik (2022). Charge extraction by linearly increasing voltage (CELIV) method for investigation of charge carrier transport and recombination in disordered materials. *Photoconductivity and Photoconductive Materials: Fundamentals, Techniques and Applications* **1**, 339–368.

[194] A. Armin, G. Juska, M. Ullah, M. Velusamy, P. L. Burn, P. Meredith, and A. Pivrikas (2014). Balanced carrier mobilities: not a necessary condition for high-efficiency thin organic solar cells as determined by MIS-CELIV. *Advanced Energy Materials* **4** (4), 1300954.

[195] S. Bange, M. Schubert, and D. Neher (2010). Charge mobility determination by current extraction under linear increasing voltages: Case of nonequilibrium charges and field-dependent mobilities. *Physical Review B* **81**, 035209.

[196] H. Bässler, D. Kroh, F. Schauer, V. Nádaždy, and A. Köhler (2021). Mapping the Density of States Distribution of Organic Semiconductors by Employing Energy Resolved–Electrochemical Impedance Spectroscopy. *Advanced Functional Materials* **31** (9), 2007738.

[197] V. Nádaždy, F. Schauer, and K. Gmucová (2014). Energy resolved electrochemical impedance spectroscopy for electronic structure mapping in organic semiconductors. *Applied Physics Letters* **105** (14), 142109.

[198] V. Nádaždy, F. Schauer, and K. Gmucová (2014). Energy resolved electrochemical impedance spectroscopy for electronic structure mapping in organic semiconductors. *Applied Physics Letters* **105** (14), 035214.

[199] J. Lorrmann, M. Ruf, D. Vocke, V. Dyakonov, and C. Deibel (2014). Distribution of charge carrier transport properties in organic semiconductors with Gaussian disorder. *Journal of Applied Physics* **115** (18), 035214.

[200] M. M. Mandoc, W. Veurman, L Koster, M. M. Koetse, J. Sweelssen, B. DE Boer, and P. W. Blom (2007). Charge transport in MDMO-PPV: PCNEPV all-polymer solar cells. *Journal of Applied Physics* **101** (10), 035214.

[201] N. G. Tsierkezos and U. Ritter (2009). Electrochemical impedance spectroscopy and cyclic voltammetry of ferrocene in acetonitrile/acetone system. *Journal of Applied Electrochemistry* **40** (2), 409–417.

[202] J. Sworakowski (2018). How accurate are energies of HOMO and LUMO levels in small-molecule organic semiconductors determined from cyclic voltammetry or optical spectroscopy? *Synthetic Metals* **235**, 125–130.

[203] D. Kroh, S. Athanasopoulos, V. Nádaždy, F.-J. Kahle, H. Bässler, and A. Köhler (2023). An Impedance Study of the Density of States Distribution in Blends of PM6: Y6 in Relation to Barrierless Dissociation of CT States. *Advanced Functional Materials* **71**, 2302520.

[204] W. Melitz, J. Shen, A. C. Kummel, and S. Lee (2011). Kelvin probe force microscopy and its application. *Surface Science Reports* **66** (1), 1–27.

[205] V. Palermo, M. Palma, and P. Samorì (2006). Electronic Characterization of Organic Thin Films by Kelvin Probe Force Microscopy. *Advanced Materials* **18** (2), 145–164.

[206] T. J. Whitcher, W. S. Wong, A. N. Talik, K. L. Woon, N Chanlek, H Nakajima, T Saisopa, and P Songsiriritthigul (2016). Investigation into the gaussian density of states widths of organic semiconductors. *Journal of Physics D: Applied Physics* **49** (32), 325106.

[207] A. R. Inigo, Y. F. Huang, J. D. White, Y. S. Huang, W. S. Fann, K. Y. Peng, and S. A. Chen (2010). Review of Morphology Dependent Charge Carrier Mobility in MEH-PPV. *Journal of the Chinese Chemical Society* **57** (3B), 459–468.

[208] S Krause, M. B. Casu, A Schöll, and E Umbach (2008). Determination of transport levels of organic semiconductors by UPS and IPS. *New Journal of Physics* **10** (8), 085001.

[209] P. Li, G. Ingram, J.-J. Lee, Y. Zhao, and Z.-H. Lu (2019). Energy disorder and energy level alignment between host and dopant in organic semiconductors. *Communications Physics* **2** (1), 2.

[210] S Olthof, W Tress, R Meerheim, B Lüssem, and K Leo (2009). Photoelectron spectroscopy study of systematically varied doping concentrations in an organic semiconductor layer using a molecular p-dopant. *Journal of Applied Physics* **106** (10), 035214.

[211] G. Paasch and S. Scheinert (2012). Problems with the Gaussian density of states in organics: definite solution, ambiguous, and hardly any solution. In: *Mathematics for Semiconductor Heterostructures Modeling, Analysis, and Numerics.* Vol. 71. American Physical Society, 32.

[212] P. Friederich, F. Symalla, V. Meded, T. Neumann, and W. Wenzel (2014). Ab initio treatment of disorder effects in amorphous organic materials: Toward parameter free materials simulation. *Journal of chemical theory and computation* **10** (9), 3720–3725.

[213] F. Symalla, P. Friederich, A. Massé, V. Meded, R. Coehoorn, P. Bobbert, and W. Wenzel (2016). Charge Transport by Superexchange in Molecular Host-Guest Systems. *Physical Review Letters* **117**, 276803.

[214] S. Kaiser, N. B. Kotadiya, R. Rohloff, A. Fediai, F. Symalla, T. Neumann, G.-J. A. Wetzelaer, P. W. Blom, and W. Wenzel (2021). De Novo Simulation of Charge Transport through Organic Single-Carrier Devices. *Journal of Chemical Theory and Computation* **17** (10), 6416–6422.

[215] P. DE Silva and T. Van Voorhis (2018). QM/MM study of static and dynamic energetic disorder in the emission layer of an organic light-emitting diode. *The Journal of Physical Chemistry Letters* **9** (6), 1329–1334.

[216] C. Poelking, M. Tietze, C. Elschner, S. Olthof, D. Hertel, B. Baumeier, F. Würthner, K. Meerholz, K. Leo, and D. Andrienko (2015). Impact of mesoscale order on open-circuit voltage in organic solar cells. *Nature Materials* **14** (4), 434–439.

[217] V. Rühle, A. Lukyanov, F. May, M. Schrader, T. Vehoff, J. Kirkpatrick, B. Baumeier, and D. Andrienko (2011). Microscopic Simulations of Charge Transport in Disordered Organic Semiconductors. *Journal of Chemical Theory and Computation* **7** (10), 3335–3345.

[218] J. Kirkpatrick, V. Marcon, J. Nelson, K. Kremer, and D. Andrienko (2007). Charge Mobility of Discotic Mesophases: A Multiscale Quantum and Classical Study. *Physical Review Letters* **98**, 227402.

[219] P. Kordt, J. J. M. VAN DER Holst, M. Al Helwi, W. Kowalsky, F. May, A. Badinski, C. Lennartz, and D. Andrienko (2015). Modeling of Organic Light Emitting Diodes: From Molecular to Device Properties. *Advanced Functional Materials* **25** (13), 1955–1971.

[220] M. R. Caira (1998). Crystalline polymorphism of organic compounds. *Design of Organic Solids* **71**, 163–208.

[221] O. D. Jurchescu, D. A. Mourey, S. Subramanian, S. R. Parkin, B. M. Vogel, J. E. Anthony, T. N. Jackson, and D. J. Gundlach (2009). Effects of polymorphism on charge transport in organic semiconductors. *Physical Review B* **80** (8), 085201.

[222] I. E. Jacobs, C. Cendra, T. F. Harrelson, Z. I. B. Valdez, R. Faller, A. Salleo, and A. J. Moulé (2018). Polymorphism controls the degree of charge transfer in a molecularly doped semiconducting polymer. *Materials Horizons* **5** (4), 655–660.

[223] Y. Shirota and H. Kageyama (2007). Charge carrier transporting molecular materials and their applications in devices. *Chemical reviews* **107** (4), 953–1010.

[224] A. Hofmann, M. Schmid, and W. Brütting (2021). The many facets of molecular orientation in organic optoelectronics. *Advanced Optical Materials* **9** (21), 2101004.

[225] I. Glowacki and Z. Szamel (2010). The nature of trapping sites and recombination centres in PVK and PVK–PBD electroluminescent matrices seen by spectrally resolved thermoluminescence. *Journal of Physics D: Applied Physics* **43** (29), 295101.

[226] G. Peter, H Bässler, W Schrof, and H Port (1985). Picosecond study of singlet exciton dynamics in polyvinylcarbazole (PVK) in the temperature range 5–300 K. *Chemical physics* **94** (3), 445–453.

[227] T. Sasakawa, T. Ikeda, and S. Tazuke (1989). Improved hole drift mobility in excimer-free polymers containing a dimeric carbazole unit. *Macromolecules* **22** (11), 4253–4259.

[228] R. H. Young (1995). Dipolar lattice model of disorder in random media analytical evaluation of the gaussian disorder model. *Philosophical Magazine B* **72** (4), 435–457.

[229] P. Borsenberger and H Bässler (1991). Concerning the role of dipolar disorder on charge transport in molecularly doped polymers. *The Journal of Chemical Physics* **95** (7), 5327–5331.

[230] P. Borsenberger and H Bässler (1992). The role of polar additives on charge transport in molecularly doped polymers. *Physica Status Solidi (b)* **170** (1), 291–302.

[231] P. Borsenberger and L. Rossi (1992). Effects of dipolar disorder on electron transport in molecularly doped polymers. *The Journal of Chemical Physics* **96** (3), 2390–2394.

[232] R. H. Young and J. J. Fitzgerald (1995). Effect of polar additives on charge transport in a molecularly doped polymer: Evaluation of disorder models. *The Journal of Chemical Physics* **102** (23), 9380–9391.

[233] P. Borsenberger, E. Magin, M. O'regan, and J. Sinicropi (1996). The role of dipole moments on hole transport in triphenylamine-doped polymers. *Journal of Polymer Science Part B: Polymer Physics* **34** (2), 317–323.

[234] V. Arkhipov, E. Emelianova, R Schmechel, and H Von Seggern (2004). Thermally stimulated luminescence versus thermally stimulated current in organic semiconductors. *Journal of non-crystalline solids* **338**, 626–629.

[235] A Kadashchuk, Y. Skryshevskii, A Vakhnin, N Ostapenko, V. Arkhipov, E. Emelianova, and H Bässler (2001). Thermally stimulated photoluminescence in disordered organic materials. *Physical Review B* **63** (11), 115205.

[236] E. W. Forsythe, D. C. Morton, C. W. Tang, and Y. Gao (1998). Trap states of tris-8-(hydroxyquinoline) aluminum and naphthyl-substituted benzidine derivative using thermally stimulated luminescence. *Applied Physics Letters* **73** (11), 1457–1459.

[237] A Kadashchuk, A Vakhnin, Y. Skryshevski, V. Arkhipov, E. Emelianova, and H Bässler (2003). Thermally stimulated luminescence in π-conjugated polymers containing fluorene and spirobifluorene units. *Chemical physics* **291** (3), 243–250.

[238] H. Bässler (1993). Charge Transport in Disordered Organic Photoconductors a Monte Carlo Simulation Study. *Physica Status Solidi (b)* **175** (1), 15–56.

[239] A Dieckmann, H Bässler, and P. Borsenberger (1993). An assessment of the role of dipoles on the density-of-states function of disordered molecular solids. *The Journal of Chemical Physics* **99** (10), 8136–8141.

[240] P. M. Borsenberger and D. S. Weiss (1998). *Organic photoreceptors for xerography*. Vol. 59. Marcel Dekker, 035214.

[241] P. Borsenberger and M. O'Regan (1995). The role of dipole moments on hole transport in triphenylamine doped poly (styrene). *Chemical physics* **200** (1-2), 257–263.

[242] A. Sugie, K. Nakano, K. Tajima, I. Osaka, and H. Yoshida (2023). Dependence of exciton binding energy on bandgap of organic semiconductors. *The Journal of Physical Chemistry Letters* **14** (50), 11412–11420.

Part III

Publications

6 Authors' Contributions

Paper 1 Monitoring the Charge-Carrier-Occupied Density of States in Disordered Organic Semiconductors under Nonequilibrium Conditions Using Thermally Stimulated Luminescence Spectroscopy   Andrei Stankevych[#], Rishabh Saxena[#], Alexander Vakhnin, Falk May, Naomi Kinaret, Denis Andrienko, Jan Genoe, Heinz Bässler, Anna Köhler, Andrey Kadashchuk

[#]Authors contributed equally.

A. Kadashchuk initiated this study, analyzed the experimental results, drafted the first version of the manuscript, and together with A. Köhler supervised this research. **I wrote the Python program for the constant time step kinetic Monte Carlo (ct-KMC) approach, ran the ct-KMC simulations, interpreted his simulation data and wrote the corresponding section of the manuscript, performed experimental thermally stimulated luminescence (TSL) measurements, upgraded the TSL experimental setup and wrote a new software for the temperature controller**. R. Saxena wrote the Python program for the variable time step (vt-KMC) approach, managed the vt-KMC simulations, adapted the kMC simulations to account for energy correlation effects, interpreted the simulation results, and wrote a section of the manuscript. A. Vakhnin contributed to the TSL measurements. N. Kinaret, F. May and Denis Andrienko computed density of states (DOS) distributions using QM/MM molecular dynamics simulations, and wrote the corresponding section of the manuscript. After discussions with H. Bässler and A. Köhler, **I**, R. Saxena, and A. Kadashchuk formulated the major conclusions of this paper. J. Genoe, H. Bässler, and A. Köhler discussed the results. A. Köhler critically revised and finalized the manuscript.

Paper 2 Density of States of OLED Host Materials from Thermally Stimulated Luminescence   Andrei Stankevych, Alexander Vakhnin, Denis Andrienko, Leanne Paterson, Jan Genoe, Ivan Fishchuk, Heinz Bässler, Anna Köhler, and Andrey Kadashchuk

A. Kadashchuk initiated and supervised this study, and wrote the manuscript. **I performed experimental thermally stimulated luminescence (TSL) studies, was responsible for the fabrication of thin organic films samples and made several important improvements in TSL setup**. **I** with support of A. Kadashchuk analyzed the data and outlined the manuscript. L. Paterson and D. Andrienko computed density of states (DOS) distributions using QM/MM molecular dynamics simulations. D. Andrienko provided critical insight into the effect of molecular polarizability on DOS width and contributed to revising the manuscript. A. Vakhnin contributed to TSL measurements. I.I. Fishchuk performed effective medium approximation (EMA) calculations, and J. Genoe contributed to discussion of the manuscript. H. Bässler and A. Köhler have provided insight into the implications of the dipolar disorder model for charge-carrier transport in disordered organic semiconductors. All authors participated in discussions of the results and contributed to revising the manuscript.

Paper 3 Molecular library of OLED host materials—Evaluating the multiscale simulation workflow Anirban Mondal, Leanne Paterson, Jaeyoung Cho, Kun-Han Lin, Bas van der Zee, Gert-Jan AH Wetzelaer, **Andrei Stankevych**, Alexander Vakhnin, Jang-Joo Kim, Andrey Kadashchuk, Paul WM Blom, Falk May, Denis Andrienko
D. Andrienko initiated and supervised the overall project. A. Mondal, L. Paterson, J. Cho, and K.-H. Lin, under the supervision of F. May and D. Andrienko, carried out all theoretical work and computed a set of material parameters in 12 common OLED host amorphous materials using quantum mechanics (QM) and molecular mechanics (MM) molecular dynamics simulations; namely, glass transition temperatures, ionization energies and electron affinities, energy disorder parameter as determined by the width of the density-of-state (DOS) distribution, and simulated charge carrier mobilities. **I** and A. Vakhnin under supervision of A. Kadashchuk were responsible for experimental study of the energy disorder in the above materials using thermally stimulated luminescence (TSL) for the purpose of benchmarking the energetic disorder calculations, which is a key material parameter of disordered organic semiconductors. **I carried out TSL measurements, prepared all the samples for TSL studies, analyzed the TSL data, and discussed with A. Kadashchuk interpretation of the obtained TSL results**. A. Vakhnin contributed to TSL measurements. A. Kadashchuk wrote the TSL-related section of the manuscript and contributed to the discussion of the manuscript. B. van der Zee, and G.-J. A. H. Wetzelaer fabricated single-carrier devices, measured the temperature-dependent current voltage characteristics, and fitted those with a drift-diffusion model to obtain the mobility and the energetic disorder, which was done under supervision of P. W. M. Blom. P. W. M. Blom and J.-J. Kim critically reviewed the experimental and theoretical results. Andrienko, A. Mondal, and L. Paterson finalized the manuscript.

Paper 4 Charge-carrier photogeneration in single-component organic carbazole-based semiconductors via low excitation power triplet-triplet annihilation Andrei Stankevych[#], Rishabh Saxena[#], Jeannine Grüne, Sebastian Lulei, Andreas Sperlich, Stavros Athanasopoulos, Alexander Vakhnin, Prakhar Sahay, Wolfgang Brütting, Vladimir Dyakonov, Heinz Bässler, Anna Köhler, Andrey Kadashchuk
[#]Authors contributed equally. Kadashchuk has initiated and organized this research; he established a relevant collaboration with Dyakonov' lab from Würzburg, and together with V. Dyakonov, they conceptualized this study and supervised it in their groups. A. Kadashchuk drafted the first manuscript. **I carried out time-resolved PL spectroscopy studies, photocurrent measurements in photodiode configuration, thermally stimulated luminescence (TSL) measurements of mCBP-CN films, measured afterglow decay kinetics, prepared all samples for optical measurements, as well as built up a TSL setup in A. Köhler group. I** with support of A. Kadashchuk analyzed the data and outlined the manuscript. R. Saxena carried out steady-state spectroscopy and PLQY measurements, PL measurements in phosphorescence mode, and performed Franck-Condon analysis of phosphorescence spectra, contributed to revising the manuscript. A. Vakhnin performed TSL measurements of P3HT. S. Athanasopoulos computed the dissociation yield of geminate electron-hole pairs and fitted the experimental photocurrent data to his analytical hopping model. S. Athanasopoulos wrote the theoretical part of the paper and provided important insights into the effects of energetic disorder on charge separation processes, especially at low temperatures. J. Grüne, S. Lulei, and A. Sperlich performed light-induced

ESR (LESR) and photoluminescence-detected magnetic resonance (PLDMR) studies under supervision of V. Dyakonov, interpreted, analyzed and discussed their experimental findings in conjunction with Stankevych's results, provided insights into photogeneration mechanism in mCBP-CN films, and critically revised the manuscript. P. Sahay developed and fabricated photodiode devices, and measured the reflection coefficients. W. Brütting critically read and commented on the manuscript. H. Bässler and A. Köhler provided important insights into the impact of energy disorder and triplet excitation dynamics on TTA-induced energy up-conversion and charge generation mechanism in organic disordered films. All authors contributed to discussions and revising the manuscript. A. Köhler completed the final editing of the manuscript.

Paper 1: Monitoring the Charge-Carrier-Occupied Density of States in Disordered Organic Semiconductors under Nonequilibrium Conditions Using Thermally Stimulated Luminescence Spectroscopy

Andrei Stankevych[#], Rishabh Saxena[#], Alexander Vakhnin, Falk May, Naomi Kinaret,
Denis Andrienko, Jan Genoe, Heinz Bässler, Anna Köhler, Andrey Kadashchuk
[#]Authors contributed equally.

Monitoring the Charge-Carrier-Occupied Density of States in Disordered Organic Semiconductors under Nonequilibrium Conditions Using Thermally Stimulated Luminescence Spectroscopy

Andrei Stankevych,[1,2,‡] Rishabh Saxena[●],[2,‡] Alexander Vakhnin,[1] Falk May,[3] Naomi Kinaret,[4] Denis Andrienko[●],[4] Jan Genoe[●],[5] Heinz Bässler,[6] Anna Köhler[●],[2,6,*] and Andrey Kadashchuk[●][1,2,5,†]

[1]*Institute of Physics, National Academy of Sciences of Ukraine, Prospect Nauky 46, 03028 Kyiv, Ukraine*

[2]*Soft Matter Optoelectronics and Bavarian Polymer Institute (BPS), University of Bayreuth, Universitätsstr. 30, 95448 Bayreuth, Germany*

[3]*Merck KGaA, Display Solutions department, Frankfurter Straße 250, 64293 Darmstadt, Germany*

[4]*Max Planck Institute for Polymer Research, Polymer Theory department, Ackermannweg 10, 5528 Mainz, Germany*

[5]*IMEC, Sensors and Actuators Technology department, Kapeldreef 75, B-3001 Leuven, Belgium*

[6]*Bayreuth Institute of Macromolecular Research (BIMF), University of Bayreuth, Universitätsstr. 30, 95448 Bayreuth, Germany*

The dynamics of charge carriers in disordered organic semiconductors is inherently difficult to probe by spectroscopic methods. Thermally stimulated luminescence (TSL) is an approach that detects the luminescence resulting from the recombination of spatially-well-separated geminate charge pairs, usually at low temperature. In this way, the density of states (DOS) for charges can be determined. In this study, we demonstrate that TSL can also be used for probing an occupied density of states formed by a low-temperature energetic relaxation of photogenerated charges. Another approach used to gain an insight into the charge-relaxation process is kinetic Monte Carlo (KMC) simulations. Here, we use both techniques to determine the energetic distribution of charges at low temperatures. We find that the charge dynamics is frustrated, yet this frustration can be overcome in TSL by using an infrared (IR) push pulse, and in KMC simulations by a long simulation time that allows for long-range tunneling. Applying the IR-push TSL to pristine amorphous films of 18 commonly used low-molecular-weight organic light-emitting diode materials, we find that the width of the occupied DOS amounts to about 2/3 of the available DOS. The same result is obtained in KMC simulations that consider spatial correlations between site energies. Without the explicit consideration of energetic correlations, the experimental values cannot be reproduced, which testifies to the importance of spatial correlations for charges.

I. INTRODUCTION

The operation of organic light-emitting diodes (OLEDs) and organic solar cells (OSCs) depends on the motion of charges. A correct description of charge transport is therefore essential if one wishes to model and predict the performance of OLEDs and OSCs. Contemporary modeling approaches include drift-diffusion simulations, kinetic Monte Carlo (KMC) simulations, and master-equation approaches [1–5]. In disordered organic semiconductors, charge transport involves energetic relaxation in a broad distribution of localized states, usually assumed to be well described by a Gaussian distribution characterized by width σ_{DOS} [6,7]. For thermal equilibrium conditions, this relaxation process is well understood. Charges that are injected or photogenerated at a random energy site in the available density of states (DOS) proceed by a sequence of energetically downward or upward hops to form an occupied density of states (ODOS). This ODOS is placed around an equilibrium energy ($\varepsilon_{\text{eq}} = -\sigma_{\text{DOS}}^2/k_B T$) below the center of the DOS with a width, σ_{ODOS}, equal to the width of the DOS (σ_{DOS}) [6–8].

The active semiconductor layer in typical disordered OLEDs or OSCs is frequently less than 100 nm thick. This implies that charges injected or photogenerated at room temperature in a DOS with $\sigma_{\text{DOS}} \approx 85$ meV do not reach the thermal equilibrium transport regime prior to being

---

*anna.koehler@uni-bayreuth.de

†kadash@iop.kiev.ua

‡A. Stankevych and R. Saxena contributed equally to this work.

054007-1

extracted or recombined [9]. The energy and width of the DOS fraction they occupy, i.e., the ODOS, differs from that under equilibrium conditions. Despite its importance for the realistic modeling of charge transport, little is known about the nature of the ODOS under nonequilibrium conditions. This study is concerned with the question of which part of the DOS is visited by charges under nonequilibrium transport.

The ODOS determines charge transport in amorphous organic semiconductor films. Yet, since charges do not emit light, they are difficult to study by direct spectroscopic means, though they can be accessed indirectly. One method to study the energetic relaxation process within the DOS consists of analyzing the decay of the time-of-flight signal. By this approach, the transition from a nondispersive to a dispersive transport regime is empirically found to occur at a critical disorder parameter $(\sigma_{DOS}/k_B T)_{cr}$ that depends on the length, L, of the sample, according to $(\sigma_{DOS}/k_B T)_{cr}^2 = 44.8 + 6.7 \log_{10} L$, with L being given in cm [6,10].

Furthermore, triplet excitations are used as probe particles to charge transport, as triplets can be monitored spectroscopically and are transported via short-range exchange interactions, similar to charge carriers [6,8,11,12]. There are limitations to this approach. Triplets are neutral unlike charges, and therefore, less susceptible to polarization-induced or dipolar energetic disorder (implying a smaller σ_{DOS}). Triplets are also more localized, so that they are often associated with a stronger distortion of the molecular backbone, and therefore, larger reorganization energy, λ [11]. Furthermore, triplets have a finite lifetime, unlike charges, which have an infinite lifetime if recombination is excluded. Nevertheless, a number of findings can be transferred, at least qualitatively, and triplet energetic relaxation has been extensively studied in the last decades [11–15]. Notably, below a characteristic temperature, the triplet energetic relaxation is found to become not only dispersive, but also progressively frustrated with a further decrease in temperature. Thermally activated jumps that otherwise promote spectral diffusion are frozen out, so that triplets remain kinetically trapped in local energy minima [12].

The nature of the energy landscape of the charge-carrier DOS was studied by Coehoorn and co-workers [16,17]. They analyzed the *I-V* characteristics in sandwich-type devices based on amorphous small-molecule organic semiconductors, measured for different layer thicknesses and temperatures, and concluded that site energies for charges were spatially correlated in these materials. Thus, it will not suffice to consider only the *width* of the DOS, but the *degree of energetic correlation* also needs to be taken into account, in particular, when describing the observed Poole-Frenkel-type field dependence of charge mobility [16–21].

Here, we employ two approaches to study the relaxation of charge carriers in the nonequilibrium regime. Experimentally, we use the technique of thermally stimulated luminescence (TSL) measurements. TSL is commonly employed to determine the width of the available DOS distribution [22–29]. Here, we advance the method by using an infrared (IR) push pulse that stimulates frustrated charges stuck in intermediate local minima to advance further in the relaxation process, thus accelerating the relaxation process at cryogenic temperatures. With this approach, we investigate 18 common low-molecular-weight OLED materials. The resulting Gaussian distribution of relaxed carriers is found to have a width $\sigma_{TSL} \approx (2/3)\sigma_{DOS}$ that we associate with the width of the ODOS in the nonequilibrium regime.

Our second approach consists of simulating the energetic relaxation of charges in the DOS with the kinetic Monte Carlo technique for the two cases of random energetic disorder and spatially correlated site energies [3]. As expected, our simulations confirm $\sigma_{ODOS} = \sigma_{DOS}$ for hopping transport at equilibrium. However, for both types of energetic disorder, our simulations also demonstrate that the narrowing of the ODOS is a genuine feature for charge transport in the nonequilibrium regime. In the case of assuming correlated disorder, we obtain $\sigma_{ODOS} = (2/3)\sigma_{DOS}$, which matches the experimental value of σ_{TSL}. In contrast, for random disorder, a narrower σ_{ODOS} results.

On the basis of the TSL and KMC results, we conclude that, for amorphous low-molecular-weight organic semiconductor films, a value of $\sigma_{ODOS} = (2/3)\sigma_{DOS}$ is representative for the width of the nonequilibrium ODOS at 5 K and that the due consideration of energetic correlation is essential for an accurate quantitative description of charge-carrier relaxation in the DOS.

II. EXPERIMENT

A. Materials

For our study, we use the OLED small organic molecule materials, the chemical structures of which are shown in Fig. 1 along with their abbreviated names. These compounds are purchased from Sigma-Aldrich, Lumtec Taiwan, with the exception of DMAC-py-TRZ, which is provided by Eli Zysman-Colman from the University of St Andrews, UK. Three materials, referred to as HTM-2, ETM-1, and TMM-1, are provided by Merck, and they denote a hole-transport, electron-transport, and triplet-matrix material, respectively. All materials are used as received, without any further purification. Thin films of the above compounds are spin coated from 20 mg/ml chloroform or toluene solutions onto cleaned quartz substrates (1000 rpm, 30 s) that result in typically 50-nm-thick layers. Subsequently, the deposited films are dried in an oven at 40 °C for 10 min and then under vacuum for 2 h to remove residual solvent.
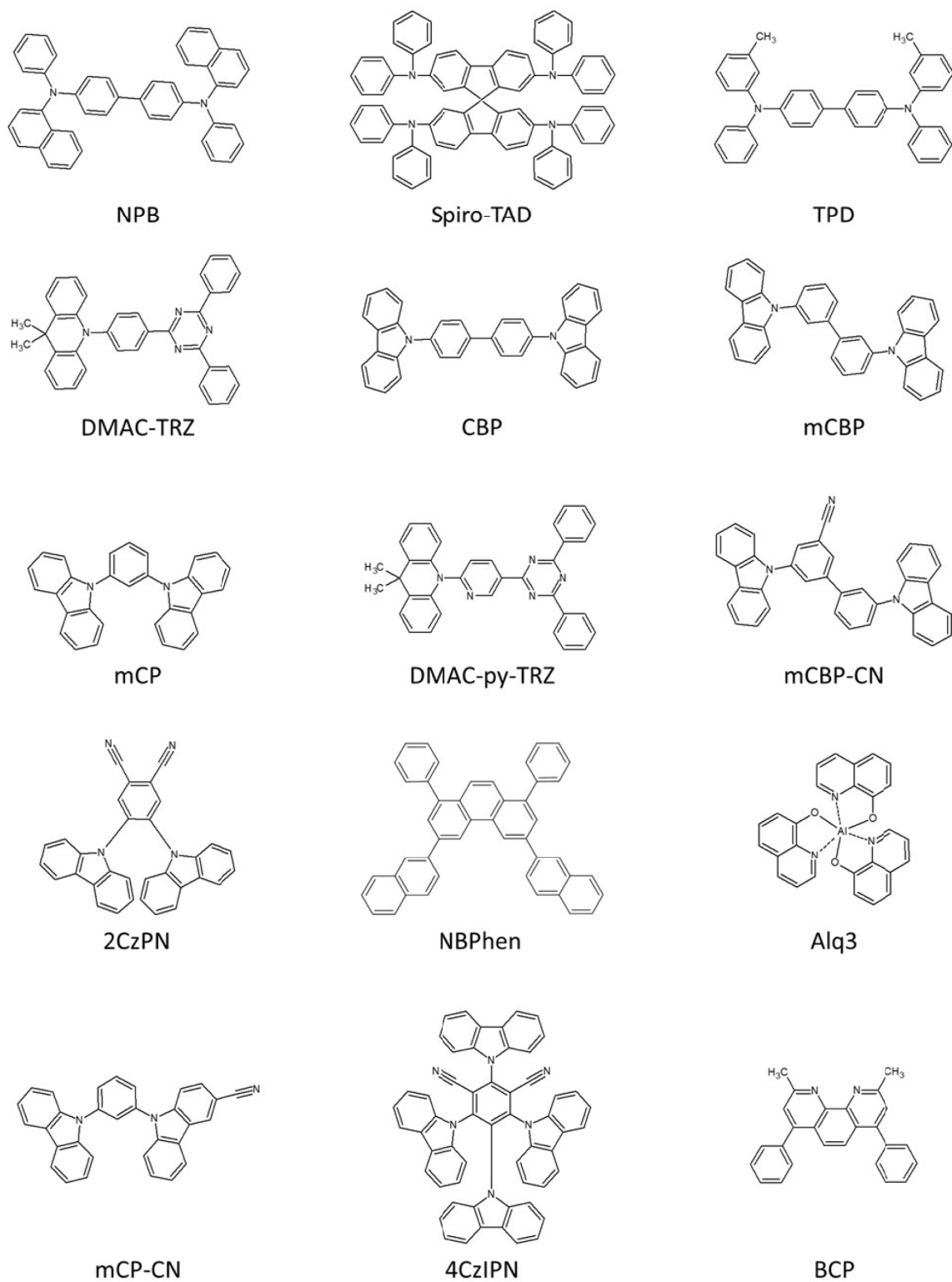
FIG. 1.   Molecular structures of the compounds used in this study. Full names are given in Note S1 of the Supplemental Material [30].

102

B. TSL techniques

TSL is the phenomenon of light emission arising after the removal of excitation (UV light, in our case) under conditions of increasing temperature. Generally, in the TSL method, the trapping states—in the case of pristine amorphous semiconductor films, for example, extrinsic impurity-related traps or the tail states of a DOS distribution—are first populated by the photogenerated charge carriers, usually at low temperatures. After terminating the excitation, the trapped charge carriers can be released by heating the sample, and the luminescence due to charge recombination is recorded as a function of temperature [$I_{\text{TSL}}(T)$]. It is important to note that, in the case of amorphous organic semiconductors, the temperature scale corresponds directly to the activation energy, E_a, for the release of carriers, as detailed further in Note S2 and Fig. S1(b) within the Supplemental Material [30] and also in Refs. [22–27]. For the organic materials studied in the present work, the $\langle E_a \rangle (T)$ dependence, as determined by the fractional (or partial) heating TSL technique [31,32], is found to be described reasonably well by the following empirical relationship [see Fig. S1(b) of the Supplemental Material [30]]:

$$\langle E \rangle (T) = 3.2 \frac{\text{meV}}{K} \times T - 91 \text{ meV}. \qquad (1)$$

TSL measurements are carried out over a temperature range from 5 to 300 K using an optical temperature-regulating helium cryostat. The following text summarizes the methodology adopted for the two different regimes of TSL measurements presented in this study. Please refer to Notes S2 and S3 of the Supplemental Material [30] for a more extensive description of the experiment and its analysis used to determine the width of the available DOS, σ_{DOS}.

1. Classical TSL

In "classical TSL" experiments, samples are cooled to 5 K and excited at 313 nm (cw excitation) for 3 min. The excitation wavelength ($\lambda_{\text{exc}} = 313$ nm) is selected from a high-pressure mercury (Hg) lamp spectrum with the help of an appropriate set of cutoff filters. After that, the samples are kept in the dark at a constant temperature (5 K) during a certain dwell time, typically 10–20 min, before the TSL heating run is started to allow the long isothermal afterglow (arising due to isothermal recombination of short-range geminate pairs) to decay to a negligible value. Then, TSL measurements are started upon heating the sample from 5 to 300 K with a linear heating ramp (at a constant heating rate, $\beta = 0.15$ K/s). TSL emission (due to the thermally activated recombination of long-range geminate pairs) is detected with a cooled photomultiplier tube operating in photon-counting mode, which is mounted adjacent to the cryostat window. The measured

TSL signals are very weak, typically ranging from several hundred to several thousand counts per second at the TSL peak maximum, depending on the material being measured. Therefore, we are not able to resolve TSL spectrally. However, using glass cutoff filters, we roughly estimate that TSL emission is mostly dominated by the intrinsic phosphorescence of the materials, while a much weaker fluorescence component is also present in TSL.

2. IR-cleansed TSL

After exciting the samples with $\lambda_{\text{exc}} = 313$ nm (like in the classical TSL method), samples are additionally irradiated with IR photons for 30 min at 5 K. IR irradiation is selected by using an IR filter with a transparency band of 900–4500 nm from the emission spectrum of the same Hg lamp. It should be noted that no sample heating occurs in the process, and the sample is immersed in liquid helium. After that, the TSL glow curve is recorded upon linear heating, just as in the case of classical TSL. We find that, as a result of such additional IR irradiation (i.e., a long IR-push pulse), the TSL curve acquires a more symmetrical profile. Hereafter, such a procedure is referred to as "*IR cleansing*," and a possible origin of the effect is discussed in Sec. II C.

C. Experimental results

Figure 2(a) shows the normalized TSL glow curves for a few exemplary organic semiconductor materials, namely, NPB, TPD, mCBP, and NBPhen, obtained under identical conditions using the "classical" TSL technique. The classical TSL glow curve of each material shown in Fig. 2(a) represents a broad band, the position of which on the temperature scale is material specific. In particular, the peak of the TSL glow curve shifts to higher temperatures as the TSL band profile broadens. Upon closer inspection of the TSL band profile, an additional shoulderlike feature becomes evident on the low-temperature side, typically at around 40 K. The relative intensity of this low-temperature component is dependent on the material (in some materials, it is observed as an additional TSL peak). Recalling that the temperature scale corresponds linearly to an activation energy for carrier release, we provisionally ascribe the low-temperature feature to the release of geminate pairs with intermediate distance, e.g., those captured by shallow low-energy sites. On the other hand, there is a possibility that a double-peak TSL curve may also be indicative of the presence of local energetic ordering in an organic film due to spatial energy correlations. As a result, one can imagine two scenarios in which a geminate charge pair might be located either within the same energy-correlated valley (if it is spatially well extended) or the sibling electrons and holes are separated between adjacent valleys. In the first case, TSL primarily probes a greatly reduced local energy disorder within an individual energy-corelated domain,
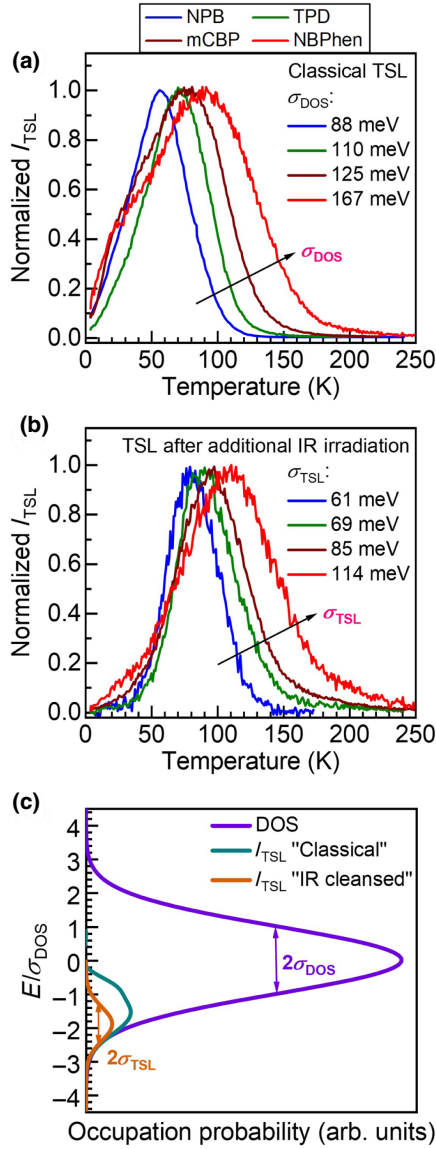
FIG. 2. (a) Normalized TSL intensity (I_{TSL}) curves measured at a constant heating rate of 0.15 K/s after excitation with 313-nm light for 3 min at 5 K in NPB, TPD, mCBP, and NBPhen films. Inset shows σ_{DOS} values obtained by classical TSL. (b) Effect of IR cleansing on the TSL curve profile of NPB, CBP, mCBP, and NBPhen. Inset shows the width of the TSL band, σ_{TSL}, determined for these materials. (c) Schematic illustration of the available DOS distribution (purple curve), classical TSL band formed after low-temperature energy relaxation (dark cyan curve), and TSL band formed after IR cleansing (orange curve). Note that the intensity of the TSL signal, proportional to the occupied density of states, is greatly enlarged for ease of illustration. This is because the concentration of trapped carriers active in TSL is many orders of magnitude smaller than the density of available localized states (DOS) in the system. Therefore, we magnified the TSL signal to demonstrate that its high-temperature part matches the DOS profile.

which results in a very-low-temperature TSL feature. In the latter case, TSL characterizes the distribution of energy barriers between the different energy-correlated valleys, which carriers have to overcome to recombine with their countercharges, and the main TSL peak is therefore relevant to the global energy disorder controlling macroscopic charge transport in a material. This might naturally yield two different TSL peaks. Nevertheless, the precise origin of the low-temperature TSL feature requires further investigation and is beyond the scope of this paper. The key point here is that, by irradiating the sample at 5 K with the 30-min IR-push pulse (IR cleansing), this shoulder-like feature becomes eliminated (effect of IR cleansing), giving rise to a symmetrical TSL peak profile. This is demonstrated in Fig. 2(b). Generally, the IR photons are absorbed by some polaronic states (radical ions) accumulated after the preceding UV excitation, and the absorbed energy is sufficient to release carriers from relatively shallow trapping states active in our TSL measurements. The latter can either recombine with their countercharges or relax towards deeper localized states. A consequence of the additional IR irradiation is that the IR-cleansed TSL peak clearly shifts to a slightly higher temperature, in comparison to the classical TSL, and it is accompanied by a decrease in intensity.

Our interpretation of these data is summarized in Fig. 2(c). In an amorphous thin film, the available density of states can be reasonably well approximated by a Gaussian distribution with standard deviation σ_{DOS}. The low dielectric constant, and consequently, large Coulomb capture radius in the organic materials (for $\varepsilon = 3.5$, this radius is as large as 10^3 nm at $T = 5$ K), precludes the generation of free charge carriers upon photoexcitation under the zero-electric-field condition relevant to TSL experiments [7,33]. Therefore, after photogeneration at low temperatures, charge carriers are produced in the form of geminate pairs of opposite charges [33], even if they are loosely bound charge pairs. The separation distance between the charges in photogenerated geminate pairs is subject to distribution. Short-range geminate pairs are rather unstable and recombine by charge tunneling at a constant temperature, giving rise to a delayed fluorescence emission [34–36] and long isothermal afterglow [23]. On the other hand, the long-range geminate pairs can avoid recombination at low temperatures (such as 5 K, relevant to TSL experiments) within a finite time. They relax to low-energy sites in the available DOS, where they shall only be released, and subsequently recombine, upon heating to elevated temperatures. They are therefore responsible for TSL in organic materials, as indicated by the dark cyan curve in Fig. 2(c). Consequently, the high-temperature edge of the TSL glow curve reflects the deep-energy tail of the available DOS, as proven by analytical theory of TSL in a random-hopping system [23,27]. Note, the Coulomb interaction between charges constituting such long-range

geminate pairs is assumed to be insignificant in comparison to the energy disorder in the system, and therefore, is neglected. An analysis of this high-temperature edge, in terms of Gaussian coordinates (see Note S3 of the Supplemental Material [30] for more details), therefore yields the standard deviation of the available DOS, σ_{DOS}, and the values obtained are indicated in Fig. 2(a). The entire band profile of the TSL glow curve itself cannot be analyzed, as it includes the contribution from kinetically trapped intermediate-range geminate pairs. The application of the IR-cleansing long IR-push pulse removes this frustration, so that the charge carriers relax deeply [37,38]. The TSL curve after IR cleansing thus represents the ODOS distribution of the relaxed charge carriers, as illustrated by the orange curve in Fig. 2(c). To estimate the width of the bell-shaped TSL band, (σ_{TSL}), we convert the temperature scale to an energy scale using Eq. (1), as detailed in Note S2 within the Supplemental Material [30]. Then we fit the IR-cleansed TSL curve with a Gaussian function and determine its standard deviation as σ_{TSL}. As discussed further below, we consider that $\sigma_{TSL} = \sigma_{ODOS}$.

The approach illustrated in detail for the four compounds of Fig. 2 is subsequently extended to a wider set of materials. Figure 3 shows the IR-cleansed TSL glow curves for all 18 organic materials used in this study, and Table I compares σ_{TSL} derived from the IR-cleansed data and σ_{DOS} parameters obtained from the classical TSL analysis. From such a comparison, we find that σ_{TSL} scales linearly with σ_{DOS} and that the ratio $\sigma_{TSL}/\sigma_{DOS} \approx 2/3$. Surprisingly, this turns out to be a general effect for all amorphous organic semiconductor films we measure so far, with a mean value of $\sigma_{TSL}/\sigma_{DOS} = 0.64 \pm 0.04$. For comparison, computed σ_{DOS} values, as obtained from quantum mechanics (QM) and molecular mechanics (MM) molecular dynamics simulations [22,28,30,39,40] are also listed in Table I. The DOS width (σ_{DOS}) obtained from classical TSL measurements are in reasonable quantitative agreement with the computed σ_{DOS}. This proves that energetic disorder values observed experimentally, including the large energetic disorder ranging from $\sigma_{DOS} = 125$ to above 200 meV (Table I), characterize the intrinsic DOS, i.e., the DOS of a chemically pure disordered material, rather than that affected by impurity-related traps.

A noteworthy observation is that for all compounds, except HTM-2, σ_{DOS} exceeds the value of 85 meV, above which charge transport in 100-nm-thick films will not reach equilibrium at room temperature prior to extraction [6,10]. Thus, the nonequilibrium ODOS deserves consideration for the description of transport in corresponding devices. Furthermore, there are two important consequences of the finding that $\sigma_{TSL}/\sigma_{DOS} \approx 2/3$. (i) From a practical perspective, this suggests a useful methodology for determining the DOS width. Experimentally, it is straightforward to estimate σ_{TSL} by Gaussian fitting of the whole TSL curve ("ODOS assessment") measured after

IR cleansing, and then to account for the factor 2/3 for obtaining σ_{DOS}. (ii) From a fundamental point of view, the observed ratio of $\sigma_{TSL}/\sigma_{DOS} \approx 2/3$ implies a kind of "spectral-narrowing" effect occurring for the ODOS at low temperatures. This experimental finding obviously requires a theoretical justification. Therefore, we further carry out a KMC-simulation-based study to gain a deeper insight into charge-carrier energetic relaxation phenomena at low temperatures.

III. KINETIC MONTE CARLO SIMULATIONS

A. Simulation techniques

The energetic relaxation of charges in a disordered organic solid is studied by using a grid-based KMC simulation method to monitor the motion of charge carriers as hopping events. The KMC simulations are done by employing an isotropic three-dimensional simulation box ($100 \times 100 \times 100$ lattice sites) with a lattice constant of $a = 1.5$ nm [41,42]. We consider both random- and spatially correlated energetic disorder. For the simulations with uncorrelated disorder, the lattice sites are assigned a random energy drawn from a Gaussian distribution $g(\varepsilon)$ with a standard deviation σ_{DOS} centered at zero energy:

$$g(\varepsilon) = \frac{N}{\sigma\sqrt{2\pi}}\exp\left[-\frac{1}{2}\left(\frac{\varepsilon}{\sigma_{DOS}}\right)^2\right]. \qquad (2)$$

For systems with correlated disorder, the energy correlations between the lattice sites are modeled using the approach suggested by Bobbert and co-workers [3]. The energy at site i is taken to be equal to the electrostatic energy resulting from permanent random dipoles, $\vec{d}_j$, of equal magnitude, d, but with random orientations on all the other organic sites, $j \neq i$. The resulting DOS is a Gaussian, with a width, σ_{DOS}, proportional to d [19]. The on-site energy, E_i, is then evaluated by using the Ewald summation method:

$$E_i = -\sum_{j \neq i} \frac{e\vec{d}_j(\vec{r}_j - \vec{r}_i)}{\varepsilon_0\varepsilon_r|\vec{r}_j - \vec{r}_i|^3}, \qquad (3)$$

with the sum over all sites j in a large cubic box of 30 lattice sites (in each direction) around site i; e is the unit charge, ε_0 is the vacuum permittivity, and ε_r is the material's relative permittivity. As pointed out by Bobbert and co-workers [3], with increasing the dimension of the box used for calculating the sum in Eq. (3), charge-dipole interactions can be considered in a progressively accurate manner. In this study, to obtain a fair compromise between accuracy and computation time, we take the sum over all sites j in a large cubic box of 30 lattice sites (in each direction) around site i. In this study, we take $\varepsilon_r = 3$ for all simulations. The resulting disorder strength is then given by
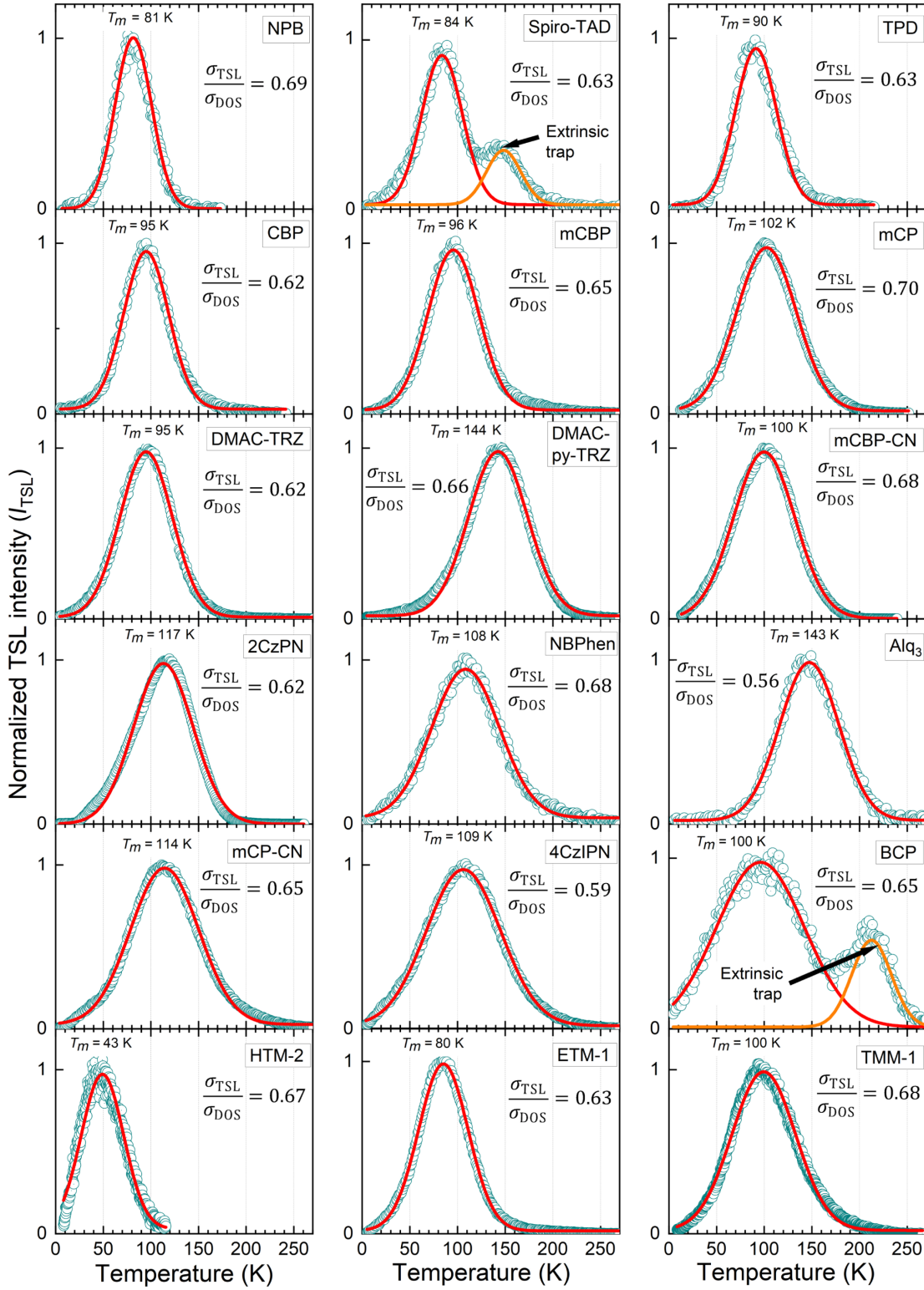
FIG. 3. TSL curves of different organic semiconductor films obtained after IR cleansing. Experimental data are shown by symbols, and solid lines are the fitted Gaussians.

106

TABLE I. Comparison between the DOS width (σ_{DOS}), energy width of the TSL peak (σ_{TSL}), and the $\sigma_{\text{TSL}}/\sigma_{\text{DOS}}$ ratio for a set of amorphous organic semiconductors. The last column shows the theoretical σ_{DOS} parameter derived from QM-MM calculations.

	Material	σ_{DOS} (meV)	σ_{TSL} (meV)	$\sigma_{\text{TSL}}/\sigma_{\text{DOS}}$	Theoretical σ_{DOS} (meV)
1	NPB	88	61	0.69	87 [28]
2	Spiro-TAD	110	69	0.63	90 [28]
3	TPD	110	69	0.63	−
4	DMAC-TRZ	110	66	0.60	129[a]
5	CBP	125	77	0.62	100 [22]
6	mCBP	131	85	0.65	122 [28]
7	mCP	140	99	0.70	160 [28],157 [39]
8	DMAC-py-TRZ	151	99	0.66	−
9	mCBP-CN	151	102	0.68	200 [22]
10	2CzPN	161	100	0.62	−
11	NBPhen	167	114	0.68	194 [28]
12	Alq3	177	99	0.56	150 [40]
13	mCP-CN	177	115	0.65	240 [22]
14	4CzIPN	213	125	0.59	220[a]
15	BCP	226	147	0.65	190 [28]
16	HTM-2	73	49	0.67	79[a]
17	ETM-1	103	65	0.63	127[a]
18	TMM-1	132	90	0.68	140[a]
Mean				0.64 ± 0.04	

[a]See the Appendix for a theoretical method of σ_{DOS} computation.

$\sigma_{\text{DOS}} \approx 2.35(ed/\varepsilon_r\varepsilon_0 a^2)$. Figures 4(a) and 4(b) illustrate the impact of spatial correlations on the energy landscape in an arbitrary X-Y plane (two-dimensional cross section) of the simulation box. In the case of a system with random disorder [Fig. 4(a)], the position of energetic peaks and valleys is found to be completely uncorrelated. On the contrary, in the case of a system with correlated disorder, the sites of higher (lower) energy depicted with blue (red) color [Fig. 4(b)] are found to be in the vicinity of other higher (lower) energy sites. The spatial correlation function, $C(r_{ij})$, which quantifies the degree of correlation between sites at a separation of r_{ij} from each other can be expressed as

$$C(r_{ij}) = \frac{\left\langle (E_i - \langle E \rangle)\,(E_j - \langle E \rangle) \right\rangle}{\left\langle (E_i - \langle E \rangle)^2 \right\rangle}, \quad (4)$$

where E_i and E_j are the energies of sites i and j separated by a distance r_{ij}, and $\langle \ldots \rangle$ represents the expectation value. $C(r_{ij})$ is 1 if E_i and E_j are fully correlated and 0 if they are uncorrelated. The spatial correlation function evaluated for the energy sites of the X-Y plane in Figs. 4(a) and 4(b) is shown in Figs. 4(c) and 4(d), respectively. While $C(r_{ij})$ is found to be 0 for the system with random disorder, it exhibits a $1/r_{ij}$ dependence for the system with randomly oriented site dipoles, as expected from the interaction of a charge with the long-range-dipole electrostatic potential of a three-dimensional ensemble of uncorrelated dipoles [19].

Hopping transitions in our system are described using Miller-Abrahams hopping rates between an initial site of energy ε_i and a final site of energy ε_j:

$$W_{ij} = \nu_0 \exp(-2\gamma R_{ij})\exp\left[-\frac{|\varepsilon_j - \varepsilon_i| + (\varepsilon_j - \varepsilon_i)}{2k_BT} \right], \quad (5)$$

where R_{ij} is the hopping distance and γ is the inverse localization radius. ν_0 is the attempt-to-escape frequency, which is usually close to an intermolecular phonon frequency; k_B is the Boltzmann constant; and T is temperature. The parameter γ is assumed to be isotropic in all directions. Unless otherwise specified, γ is chosen as 2 nm^{-1} (such that $2\gamma a = 6$), as this value is a representative value commonly utilized in theoretical modeling of hopping-charge transport in amorphous organic semiconductors. To consider transitions of carriers to non-nearest hopping sites, we implement variable-range hopping in the KMC simulations by allowing long-distance jumps up to the tenth-nearest neighbor. The probabilities of such jumps are determined by the carrier localization parameter ($2\gamma a$).

Furthermore, both variable-time-step (VT) KMC and constant-time-step (CT) KMC approaches are utilized to solve the master equation. For VT KMC simulations, the following procedure is employed. At the beginning of the simulation, $t = 0$, a charge carrier is generated randomly at one of the lattice sites. At each kinetic step, the charge can hop to any of the nearest-neighbor sites. In the case of KMC simulations in the VRH regime, a charge carrier is also allowed to access non-nearest hopping sites. Every permissible hop is treated as an event, and for each event,
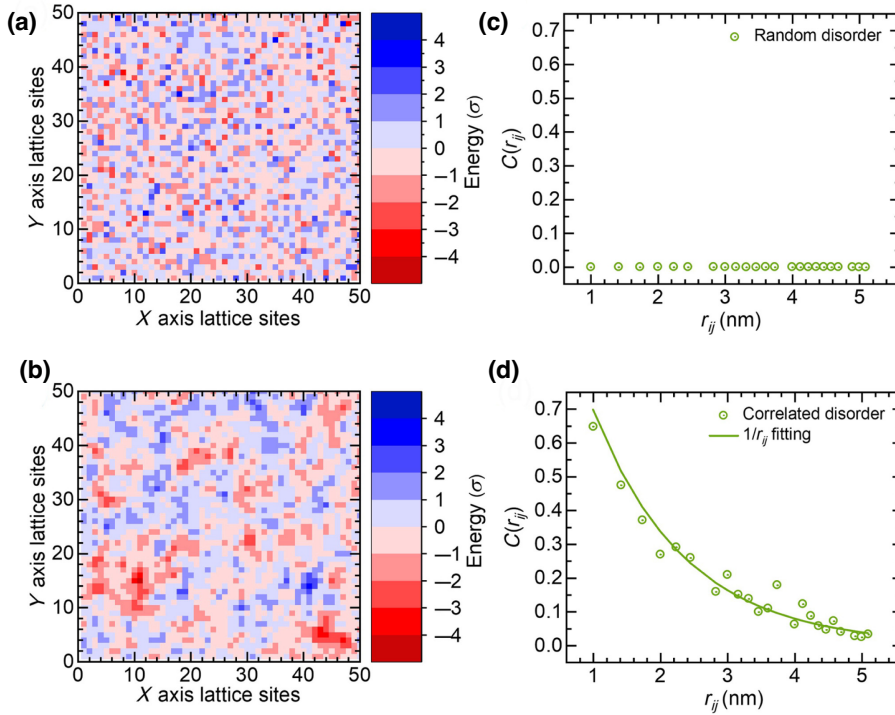
FIG. 4. Heatmap of energetic landscape for a system with (a) random disorder and (b) correlated disorder. Variation of spatial energy correlation function, $C(r_{ij})$ [see Eq. (4)] with distance for (c) random disorder system and (d) correlated disorder system.

i, the rate, W_i, is calculated. For the selection of an event, first, for each event i, the partial sum, $S_i = \sum_{j=1}^{i} W_{ij}$, is calculated. A random number, φ, is drawn from the interval (0, 1] and from all possible events; the event i for which $S_{i-1} < \varphi W_T \leq S_i$ holds is selected, with $W_T = \sum_{j=1}^{N_{tot}} W_{ij}$ and N_{tot} being the total number of events (permissible hops). The selected event is executed and the simulation time (t) is updated by the waiting time, $\tau_w = -\ln(X)/W_T$, where X is a random number between 0 and 1.

In the CT KMC simulations, total number of hopping neighbors, N_{tot}, is defined within a cube consisting of $5 \times 5 \times 5$ lattice sites. A hopping event from state i to a generic state j ($i \neq j$) is sampled uniformly from $N_{j...tot}$ hopping neighbors, and rate W_{ij} is calculated. The event is accepted if the associated hopping probability $f_{ij} = (W_{ij}/v_0) > n$, where n is a uniform number between 0 and 1, and v_0 is the rate in a lattice without disorder. Simulation time (t) is updated by $\Delta t = (1/v_0 N_{tot})\ln(1/X)$, where X is a random number, such that $X \in (0, 1]$. If the event is accepted, event $i \rightarrow j$ is executed and charge-carrier coordinates are updated. The timescale is defined by $t_0 = 1/(v_0 N_{tot})$.

Here, the CT KMC simulation method is used to gain an insight into the charge-carrier energy relaxation in short and intermediate time regimes. As the charge carriers relax within the DOS, the hopping rates, W_{ij} (and W_T), can decrease abruptly (by orders of magnitude), even if the number of hopping sites remains constant. Thus, the majority of CT KMC simulation trials are rejected, leading

to computationally intensive simulations. On the other hand, in VT KMC simulations, the time step is evaluated as the inverse of W_T, which leads to a nonlinear increase in the time step as the charge carriers relax in energy. As a result, we lose temporal resolution, and hence, the VT KMC simulation results will be parametrized in terms of the number of hops. However, this allows us to examine the long-time limit of the charge-carrier relaxation process at a reasonable computational cost using the VT KMC simulation method.

B. Simulation results

As mentioned in Sec. II, the TSL curve itself is expected to map a distribution of charge carriers localized within the lower-energy states of the DOS distribution, i.e., the ODOS distribution, formed because of the downward hopping of charges within the DOS at 5 K. For comparison with the TSL experiments, we are therefore interested in the long-time limit of the energetic relaxation of the charges, and hence, we consider VT KMC simulation results. The selected simulation temperature ($T = 5$ K) corresponds to a "nonactivated relaxation" mode [10], often termed the regime of purely downward hopping motion. In contrast, at a moderate degree of disorder (and high enough temperature), charge carriers enter the regime of "activated relaxation" after a critical time (known as the segregation time) [14]. As in previous theoretical studies of

low-temperature energy relaxation and TSL in a random-hopping system [23,27], we assume a very weak inter-action between charges within long-range loosely bound geminate pairs responsible for TSL, and therefore, disregard the Coulomb contribution to the difference in energies of neighboring localized sites and to the jump rate. Thus, the energy-relaxation process in TSL is treated the same as that for noninteracting charge carriers.

The evolution of the distribution of charge carriers in a system with random disorder of the DOS width, $\sigma_{DOS} = 50$ meV, is depicted in Fig. 5(a). Data illustrated are the Gaussian fit results of the energy distribution of charges obtained after a certain number of hops. As shown and discussed further below [see also Fig. S3(a) within the Supplemental Material [30]], the actual distribution of occupied sites after a few hops is not fully symmetric. While the low-energy part, being limited by the number of available neighbors, follows the Gaussian distribution, the high-energy part falls off more steeply. The Gaussian fits to the overall shape are, however, sufficient to capture the general features of the evolution.

In particular, we observe that, with an increasing number of hops, the energy distribution of charges moves to deeper localized states and narrows. The mean energy ($\langle \varepsilon \rangle$) and width ($\sigma$) of the charge-carrier ensemble, both normalized by the DOS width (σ_{DOS}), are plotted in Fig. 5(b) as a function of number of hops. A significant initial drop in the mean energy is observed, followed by a decrease in the relaxation rate. The largest shift in mean energy

($\langle \varepsilon \rangle \approx -2.5\ \sigma_{DOS}$) is observed within the first 20 hops [Figs. 5(a) and 5(b)]. This is because only the newly visited sites contribute to the shift in the mean energy, $\langle \varepsilon \rangle$ [8,14,43], and as the charges relax to deeper localized states, the availability of suitable energy sites decreases. In other words, once a charge is captured by a deep trap, it oscillates infinitely and never leaves the local minima. This feature is also captured in the VT KMC simulations. As shown further in Fig. S2 within the Supplemental Material [30], the number of newly visited sites increases significantly within the first 20 hops followed by a slow increase for a higher number of hops. It is to be noted that even after 10^6 hops the number of newly visited sites remains less than 10, in agreement with previous reports [8,14,43].

Analogous to the evolution of the mean energy, a considerable initial narrowing of the energy distribution of the charges is followed by an almost constant σ as the number of hops is increased further. Since dynamic equilibrium is unattainable at 5 K, the charge packet evolves infinitely with simulation time. However, a further increase in simulation time should not drastically affect the distribution of charges oscillating in the vicinity of local minima, and hence, the charge ensemble after 10^6 hops can be considered as the ODOS distribution of the charges. We are particularly interested in the distribution of the ODOS.

In the original Gaussian disorder model (GDM) [6], any spatial correlations between the energies of the hopping sites are disregarded. The inclusion of correlations between the energies of adjacent sites in the correlated disorder
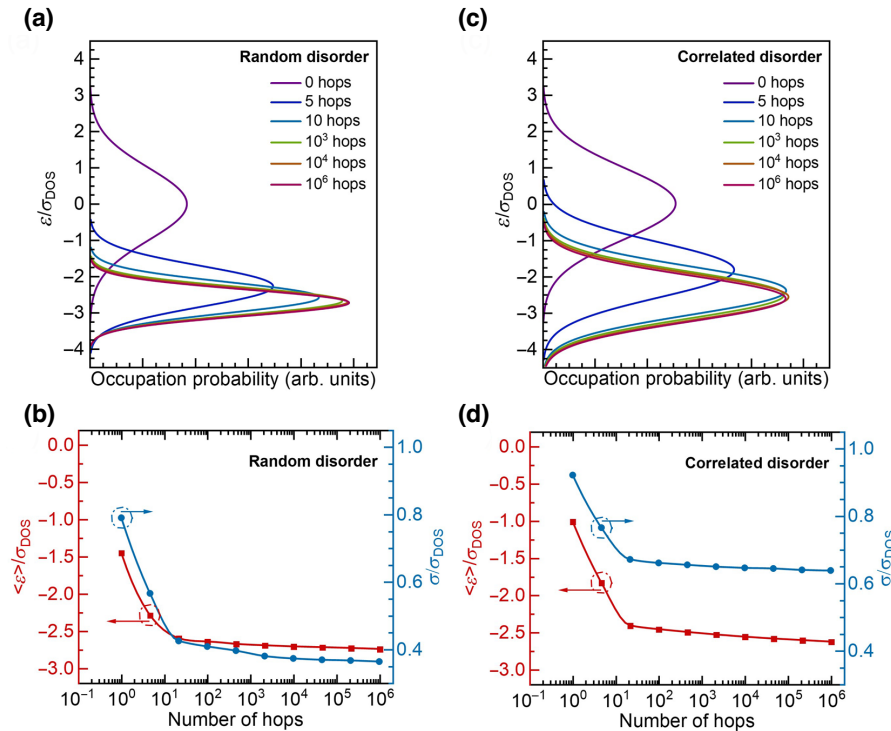
FIG. 5. VT KMC simulation results. Evolution of charge distribution with the number of hops for a system with (a) random and (c) spatially correlated energetic disorder. Data illustrated are Gaussian fit results of the energy distribution of charges obtained after the specified number of hops at 5 K. Variation of mean energy ($\langle \varepsilon \rangle$) and width ($\sigma$) of the charge-energy distribution (both normalized by the DOS width, σ_{DOS}) with the number of hops for (b) random and (d) correlated disorder.

model is crucial in predicting the Poole-Frenkel mobility field dependence over a broad field range [16–19,21]; however, the impact of correlation has never been considered in the context of the energetic relaxation of charges. Since the materials used in this study are polar materials [22,28,44] and the TSL measurements are performed at zero fields, we now turn our attention to the results obtained for charge-carrier relaxation in an energy-correlated medium. Like the system with random energetic disorder [Fig. 5(a)], the charge ensemble shifts to lower energy and narrows in the case of correlated disorder system as well [Fig. 5(c)]. However, unlike the uncorrelated disorder system, the narrowing effect is considerably weaker in the system with spatially correlated disorder. We surmise that for random disorder all hops to the new sites dominantly contribute to narrowing; in contrast, hops among correlated sites with almost the same energies cause only limited energy loss. It can be seen from Fig. 5(d) that, within the span of the first 20 hops, the width of the energy distribution of the charges reduces to 0.42 σ_{DOS} for random disorder versus 0.67 σ_{DOS} for correlated disorder, leading eventually to a larger ODOS width of $\sigma_{ODOS} = 0.64 \times \sigma_{DOS}$ [Fig. S3(b) in the Supplemental Material [30]]. $\langle \varepsilon \rangle$ is set to 0 prior to the first hop. It decreases significantly within the course of first 20 hops followed by a slow logarithmic dependence on the number of hops [Fig. 5(d)]. The shift in mean energy after 10^6 hops is almost equal for the systems with correlated ($\langle \varepsilon \rangle \approx -2.6 \, \sigma_{DOS}$) or random disorder ($\langle \varepsilon \rangle \approx -2.7 \, \sigma_{DOS}$). In general, the nonactivated relaxation of carriers clearly takes place at such low temperatures and the average rate of distribution narrowing decreases with increasing number of hops. Accounting for the spatial energy correlations, which are indeed present

in organic media, allows experimentally obtained values for the ODOS width to be reproduced, i.e., the calculated σ_{ODOS} in a correlated system is approximately equal to σ_{TSL} evaluated experimentally.

Finally, it is worth mentioning that the ratio of $\sigma_{ODOS}/\sigma_{DOS} = 0.64$ obtained for correlated disorder shows virtually no dependence on either dielectric permittivity, ε_r, or the amount of dipolar disorder ranging from 50 to 150 meV, implying that the effect does not depend on the polarity of the materials and the DOS width. We observe a very small impact of the $2\gamma a$ factor, varied between 1.5 and 12, on the above ratio. On the other hand, since the lattice constant, a, and the inverse localization radius, γ, are not expected to differ significantly for the low-molecular-weight materials considered herein, it is therefore not surprising that the experimentally obtained 2/3 ratio is common to all of them.

1. Temperature and time dependence

So far, we focus on the nonactivated relaxation process, i.e., carrier jumps can only take place to lower-energy sites. We next take thermal activation into account for both a system with random disorder and with correlated disorder ($\sigma_{DOS} = 50$ meV), as shown in Figs. 6(a) and 6(b), respectively. We use the CT KMC simulation approach to obtain a dependence in the hopping time rather than in the number of hops. This allows for precise temporal tracking of charge-carrier relaxation.

A significant drop of mean energy is observed for $t < 10^4 t_0$, indicating fast initial energy dissipation for all simulated temperatures. This is followed by a slower dissipation process at longer times. A particular notable feature of
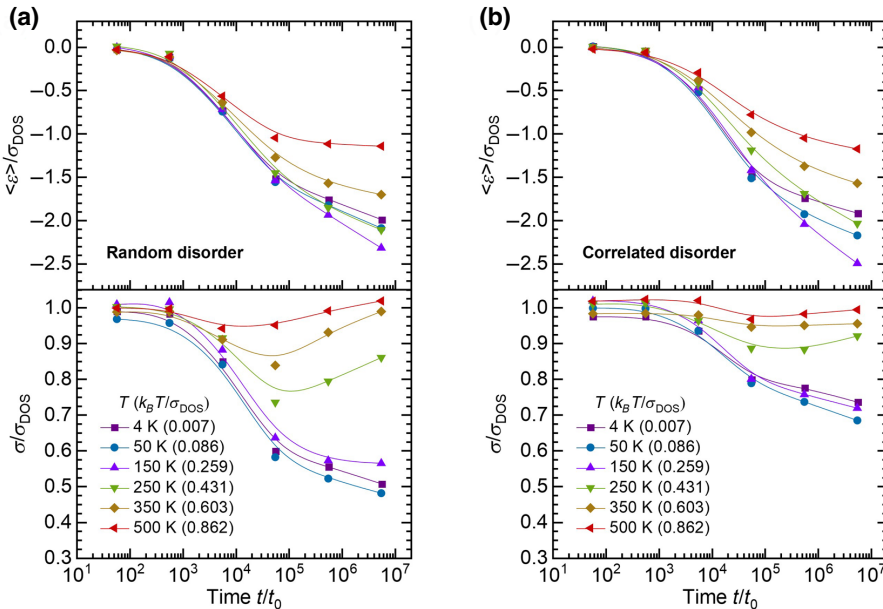
FIG. 6. CT KMC simulation results. Simulated normalized variation of mean energy ($\langle \varepsilon \rangle / \sigma_{DOS}$, top panels) and the energetic width (σ / σ_{DOS}, bottom panels) of the distribution of charges as a function of simulation time at variable temperatures for a system with (a) random disorder and (b) correlated disorder. Results are shown for CT KMC simulations performed for a DOS distribution of width $\sigma_{DOS} = 50$ meV. Solid lines serve as a guide to the eye.

the temperature dependence of charge-carrier relaxation is that the mean energy (at $t = 10^7 t_0$) decreases upon cooling from 500 to 150 K but then increases when the temperature is further reduced to 4 K. This phenomenon can be explained by the concept of frustrated spectral diffusion. The key idea is the following. The charges relax in the DOS by executing jumps to neighboring sites. These jumps may be downhill in energy or uphill, provided there is sufficient thermal energy for uphill jumps. As the temperature reduces, uphill jumps become less likely and are eventually frozen out. However, to get to lower-energy sites via nearest-neighbor-jumps, occasional uphill jumps may be required. Their freezing out can therefore frustrate the overall relaxation process, so that the carriers remain in a local energy minimum. The occurrence of this frustrated spectral diffusion is observed experimentally for triplet excitations [11]. KMC simulations by Athanasopoulos *et al.* demonstrate that frustration can be lifted if more neighboring sites are available or if jumps can occur to sites further away [12]. The top panels of Figs. 6(a) and 6(b) thus illustrate the impact that falling out of thermal equilibrium—here below 150 K (corresponding to $k_B T / \sigma_{DOS} < 0.26$)—has on the mean energy of the charges. The bottom panels of Figs. 6(a) and 6(b) focus on the effect of energy relaxation on the ODOS width. For $t < 10^4 t_0$, the width reduces with increasing time. At longer times, this reduction continues for temperatures below 150 K. In contrast, for higher temperatures, the width increases as time proceeds. This effect occurs in a similar manner for both random and correlated disorder, yet the overall reduction of the width is significantly reduced when correlated disorder is considered.

IV. DISCUSSION AND CONCLUSIONS

In amorphous organic semiconductor films, energetic relaxation of excitations occurs by a sequence of random hops. The condition of finding a low-energy hopping site is easily met in the center of the DOS, so that downhill hops are fast. Yet, for the hopping sites in the tail of the DOS, suitable hopping sites are further apart, which slows down the transfer. As a result, the excitations generated in the center (or high-energy part) of the DOS distribution relax faster than the ones generated in the tail of the DOS. Figure 7(a) demonstrates the temporal evolution of the energy distribution of the charge carriers generated uniformly over the DOS at high temperatures (T) and/or low σ_{DOS}, i.e., in the regime of equilibrium transport. The distribution shows some narrowing at *earlier times* because of the domination of downwards hops in such a time domain. However, as time progresses, the carrier distribution starts to broaden, as the carriers in lower part of the DOS start relaxing at later times via executing upward hops. Such a nonmonotonous temporal evolution of relaxed

carrier distributions [Fig. 7(a)] is obtained because the carrier's capture by local energetic minima is much faster than its release. Eventually, thermal equilibrium is established, and ODOS is formed around the equilibrium energy ($\varepsilon_{eq} = -\sigma_{DOS}^2 / k_B T$) with a width, σ_{ODOS}, equal to the width of the DOS (σ_{DOS}) [6]. On the contrary, at low temperatures, and consequently in the regime of nonequilibrium dispersive transport ($\sigma_{DOS}/k_B T \gg 1$; high σ_{DOS} or low T), the thermal equilibrium is unattainable. Therefore, at low temperatures, the photogenerated excitations hop towards the lower-energy sites until they reach the DOS tail [Fig. 7(b)]. At any instance in time, irrespective of the mean energy of the relaxed charge-carrier ensemble, the excitations at relatively higher-energy sites within the DOS still relax faster than the excitations at relatively deeper energy sites. As a result, the width (σ_{ODOS}) of the relaxed charge-carrier ensemble decreases monotonously with increasing time [Fig. 7(b)]. These two scenarios are well reproduced in the CT KMC simulation results presented in Fig. 6, which clearly demonstrate that ODOS narrowing is a consequence of nonequilibrium transport. This is also corroborated by previous reports, which suggest that in the regime of equilibrium transport such a narrowing is absent [6,14]. The observation that an ODOS smaller than the full DOS width is a result of the nonequilibrium nature of the transport has not been made before. It is a significant result of our study.

As briefly mentioned in Secs. I and III, the energetic relaxation has already been extensively studied for singlet and triplet excitations and is manifested as spectral diffusion in this context [45]. Experimentally, spectral diffusion is visualized as the bathochromic shift of fluorescence and phosphorescence with temperature for many conjugated systems, such as poly(*p*-phenylenevinylene) [46], poly(*p*-phenylene) [11–13], and polyfluorenes [12,47], as well as for small-molecule materials, such as thermally activated delayed fluorescence emitters [48] and dendrimers [49]. It is also crucial in analyzing the photocurrent and photoluminescence spectra of charge-transfer states in donor-acceptor blends, commonly used as an active layer in organic solar cells [50–53]. Although a lot of attention is given to the shift in the mean energy of the relaxed excitation ensemble as spectral diffusion progresses, spectral narrowing is often not analyzed nor discussed [12,47]. Recently, Kahle *et al.* [54] pointed out that the experimentally observed fluorescence linewidths were significantly lower than those of absorption. This implies that the radiative decay of excitations occurs before spectral diffusion attains equilibrium, and thus, further illustrates the importance of spectral narrowing studies in the regime of nonequilibrium transport.

While the migration of singlet and triplet excitations can be examined spectroscopically, it is difficult to monitor the diffusion of charges. Though the charge-carrier relaxation dynamics process cannot be probed with TSL,
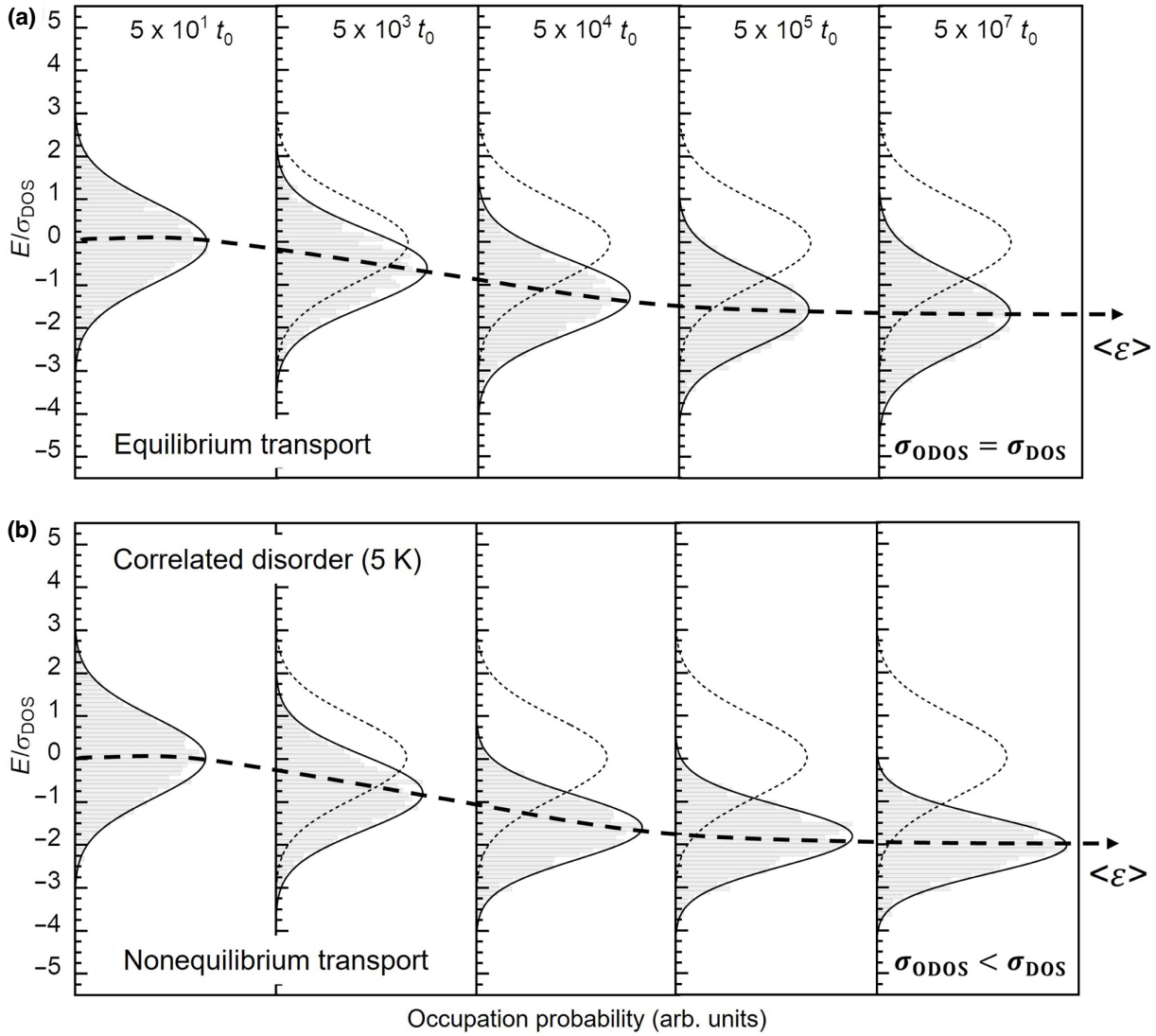
FIG. 7. Schematic representation of the temporal evolution of the charge-carrier ensemble for (a) equilibrium transport (b) nonequilibrium transport for selected time intervals. Initial distribution is indicated throughout by the dotted line for reference.

the latter technique allows us to investigate the ODOS distribution formed as a result of the charge-carrier relaxation process. As shown in the KMC simulation results of Figs. 5 and 6, relaxation never achieves equilibrium at low temperatures. Although the rate of relaxation is fast at earlier times, it slows down as time progresses. At long delay times after excitation, the mean energy and energetic width of the charge-carrier ensemble virtually saturates. It is therefore important to point out that, since the process of photogeneration and relaxation of excitations take place at liquid-helium temperature in TSL experiments, the TSL experiments probe a quasistationary ODOS distribution. Thus, as theoretically illustrated by Arkhipov *et al.* [27],

the TSL experiments can serve as a direct optical probe of the energetic disorder of the organic semiconductor films.

In summary, the TSL technique can be used to probe the distribution of relaxed charge carriers trapped within the DOS formed as a result of energetic relaxation of charges within the DOS at low temperatures. The high-temperature wing of the classical TSL curve is an exact replica of the deeper portion of the DOS distribution, and thus, its Gaussian analysis yields the available DOS width, σ_{DOS}. Moreover, a Gaussian fit of the IR-cleansed TSL curve (σ_{TSL}) allows us to determine the ODOS width. TSL experiments conducted on pristine amorphous films of 18 low-molecular-weight organic materials commonly

used in the fabrication of OLEDs lead to the observation that the ODOS distribution formed at low temperatures is narrower than that of the DOS, with a universal ratio of $\sigma_{TSL}/\sigma_{DOS} = \sigma_{ODOS}/\sigma_{DOS} \approx 2/3$. To gain a deeper insight into this effect, we perform KMC simulations of the charge-carrier energetic relaxation process within the DOS. The KMC-simulation-based study illustrates that the spectral narrowing effect, as observed in TSL experiments, is a genuine property of carrier relaxation within the Gaussian DOS at low temperature and that spatial correlations among the energy of the hopping sites significantly reduce this narrowing effect. The results obtained within this study contribute to a better understanding of the properties of organic charge-transporting layers in both OLEDs and hybrid perovskite-based light-emitting devices. The finding of ODOS narrowing under a nonequilibrium transport regime should be considered by established hopping transport theories and might also be incorporated into device simulation tools.

APPENDIX: THEORETICAL METHOD OF σ_{DOS} COMPUTATION

For morphology simulations, we adapt the Optimized Potentials for Liquid Simulations–All Atom force field (OPLS-AA) [55–57]. All Lennard-Jones parameters are taken from this force field, and we use the OPLS combination rules and a fudge factor of 0.5 for 1–4 interactions. Atomic partial charges are computed via the Merz-Kolmann method by fitting the electrostatic potential of the electron density for DFT calculations performed at the B3LYP/6-31G(d) level [58]. For parametrization of dihedral potentials the molecules are partitioned into rigid fragments [59]. By fitting fixed values of the dihedral angle between rigid fragments, molecular geometry is optimized using xTB version 6.2. [60]. The resulting potential energy surface is then fitted to the Ryckaert-Belleman polynomial, $V_{RB}(\theta) = \sum_{n=0}^{5} (\cos \theta)^n$. The long-range electrostatic interactions are treated by using the

smooth-particle-mesh Ewald technique. A cutoff of 1.3 nm is used for nonbonded interactions. The equations of motion are integrated with a time step of 0.002 ps. All molecular dynamics simulations are performed in the *NPT* ensemble using the canonical velocity-rescaling thermostat [61] and the Berendsen barostat [62], as implemented in the GROMACS simulation package [63,64].

To obtain the *amorphous* morphology, systems of 243, 256, and 175 molecules for TMM-1, ETM-1, and HTM-2, respectively, are randomly inserted into the simulation box using packmol to give an isotropic cubic simulation box [65]. These systems are then simulated in the *NPT* ensemble at $T = 700$ K, $P = 1$ bar for 1 ns before cooling to 300 K during at a rate of 10 K/ns. Fast cooling freezes the isotropic orientation of the high-temperature liquid, leading to an amorphous molecular ordering.

Using the molecular dynamics trajectories, we evaluate the anion, cation, and neutral-state energies for each molecule in a morphology using a perturbative approach [66–68]. In this approach, the total energy is a sum of the gas-phase, electrostatic, and induction contributions, $E_{e,h,n} = E_{e,h,n}^{gas} + E_{e,h,n}^{stat} + E_{e,h,n}^{ind}$. To evaluate the electrostatic contribution, we calculate the Coulombic sums of distributed atomic multipoles up to the fourth order. The induction contributions to site energies are calculated self-consistently using the Thole mode [69,70], on the basis of the atomic polarizabilities and distributed multipoles obtained by using the Gaussian Distributed Multipole Analysis parametrization scheme for a cation, anion, and neutral molecule. All calculations are performed using the aperiodic Ewald summation scheme [71], as implemented in the in-house-developed VOTCA package [72].

---

[1] W. Pasveer, J. Cottaar, C. Tanase, R. Coehoorn, P. Bobbert, P. Blom, D. De Leeuw, and M. Michels, Unified Description of Charge-Carrier Mobilities in Disordered Semiconducting Polymers, Phys. Rev. Lett. **94**, 206601 (2005).

[2] S. L. van Mensfoort, S. Vulto, R. A. Janssen, and R. Coehoorn, Hole transport in polyfluorene-based sandwich-type devices: Quantitative analysis of the role of energetic disorder, Phys. Rev. B **78**, 085208 (2008).

[3] J. Van der Holst, F. Van Oost, R. Coehoorn, and P. Bobbert, Monte Carlo study of charge transport in organic sandwich-type single-carrier devices: Effects of Coulomb interactions, Phys. Rev. B **83**, 085206 (2011).

[4] N. Tessler, Y. Preezant, N. Rappaport, and Y. Roichman, Charge transport in disordered organic materials and its relevance to thin-film devices: A tutorial review, Adv. Mater. **21**, 2741 (2009).

[5] L. J. Koster, E. Smits, V. Mihailetchi, and P. W. Blom, Device model for the operation of polymer/fullerene bulk heterojunction solar cells, Phys. Rev. B **72**, 085205 (2005).

[6] H. Bässler, Charge transport in disordered organic photo-conductors. A Monte Carlo simulation study, Phys. Status Solidi B **175**, 15 (1993).

[7] A. Köhler and H. Bässler, *Electronic processes in organic semiconductors: An introduction* (John Wiley & Sons, Weinheim, 2015).

[8] H. Bässler, in *Disorder Effects on Relaxational Processes*, edited by R. Richter, A. Blumen (Springer, Berlin Heidelberg New York, 1994), pp. 485.

[9] P. Borsenberger, L. T. Pautmeier, and H. Bässler, Nondispersive-to-dispersive charge-transport transition in disordered molecular solids, Phys. Rev. B **46**, 12145 (1992).

[10] P. Borsenberger, R. Richert, and H. Bässler, Dispersive and nondispersive charge transport in a molecularly doped polymer with superimposed energetic and positional disorder, Phys. Rev. B **47**, 4289 (1993).

[11] S. T. Hoffmann, H. Bässler, J.-M. Koenen, M. Forster, U. Scherf, E. Scheler, P. Strohriegl, and A. Köhler, Spectral diffusion in poly (*para*-phenylene)-type polymers with different energetic disorder, Phys. Rev. B **81**, 115103 (2010).

[12] S. Athanasopoulos, S. T. Hoffmann, H. Bässler, A. Köhler, and D. Beljonne, To hop or not to hop? Understanding the temperature dependence of spectral diffusion in organic semiconductors, J. Phys. Chem. Lett. **4**, 1694 (2013).

[13] S. T. Hoffmann, E. Scheler, J.-M. Koenen, M. Forster, U. Scherf, P. Strohriegl, H. Bässler, and A. Köhler, Triplet energy transfer in conjugated polymers. III. An experimental assessment regarding the influence of disorder on polaronic transport, Phys. Rev. B **81**, 165208 (2010).

[14] B. Ries, H. Bässler, M. Grünewald, and B. Movaghar, Monte Carlo study of relaxation and diffusion in glassy systems, Phys. Rev. B **37**, 5508 (1988).

[15] R. Richert and H. Bässler, Energetic relaxation of triplet excitations in vitreous benzophenone, Chem. Phys. Lett. **118**, 235 (1985).

[16] S. Van Mensfoort, V. Shabro, R. De Vries, R. Janssen, and R. Coehoorn, Hole transport in the organic small molecule material α-NPD: Evidence for the presence of correlated disorder, J. Appl. Phys. **107**, 113710 (2010).

[17] S. Van Mensfoort, R. De Vries, V. Shabro, H. Loebl, R. Janssen, and R. Coehoorn, Electron transport in the organic small-molecule material BAlq—the role of correlated disorder and traps, Org. Electron. **11**, 1408 (2010).

[18] D. H. Dunlap, P. E. Parris, and V. M. Kenkre, Charge-Dipole Model for the Universal Field Dependence of Mobilities in Molecularly Doped Polymers, Phys. Rev. Lett. **77**, 542 (1996).

[19] S. V. Novikov, D. H. Dunlap, V. M. Kenkre, P. E. Parris, and A. V. Vannikov, Essential Role of Correlations in Governing Charge Transport in Disordered Organic Materials, Phys. Rev. Lett. **81**, 4472 (1998).

[20] S. Novikov and A. Vannikov, Hopping charge transport in disordered organic materials: Where is the disorder?, J. Phys. Chem. C **113**, 2532 (2009).

[21] M. Bouhassoune, S. Van Mensfoort, P. Bobbert, and R. Coehoorn, Carrier-density and field-dependent charge-carrier mobility in organic semiconductors with correlated Gaussian disorder, Org. Electron. **10**, 437 (2009).

[22] A. Stankevych, A. Vakhnin, D. Andrienko, L. Paterson, J. Genoe, I. Fishchuk, H. Bässler, A. Köhler, and A.

Kadashchuk, Density of States of OLED Host Materials from Thermally Stimulated Luminescence, Phys. Rev. Appl. **15**, 044050 (2021).

[23] A. Kadashchuk, Y. Skryshevskii, A. Vakhnin, N. Ostapenko, V. Arkhipov, E. Emelianova, and H. Bässler, Thermally stimulated photoluminescence in disordered organic materials, Phys. Rev. B **63**, 115205 (2001).

[24] A. Kadashchuk, N. Ostapenko, V. Zaika, and S. Nešpurek, Low-temperature thermoluminescence in poly (methylphenylsilylene), Chem. Phys. **234**, 285 (1998).

[25] A. Kadashchuk, Y. Skryshevski, Y. Piryatinski, A. Vakhnin, E. Emelianova, V. Arkhipov, H. Bässler, and J. Shinar, Thermally stimulated photoluminescence in poly (2, 5-dioctoxy *p*-phenylene vinylene), J. Appl. Phys. **91**, 5016 (2002).

[26] A. Kadashchuk, D. Weiss, P. Borsenberger, S. Nešpurek, N. Ostapenko, and V. Zaika, The origin of thermally stimulated luminescence in neat and molecularly doped charge transport polymer systems, Chem. Phys. **247**, 307 (1999).

[27] V. Arkhipov, E. Emelianova, A. Kadashchuk, and H. Bässler, Hopping model of thermally stimulated photoluminescence in disordered organic materials, Chem. Phys. **266**, 97 (2001).

[28] A. Mondal, L. Paterson, J. Cho, K.-H. Lin, B. van der Zee, G.-J. A. Wetzelaer, A. Stankevych, A. Vakhnin, J.-J. Kim, and A. Kadashchuk, Molecular library of OLED host materials—evaluating the multiscale simulation workflow, Chem. Phys. Rev. **2**, 031304 (2021).

[29] A. Kadashchuk, A. Vakhnin, Y. Skryshevski, V. Arkhipov, E. Emelianova, and H. Bässler, Thermally stimulated luminescence in π-conjugated polymers containing fluorene and spirobifluorene units, Chem. Phys. **291**, 243 (2003).

[30] See the Supplemental Material at http://link.aps.org/supplemental/10.1103/PhysRevApplied.19.054007 for the full names of compounds used in this study (Note S1); more details about the fractional thermally stimulated luminescence methodology (Note S2); and determination of the DOS width, σ_{DOS}, by TSL (Note S3).

[31] I. Tale, Trap spectroscopy by the fractional glow technique, Phys. Status Solidi A **66**, 65 (1981).

[32] A. Kadashchuk, N. I. Ostapenko, Yu. A. Skryshevskii, V. I. Sugakov, and T. O. Susokolova, Clusters of dipole charge-carrier capture centers in organic crystals, Mol. Cryst. Liq. Cryst. **201**, 167 (1991).

[33] V. Arkhipov, E. Emelianova, R. Schmechel, and H. Von Seggern, Thermally stimulated luminescence versus thermally stimulated current in organic semiconductors, J. Non-Cryst. Solids **338**, 626 (2004).

[34] B. Schweitzer, V. Arkhipov, U. Scherf, and H. Bässler, Geminate pair recombination in a conjugated polymer, Chem. Phys. Lett. **313**, 57 (1999).

[35] V. Nikitenko, D. Hertel, and H. Bässler, Dispersive geminate recombination in a conjugated polymer, Chem. Phys. Lett. **348**, 89 (2001).

[36] A. Gerhard and H. Bässler, Delayed fluorescence of a poly (*p*-phenylenevinylene) derivative: Triplet–triplet annihilation versus geminate pair recombination, J. Chem. Phys. **117**, 7350 (2002).

[37] C. L. Braun, S. Smirnov, S. S. Brown, and T. Scott, Picosecond transient absorption measurements of geminate

electron-cation recombination, J. Phys. Chem. **95**, 5529 (1991).

[38] A. A. Bakulin, A. Rao, V. G. Pavelyev, P. H. van Loos-drecht, M. S. Pshenichnikov, D. Niedzialek, J. Cornil, D. Beljonne, and R. H. Friend, The role of driving energy and delocalized states for charge separation in organic semiconductors, Science **335**, 1340 (2012).

[39] P. de Silva and T. Van Voorhis, QM/MM study of static and dynamic energetic disorder in the emission layer of an organic light-emitting diode, J. Phys. Chem. Lett. **9**, 1329 (2018).

[40] A. Lukyanov and D. Andrienko, Extracting nondispersive charge carrier mobilities of organic semiconductors from simulations of small systems, Phys. Rev. B **82**, 193202 (2010).

[41] R. Saxena, T. Meier, S. Athanasopoulos, H. Bässler, and A. Köhler, Kinetic Monte Carlo Study of Triplet-Triplet Anni-hilation in Conjugated Luminescent Materials, Phys. Rev. Appl. **14**, 034050 (2020).

[42] R. Saxena, V. Nikitenko, I. Fishchuk, Y. V. Burdakov, Y. V. Metel, J. Genoe, H. Bässler, A. Köhler, and A. Kadashchuk, Role of the reorganization energy for charge transport in disordered organic semiconductors, Phys. Rev. B **103**, 165202 (2021).

[43] B. Movaghar, B. Ries, and M. Grünewald, Diffusion and relaxation of energy in disordered systems: Departure from mean-field theories, Phys. Rev. B **34**, 5574 (1986).

[44] X. De Vries and R. Coehoorn, Vibrational mode contri-bution to the dielectric permittivity of disordered small-molecule organic semiconductors, Phys. Rev. Mater. **4**, 085602 (2020).

[45] S. C. Meskers, J. Hübner, M. Oestreich, and H. Bässler, Dispersive relaxation dynamics of photoexcitations in a polyfluorene film involving energy transfer: Experiment and Monte Carlo simulations, J. Phys. Chem. B **105**, 9139 (2001).

[46] S. T. Hoffmann, H. Bässler, and A. Köhler, What deter-mines inhomogeneous broadening of electronic transitions in conjugated polymers?, J. Phys. Chem. B **114**, 17037 (2010).

[47] S. T. Hoffmann, S. Athanasopoulos, D. Beljonne, H. Bässler, and A. Köhler, How do triplets and charges move in disordered organic semiconductors? A Monte Carlo study comprising the equilibrium and nonequilibrium regime, J. Phys. Chem. C **116**, 16371 (2012).

[48] F. B. Dias, T. J. Penfold, and A. P. Monkman, Photophysics of thermally activated delayed fluorescence molecules, Methods Appl. Fluoresc. **5**, 012001 (2017).

[49] D. Sun, R. Saxena, X. Fan, S. Athanasopoulos, E. Duda, M. Zhang, S. Bagnich, X. Zhang, E. Zysman-Colman, and A. Köhler, Regiochemistry of donor dendrons controls the performance of thermally activated delayed fluorescence dendrimer emitters for high efficiency solution-processed organic light-emitting diodes, Adv. Sci. **9**, 2201470 (2022).

[50] Y. Liu, K. Zojer, B. Lassen, J. Kjelstrup-Hansen, H.-G. Rubahn, and M. Madsen, Role of the charge-transfer state in reduced Langevin recombination in organic solar cells: A theoretical study, J. Phys. Chem. C **119**, 26588 (2015).

[51] F.-J. Kahle, A. Rudnick, H. Bässler, and A. Köhler, How to interpret absorption and fluorescence spectra of charge

transfer states in an organic solar cell, Mater. Horiz. **5**, 837 (2018).

[52] T. Upreti, S. Wilken, H. Zhang, and M. Kemerink, Slow relaxation of photogenerated charge carriers boosts open-circuit voltage of organic solar cells, J. Phys. Chem. Lett. **12**, 9874 (2021).

[53] A. Melianas, N. Felekidis, Y. Puttisong, S. C. Meskers, O. Inganäs, W. M. Chen, and M. Kemerink, Nonequilib-rium site distribution governs charge-transfer electrolumi-nescence at disordered organic heterointerfaces, Proc. Natl. Acad. Sci. U. S. A. **116**, 23416 (2019).

[54] F. J. Kahle, A. Rudnick, S. Wedler, R. Saxena, R. Ammen-häuser, U. Scherf, S. Bagnich, H. Bässler, and A. Köhler, Static and dynamic disorder of charge transfer states probed by optical spectroscopy, Adv. Energy Mater. **12**, 2103063 (2022).

[55] W. L. Jorgensen and J. Tirado-Rives, Potential energy func-tions for atomic-level simulations of water and organic and biomolecular systems, Proc. Natl. Acad. Sci. U. S. A. **102**, 6665 (2005).

[56] W. L. Jorgensen and J. Tirado-Rives, The OPLS [opti-mized potentials for liquid simulations] potential functions for proteins, energy minimizations for crystals of cyclic peptides and crambin, J. Am. Chem. Soc. **110**, 1657 (1988).

[57] W. L. Jorgensen, D. S. Maxwell, and J. Tirado-Rives, Development and testing of the OPLS all-atom force field on conformational energetics and properties of organic liquids, J. Am. Chem. Soc. **118**, 11225 (1996).

[58] U. C. Singh and P. A. Kollmann, An approach to computing electrostatic charges for molecules, J. Comput. Chem. **5**, 129 (1984).

[59] C. Poelking, E. Cho, A. Malafeev, V. Ivanov, K. Kremer, C. Risko, J.-L. Brédas, and D. Andrienko, Characterization of charge-carrier transport in semicrystalline polymers: Elec-tronic couplings, site energies, and charge-carrier dynam-ics in poly (bithiophene-*alt*-thienothiophene)[PBTTT], J. Phys. Chem. C **117**, 1633 (2013).

[60] C. Bannwarth, E. Caldeweyher, S. Ehlert, A. Hansen, P. Pracht, J. Seibert, S. Spicher, and S. Grimme, Extended tight-binding quantum chemistry methods, WIREs Com-put. Mol. Sci. **11**, e01493 (2020).

[61] G. Bussi, D. Donadio, and M. Parrinello, Canonical sam-pling through velocity rescaling, J. Chem. Phys. **126**, 014101 (2007).

[62] H. J. Berendsen, J. v. Postma, W. F. van Gunsteren, A. DiNola, and J. R. Haak, Molecular dynamics with coupling to an external bath, J. Chem. Phys. **81**, 3684 (1984).

[63] B. Hess, C. Kutzner, D. Van Der Spoel, and E. Lindahl, GROMACS 4: Algorithms for highly efficient, load-balanced, and scalable molecular simulation, J. Chem. Theory Com-put. **4**, 435 (2008).

[64] S. Pronk, S. Páll, R. Schulz, P. Larsson, P. Bjelkmar, R. Apostolov, M. R. Shirts, J. C. Smith, P. M. Kas-son, D. van der Spoel, B. Hess, and E. Lindahl, GRO-MACS 4.5: A high-throughput and highly parallel open source molecular simulation toolkit, Bioinformatics **29**, 845 (2013).

[65] L. Martínez, R. Andrade, E. G. Birgin, and J. M. Martínez Packmol: A package for building initial configurations for molecular dynamics simulations, J. Comput. Chem. **30**, 2157 (2009).

[66] A. Stone, *The theory of intermolecular forces* (OUP oxford, Oxford, 2013).

[67] G. D'Avino, L. Muccioli, F. Castet, C. Poelking, D. Andrienko, Z. G. Soos, J. Cornil, and D. Beljonne, Electrostatic phenomena in organic semiconductors: Fundamentals and implications for photovoltaics, J. Phys.: Condens. Matter **28**, 433002 (2016).

[68] C. Poelking and D. Andrienko, Long-range embedding of molecular ions and excitations in a polarizable molecular environment, J. Chem. Theory Comput. **12**, 4516 (2016).

[69] B. T. Thole, Molecular polarizabilities calculated with a modified dipole interaction, Chem. Phys. **59**, 341 (1981).

[70] P. T. Van Duijnen and M. Swart, Molecular and atomic polarizabilities: Thole's model revisited, J. Phys. Chem. A **102**, 2399 (1998).

[71] A. J. Stone, Distributed multipole analysis: Stability for large basis sets, J. Chem. Theory Comput. **1**, 1128 (2005).

[72] V. Rühle, A. Lukyanov, F. May, M. Schrader, T. Vehoff, J. Kirkpatrick, B. Baumeier, and D. Andrienko, Microscopic simulations of charge transport in disordered organic semiconductors, J. Chem. Theory Comput. **7**, 3335 (2011).

Supplemental Material

Monitoring the charge-carrier-occupied density of states in disordered organic semiconductors under nonequilibrium conditions using thermally stimulated luminescence spectroscopy

Andrei Stankevych,[1,2,†] Rishabh Saxena,[2,†] Alexander Vakhnin,[1] Falk May,[3] Naomi Kinaret,[4] Denis Andrienko,[4] Jan Genoe,[5] Heinz Bässler,[6] Anna Köhler,[2,6*] and Andrey Kadashchuk[1,2,5*]

[1] Institute of Physics, National Academy of Sciences of Ukraine, Prospect Nauky 46, 03028 Kyiv, Ukraine

[2] Soft Matter Optoelectronics and Bavarian Polymer Institute (BPS), Universitätsstrasse 30, 95448 Bayreuth, Germany

[3] Merck KGaA, Display Solutions, Frankfurter Straße 250, 64293 Darmstadt, Germany

[4] Max Planck Institute for Polymer Research, Ackermannweg 10, 5528 Mainz, Germany

[5] IMEC, Kapeldreef 75, B-3001 Leuven, Belgium

[6] Bayreuth Institute of Macromolecular Research (BIMF), Universitätsstrasse 30, 95448 Bayreuth, Germany

[†] Authors contributed equally to this work

*Corresponding author: kadash@iop.kiev.ua, anna.koehler@uni-bayreuth.de

Note S1: Full names of the compounds used in this study.

The full names of the molecular structures presented in Figure 1 of the main text are as follows:

N,N'-Di(1-naphthyl) -N,N'-diphenyl-(1,1'-biphenyl)-4,4'-diamine (NPB), N,N'-Di(1-naphthyl)-N,N'-diphenyl-(1,1'-biphenyl)-4,4'-diamine (Spiro-TAD), N,N'-Bis(3-methylphenyl)-N,N'-diphenylbenzidine (TPD), 10-(4-(4,6-Diphenyl-1,3,5-triazin-2-yl)phenyl)-9,9-dimethyl-9,10-dihydroacridine (DMAC-TRZ), 4,4'-Bis(N-carbazolyl)-1,1'-biphenyl (CBP), 3,3'-(di(9H-carbazol-9-yl)-1,1'-biphenyl (mCBP), 1,3-Bis(N-carbazolyl)benzene (mCP), 10-(4-(4,6-Diphenyl-1,3,5-triazin-2-yl) pyridin-3-yl)-9,9-dimethyl-9,10-dihydroacridine (DMAC-py-TRZ), 3',5-di(9H-carbazol-9-yl)-[1,1'-biphenyl]-3- carbonitrile (mCBP-CN), 4,5-Bis(carbazol-9-yl)-1,2-dicyanobenzene (2CzPN), 2,9-Dinaphthalen-2-yl-4,7-diphenyl-1,10-phenanthroline (NBPhen), Tris(8-hydroxyquinoline)aluminum (Alq3), 9-(3-(9H-Carbazol-9-yl)phenyl)-9H-carbazole-3-carbonitrile (mCP-CN), 1,2,3,5-Tetrakis (carbazol-9-yl)-4,6-dicyanobenzene, 2,4,5,6-Tetrakis(9H-carbazol-9-yl) isophthalonitrile (4CzIPN) and 2,9-Dimethyl-4,7-diphenyl-1,10-phenanthroline (BCP).

Note S2: Fractional thermally stimulated luminescence (TSL) methodology.

Fractional heating of TSL is widely used for quantifying the energies of the trapping states in solids. The TSL glow curve, $I_{TSL}(T)$, of disordered organic solids typically display broad and unstructured bands due to a complicated convolution of contributions from quasi-continuous distribution of localized states and traps with different energies. Therefore, additional TSL measurements in *'fractional heating'* regime must be performed to extract the information about the trap energetics and distribution [31,32]. In the fractional (or partial) heating TSL technique [31], which is basically an extension of the "initial rise method", we apply a temperature-cycling program in which many small heating/cooling cycles are superimposed on a constant heating ramp. This allows determining the activation energies ($\langle E_a \rangle$) of the traps with high accuracy. This technique is especially useful when different groups of traps are not well separated in energy or are continuously distributed in energy [31-33].

The main idea of fractional TSL technique is the following: during each heating cycle i, the sample is heated from an initial temperature $T_i = T_0 + (i-1)\Delta T_1$ (T_0 = 5 K, ΔT_1 = 3 K) to the final temperature $T_{f,i} = T_i + \Delta T_2$ (ΔT_2 = 10…20 K) using a constant heating rate β (for schematic illustration, see Figure

S1a). The emitted light intensity, $I_{TSL}(T)$, is recorded during the heating process, as shown in Figure S1b. The sample is then cooled down to the initial temperature. The sample is further heated to a higher temperature T_{i+1} using the same constant heating rate and then cooled down again. During the subsequent heating/cooling cycles, deeper and deeper traps are emptied, and the consecutive activation energy $\langle E_a \rangle_i$ for each heating cycle is calculated (as demonstrated in Figure S1c) by performing an Arrhenius analysis of the fractional TSL data:

$$\langle E_a \rangle_i = -\frac{d[ln\, I_{TSL}(T)]}{d(1/k_B T)}; \ at \ \ \beta = const \tag{S1}$$

where $I_{TSL}(T)$ is the intensity of the TSL, T is the temperature, k_B is the Boltzmann constant. The whole spectrum of activation energies can be scanned by an incremental increase of ΔT_1. Obviously, the higher is the temperature of a measuring cycle the deeper localized states can be emptied. The calculated activation energies can then be plotted against the mean temperature of the heating cycle for which a given $\langle E_a \rangle$ value was obtained [31,32]. Therefore, *the $\langle E_a \rangle(T)$ dependence is the main outcome of the fractional TSL measurements*. We found that, for the organic materials studied in the present work, $\langle E_a \rangle$ increases linearly with temperature (Figure S2) and can be described reasonably well by the following empirical relation:

$$\langle E \rangle(T) = 3.2 \frac{meV}{K} \times T - 91 \ meV \tag{S2}$$

In this work, this empirical calibration, Eq. (S2), is used to convert the temperature scale to a trap energy scale for the analysis of our TSL data. It is worth emphasizing that such kind of linear relation for $\langle E_a \rangle(T)$ has also been justified for disordered organic semiconductors by analytical variable range hopping calculations [27] and has also been observed in our previous experimental studies [22-26].

A trap distribution function, $H(E)$, is then determined in arbitrary units as follows [31]:

$$H(E) \propto \frac{I(E)}{d\langle E \rangle/dT} \tag{S3}$$

where $I(E)$ is TSL curve after converting the temperature scale to the energy scale by means of empirically accessible $\langle E_a \rangle(T)$ dependence obtained by Eq. (S1). As one can see from Eq.(S3), in the case when $\langle E \rangle(T)$ is a linear function (e.g., as given by Eq.(S2)), the TSL intensity dependence $I(T)$ is an exact replica of populated trap distribution function $H(E)$, that was also predicted in Ref. [27].

More details of the fractional TSL measurements have been described elsewhere [22] .
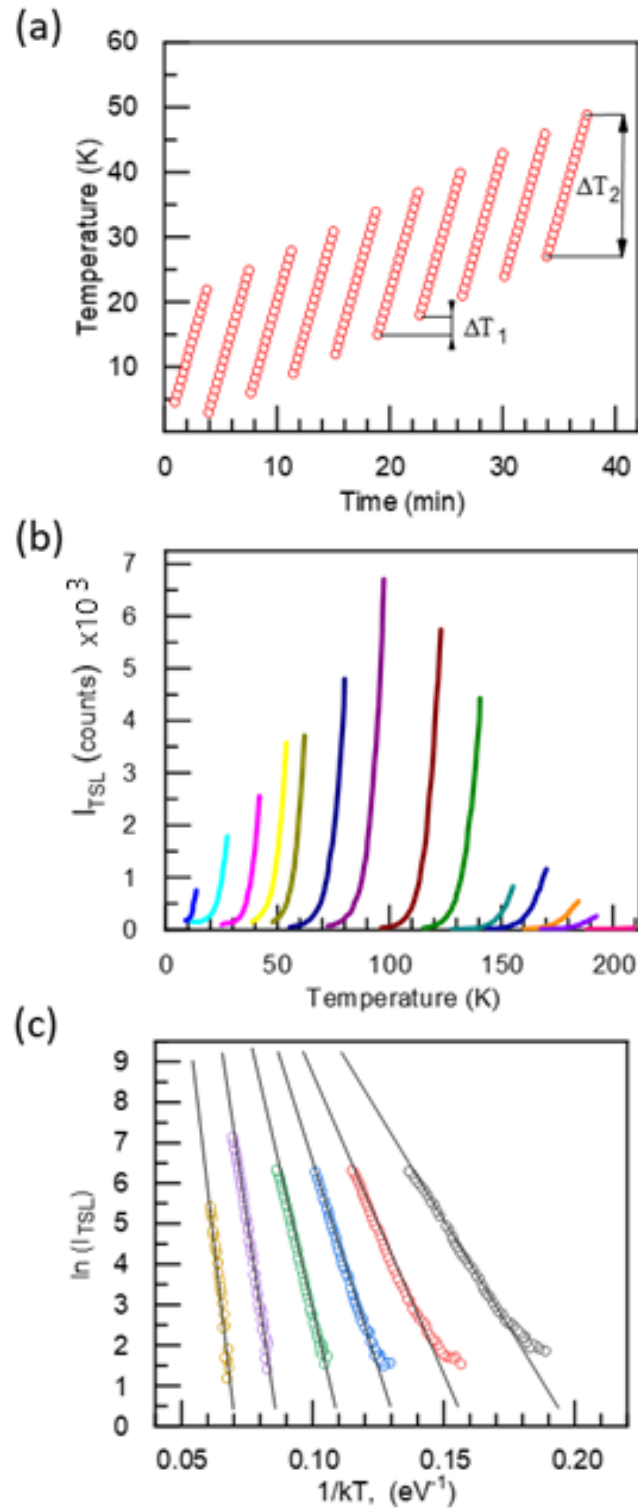
Figure S0: a) Schematic illustration of heating/cooling cycles used in fractional TSL method, b) TSL intensity (I_{TSL}) measured during heating cycles, and c) Arrhenius plots ($\ln (I_{TSL})$ $vs.$ $1/T$) illustrated for different heating cycles to calculate activation energy ($\langle E_a \rangle$) during each heating cycle.

Note S3: Determination of DOS width, σ_{DOS}, by TSL.

An important aspect of applying low-temperature TSL to organic disordered solids is that it allows direct determination of the DOS distribution, in particular the σ_{DOS} parameter. As demonstrated by Arkhipov *et al.* [27] using variable-range hopping (VRH) calculations, a specific feature of the low-temperature energy relaxation of charge-carriers in such amorphous materials is that the shape of high-temperature wing of the TSL glow curve always *follows the DOS distribution* [23,27] and thus yields the effective DOS width. This is due to the energy distribution of carriers localized bellow the demarcation energy is found to be determined solely by the DOS distribution rather than the probability of site occupancy [27]. This forms the basis for the methodology of determining the DOS width, σ_{DOS}, by analyzing the shape of high-temperature (and thus high activation energy) wing of the TSL curve, which has been experimentally demonstrated before for different organic semiconducting polymers and small-molecule systems [22-27]. Hereafter, this method will be referred as "DOS assessment" TSL analysis method. In brief, it can be summarized as follows: First, one has to convert the temperature scale of a TSL curve to an energy scale using Eq.(S2) (Figure S1c). As described in Note S2, it is obtained by employing TSL measurements in '*fractional heating*' regime. Such empirical calibration Eq.(S2) is then used to translate the temperature scale in Figure S1a to a trap energy scale ($\langle E_a \rangle$). Subsequently, the logarithm of TSL intensity (I_{TSL}) is plotted against $\langle E_a \rangle^2$ (Figure S3b). The high-$\langle E_a \rangle$ part of the plot in Figure S3b reveals a Gaussian dependence ($\ln(I_{TSL}) = -\langle E_a \rangle^2 / 2\sigma_{DOS}^2$) for all samples and the slope of the straight line yields the width of the DOS (σ_{DOS}). The energetic disorder parameters inferred from TSL of the above OLED host materials from 88 meV to 176 meV (inset of Fig.S1b) for the least disordered NPB and the most disordered NBPhen, respectively. The "DOS assessment" method of TSL analysis has been extensively applied by the Kadashchuk group to a great variety of small molecules and conjugated polymers [22-28] and the determined σ_{DOS} values were found to be in good agreement with that obtained from charge transport measurements and from molecular dynamics simulations [28].
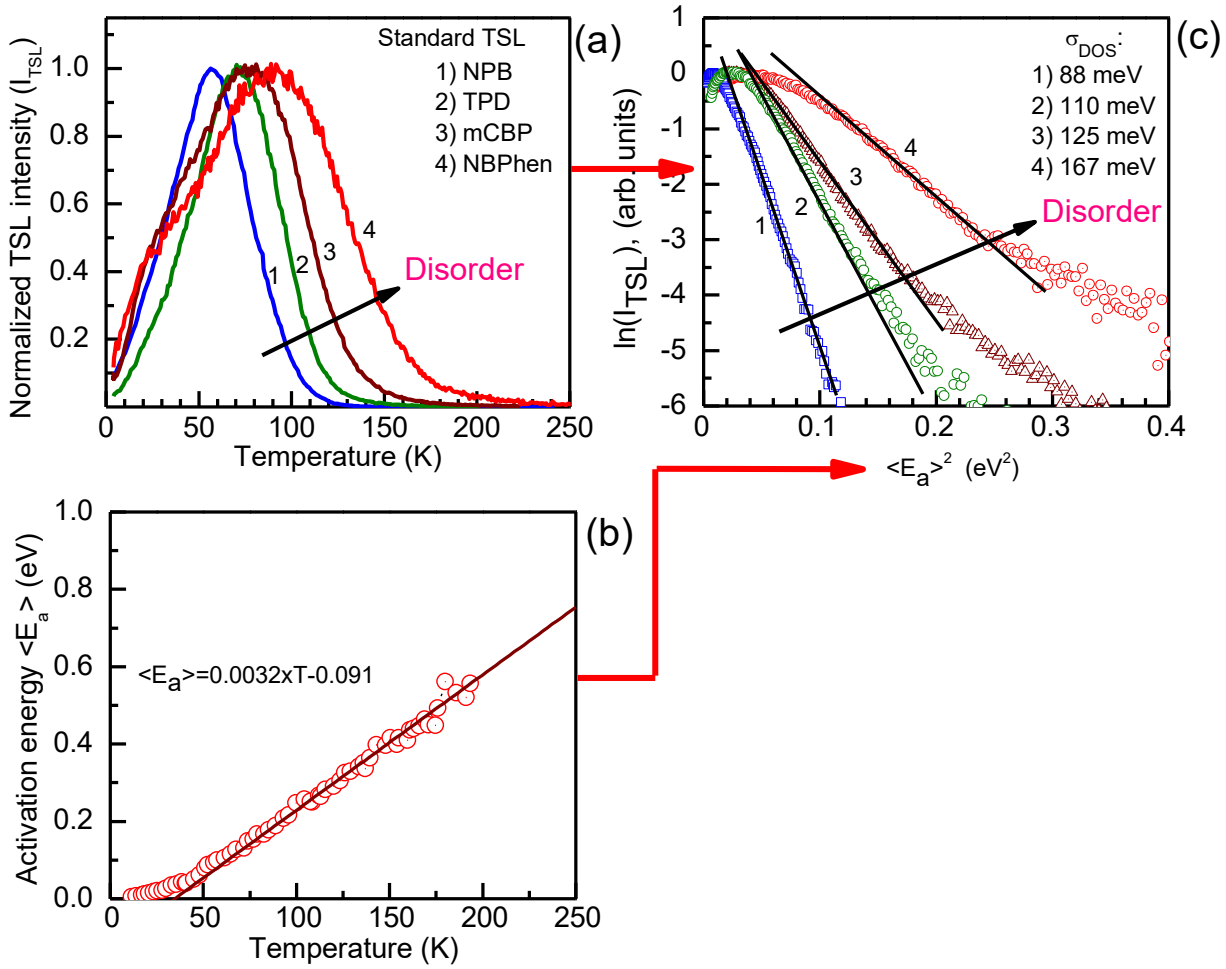
Figure S1: a) Normalized 'classical TSL' glow curves (I_{TSL}) measured at a constant heating rate after 313nm-light excitation with at 5 K in NPB, TPD, mCBP and NBPhen films (curve 1, 2, 3, and 4, respectively); b) The temperature dependence of the mean activation energy $< E_a >$ as obtained by fractional TSL (symbols) for organic semiconductor materials studied in this paper and extrapolation by an empirical expression, Eq. (S2) (solid line); c) Gaussian analysis of the high temperature wings of the TSL curves shown in (a) by the TSL "DOS assessment" method; namely, the logarithm of I_{TSL} is plotted against $\langle E_a \rangle^2$ after the temperature scale is converted to the energy scale using the empirical $< E_a > (T)$ dependence shown in (b). The slope of the straight lines is a measure of the DOS width (σ_{DOS}), and the extracted σ_{DOS} -parameters are indicated in the Inset. Note that some films also revealed a more slowly decaying deep exponential tail at the lowest portion of the DOS, following on from the Gaussian distribution. This slower decaying feature can be of a multiple origin, as described in our previous work [22], and is beyond the scope of the present study.
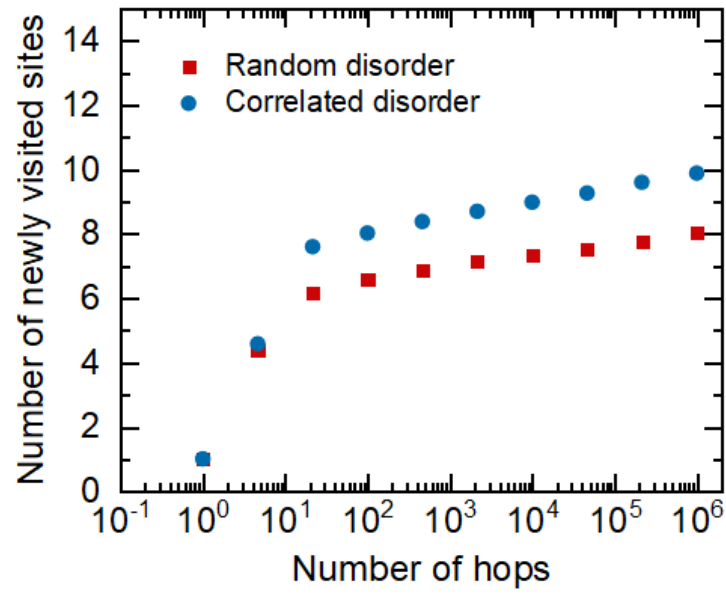
Figure S2: vt-KMC simulation results - comparison of the newly visited sites as a function of number of hops for system with random and correlated disorder.
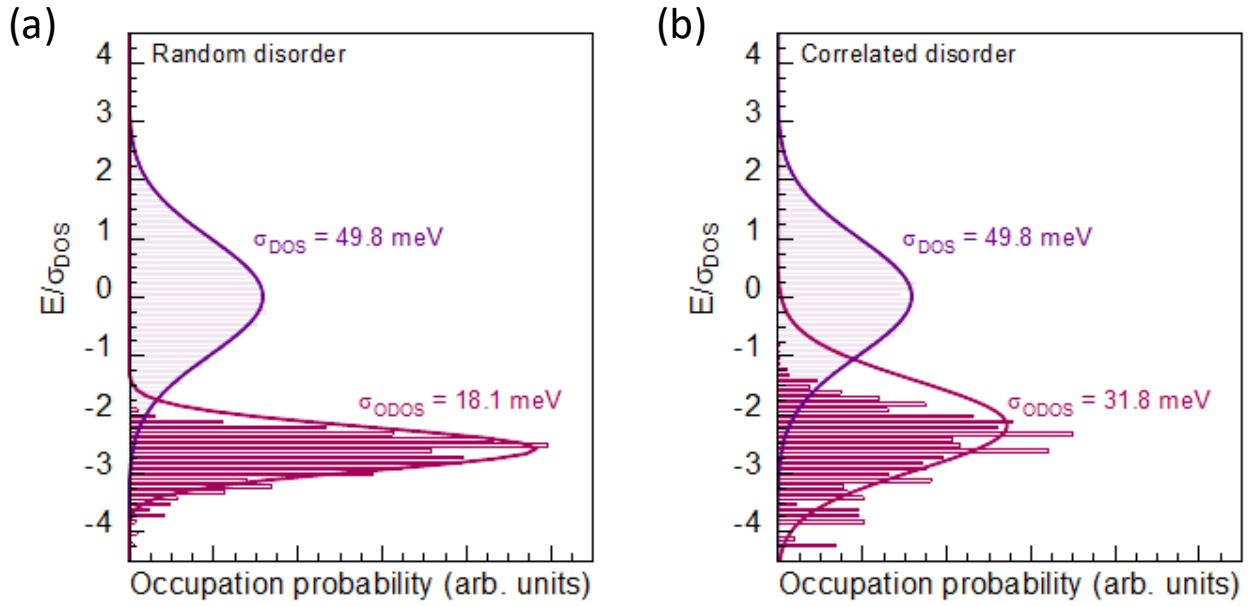
Figure S3: vt-KMC simulation results – comparison of ODOS distribution (after 10^6 hops) for system with random (a) and correlated (b) disorder.
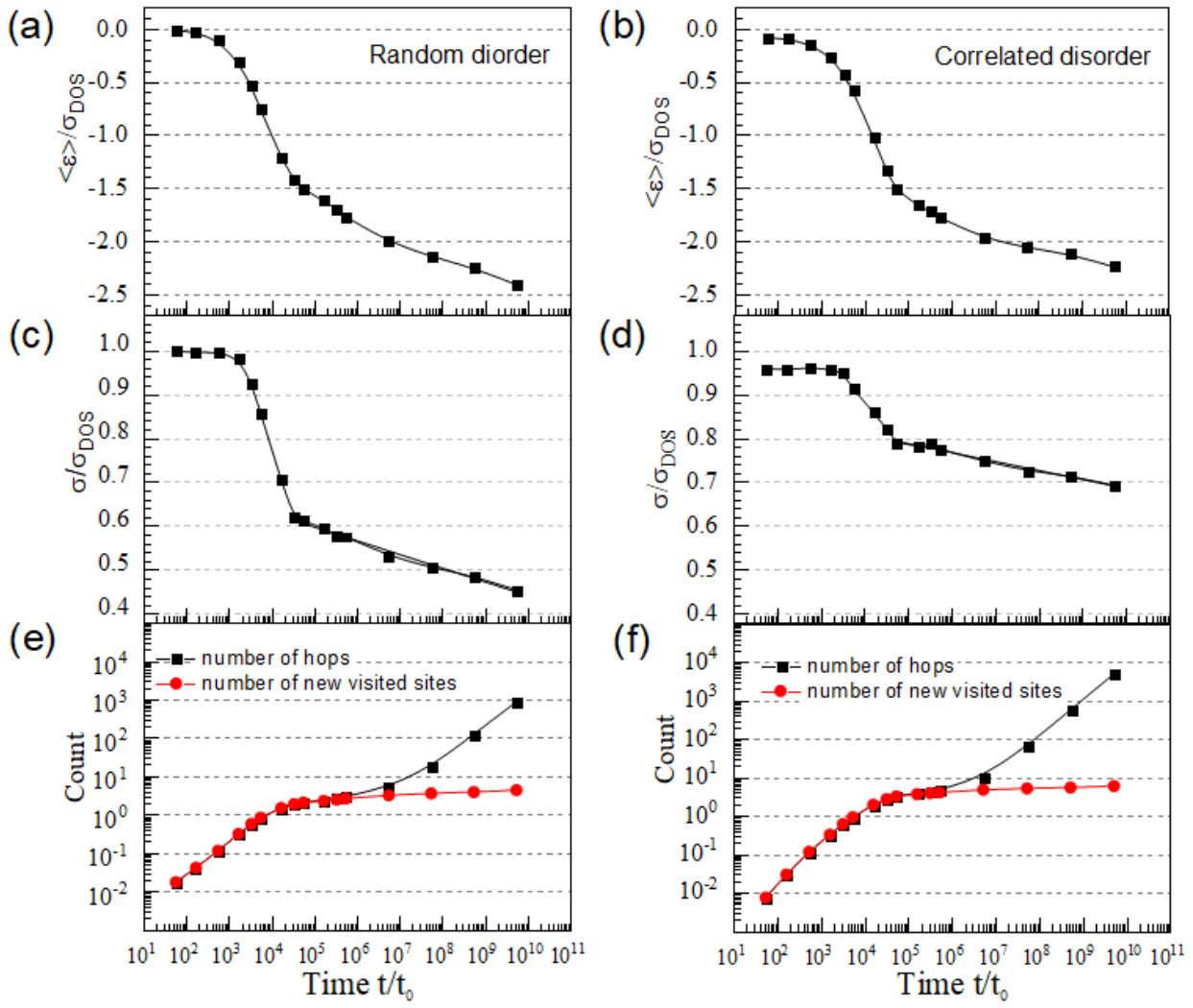
Figure S4: ct-KMC simulation results - mean energy of the distribution of hopping carriers normalized by the width of DOS ($< \varepsilon >/\sigma_{DOS}$) as a function of simulated time for a) random and b) correlated disorder system. Energetic width of the distribution of hopping carriers normalized by the width of DOS (σ/σ_{DOS}) as a function of simulated time for c) random and d) correlated disorder system. Number of new visited sites and number of hops as function of time for e) random and f) correlated disorder system.
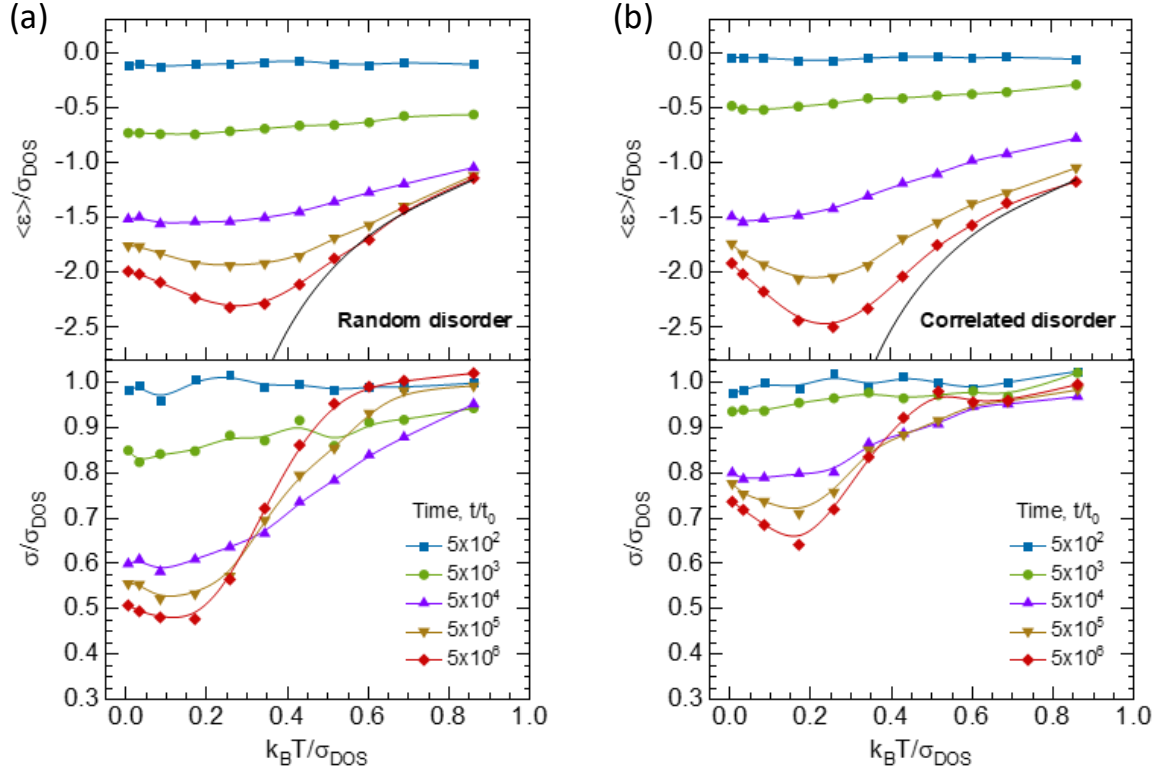
Figure S5: ct-KMC simulation results - the simulated normalized variation of mean energy ($< \varepsilon > /\sigma_{DOS}$, top panels) and the energetic width (σ/σ_{DOS}, bottom panels) of the distribution of charges as a function of $k_B T/\sigma_{DOS}$ at variable simulation time for a system with a) random disorder and b) correlated disorder. Results are shown for ct-KMC simulations performed for a DOS distribution of width, σ_{DOS} = 50 meV. The black solid line in the top panels indicates the spectral relaxation expected for thermal equilibrium according to $< \varepsilon > /\sigma_{DOS} = -\sigma_{DOS}/k_B T$. Other solid lines guide the eye.

References:

[22] A. Stankevych, A. Vakhnin, D. Andrienko, L. Paterson, J. Genoe, I. Fishchuk, H. Bässler, A. Köhler, and A. Kadashchuk, Density of states of OLED host materials from thermally stimulated luminescence, Physical Review Applied **15**, 044050 (2021).

[23] A. Kadashchuk, Y. Skryshevskii, A. Vakhnin, N. Ostapenko, V. Arkhipov, E. Emelianova, and H. Bässler, Thermally stimulated photoluminescence in disordered organic materials, Phys. Rev. B **63**, 115205 (2001).

[24] A. Kadashchuk, N. Ostapenko, V. Zaika, and S. Nešpurek, Low-temperature thermoluminescence in poly (methyl-phenylsilylene), Chem. Phys. **234**, 285 (1998).

[25] A. Kadashchuk, Y. Skryshevski, Y. Piryatinski, A. Vakhnin, E. Emelianova, V. Arkhipov, H. Bässler, and J. Shinar, Thermally stimulated photoluminescence in poly (2, 5-dioctoxy p-phenylene vinylene), J. Appl. Phys. **91**, 5016 (2002).

[26] A. Kadashchuk, D. Weiss, P. Borsenberger, S. Nešpurek, N. Ostapenko, and V. Zaika, The origin of thermally stimulated luminescence in neat and molecularly doped charge transport polymer systems, Chem. Phys. **247**, 307 (1999).

[27] V. Arkhipov, E. Emelianova, A. Kadashchuk, and H. Bässler, Hopping model of thermally stimulated photoluminescence in disordered organic materials, Chem. Phys. **266**, 97 (2001).

[28] A. Mondal, L. Paterson, J. Cho, K-H. Lin, B. van der Zee, G-J. A. H. Wetzelaer, A. Stankevych, A. Vakhnin, J.-J. Kim, A. Kadashchuk, P. W. M. Blom, F. May, and D. Andrienko, Molecular library of OLED host materials—Evaluating the multiscale simulation workflow, Chem. Phys. Rev. **2**, 031304 (2021).

[31] I. Tale, Trap spectroscopy by the fractional glow technique, Phys. Stat. Sol. A 66, 65 (1981).

[32] A. Kadashchuk , N. I. Ostapenko , Yu. A. Skryshevskii , V. I. Sugakov and T.O. Susokolova, Clusters of Dipole Charge-Carrier Capture Centers in Organic Crystals, Mol. Cryst. Liq. Cryst. **201**, 167 (1991)

Paper 2: Density of States of OLED Host Materials from Thermally Stimulated Luminescence

Andrei Stankevych, Alexander Vakhnin, Denis Andrienko, Leanne Paterson, Jan Genoe, Ivan Fishchuk, Heinz Bässler, Anna Köhler, and Andrey Kadashchuk

Density of States of OLED Host Materials from Thermally Stimulated Luminescence

Andrei Stankevych,[1] Alexander Vakhnin,[1] Denis Andrienko,[2] Leanne Paterson,[2] Jan Genoe,[3]
Ivan Fishchuk,[4] Heinz Bässler,[5] Anna Köhler,[5,6] and Andrey Kadashchuk[1,3,*]

[1] *Institute of Physics, Natl. Academy of Sciences of Ukraine, Prospect Nauky 46, 03028 Kyiv, Ukraine*
[2] *Max Planck Institute for Polymer Research, Ackermannweg 10, 5528 Mainz, Germany*
[3] *IMEC, Kapeldreef 75, 3001 Leuven, Belgium*
[4] *Institute for Nuclear Research, Natl. Academy of Sci. of Ukraine, Prospect Nauky 47, 03028 Kyiv, Ukraine*
[5] *Bayreuth Institute of Macromolecular Research (BIMF), Universitätsstr. 30, 95448 Bayreuth, Germany*
[6] *Soft Matter Optoelectronics and Bavarian Polymer Institute (BPS), Universitätsstr. 30, 95448 Bayreuth, Germany*

The electronic density of states (DOS) plays a central role in controlling the charge-carrier transport in amorphous organic semiconductors, while its accurate determination is still a challenging task. We apply the low-temperature fractional thermally stimulated luminescence (TSL) technique to determine the DOS of pristine amorphous films of organic light-emitting diode (OLED) host materials. The DOS width is determined for two series of hosts, namely, (i) carbazole-biphenyl derivatives, 4,4′-bis(*N*-carbazolyl)-1,1′-biphenyl (CBP), 3,3′-di(9*H*-carbazol-9-yl)-1,1′-biphenyl (mCBP), and 3′,5-di(9*H*-carbazol-9-yl)-[1,1′-biphenyl]-3-carbonitrile (mCBP-CN), and (ii) carbazole-phenyl (CP) derivatives, 1,3-bis(*N*-carbazolyl)benzene (mCP) and 9-[3-(9*H*-carbazol-9-yl)phenyl]-9*H*-carbazole-3-carbonitrile (mCP-CN). TSL originates from radiative recombination of charge carriers thermally released from the lower-energy part of the intrinsic DOS that causes charge trapping at very low temperatures. We find that the intrinsic DOS can be approximated by a Gaussian distribution, with a deep exponential tail accompanying this distribution in CBP and mCBP films. The DOS profile broadens with increasing molecular dipole moments, varying from 0 to 6 D, in a similar manner within each series, in line with the dipolar disorder model. The same molecular dipole moment, however, leads to a broader DOS of CP compared with CBP derivatives. Using computer simulations, we attribute the difference between the series to a smaller polarizability of cations in CP derivatives, leading to weaker screening of the electrostatic disorder by induction. These results demonstrate that the low-temperature TSL technique can be used as an efficient experimental tool for probing the DOS in small-molecule OLED materials.

I. INTRODUCTION

Determination of the electronic density of states (DOS) in disordered organic solids is of fundamental importance for the accurate physical understanding and modeling of charge-carrier transport in organic functional semiconductors and electronic devices. A Gaussian shape, $g(\varepsilon) \propto \exp[-1/2(\varepsilon/\sigma)^2]$, where σ is the width of the DOS, is a common approximation used for neat disordered organic solids [1–3], such as low-molecular-weight glasses and semiconducting polymers. Nondispersive photocurrent transients observed in amorphous organic materials [3] unambiguously support the notion of a Gaussian shape, rather than an exponential DOS [4,5]. The point is that, in the case of an exponential DOS, the time-of-flight

(TOF) transients should always be dispersive because they would never equilibrate during the transit time at small carrier concentrations and should follow a dispersive transport model. The Gaussian DOS is also predicted by the central limit theorem, since the interaction energy of a charged molecule embedded in a random polarizable environment depends on a large number of neighboring neutral molecules [1,2].

Despite the success of the Gaussian disorder formalism, particularly for neat organic semiconductor films, the exact shape of the DOS can deviate from a Gaussian shape, for instance, in the far tail region of the DOS [6] or in doped organic films where the DOS is distorted by ionized dopants [7]. Consequently, charge-transport characteristics in sandwich-type diodes are often modeled by assuming that the DOS is a superposition of Gaussian and exponentially distributed trap states [8]. Recently, May *et al.*

128

[9] showed that deep exponential tails could develop for molecules with large changes in molecular polarizability upon charging. Several direct experimental measurements of the DOS shape also demonstrate that the center of the DOS distribution is indeed Gaussian, but the tails can have a more complex structure [10,11].

The experimental determination of the DOS profile, however, is far from trivial. In contrast to inorganic semiconductors, the DOS of organic systems is not amenable to optical probing, because the direct optical transitions between the valence and conduction states are weak and masked by strong exciton transitions [12,13]. A number of experimental techniques are used to probe the DOS of organic films, such as temperature-dependent space-charge-limited-current spectroscopy [14], ultraviolet photoelectron spectroscopy (UPS) [15], inverse photoemission spectroscopy (IPS) [16], Kelvin probe force microscopy (KPFM) [10,11], the electrochemically gated transistor approach [17], as well as thermally stimulated luminescence (TSL) [18]. A clear advantage of TSL is that it is a purely optical and electrode-free technique. This helps to eliminate interface or contact effects, and it allows DOS measurements in materials with low charge-carrier mobilities and in systems with large energy disorder where charge transport is very dispersive.

TSL is the phenomenon of luminescent emission after removal of excitation (UV light in our case) under conditions of increasing temperature. First, photogenerated charge carriers populate trap states, usually at very low temperatures. Once the sample is heated, typically with a linear temperature ramp, trapped charge carriers are released and then recombine, producing luminescence emission. Technically, TSL is a relatively simple technique with straightforward data analysis. However, it should be noted that the mechanism of TSL in amorphous organic semiconductors with a broad energy distribution of strongly localized states differs from the mechanism commonly accepted for crystalline materials with band-type transport, where a discrete trapping-level model is applicable. A specific feature of amorphous solids is that localized states within the lower energy part of the intrinsic DOS distribution can give rise to shallow charge trapping at very low temperatures, and, as a consequence, TSL can be observed even in materials where the "trap-free limit" is postulated. Since TSL measurements are normally performed after a long dwell time after photoexcitation, the initial energy distribution of localized carriers is formed after low-temperature energy relaxation of photogenerated carriers within a Gaussian distribution of DOS and, therefore, the first thermally assisted jumps of relaxed carriers are considered as the rate-limiting steps determining TSL. This is in contrast to thermally stimulated conductivity, which is believed to be governed by the interplay between trapping and detrapping processes [4]. The theoretical background for the application of TSL for probing

the DOS distribution in disordered organic systems has been developed [18,19] using a variable-range hopping formalism and the concept of thermally stimulated carrier random walk within a positionally and energetically random system of hopping sites. The theory proves that the high-temperature wing of the TSL curve in such amorphous materials should be an exact replica of the deeper portion of the DOS distribution [18,19] and yields the effective DOS width.

TSL is particularly suitable for probing the DOS and extrinsic traps in luminescent organic materials, such as π- and σ-conjugated polymers [18,20–26], molecularly doped polymers [27,28], oligomers [29], and hybrid organic-inorganic perovskite films [30]. Here, we use TSL to characterize the DOS in spin-coated films of two series of organic semiconducting materials of different polarity, based on small-molecule carbazole-biphenyl (CBP) derivatives, CBP, mCBP, and mCBP-CN (series 1), and carbazole-phenyl (CP) derivatives, mCP and mCP-CN (series 2), the chemical structures of which are shown in Fig. 1. These materials are widely used as hosts for blue triplet emitters or for emitters based on thermally activated delayed fluorescence (TADF) in organic light-emitting diodes (OLEDs), due to their wide band gaps and high triplet energies. They are also used as charge-transporting layers in both OLED and hybrid perovskite-based light-emitting devices. A suitable polarity of these materials is important for optimizing the performance of TADF-based OLED devices.

In our study, the TSL data are analyzed using the Gaussian disorder formalism, based on a thermal release of charge carriers from the lower-energy part of the intrinsic DOS distribution. We find that, for materials with similar core chemical structures, the DOS broadens with increasing dipole moment, in essentially the same manner for both series of CBP and CP derivatives, in agreement with the dipolar disorder model. Systematic differences in the DOS widths are observed between these two different series of derivatives. This is attributed to different nonpolar contributions to the DOS of these materials, which are analyzed using a theoretical approach based on the distributed electrostatic model. Large DOS widths are found in strongly polar hosts, and good agreement between experimental and computational results proves the intrinsic character of the large energy disorder in these materials. TSL measurements also show that the Gaussian-shaped DOS of CBP and mCBP are both accompanied by a deep exponential tail.

II. EXPERIMENT

A. Materials

CBP, mCBP, mCBP-CN, mCP, and mCP-CN are purchased from Lumtec Corp. and used as received. Thin films of the above compounds are spin-coated from
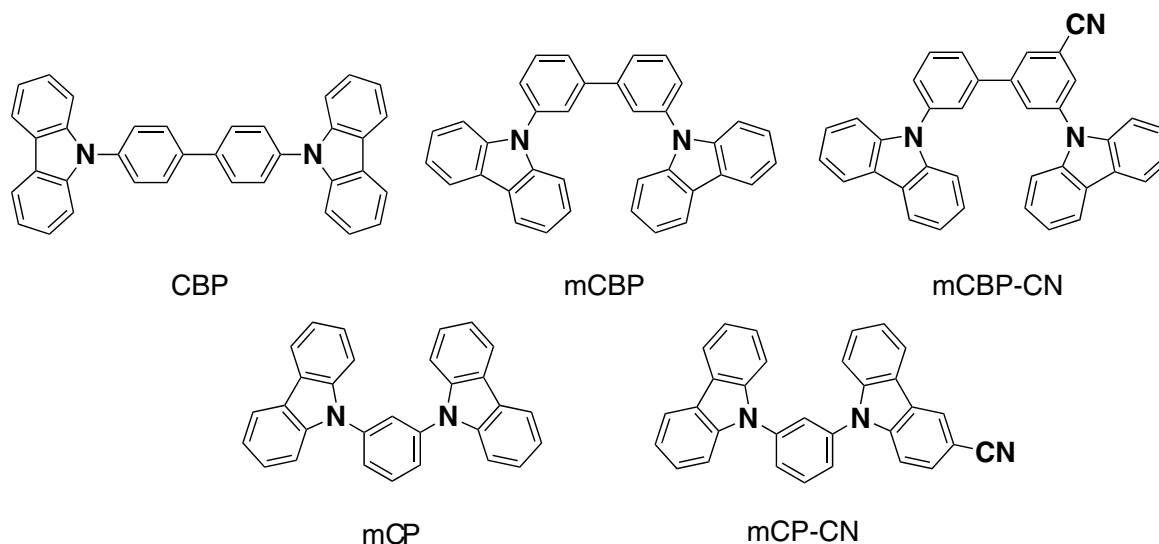
FIG. 1.   Molecular structures of compounds used in this study. CBP derivatives, 4,4′-bis(*N*-carbazolyl)-1,1′-biphenyl (CBP); 3,3′-di(9*H*-carbazol-9-yl)-1,1′-biphenyl (mCBP); and 3′,5-di(9*H*-carbazol-9-yl)-[1,1′-biphenyl]-3-carbonitrile (mCBP-CN). CP derivatives, 1,3-bis(*N*-carbazolyl)benzene (mCP) and 9-[3-(9*H*-carbazol-9-yl)phenyl]-9*H*-carbazole-3-carbonitrile (mCP-CN).

20 mg/ml chloroform solutions onto cleaned quartz substrates (1000 rpm, 30 s) that result in typically 150-nm-thick layers. Subsequently, the deposited films are dried in an oven at 40 °C for 10 m and then under vacuum for 2 h to remove residual solvent.

B. TSL technique

TSL measurements are carried out over a temperature range from 4.2 to 300 K with an accuracy better than 0.1 K using an optical temperature-regulating liquid-helium bath cryostat designed and fabricated by the Cryogenic Technologies Laboratory [77] at the Institute of Physics of National Academy of Sciences of Ukraine. In this type of cryostat, the sample is attached to the end of a sample manipulator and is suspended in a helium heat-transfer gas environment inside the inner sample chamber. The sample temperature is controlled by the temperature controller unit in a twofold manner: (i) via two separate heating elements (one is integrated into the sample holder, directly heating the sample, and the second one is mounted in the sample chamber, heating the heat-transfer gas), and (ii) by regulating the helium flow between the helium bath and the sample chamber via control of the He gas pressure in the sample chamber.

In TSL experiment, samples are cooled to 4.2 K and irradiated for 30 s with $\lambda_{exc} = 313$ nm light (cw excitation, light power density is about 5 mW/cm^2) selected by appropriate set of cutoff filters from a high-pressure 250 W Hg lamp. No sample heating occurs during UV-light illumination and the sample is immersed in liquid helium. The studied organic films do not exhibit any notable photodegradation during the measurements. TSL measurements are done as follows: first, after terminating photoexcitation, the samples are kept in the dark at a constant temperature, $T = 4.2$ K, during a certain dwell time (typically for 10 min) to allow all isothermal emission processes, like phosphoresce and isothermal recombination of short-range geminate charge-carrier pairs, to decay to a negligible level. Then TSL is detected upon heating the sample, and TSL emission is detected in photon-counting mode with a cooled photomultiplier positioned next to the cryostat window.

TSL measurements are performed in two different regimes: uniform heating at a constant heating rate β of 0.15 K/s and under the fractional heating regime. Details of the TSL measurements are described elsewhere [21,22,27]. The method of fractional TSL avoids the disadvantages of common glow curve methods based on the constant heating rate – it is characterized by greater accuracy and a high resolving power, and it does not require knowledge of the frequency factors and retrapping probabilities [31,32]. The low-temperature fractional TSL is extensively applied by our group to investigate charge-carrier trapping in a great variety of organic semiconductor materials. The fractional heating TSL technique (also called the fractional glow technique), originally proposed by Gobrecht and Hofmann [32] is an extension of the initial rise method and is based on cycling the sample with a large number of small temperature oscillations superimposed on a uniform heating ramp. The main reason for applying this method is that the usual quantitative evaluation of the

TSL glow curves is very inaccurate, or even impossible, if the traps are continuously distributed in energy or if there are several types of traps with discrete but very close lying activation energies. In this case, the glow peaks fuse together, and individual glow maxima may not be discernible. The mean activation energy, E, is determined during each temperature cycle with a temperature change, ΔT, as

$$E(T) = -\frac{d[\ln I(T)]}{d(1/kT)}; \text{ at } \beta = \text{const}, \ \Delta T \ll T, \ n \ll n_{\text{tot}}$$
(1)

where $I(T)$ is the intensity of the TSL, T is the temperature, and k is the Boltzmann constant. Here, n is the number of charge carriers released during each temperature cycle, and n_{tot} is the total number of carriers trapped by the same sort of traps. These conditions determine the so-called "initial rise method," which is actually the basis for Eq. (1). Since a temperature oscillation, ΔT, is usually much less than the mean value of T, E can be assumed to equal $E(T)$, the activation energy of traps emptied at temperature T. A trap distribution function, $H(E)$, can be determined in arbitrary units as [31–33]

$$H(E) \propto \frac{I(E)}{dE/dT},$$
(2)

where $I(E)$ is TSL after converting the temperature scale to the energy scale by means of empirically accessible $E(T)$ dependence obtained by Eq. (1). As one can see from Eq. (2), in the case when $E(T)$ is a linear function, the TSL intensity dependence, $I(T)$, is an exact replica of the populated trap distribution function [19]. The frequency factor at the maximum of TSL peak, S, is given by

$$S = E_m\beta/kT_m^2 exp(E_m/kT_m)$$
(3)

where T_m and E_m are the temperature and activation energy of the maximum of the TSL peak, respectively. All measurements are done under a helium atmosphere.

C. Computer simulations

For morphology simulations, we adapt the all-atom optimized potentials for liquid simulations (OPLS-AA) force field [34–36]. All Lennard-Jones parameters are taken from this force field and we use the OPLS combination rules and the fudge factor of 0.5 for 1–4 interactions. Atomic partial charges are computed via the charges from electrostatic potentials using a Grid-based method (CHELPG) scheme [37]. We partition the molecules into rigid fragments: carbazoles and bridge groups in between. These rigid fragments are oriented with respect to one another, such that conformers exhibit different energies,

as a result of different electrostatic interactions. The dihedral interaction potentials that connect these fragments are parameterized as described elsewhere [38]: for each fixed value of the dihedral angle, the geometry is optimized at the m06-2x/6-311g(d,p) level. The potential difference is then fitted to the Ryckaert-Belleman polynomial, $V_{\text{RB}}(\theta) = \sum_{n=0}^{5}(\cos \theta)^n$.

The long-range electrostatic interactions are treated by using the smooth-particle-mesh Ewald technique. A cutoff of 1.3 nm is used for the nonbonded interactions. The equations of motion are integrated with a time step of 0.002 ps. All molecular dynamics (MD) simulations are performed in the *NPT* ensemble using the canonical velocity-rescaling thermostat [39] and the Berendsen barostat [40], as implemented in the GROMACS simulation package [41,42].

To obtain the *amorphous* morphology, 3000 molecules are prearranged on a lattice and compressed (anisotropic *NPT* barostat) at $T = 800$ K for 1 ns. The system is then cooled to 300 K during a 1 ns run. Fast cooling freezes the isotropic orientation of the high-temperature liquid, leading to amorphous molecular ordering.

Using the molecular dynamics trajectories, we evaluate the anion, cation, and neutral-state energies for each molecule in a morphology using a perturbative approach [43–45]. In this approach, the total energy is a sum of the gas-phase, electrostatic, and induction contributions, $E_{e,h,n} = E_{e,h,n}^{\text{gas}} + E_{e,h,n}^{\text{stat}} + E_{e,h,n}^{\text{ind}}$. To evaluate the electrostatic contribution, we use distributed atomic multipoles up to the fourth order. The induction contributions to site energies are calculated self-consistently using the Thole mode [46,47] on the basis of the atomic polarizabilities and distributed multipoles obtained by using the GDMA program [48] for a cation, anion, and a neutral molecule. All calculations are performed using the aperiodic Ewald summation scheme [45], as implemented in the in-house-developed VOTCA package [49].

III. RESULTS

A. DOS probing by TSL measurements

Surprisingly, strong thermoluminescence signals induced by UV radiation at liquid-helium temperature are observed in neat thin films made of both CBP and CP derivatives studied in the present work. First, we consider TSL measurements in thin films of CBP derivatives. A typical TSL glow curve of a mCBP-CN film measured after photoexcitation with 313 nm at 4.2 K is presented in Fig. 2(a) and it reveals a broad slightly asymmetric band, with the maximum at $T_m \cong 93$ K. The asymmetric shape of the TSL band might be due to overlapping of the main high-temperature peak at 93 K, with a weaker low-temperature peak at around 40 K, as depicted by curves 1′ and 1″ in Fig. 2(a). The TSL signal is observed immediately upon heating the sample and extends to about
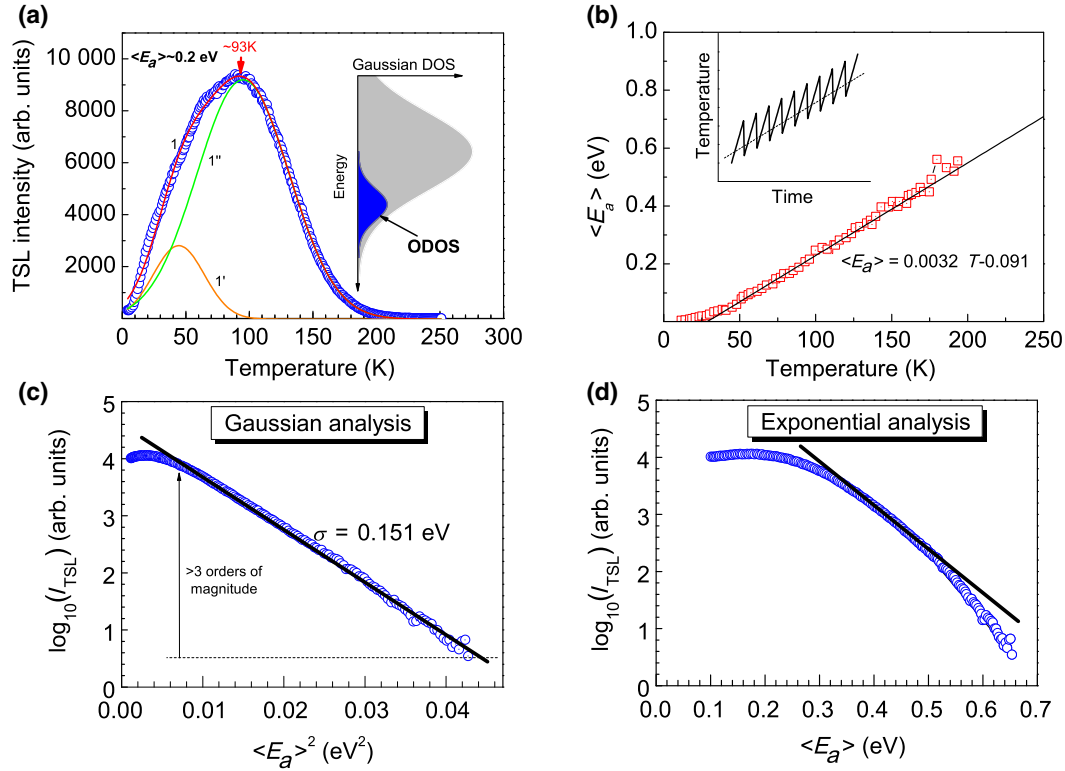
FIG. 2.   (a) Spectrally integrated TSL glow curve measured after excitation with 313 nm light for 3 min at 4.2 K for mCBP-CN film. Curves 1′ and 1″ represent deconvolution of the TSL band (curve 1) into two Gaussians. Inset shows schematic DOS distribution together with the distribution of trapped charge carriers at liquid-helium temperature after energy relaxation. (b) Temperature dependence of the mean activation energy $\langle E_a \rangle$ as obtained by fractional TSL (symbols) and extrapolation by an empirical expression, Eq. (4) (solid line). Inset shows schematic picture to illustrate principle of fractional TSL regime, when temperature oscillations are superimposed on uniform heating. (c) Gaussian analysis of the high-energy part of the TSL curve. (d) Same data as in (c) but plotted in exponential representation.

220 K, as expected for a disordered material devoid of deep charge-carrier traps. It is qualitatively similar to TSL phenomena observed in other organic disordered systems studied before [18–23] and can be ascribed to detrapping of charge carriers from the localized states that occupy the lower-energy part of the intrinsic DOS distribution, as schematically shown in the inset of Fig. 2(a). The fact that TSL in mCBP-CN films extends to moderately high temperatures is evidence of relatively strong energy disorder in this material, compared, for instance, with conventional semiconducting polymers, such as a methyl-substituted ladder-type poly(*para*-phenylene) [18] and a polyfluorene derivative [20] with reduced energy disorder. Yet, it is closer to the TSL peak observed before in TSL of vacuum-deposited films of AlQ$_3$ [50].

Similar to previously studied photoconducting polymers [18–22,27], the mCBP-CN film is characterized by a quasicontinuous trap distribution, with a mean activation energy, E_a, that is linearly increasing with temperature [Fig. 2(b)], as revealed by fractional TSL measurements

(see the Experiment Section II B for details). The temperature dependence of E_a (in eV) can be described by the following empirical relation:

$$E_a(T) = 0.0032T - 0.091. \qquad (4)$$

The empirical expression given by Eq. (4) supports the basic formula of Simmons-Taylor theory [51] for a thermally stimulated current (TSC), which predicts a qualitatively similar linear temperature dependence of the apparent activation energy. It is worth noting that such kinds of linear relationship for $E_a(T)$ are also justified by analytically variable range-hopping calculations for disordered organic semiconductors [18,19]. The mean activation energy and frequency-to-escape factor at the maxima of the TSL peak, $T_m \sim 93$ K, are $E_a \cong 0.2$ eV and $\langle S \rangle = 2.7 \times 10^9$ s^{-1}, respectively. The meaning of the frequency-to-escape factor in disordered solids will be discussed in more detail in Sec. IV B.

132

TABLE I.   Dipole moment (p), polarizability of a neutral molecule ($\alpha_{neutr.}$), polarizability of a cation ($\alpha_{cation.}$), and width of the Gaussian DOS (σ) evaluated by TSL and computer simulations; dipolar disorder component (σ_{dip}) estimated from TSL data; and width of superimposed exponential low-energy tail (T_0) evaluated from TSL data.

Material	Dipole moment, p (D)	$\alpha_{neutr.}$ (Bohr^3)	α_{cation} (Bohr^3)	DOS width (TSL) σ (eV)	σ_{dip} (eV)	T_0, (K)	DOS width (simulations) σ (eV)
CBP	0.04[a]	670[b]	3200[b]	0.125	0	716	0.10
mCBP	2.15[a]	600[b]	3000[b]	0.131	0.039	673	0.12
mCBP-CN	4.6[a]	600[b]	3000[b]	0.151	0.085	–	0.20
mCP	1.35[a]	450[b]	1500[b]	0.140	0.024	–	0.16
mCP-CN	6[a]	540[b]	1500[b]	0.177	0.111	–	0.24

[a]Calculated by using the M062X functional in density-functional theory.
[b]Calculated using a perturbative approach, as implemented in the Gaussian 09 package (opt = polar) keyword [78].

Using an empirical calibration of Eq. (4) to convert the temperature scale to a trap-energy scale, and then plotting the high-temperature part of the TSL signal intensity logarithmically either against E_a^2 or E_a, allows for a "Gaussian" or an "Exponential analysis," respectively, as shown in Figs. 2(c) and 2(d). It proves that the high-temperature part of a TSL curve becomes a straight line when plotting $\ln(I_{TSL})$ versus E_a^2 [Fig. 2(c)]. It is remarkable to see an almost perfect Gaussian fit of the high-temperature part of the measured curve observed over three decades of TSL intensity variation [Fig. 2(c)], whereas the same data plotted in the $\log(I_{TSL})$ versus E_a representation show a clear deviation from an exponential dependence [Fig. 2(d)]. This observation provides strong support for a Gaussian shape of the DOS profile in this material. The slope of the straight line in Fig. 2(c) is a measure of the DOS width. The energy disorder parameter $\sigma = 0.151$ eV is obtained for the mCBP-CN film, which is very close to the disorder parameter $\sigma = 0.15$ eV estimated for AlQ$_3$ films [52] by

charge-transport measurements. Such a relatively strong energy disorder is expected for polar materials – the dipole moments for AlQ$_3$ [52] and mCBP-CN are 4.9 and 4.6 D, respectively (Table I). It is worth noting that the above Gaussian analysis used here is conceptually similar to that earlier employed by Bässler [53] and Eiermann *et al.* [54] using the TSC technique for studying the width of the DOS distribution in disordered tetracene layers, by analyzing the shape of the high-energy part of a TSC peak.

Figure 3(a) compares normalized TSL curves measured for CBP, mCBP, and mCBP-CN films under the same conditions. All of these host materials reveal a characteristic TSL peak, which features a clear shift and progressive broadening towards higher temperatures with increasing molecular dipole moment [Fig. 3(a)]. The TSL peak maximum [depicted by arrows in Fig. 3(a)] also shifts from $T_m \cong 72$ K for CBP to $T_m \cong 78$ and 93 K for mCBP and mCBP-CN films, respectively (Table I). The latter effect is a clear sign of increasing energy disorder
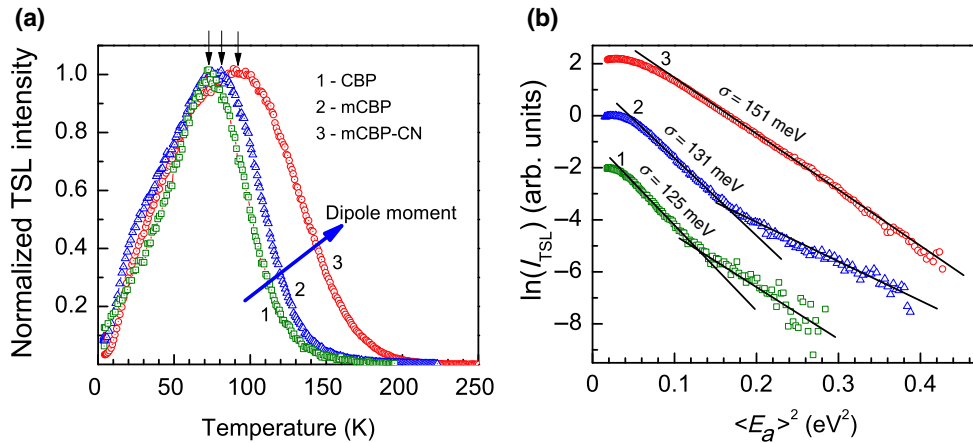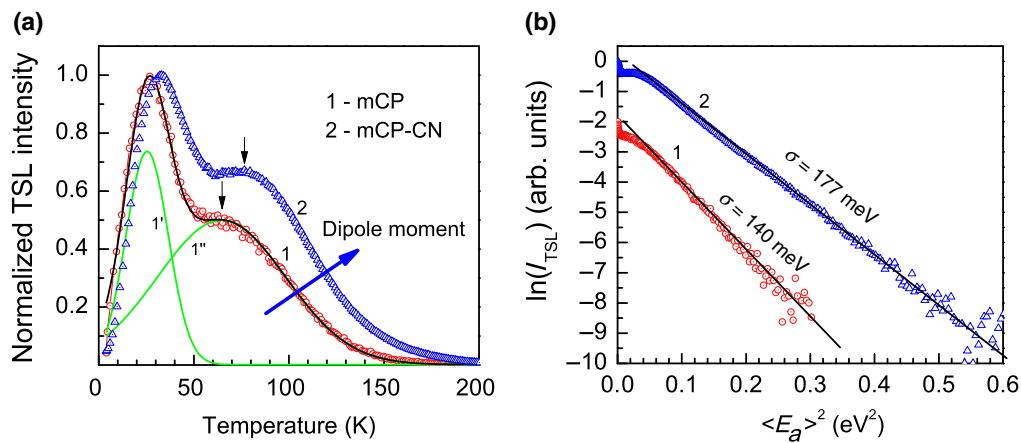

FIG. 3.   (a) Normalized TSL glow curves measured after excitation with 313 nm light for 3 min at 4.2 K for CBP, mCBP, and mCBP-CN films (curves 1, 2, and 3, respectively); (b) Gaussian analysis of high-temperature parts of TSL curves shown in (a). Curves are vertically shifted with respect to each other for clarity.

in this sequence of host materials from the same series of CBP derivatives. The shift is a consequence of the fact that the mean activation energy, which carriers reach in the course of their downward hopping relaxation at very low temperature within a Gaussian DOS, is directly proportional to energy-disorder parameter σ [55].

A Gaussian analysis of the high-temperature parts of TSL curves for CBP, mCBP, and mCBP-CN films, using Eq. (4), as described above, is shown in Fig. 3(b). The plot reveals a Gaussian dependence in all samples—its slope yields the width of the DOS, which increases with increasing dipole moment from 0.125 eV for virtually non-polar CBP ($p \cong 0$ D) to 0.131 and 0.151 eV for mCBP ($p = 2.15$ D) and mCBP-CN ($p = 4.6$ D), respectively (cf. Table I). This points to an important role of the dipolar-disorder effects on the increase of the energy disorder in this series of CBP derivatives, with increasing dipole moments of constituent molecules. The disorder parameter $\sigma = 0.112$ eV [56] is inferred for evaporated CBP films from charge-transport measurements, which is comparable to the value of $\sigma = 0.125$ eV we obtain here for the spin-coated CBP film.

A remarkable observation of this study is that CBP and mCBP films also reveal slower-decaying deep exponential tails at the lowest portion of the DOS, following the Gaussian distribution. Fitting the deep tail with exponential distribution $g(\varepsilon) \propto \exp(\varepsilon/kT_0)$, where T_0 is the characteristic width of the exponential distribution (for energies $\varepsilon < 0$), yields 716 and 673 K, for CBP and mCBP films, respectively (Table I).

Next, we compare the TSL properties of the above CBP derivatives with another series of host materials, based on CP derivatives. TSL glow curves measured under the same conditions for mCP and mCP-CN films are shown in Fig. 4(a) (curves 1 and 2, respectively). Although these films exhibit a TSL signal within a similar temperature range, from 4.2 to about 200 K, to that of the CBP derivatives [cf. Fig. 3(a)], the shapes of their TSL curves are significantly different. The TSL curve of mCP clearly consists of two overlapping peaks with T_m at 25 and 65 K, respectively, as shown by deconvolution of the measured TSL curve into two Gaussian peaks (curves 1′ and 1″ in Fig. 4). It is noteworthy that the low-temperature feature with $T_m = 25$ K dominates in intensity. A similarly shaped TSL is found in the strongly polar mCP-CN film ($p = 6$ D) [Fig. 4(a), curve 2], which also consists of two overlapping peaks, but are shifted towards higher temperatures with T_m at 33 and 78 K. We should, however, note that a low-temperature feature is also noticeable in TSL curves of mCBP and mCBP-CN films, but it is significantly weaker and seen as just a weak shoulder [cf. curve 1′ in Fig. 2(a)]. Our complementary studies demonstrate that the low-temperature TSL feature in these materials arises due to frustrated energy relaxation [57] of charge carriers photogenerated at 5 K, and therefore, some of them get stuck in the upper portion of the DOS; this effect will be explored in greater detail in future works of the authors. Since only the deeper portion of the DOS profile controls charge transport in amorphous organic semiconductors, the high-temperature TSL feature, peaking at 65 and 78 K in mCP and mCP-CN, respectively, is expected to be of practical relevance (we refer to it as the "main TSL peak"), and thus, is analyzed below.

The mean activation energy E_a is measured in mCP and mCP-CN films as a function of temperature by fractional TSL and in both materials it exhibits a similar temperature dependence to that given by Eq. (4). Gaussian analysis of the high-temperature parts of TSL curves for mCP and mCP-CN films is done as described above for other host materials and is presented in Fig. 4(b) as curves 1 and 2,

FIG. 4. (a) Normalized TSL glow curve measured after excitation with 313 nm light for 3 min at 4.2 K for mCB and mCP-CN films (curves 1 and 2, respectively). Curves 1′ and 1″ represent deconvolution of the TSL curve of mCP (curve 1) into two Gaussian peaks; (b) Gaussian analysis of high-temperature part of the corresponding TSL curves shown in (a).

respectively. The energy-disorder parameter, σ, in these materials is inferred from the slope of the high-temperature part of TSL curves plotted in a Gaussian representation: $\ln(I_{TSL})$ versus E_a^2. Both materials show a nice Gaussian fitting of the high-temperature parts of the measured curves over several decades of TSL intensity variation. Since the TSL signal in the mCP-CN film is significantly stronger than that in mCP, we are able to extend its Gaussian analysis towards deeper energies [Fig. 4(b), curve 2]. The results in Fig. 4(b) demonstrate a clear impact of the magnitude of the dipole moments on the width of the DOS, which increases from $\sigma = 0.140$ eV for moderately polar mCB ($p = 1.35$ D) to 0.177 eV in strongly polar mCP-CN ($p = 6$ D). This suggests a rather significant energy disorder that is inherent in CB derivatives.

B. Computation of the DOS distribution

To provide deeper insights into the DOS structure and independent verification of the DOS parameters probed by the TSL technique in the above OLED host materials, we carry out computer simulations. To evaluate the DOS distribution of the amorphous systems, we initially employ atomistic MD simulations to generate the amorphous morphologies, as described in Sec. II C. We then use quantum chemical calculations and polarizable force fields to compute site energies. Using the simulated amorphous morphologies, site energies of all molecules are evaluated by using the parameterized (see the Sec. II C) polarizable force fields. The corresponding DOS, shown in Fig. 5, have Gaussian shapes with variances σ.

The DOS widths σ inferred from the simulation results are listed in Table I. Despite the similarity in chemical structures of CBP derivatives, the energy disorder varies over a broad range in these materials from 0.10 eV to 0.12 and 0.20 eV for CBP, mCBP, and mCBP-CN, respectively.
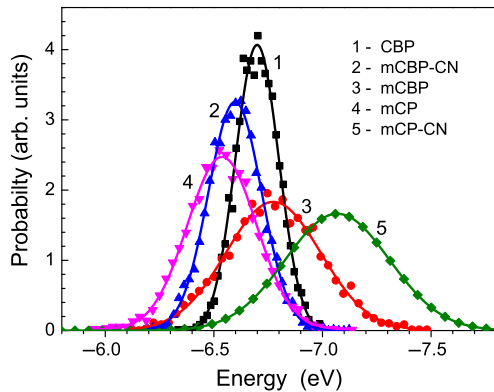
As expected, the smallest energy disorder is found in CBP films and this can be readily explained by the symmetric molecular structure: its ground-state dipole moment is virtually zero. As a result, the first nonvanishing electrostatic contribution is due to the interaction of the charge carrier and the quadrupole moments of the surrounding molecules. Since this contribution is much smaller than the charge-dipole interaction, the energetic disorder of these compounds is relatively small, in the order of 0.1 eV. The shift of the ionization potential in a solid state is mostly due to induction stabilization, and the shape of the density of states is Gaussian. The dipole moment increases sequentially in mCBP and mCBP-CN molecules, which gives rise to the increase of charge-dipole integration and hence to a larger electrostatic contribution to the energetic disorder in these materials. This verifies that dipolar disorder is responsible for the significant increase in the energy disorder within the series of CBP derivatives. Such a conclusion is, however, valid for compounds of the same family, in our case, with similar molecular polarizabilities. Indeed, the DOS simulations confirm that the CBP, mCBP, and mCBP-CN family has similar polarizability of cations and neutral molecules (see Table I), and hence, their DOS width increases with the molecular dipole moment. mCP has a significantly smaller polarizability of the cation compared with mCBP (~ 1500 vs ~ 3000 Bohr^3, see Table I). Therefore, screening of the electrostatic disorder by the induction interactions is smaller than that for mCBP, giving rise to a DOS width of 0.16 eV for mCP.

It is pertinent to note that dipole moments can vary considerably with molecular conformations. Different conformers lead to variations in the molecular dipole

FIG. 5. DOS distributions calculated for CBP, mCBP, mCBP-CN, and mCP (curves 1, 2, 3, and 4, respectively) employing molecular dynamics simulations. Solid lines depict Gaussian fits to data.
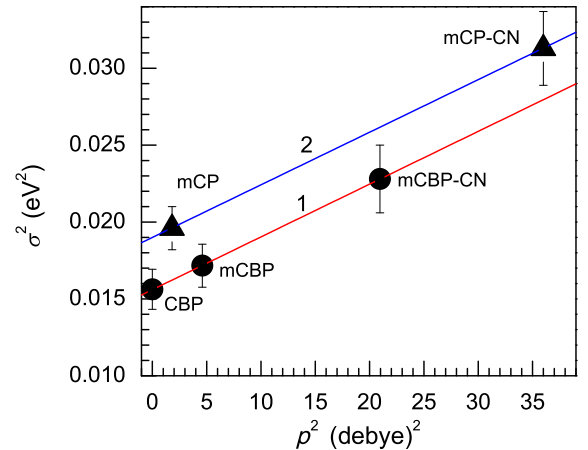
FIG. 6. Estimated disorder parameter versus dipole moment for two series of OLED host materials: CBP and CP derivatives (solid circles and triangles, respectively). Solid lines are results of fitting of experimental data with Eqs. (5) and (6) using $c = 1$ and $\varepsilon = 3.13$ [71].

moment in the amorphous morphologies. The distribution of dipole moments in the morphology inferred from MD simulations normally features a fairly broad peak [75] around a certain value that can, to a certain extent, be used as the "average" dipole moment. We are not claiming that this trend is universal for all organic semiconductors, especially taking into account that the distributions of dihedral angles are sensitive to the deposition protocols. However, in our host materials, the average dipole moments inferred from MD simulations [75] are found to correlate well with those shown in Table I and are used for the analysis depicted in Fig. 6.

IV. DISCUSSION

The DOS widths determined by the TSL techniques are in reasonable agreement with the computation results (cf. Table I), predicting a significant variation in energy disorder among the considered host materials. Although the obtained experimental values somewhat deviate from the simulated σ values, mostly in systems with strong energy disorder, they do demonstrate a remarkably *similar trend* in the variation of energetic disorder among these materials. The reason for the discrepancy between the widths of the DOS probed by TSL and that obtained by computer simulations should be a subject of further research.

A comparison of the DOS parameters determined by TSL and by computer simulations (Fig. 5) has two important implications: (i) It confirms that the large energetic disorder observed experimentally (ranging from $\sigma = 0.125$ to 0.177 eV) characterizes the *intrinsic* DOS, i.e., the DOS of a chemically pure disordered material, rather than that affected by impurity-related traps. Therefore, charge transport in such OLED hosts is expected to be inherently very dispersive. (ii) It reveals the utmost importance of the polarizability of the cation for the DOS width, which is a key finding in the present study. As attested by computer simulations, the physical reason for the enlarged energetic disorder in CP derivatives compared with CBP ones can be attributed to much smaller polarizability of their cation states, owing to the more rigid chemical structure of these molecules, and thus, smaller screening effect.

The calculated DOS distributions in Fig. 5 yield not only the variances, σ, of their Gaussian shapes, but also the energy positions of the HOMO levels. On the other hand, methods based on thermally activated spectroscopy, like TSL or TSC, use thermal energy generated by heat to probe localized states occupied by charge carriers within intrinsic (or extrinsic) DOS. Since such an energy is much less than that of the energy corresponding to the HOMO-LUMO gap, it can only characterize the DOS parameters. Nonetheless, in host-guest compositions, TSL can potentially yield the energy difference between corresponding HOMO or LUMO levels of host and guest materials, if

guest molecules create a hole or an electron trap, respectively, in the host material.

A. Effect of dipole moments

Next, we discuss the effect of the dipole moments, of the materials studied here, on the width of the DOS evaluated by the TSL technique. As it has long been suggested, the total width σ in a polar amorphous organic solid can be decomposed into a dipolar component, σ_{dip}, and a so-called van der Waals component, σ_{vdW} [3,58]. If different energy-disorder contributions are independent and follow Gaussian statistics, then the total width is

$$\sigma^2 = \sigma_{\mathrm{vdW}}^2 + \sigma_{\mathrm{dip}}^2. \tag{5}$$

The term σ_{vdW} in Eq. (5) is used here to describe the whole nondipolar disorder component, despite its physical origin being solely attributed to the variation of the interaction of a charged molecule with induced dipole moments in the molecular environment [59,60]. Borsenberger and Weiss [3] proposed that fluctuations of relative orientations and intermolecular distances between the hopping site and surrounding molecules created fluctuations of the induced dipolar cloud in nearby molecules, which made the major contribution to σ_{vdW}. Subsequently, it is recognized that quadrupole moments can be sufficiently high in nonpolar materials with zero dipole moment, and hence, variation of charge-quadrupole interactions can also contribute to the energy disorder [9,61]. Therefore, to adhere to established terminology, we imply here that σ_{vdW} encompasses contributions from all sources of energy disorder, excluding the dipolar contribution. In other words, it describes the total energy disorder in a nonpolar system.

The dipolar disorder, σ_{dip}, contributes strongly to the overall energy disorder in polar organic solids, and it leads to a stronger DOS broadening compared with the charge-quadrupole interaction [61]. σ_{dip} arises due to randomly oriented permanent molecular dipoles that generate fluctuation in the electrostatic potential due to charge-dipole interactions, in addition to the disorder that is already present in nonpolar systems, which leads to DOS broadening [3]. Dieckmann *et al.* [58] originally obtained an expression for the dipolar component using Monte-Carlo numerical calculations. Subsequent analytical calculation by Young [62] has confirmed the Gaussian form of the DOS in polar systems and the relation for σ_{dip} is derived as

$$\sigma_{\mathrm{dip}} = \frac{7.04}{a^2 \varepsilon} c^{1/2} p \ (\text{in eV}) \tag{6}$$

where a is the intersite distance (lattice constant) in Angstrom, ε is the dielectric constant, c is the fraction of the lattice occupied by dipoles (in our case $c=1$), and p is the dipole moment in debye. Although, as recently

recognized [63], accounting for the individual molecular polarizabilities and nearest-neighbor interactions might lead to deviation from the suggested $1/\varepsilon$ dependence in Eq. (6), the dipolar disorder σ_{dip} is predicted to scale linearly with dipole moment. An analysis based on Eq. (6), in conjunction with Eq. (1), is widely used to evaluate the dipolar-disorder contribution to the overall energy disorder from charge-transport measurements in small-molecule organic glasses [3,64–66] and molecularly doped polymers, [3,60,67–69] with different dipole moments and dipole concentration, which justifies the applicability of Eq. (6).

Assuming the σ_{vdW} component is a constant for materials within the same series of derivatives, Eqs. (2) and (3) provide a means for analyzing the effect of the dipole moments of different compounds on the total width, by plotting σ^2 versus p^2. Figure 6 (curve 1) clearly shows the predicted linear relationship for the CPB derivatives, CBP, mCBP, and mCBP-CN (solid circles), indicating the justification for the analysis. The nonpolar component σ_{vdW} for this series of derivatives is equal to the DOS width, $\sigma = 0.125$ eV, obtained for a nonpolar CBP film. Using $\sigma_{vdW} = 0.125$ eV, Eq. (5) yields the dipolar component $\sigma_{dip} = 0.039$ and 0.085 meV, for polar mCBP and mCBP-CN, respectively (Table I). The intersite distance, $a = 11$ Å, may be estimated from the slope of solid line 1 in Fig. 6 using Eq. (6). It agrees well with the effective lattice constant $a = 12$ Å estimated recently for CBP films from charge-transport measurements [70].

A qualitatively similar trend with increasing dipole moment is found for a series of CP derivatives (Fig. 6, curve 2), although only two host materials (mCP and mCP-CN) of this series are available to us. The energy-disorder parameter demonstrates a strong increase with increasing dipole moment from 1.35 to 6 D for mCP and mCP-CN, respectively (Fig. 6, solid triangles). It is remarkable that this dependence in the σ^2 versus p^2 representation features almost the same slope (curves 2 in Fig. 6) as that of the linear dependence obtained for the above CBP derivatives (curve 1), but is offset with respect to the latter. These observations suggest that the dipolar-disorder component increases in a similar manner with increasing dipole moments for both series of materials, while the nonpolar σ_{vdW} disorder component differs significantly for them. The value of $\sigma_{vdW} = 0.138$ eV is determined for mCP and mCP-CN from the $p^2 = 0$ intercept of curve 2 (Fig. 6), which turns out to be significantly larger than the value of $\sigma_{vdW} = 0.125$ eV determined for the above series of CBP derivatives. Using the above σ_{vdW} value, Eq. (5) yields $\sigma_{dip} = 0.024$ and 0.111 meV, for mCB and mCB-CN films, respectively (Table I). The above findings suggest that the enlarged energy disorder in CP, compared with CBP, derivatives, mostly relates to the intrinsically larger nondipolar component of energy disorder.

The correlation of the observed dipole effect on DOS width, as determined by the TSL technique, with the prediction of the dipolar disorder model [62], is striking. It implies that the OLED host materials considered here behave similarly to conventional amorphous organic photoconductors, as previously studied by the TOF technique in the form of neat molecular glasses [3,64–66] or as charge-transporting molecules in molecularly doped polymers [3,60,67–69]. It should be noted that the dipolar-disorder model given by Eq. (6) does not consider variations in the molecular dipole moment caused by different conformers in the amorphous morphologies. However, despite the simplification, we believe that this model can provide a good first-order approximation for a description of the dipolar-induced DOS broadening in our OLED hosts. Notably, the dependence presented in Fig. 6 and concomitant analysis is generally not a surprising result for the class of organic semiconducting materials. There are numerous similar findings in the literature for the width of the DOS inferred from charge-mobility measurements in different polar systems. The key result of the present work is that the same effects are observed using a purely optical experimental approach.

Finally, it worth mentioning that Hoffmann *et al.* [76] have recently demonstrated that, in contrast to small-molecule organic materials, the inhomogeneous broadening of the DOS for holes and neutral excitons can be remarkably similar in the case of conjugated polymers. This is suggested to be a characteristic feature of conjugated polymers, in which disorder results predominantly from the statistical variation of the lengths of the conjugated segments, rather than from van der Waals coupling among the chains and can be used for the prediction of the DOS for holes from simple optical spectroscopy. This effect is observed for a series of conjugated alternating phenanthrene indenofluorene copolymers [76] and probably more research is needed to confirm such a correlation by involving more copolymer materials.

B. DOS shapes

Another interesting finding of this study is (i) direct observation, using an optical method (TSL), of a pronounced deep exponential tail that follows a Gaussian distribution; and (ii) that this effect turns out to be material dependent—it is seen in CBP and mCBP films, while mCBP-CN, mCP, and mCP-CN host materials feature solely a Gaussian profile with a negligible, if any, exponential tail [cf. Figs. 3(b) and 4(b)]. The origin of such qualitatively different DOS distributions in organic solids deserves more thorough investigation, involving more amorphous organic semiconducting materials, going beyond the scope of the present study. However, a deep exponential tail in disordered organic semiconductors is not a surprising result, but has previously been reported

using different methods. In a series of publications by Van Mensfoort *et al.* [8,72,73], they claimed that their drift-diffusion device model provided a much better description of the experimental temperature-dependent *IV* characteristics measured in some amorphous organic semiconductor (AOS) materials, if one assumes a combination of a Gaussian density of transport states plus superimposed exponential density of trap states. They assume that the charge traps can be responsible for the exponential tail and suggest the following cumulative DOS in realistic organic semiconducting materials [8,72,73]:

$$g(\varepsilon) = \frac{N_t}{\sqrt{2\pi\sigma^2}}\exp\left(-\frac{\varepsilon^2}{2\sigma^2}\right) + \frac{N_{\text{trap}}}{kT_0}\exp\left(\frac{\varepsilon}{kT_0}\right), \quad (7)$$

where σ and N_t are the Gaussian DOS width and the density of transport sites, respectively. T_0 and N_{trap} are the characteristic width of the exponential distribution (for energies $\varepsilon < 0$) and the density of trap sites, respectively. This idea was supported by Hulea *et al.* [17], who scanned the DOS distribution of a poly(p-phenylene vinylene) film over a wide energy range using an electrochemically gated transistor and found an almost exponential trap distribution at the deep tail superimposed onto an intrinsic Gaussian DOS distribution. Moreover, several KPFM studies [10,11] provide direct evidence that AOS materials exhibit both a central Gaussian DOS and an exponential tail.

Several theoretical explanations are suggested for the complex DOS distribution observed in AOS. May *et al.* [9] demonstrate that, in a material with molecular dipole moments, exponential tails can develop if negatively or positively charged sites are strongly polarizable. This results in large *induced* dipoles on these charged sites and thereby increases their interaction with the polar environment. Such nonlinear effects of dipolar fields give rise to strong potential fluctuation and thereby lead to the appearance of an exponential tail. Additionally, the same group has recently found that a HOMO level position below 6 eV and LUMO above 3.6 eV, in organic semiconductors, can facilitate hole and electron trapping, respectively [74].

Interestingly, our observations seem to be consistent with the above prediction for a trap-free energy window: virtually no exponential tail is observed for mCP films [cf. Fig. 4(b)], where the HOMO level is at 5.9 eV, i.e., within a "trap-free energy window," inside which organic semiconductors normally do not experience charge trapping [74]. The above concept implies that materials with an ionization energy lower than 6 eV will not exhibit trap-limited hole transport, similarly, an electron affinity above 3.6 eV will not cause electron trapping to limit electron transport [74]. We also find a similar picture in 10-[4-(4,6-diphenyl-1,3,5-triazin-2-yl)phenyl]-9,9-dimethylacridine films featuring no deep exponential tail (not shown here) and where the HOMO level is at 5.8 eV, which is consistent with trap-free conditions. Therefore, we assume that the pure

Gaussian distribution observed over a wide energy range might be related to the absence of a significant number of extrinsic traps in this material. On the other hand, mCBP has a HOMO at 6.1 eV, which should facilitate extrinsic charge (hole) trapping, correlated with a very pronounced exponential tail observed by TSL [curve 2 in Fig. 3(b)]. In the case of mCBP-CN and mCP-CN, extrinsic traps are expected, as suggested by consideration of the position of the HOMO-LUMO level. However, we hypothesize that significantly stronger molecular dipole moments in mCBP-CN and mCP-CN might dampen the field variations due to induced dipoles, which give rise predominantly to the Gaussian distribution observed in our experiments [cf. curves 3 and 2 in Figs. 3(b) and 4(b), respectively]. These issues definitely require thorough investigation, which goes beyond the scope of the present study.

Finally, we discuss the implication of the "frequency-to-escape" factor, $\langle S \rangle = 2.7 \times 10^9 \text{ s}^{-1}$, estimated at the maximum of the TSL peak (cf. Fig. 2). Since both the TSL and the hopping charge-transport process in disordered organic semiconductors are controlled by thermally assisted jumps of relaxed carriers, the mechanisms of which are successfully described in terms of the Miller-Abrahams jump rates [1], it is highly likely that the "frequency-of-escape frequency" has the same meaning in both cases. For disordered semiconductors, it presents the probability of a charge-carrier hop, i.e., tunnels, when energetic resonance occurs. This probability decreases exponentially with the hopping distance, ρ, and is usually described in terms of a homogenous lattice gas (also called the lattice gas model [3]) as

$$\nu = \nu_0 \exp(-2\rho/\rho_0), \quad (8)$$

where ρ_0 is a wave function decay parameter and ν_0 is a frequency factor, which is typically assumed to be equal to the vibrational frequency of about 10^{13} s^{-1}. The lattice gas model is based on the assumption that the hopping distance can be described as $\rho = (M/A\delta)^{1/3}$, where M is the molecular weight, A is the Avogadro number, and δ is the sample density. The model ignores the distribution of hopping distances and the distribution of hopping-site energies. Eq. (8) is a key relationship that describes the dependence of charge mobility on the concentration of charge-transporting molecules in molecularly doped polymers [3]. Assuming that the hopping distance, ρ, in mCBP-CN films is equal to the average lattice constant, $a = 11$ Å, as estimated above for this material, and that the estimated TSL frequency-to-escape factor, $\langle S \rangle = 2.7 \times 10^9 \text{ s}^{-1}$, can be described by the lattice gas model, Eq. (8) yields the wave-function decay parameter, $\rho_0 = 2.68$ Å. This parameter coincides very well with that reported in the literature [3] for conventional charge-transporting molecules, which is typically within a range of 1–2 Å and less often approaches 3 Å. Thus, the relatively

large wave-function decay parameter implies an enhanced intermolecular electronic coupling, which should promote good transport behavior in this material. This is in line with recent simulation results [70] that predict a large average coupling in CBP due to the specific shape of its electronic orbitals, which are uniformly distributed over the periphery of the molecule. This facilitates the overlap of states participating in charge transport and, as a result, leads to a fairly large mobility prefactor of $\mu_0 = 0.8 \text{ cm}^2\text{V}^{-1}\text{s}^{-1}$ in this material.

V. CONCLUSIONS

We demonstrate that the DOS distribution in neat OLED host materials can be well determined by the low-temperature fractional TSL technique. This is proven by comparison of the TSL results with DOS parameters obtained by computer simulations, as carried out in the present study, and from available charge-transport measurements. We perform comparative TSL studies of two series of OLED host materials possessing different polarities: (i) CBP, mCBP, and mCBP-CN; and (ii) mCP and mCP-CN. Their dipole moments vary from almost zero for nonpolar CBP to 6 D in strongly polar mCP-CN. We find that the DOS distribution broadens significantly with increasing molecular dipole moments, which can be well described by the dipolar-disorder model, but only for materials belonging to the same series of derivatives that possess similar polarizability of cations and neutral molecules. We find that the DOS widths of these two series of materials are offset by a constant amount, with a broader DOS for CP derivatives, compared with CBP-based compounds at equivalent polarity. This is confirmed by simulations that demonstrate a similar trend in the variation of DOS. Larger energetic disorder in CP derivatives is attributed to smaller polarizability of both their neutral and cation states. Therefore, the electrostatic disorder of CP derivatives is not screened by induction as much as the disorder of CBP derivatives. Additionally, the significant nonpolar component of the disorder observed in CP derivatives is consistent with the theoretical prediction. The dipolar energy-disorder component of the DOS, as extracted from the TSL experiment, demonstrates a similar increase with the magnitude of the molecular dipole moment for all materials considered in this work, implying that the dipolar-disorder model is applicable to such OLED host materials. Such behavior is expected if the intersite distance is similar in these systems. Finally, we find that a deep exponential tail accompanies a Gaussian distribution in CBP and mCBP films. The origin of this effect will be the subject of further investigation by the authors.

ACKNOWLEDGMENTS

[1] H. Bässler, Charge transport in disordered organic photoconductors a monte carlo simulation study, Phys. Status Solidi B **175**, 15 (1993).

[2] A. Köhler and H. Bässler, *Electronic Processes in Organic Semiconductors: An Introduction* (John Wiley & Sons, Weinheim, 2015).

[3] P. M. Borsenberger and D. Weiss, *Organic Photoreceptors for Xerography* (CRC Press, New York, 1998).

[4] S. D. Baranovskii, Mott lecture: Description of charge transport in disordered organic semiconductors: Analytical theories and computer simulations, Phys. Status Solidi A **215**, 1700676 (2018).

[5] J. Oelerich, D. Huemmer, and S. Baranovskii, How to Find out the Density of States in Disordered Organic Semiconductors, Phys. Rev. Lett. **108**, 226403 (2012).

[6] S. V. Novikov, Far tails of the density of states in amorphous organic semiconductors, J. Chem. Phys. **143**, 164510 (2015).

[7] V. Arkhipov, P. Heremans, E. Emelianova, and H. Baessler, Effect of doping on the density-of-states distribution and carrier hopping in disordered organic semiconductors, Phys. Rev. B **71**, 045214 (2005).

[8] S. Van Mensfoort, J. Billen, S. Vulto, R. Janssen, and R. Coehoorn, Electron transport in polyfluorene-based sandwich-type devices: Quantitative analysis of the effects of disorder and electron traps, Phys. Rev. B **80**, 033202 (2009).

[9] F. May, B. Baumeier, C. Lennartz, and D. Andrienko, Can Lattice Models Predict the Density of States of Amorphous Organic Semiconductors?, Phys. Rev. Lett. **109**, 136401 (2012).

[10] O. Tal, Y. Rosenwaks, Y. Preezant, N. Tessler, C. Chan, and A. Kahn, Direct Determination of the Hole Density of States in Undoped and Doped Amorphous Organic Films with High Lateral Resolution, Phys. Rev. Lett. **95**, 256405 (2005).

[11] K. Celebi, P. Jadhav, K. Milaninia, M. Bora, and M. Baldo, The density of states in thin film copper phthalocyanine measured by kelvin probe force microscopy, Appl. Phys. Lett. **93**, 317 (2008).

[12] M. Pope and C. E. Swenberg, Electronic processes in organic solids, Annu. Rev. Phys. Chem. **35**, 613 (1984).

[13] H. Bässler, in *Disorder Effect on Relaxational Processes*, edited by Richert R., Blumen A. (Springe-Verlagr, Berlin Heidelberg New York, 1994), pp. 485–507.

[14] F. Schauer, S. Nešpůrek, and H. Valerián, Temperature dependent space-charge-limited currents in amorphous and disordered semiconductors, J. Appl. Phys. **80**, 880 (1996).

[15] S. Olthof, S. Mehraeen, S. K. Mohapatra, S. Barlow, V. Coropceanu, J.-L. Brédas, S. R. Marder, and A. Kahn, Ultralow Doping in Organic Semiconductors: Evidence of Trap Filling, Phys. Rev. Lett. **109**, 176601 (2012).

[16] V. Y. Aristov, O. Molodtsova, V. Maslyuk, D. Vyalikh, V. Zhilin, Y. A. Ossipyan, T. Bredow, I. Mertig, and M. Knupfer, Electronic structure of pristine CuPc: Experiment and calculations, Appl. Surf. Sci. **254**, 20 (2007).

[17] I. Hulea, H. Brom, A. Houtepen, D. Vanmaekelbergh, J. Kelly, and E. Meulenkamp, Wide Energy-Window View on the Density of States and Hole Mobility in Poly (p-Phenylene Vinylene), Phys. Rev. Lett. **93**, 166601 (2004).

[18] A. Kadashchuk, Y. Skryshevskii, A. Vakhnin, N. Ostapenko, V. Arkhipov, E. Emelianova, and H. Bässler, Thermally stimulated photoluminescence in disordered organic materials, Phys. Rev. B **63**, 115205 (2001).

[19] V. Arkhipov, E. Emelianova, A. Kadashchuk, and H. Bässler, Hopping model of thermally stimulated photoluminescence in disordered organic materials, Chem. Phys. **266**, 97 (2001).

[20] A. Kadashchuk, A. Vakhnin, Y. Skryshevski, V. Arkhipov, E. Emelianova, and H. Bässler, Thermally stimulated luminescence in π-conjugated polymers containing fluorene and spirobifluorene units, Chem. Phys. **291**, 243 (2003).

[21] A. Kadashchuk, N. Ostapenko, V. Zaika, and S. Nešpurek, Low-temperature thermoluminescence in poly (methylphenylsilylene), Chem. Phys. **234**, 285 (1998).

[22] A. Kadashchuk, Y. Skryshevski, Y. Piryatinski, A. Vakhnin, E. Emelianova, V. Arkhipov, H. Bässler, and J. Shinar, Thermally stimulated photoluminescence in poly (2, 5-dioctoxy p-phenylene vinylene), J. Appl. Phys. **91**, 5016 (2002).

[23] S. A. Patil, U. Scherf, and A. Kadashchuk, New conjugated ladder polymer containing carbazole moieties, Adv. Funct. Mater. **13**, 609 (2003).

[24] A. Kadashchuk, S. Schols, A. Vakhnin, J. Genoe, and P. Heremans, Triplet dynamics and charge carrier trapping in triplet-emitter doped conjugated polymers, Chem. Phys. **358**, 147 (2009).

[25] A. Kadashchuk, V. I. Arkhipov, C.-H. Kim, J. Shinar, D.-W. Lee, Y.-R. Hong, J.-I. Jin, P. Heremans, and H. Bässler, Localized trions in conjugated polymers, Phys. Rev. B **76**, 235205 (2007).

[26] I. Fishchuk, A. Kadashchuk, A. Vakhnin, Y. Korosko, H. Bässler, B. Souharce, and U. Scherf, Transition from trap-controlled to trap-to-trap hopping transport in disordered organic semiconductors, Phys. Rev. B **73**, 115210 (2006).

[27] A. Kadashchuk, D. Weiss, P. Borsenberger, S. Nešpurek, N. Ostapenko, and V. Zaika, The origin of thermally stimulated luminescence in neat and molecularly doped charge transport polymer systems, Chem. Phys. **247**, 307 (1999).

[28] A. Kadashchuk, D. Weiss, P. Borsenberger, N. Ostapenko, V. Zaika, and Y. Skryshevski, Effect of extrinsic traps on

thermally stimulated luminescence in molecularly doped polymers, Synth. Met. **109**, 177 (2000).

[29] P. V. Soroka, A. Y. Vakhnin, Y. A. Skryshevskiy, O. P. Boiko, M. I. Anisimov, Y. L. Slominskiy, V. G. Nazarenko, J. Genoe, and A. Kadashchuk, Charge carrier trapping in highly-ordered lyotropic chromonic liquid crystal films based on ionic perylene diimide derivatives, Eur. Phys. J.: Appl. Phys. **68**, 30201 (2014).

[30] A. Fakharuddin, W. Qiu, G. Croes, A. Devižis, R. Gegevičius, A. Vakhnin, C. Rolin, J. Genoe, R. Gehlhaar, A. Kadashchuk, V. Gulbinas, and P. Heremans, Reduced efficiency roll-Off and improved stability of mixed 2D/3D perovskite light emitting diodes by balancing charge injection, Adv. Funct. Mater. **29**, 1904101 (2019).

[31] I. Tale, Trap spectroscopy by the fractional glow technique, Phys. Status Solidi A **66**, 65 (1981).

[32] H. Gobrecht and D. Hofmann, Spectroscopy of traps by fractional glow technique, J. Phys. Chem. Solids **27**, 509 (1966).

[33] Y. Gorohovatsky and H. Bordovsky, *Thermally Activational Current Spectroscopy of High-Resistance Semiconductors and Dielectrics* (Izd. Nauka, Moscow, 1991).

[34] W. L. Jorgensen and J. Tirado-Rives, Potential energy functions for atomic-level simulations of water and organic and biomolecular systems, Proc. Natl. Acad. Sci. **102**, 6665 (2005).

[35] W. L. Jorgensen and J. Tirado-Rives, The OPLS [optimized potentials for liquid simulations] potential functions for proteins, energy minimizations for crystals of cyclic peptides and crambin, J. Am. Chem. Soc. **110**, 1657 (1988).

[36] W. L. Jorgensen, D. S. Maxwell, and J. Tirado-Rives, Development and testing of the OPLS all-atom force field on conformational energetics and properties of organic liquids, J. Am. Chem. Soc. **118**, 11225 (1996).

[37] C. M. Breneman and K. B. Wiberg, Determining atom-centered monopoles from molecular electrostatic potentials. The need for high sampling density in formamide conformational analysis, J. Comput. Chem. **11**, 361 (1990).

[38] C. Poelking, E. Cho, A. Malafeev, V. Ivanov, K. Kremer, C. Risko, J.-L. Brédas, and D. Andrienko, Characterization of charge-carrier transport in semicrystalline polymers: Electronic couplings, site energies, and charge-carrier dynamics in poly (bithiophene-alt-thienothiophene)[PBTTT], J. Phys. Chem. C **117**, 1633 (2013).

[39] G. Bussi, D. Donadio, and M. Parrinello, Canonical sampling through velocity rescaling, J. Chem. Phys. **126**, 014101 (2007).

[40] H. J. Berendsen, J. v. Postma, W. F. van Gunsteren, A. DiNola, and J. R. Haak, Molecular dynamics with coupling to an external bath, J. Chem. Phys. **81**, 3684 (1984).

[41] B. Hess, C. Kutzner, D. Van Der Spoel, and E. Lindahl, GROMACS 4: Algorithms for highly efficient, load-balanced, and scalable molecular simulation, J. Chem. Theory Comput. **4**, 435 (2008).

[42] S. Pronk, S. Páll, R. Schulz, P. Larsson, P. Bjelkmar, R. Apostolov, M. R. Shirts, J. C. Smith, P. M. Kasson, D. van der Spoel, B. Hess, and E. Lindahl, GROMACS 4.5: A high-throughput and highly parallel open source molecular simulation toolkit, Bioinformatics **29**, 845 (2013).

[43] A. Stone, *The Theory of Intermolecular Forces* (Clarendon Press, Oxford, 1997).

140

[44] G. D'Avino, L. Muccioli, F. Castet, C. Poelking, D. Andrienko, Z. G. Soos, J. Cornil, and D. Beljonne, Electrostatic phenomena in organic semiconductors: Fundamentals and implications for photovoltaics, J. Phys.: Condens. Matter. **28**, 433002 (2016).

[45] C. Poelking and D. Andrienko, Long-range embedding of molecular ions and excitations in a polarizable molecular environment, J. Chem. Theory Comput. **12**, 4516 (2016).

[46] B. T. Thole, Molecular polarizabilities calculated with a modified dipole interaction, Chem. Phys. **59**, 341 (1981).

[47] P. T. Van Duijnen and M. Swart, Molecular and atomic polarizabilities: Thole's model revisited, J. Phys. Chem. A **102**, 2399 (1998).

[48] A. J. Stone, Distributed multipole analysis: Stability for large basis sets, J. Chem. Theory Comput. **1**, 1128 (2005).

[49] V. Rühle, A. Lukyanov, F. May, M. Schrader, T. Vehoff, J. Kirkpatrick, B. R. Baumeier, and D. Andrienko, Microscopic simulations of charge transport in disordered organic semiconductors, J. Chem. Theory Comput. **7**, 3335 (2011).

[50] E. W. Forsythe, D. C. Morton, C. W. Tang, and Y. Gao, Trap states of tris-8-(hydroxyquinoline) aluminum and naphthyl-substituted benzidine derivative using thermally stimulated luminescence, Appl. Phys. Lett. **73**, 1457 (1998).

[51] J. Simmons and G. Taylor, High-field isothermal currents and thermally stimulated currents in insulators having discrete trapping levels, Phys. Rev. B **5**, 1619 (1972).

[52] G. G. Malliaras, Y. Shen, D. H. Dunlap, H. Murata, and Z. H. Kafafi, Nondispersive electron transport in Alq 3, Appl. Phys. Lett. **79**, 2582 (2001).

[53] H. Bässler, Localized states and electronic transport in single component organic solids with diagonal disorder, Phys. Stat. Sol. B **107**, 9 (1981).

[54] R. Eiermann, W. Hofberger, and H. Bässler, Localized valence states in the forbidden gap of non-crystalline tetracene, J. Non·Cryst. Solids **28**, 415 (1978).

[55] B. Movaghar, B. Ries, and M. Grünewald, Diffusion and relaxation of energy in disordered systems: Departure from mean-field theories, Phys. Rev. B **34**, 5574 (1986).

[56] M. Era, K. Mori, and N. Mototsu, Analysis of hole mobility of fluorene derivative films based on the disorder model and relationship between disorder free mobility and reorganization energy in the marcus theory. In *Organic Light Emitting Materials and Devices XVII*, edited by F. So and C. Adachi (International Society for Optics and Photonics, 2013), Vol. 8829, p. 88290N.

[57] S. Athanasopoulos, S. T. Hoffmann, H. Bässler, A. Köhler, and D. Beljonne, To hop or not to hop? understanding the temperature dependence of spectral diffusion in organic semiconductors, J. Phys. Chem. Lett. **4**, 1694 (2013).

[58] A. Dieckmann, H. Bässler, and P. Borsenberger, An assessment of the role of dipoles on the density-of-states function of disordered molecular solids, J. Chem. Phys. **99**, 8136 (1993).

[59] P. Borsenberger and H. Bässler, Concerning the role of dipolar disorder on charge transport in molecularly doped polymers, J. Chem. Phys. **95**, 5327 (1991).

[60] P. Borsenberger, *Electrical and Related Properties of Organic Solids* (Springer, Dordrecht, 1997), pp. 25.

[61] S. Novikov and A. Vannikov, *Hopping charge transport in disordered organic materials: Where is the disorder?*, J. Phys. Chem. C **113**, 2532 (2009).

[62] R. H. Young, Dipolar lattice model of disorder in random media analytical evaluation of the Gaussian disorder model, Philos. Mag. B **72**, 435 (1995).

[63] C. Madigan and V. Bulović, Charge Carrier Energy Disorder in Polar Amorphous Organic Thin Films, Phys. Rev. Lett. **97**, 216402 (2006).

[64] P. Borsenberger, M. Detty, and E. Magin, Electron transport in vapor deposited molecular glasses, Phys. Stat. Sol. B **185**, 465 (1994).

[65] P. M. Borsenberger and J. J. Fitzgerald, Effects of the dipole moment on charge transport in disordered molecular solids, J. Phys. Chem. **97**, 4815 (1993).

[66] V. Mimaite, J. V. Grazulevicius, R. Laurinaviciute, D. Volyniuk, V. Jankauskas, and G. Sini, Can hydrogen bonds improve the hole-mobility in amorphous organic semiconductors? experimental and theoretical insights, J. Mater. Chem. C **3**, 11660 (2015).

[67] P. Borsenberger, E. Magin, M. O'regan, and J. Sinicropi, The role of dipole moments on hole transport in triphenylamine-doped polymers, J. Polym. Sci., Part B: Polym. Phys. **34**, 317 (1996).

[68] P. Borsenberger and M. O'Regan, The role of dipole moments on hole transport in triphenylamine doped poly (styrene), Chem. Phys. **200**, 257 (1995).

[69] R. H. Young and J. J. Fitzgerald, Effect of polar additives on charge transport in a molecularly doped polymer: Survey of various additives, J. Chem. Phys **102**, 2209 (1995).

[70] N. B. Kotadiya, A. Mondal, S. Xiong, P. W. Blom, D. Andrienko, and G. J. A. Wetzelaer, Rigorous characterization and predictive modeling of hole transport in amorphous organic semiconductors, Adv. Electron. Mater. **4**, 1800366 (2018).

[71] P. K. Nayak and N. Periasamy, Calculation of ionization potential of amorphous organic thin-films using solvation model and DFT, Org. Electron. **10**, 532 (2009).

[72] S. Van Mensfoort, R. De Vries, V. Shabro, H. Loebl, R. Janssen, and R. Coehoorn, Electron transport in the organic small-molecule material BAlq—the role of correlated disorder and traps, Org. Electron. **11**, 1408 (2010).

[73] S. Van Mensfoort and R. Coehoorn, Effect of Gaussian disorder on the voltage dependence of the current density in sandwich-type devices based on organic semiconductors, Phys. Rev. B **78**, 085207 (2008).

[74] N. B. Kotadiya, A. Mondal, P. W. Blom, D. Andrienko, and G.-J. A. Wetzelaer, A window to trap-free charge transport in organic semiconducting thin films, Nat. Mater. **18**, 1182 (2019).

[75] A. Mondal, L. Paterson, J. Cho, K.-H. Lin, B. van der Zee, G. Wetzelaer, A. Stankevych, A. Vakhnin, J. Kim, A. Kadashchuk, P. W. M. Blom, F. May, and D. Andrienko, Physical Properties of OLED Host Materials (submitted to Chemical Physics Review, 2021).

[76] S. T. Hoffmann, F. Jaiser, A. Hayer, H. Bässler, T. Unger, S. Athanasopoulos, D. Neher, and A. Köhler, How do disorder, reorganization, and localization influence the hole mobility in conjugated copolymers?, J. Am. Chem. Soc. **135**, 1772 (2013).

[77] http://www.iop.kiev.ua/∼cryo/index_en.php.

[78] https://gaussian.com/polar/.

Paper 3: Molecular library of OLED host materials—Evaluating the multiscale simulation workflow

Anirban Mondal, Leanne Paterson, Jaeyoung Cho, Kun-Han Lin, Bas van der Zee, Gert-Jan AH Wetzelaer, **Andrei Stankevych**, Alexander Vakhnin, Jang-Joo Kim, Andrey Kadashchuk, Paul WM Blom, Falk May, Denis Andrienko

Molecular library of OLED host materials—Evaluating the multiscale simulation workflow

Anirban Mondal ; Leanne Paterson; Jaeyoung Cho ; Kun-Han Lin; Bas van der Zee;
Gert-Jan A. H. Wetzelaer; Andrei Stankevych; Alexander Vakhnin; Jang-Joo Kim; Andrey Kadashchuk;
Paul W. M. Blom ; Falk May; Denis Andrienko

Check for updates

View Online   Export Citation

Articles You May Be Interested In

Designing workflows for materials characterization

Appl. Phys. Rev. (March 2024)

Design considerations for digital light processing bioprinters

Appl. Phys. Rev. (July 2024)

High-throughput screening of tribological properties of monolayer films using molecular dynamics and machine learning

J. Chem. Phys. (April 2022)

Molecular library of OLED host materials—Evaluating the multiscale simulation workflow (F) (SCI)

Anirban Mondal,[1] (iD) Leanne Paterson,[1] Jaeyoung Cho,[1,2] (iD) Kun-Han Lin,[1] Bas van der Zee,[1]
Gert-Jan A. H. Wetzelaer,[1] Andrei Stankevych,[3] Alexander Vakhnin,[3] Jang-Joo Kim,[2] Andrey Kadashchuk,[3,4]
Paul W. M. Blom,[1] (iD) Falk May,[5] and Denis Andrienko[1,a)] (iD)

AFFILIATIONS

[1]Max Planck Institute for Polymer Research, Ackermannweg 10, 55128 Mainz, Germany

[2]Department of Materials Science and Engineering and the Center for Organic Light Emitting Diode, Seoul National University, Seoul, 151-744, South Korea

[3]Institute of Physics, National Academy of Sciences of Ukraine, Prospect Nauky 46, 03028 Kyiv, Ukraine

[4]IMEC, Kapeldreef 75, B-3001 Leuven, Belgium

[5]Merck KGaA, 64293 Darmstadt, Germany

[a)]Author to whom correspondence should be addressed: denis.andrienko@mpip-mainz.mpg.de

ABSTRACT

Amorphous small-molecule organic materials are utilized in organic light emitting diodes (OLEDs), with device performance relying on appropriate chemical design. Due to the vast number of contending materials, a symbiotic experimental and simulation approach would be greatly beneficial in linking chemical structure to macroscopic material properties. We review simulation approaches proposed for predicting macroscopic properties. We then present a library of OLED hosts, containing input files, results of simulations, and experimentally measured references of quantities relevant to OLED materials. We find that there is a linear proportionality between simulated and measured glass transition temperatures, despite a quantitative disagreement. Computed ionization energies are in excellent agreement with the ultraviolet photoelectron and photoemission spectroscopy in air measurements. We also observe a linear correlation between calculated electron affinities and ionization energies and cyclic voltammetry measurements. Computed energetic disorder correlates well with thermally stimulated luminescence measurements and charge mobilities agree remarkably well with space charge–limited current measurements. For the studied host materials, we find that the energetic disorder has the greatest impact on the charge carrier mobility. Our library helps to swiftly evaluate properties of new OLED materials by providing well-defined structural building blocks. The library is public and open for improvements. We envision the library expanding and the workflow providing guidance for future OLED material design.

TABLE OF CONTENTS

145

INTRODUCTION

In recent years, display and lighting technologies based on organic light emitting diodes (OLEDs) have steadily increased in popularity, from the automotive industry to smart phones and televisions. Not only do they offer improved image quality via a greater contrast ratio when compared with the liquid crystal display (LCD) technology, but the flexible and transparent possibilities of OLEDs make them an innovative choice in a competitive market. OLEDs usually comprise multiple layers of small organic molecules, sandwiched between two electrodes. Each layer is tailored for a specific functionality to facilitate balanced charge carrier injection and transport to the emissive layer, where the charge carriers recombine to form excitons and consequently photons, achieving a desirable wavelength of emission.[1–3]

One of the major advantages of using organic molecules is the possibility of manipulating chemical composition to target specific properties, such as emission color and charge carrier transport abilities. The aim of OLED material design is to achieve an optimal balance between stability, efficiency, operational driving voltage, and color coordinate of the device. However, molecular design often relies on chemical intuition and with a vast number of potential candidates for each of the layers, this approach is inherently flawed. Therefore, in order to optimize design a systematic approach which links chemical structure to macroscopic properties would be greatly beneficial.[4,5] Ideally, this would focus solely on *in silico* prescreening, prior to synthesis. Predictive computational modeling is, however, not yet sufficiently accurate for this task exclusively[6] and with experimental prescreening being an extensive and costly procedure, a collective experimental and *in silico* approach presents a favorable alternative.

The *in silico* evaluation of organic materials involves accurate prediction of device characteristics from the corresponding molecular building blocks, which requires simulations over a broad range of length and timescales. The multiscale simulation techniques, as depicted in Fig. 1, help us to establish links between microscopic and macroscopic material properties. Here, quantum chemical calculations are used to obtain gas-phase geometries of a neutral molecule, its cation and anion, as well as ionization energies and electron affinities. The material morphology is then simulated by molecular dynamics (MD), with classical force fields describing atomistic interactions. Polarizable force fields are then used to account for electrostatic effects upon charge/exciton transfer. Kinetic Monte Carlo (KMC) is then used to perform charge transport simulations, whereby it is possible to extract macroscopic observables, such as charge carrier mobilities, by solving the master equation.[5,7–13]

It is clear that the morphology is an integral part of the simulations, and it is often a challenge to generate morphologies representative of experimental systems. For this task, both the classical force fields and the more computationally demanding polarizable force fields have to be parameterized. Experimental input at this stage ensures the accuracy of the structural predictions using the classical force fields, while polarizable force fields can be parametrized from the first principles. The parametrization of these force fields is a tedious task and impossible for the vast number of organic compounds required for prescreening.[14–16] To overcome this, it is possible to use the similarities among the molecules most likely to be experimentally investigated, in order to create molecular fragments or building blocks, including the force field parameters. The concept of an extendable molecular library containing these well-defined building blocks required to generate realistic morphologies would then permit the swift characterization of new systems.

For this concept to be brought to a realization, a well-defined simulation workflow capable of predicting relevant system properties from the chemical structure, must first be approved. Therefore, the accuracy and reliability of the various simulation techniques of this workflow, is the subject of the present work. To establish a starting point, simulation results for 12 small organic molecules are summarized, the molecular structures of which are shown in Fig. 2. The individual steps of the simulation workflow are scrutinized and directly compared to experimental results for the glass transition temperature,
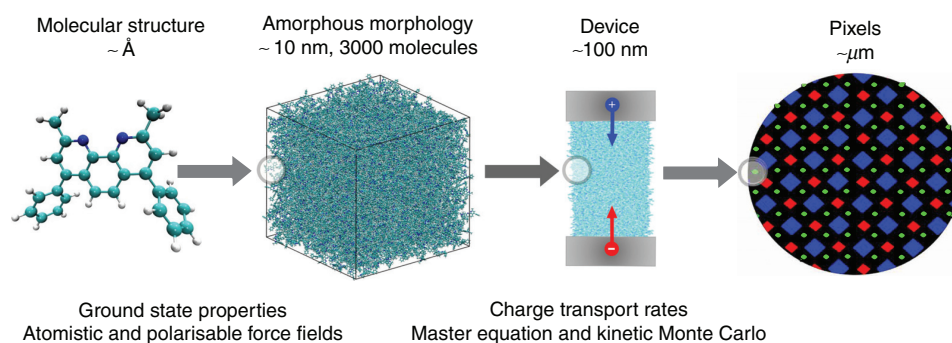
FIG. 1. OLED modeling multiscale simulation workflow. Starting from the first principles calculations of an isolated molecule, combined with atomistic force fields to generate the amorphous morphology, with the use of molecular dynamics. Polarizable force fields are used to account for the environmental effects on the density of states. Site energies, reorganization energies, and electronic coupling elements are computed, followed by the charge transfer rates. Kinetic Monte Carlo is used to solve the master equation, to study charge dynamics (e.g., carrier mobilities), giving macroscopic device characteristics.
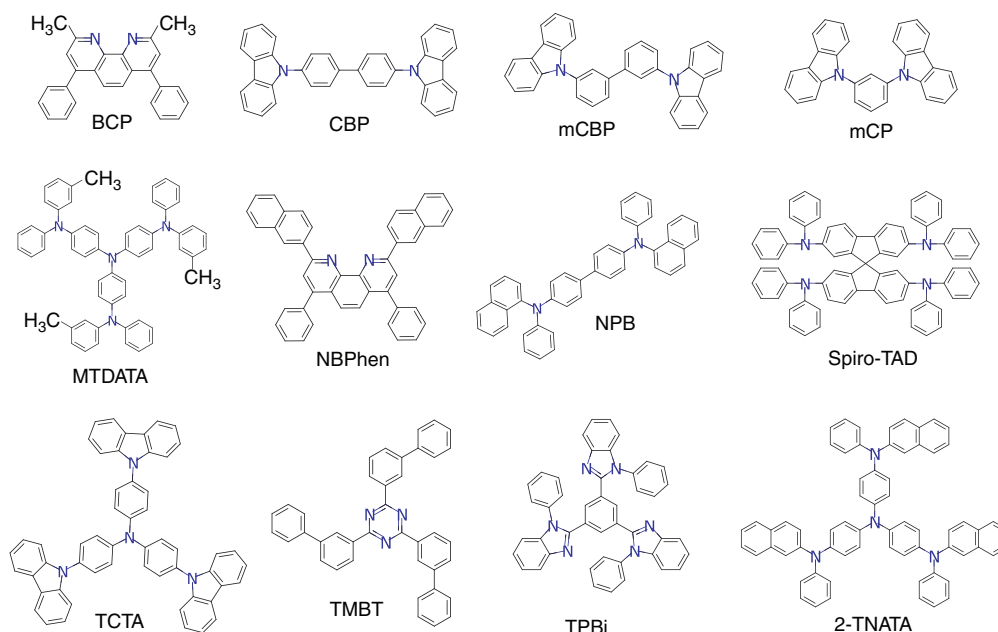
09 January 2025 14:14:36

FIG. 2. Chemical structures of the 12 small organic molecules investigated for the OLED material library: BCP, CBP, mCBP, mCP, MTDATA, NBPhen, NPB, TCTA, TMBT, TPBi, Spiro-TAD, and 2-TNATA.

energetic disorder, ionization energy in the solid-state, and charge carrier mobilities. By doing so, the outlined simulation workflow and the force fields used can be validated, allowing for the expansion of the library and further structures to be investigated.

While this review focuses on one multiscale simulation procedure, it is worth emphasizing that there are several different computational approaches for the consideration of organic semiconductors. One such method highlights the importance of using a fully quantum mechanical approach for charge dynamics to improve on semiclassical Marcus rates.[17] Quantum chemical methods can also be used for evaluating ground and excited state properties of organic electronic materials. However, standard DFT functionals can lead to errors surrounding localization and delocalization of electron and hole densities, prompting the use of tuned long-range corrected hybrid functionals.[18] Excited state properties have also been evaluated using many-body Green's function theory and GW approximation with the Bethe–Salpeter equation (GW-BSE).[19–24] In terms of charge transport, KMC has been used to study degradation and the sensitivity of OLED device lifetime and efficiency, in relation to material-specific parameters, to aid with design strategies with regard to energy levels.[25] Additionally, KMC models with molecular-level resolution have been developed for investigating organic field-effect transistors (OFETs).[26] Computational methods have also been used to investigate chiral composition–dependent charge mobilities, helping to link variations of molecular chirality to charge transport properties.[27] Multiscale simulations have also aided with the study of photoluminescence quenching mechanisms in phosphorescent OLEDs.[28] Therefore, it is clear that predictive multiscale protocols are essential in the search and the design of novel materials for organic electronic devices.[4]

GLASS TRANSITION TEMPERATURE

In addition to electronic properties, the thermal stability of an organic material is essential in determining its suitability to be used in OLED devices. To enhance the device's lifetime, materials which are less susceptible to thermal degradation are targeted, particularly making use of materials with a high glass transition temperature, T_g. When the device is operational, the flow of current results in Ohmic heating within the organic layers and due to this local heating, materials which have a low T_g experience a higher degree of molecular vibrations[29] and chemical decomposition, resulting in lower stability. Furthermore, high T_g also prevents morphology changes during postprocessing of devices, like unwanted partial re-crystallization. Therefore, accurate predictions of the T_g value for OLED materials can serve as a method of screening thermally stable candidates. The T_g for the 12 organic materials was obtained by MD simulations, as outlined in the Methods section, the values are listed in Table I, and the comparison to experimental values is shown in Fig. 3. The experimental values are listed as referenced values from previous studies, or as new experimental values obtained by differential scanning calorimetry (DSC), as outlined in the Methods section.

The simulation results show a systematic overestimation of T_g for all systems, in comparison to the experimental values, except for TMBT. This overestimation is expected as the process of obtaining the simulated morphologies, outlined in the Methods section, involves thermal annealing above T_g, followed by a fast-cooling process. The simulated morphologies often disagree with experiment, as the cooling rates are much faster in simulation compared to experiment and reproducing the realistic molecular packing requires long simulation times. Additionally, the relaxation times of typical OLED depositions

TABLE I. Glass transition temperature (T_g): Comparison between simulation and experiment, including referenced literature (experimental) values for the 12 systems. For BCP, the T_g was not detectable (ND) experimentally, as there was no significant kink in calorimetric measurements.

System	T_g (°C)		
	Simulation	Experiment	Literature
BCP	143.6	ND	89[30]
CBP	133.0	115	109[29]
mCBP	155.3	93.1	97[31]
mCP	140.3	66	60[32]
MTDATA	164.7	78	75[33]
NBPhen	238.2	· · ·	105[34]
NPB	166.9	99.5	98[32]
Spiro-TAD	217.6	135	133[35]
TCTA	184.7	154	151[33]
TMBT	68.5	57	95[36]
TPBi	204.8	· · ·	127[37]
2-TNATA	212.2	· · ·	110[38]

cannot be achieved by the slow molecular dynamics close to T_g. Furthermore, the deposition conditions can have a significant impact on molecular orientation,[39,40] such that experimental T_g values may also show variation, particularly for systems with low T_g, for example TMBT or also BCP, where T_g was not detectable (as there was no significant kink in calorimetric measurements, described in the Methods section) despite a previously reported value in the literature.[30] For some of the compounds, such as TMBT, it is known that vacuum deposition leads to molecular alignment, i.e., molecular orientations are not random. This effect is not accounted for in our outlined protocol, as it is difficult to reproduce in simulations; large timescales are
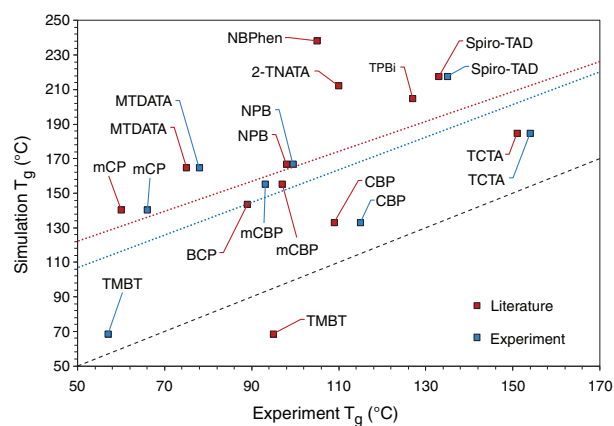
FIG. 3. Comparison of simulation and experiment T_g values (blue) with linear correlation (blue dashed line) $R^2 = 0.53$. Experimental values found in the literature are also compared (red) with linear correlation (red dashed line) $R^2 = 0.22$. The linear relationship ($x = y$) is shown by the black dashed line.

necessary to cover the diffusion process of evaporated materials, mimicking experimental film-growth rates of 1 Å/s.[39,41,42]

In order to accurately predict the glass transition temperature from the morphology, it is clear that slower deposition rates must be employed, for example with simulation methods such as coarse graining.[39,43] An alternative to predict T_g for OLED materials is a quantitative structure–property relationship approach,[44] with the use of topological indices[45] and various descriptors. However, this only allows to interpolate within known chemical space. Despite the inaccurate prediction of the T_g values, the proceeding simulation results will show that this does not have a significant impact on the charge transport simulations and mobilities for the materials in this study.

CHARGE TRANSPORT

In disordered organic materials, due to weak intermolecular coupling[46] and relatively large energetic disorder, the charges are localized and propagate by a successive hopping process from one molecule in the system to the next. The hopping rate between two sites in a material is characterized as a thermally activated transport process, where the rate can be expressed in terms of the Marcus rate equation,[47–49]

$$\omega_{ij} = \frac{2\pi}{\hbar} \frac{J_{ij}^2}{\sqrt{4\pi\lambda_{ij}k_B T}} \exp\left[-\frac{\left(\Delta E_{ij} - \lambda_{ij}\right)^2}{4\lambda_{ij}k_B T}\right]. \tag{1}$$

Here T is the temperature, k_B is Boltzmann's constant, λ_{ij} is the reorganization energy, J_{ij} is the electronic coupling matrix element, and $\Delta E_{ij} = E_i - E_j$ is the driving force or site energy difference between two neighboring sites, where E_i is the site energy of molecule i.[50] The site energy includes the internal molecular energy (E_i^{int}) and interaction with the environment, including the electrostatic (E_i^{elec}) and induction (E_i^{ind}) contributions. It is calculated as $E_i = E_i^{int} + E_i^{elec} + E_i^{ind} + q\mathbf{F} \cdot \mathbf{r}_i$, where q is the hopping carrier charge, $\mathbf{F}$ is an applied external field, and $\mathbf{r}_i$ is the center-of-mass of molecule i.[5] For computational efficiency, here we use the Marcus rate expression; the entire scheme can be also adapted to the quantum treatment of vibrational modes.[17] The microscopic quantities, such as reorganization energy, electronic coupling, etc., are computed from first principles and serve as an input to the master equation, the solution of which gives charge carrier mobilities.[51,52]

The methodology of obtaining the reorganization energies and electronic coupling elements is described in the Methods section. The reorganization energies for each material are listed in Table S1 and electronic coupling elements are shown in Fig. S1, of the supplementary material. Even though the variations of the reorganization energies and electronic coupling elements lead to variations in the simulated mobility, μ, the most significant parameter is the distribution of site energies E_i within the system, characterized by the energetic disorder σ. To a certain extent, this is anticipated, as the mobility is exceptionally sensitive to changes in the width of the disorder distribution, for example, $\mu \propto \exp[-C\left(\frac{\sigma}{k_B T}\right)^2]$.[53–55] The energetic disorder stems from the disorder on the local electronic states which, as we will see in Fig. 4, is Gaussian-distributed.

DENSITY OF STATES

To evaluate the site energies of holes and electrons in the 12 systems, a perturbative scheme was used, as outlined in the Methods section. The distributions of the on-site energy differences, i.e., the differences between the energies of the system when a selected molecule
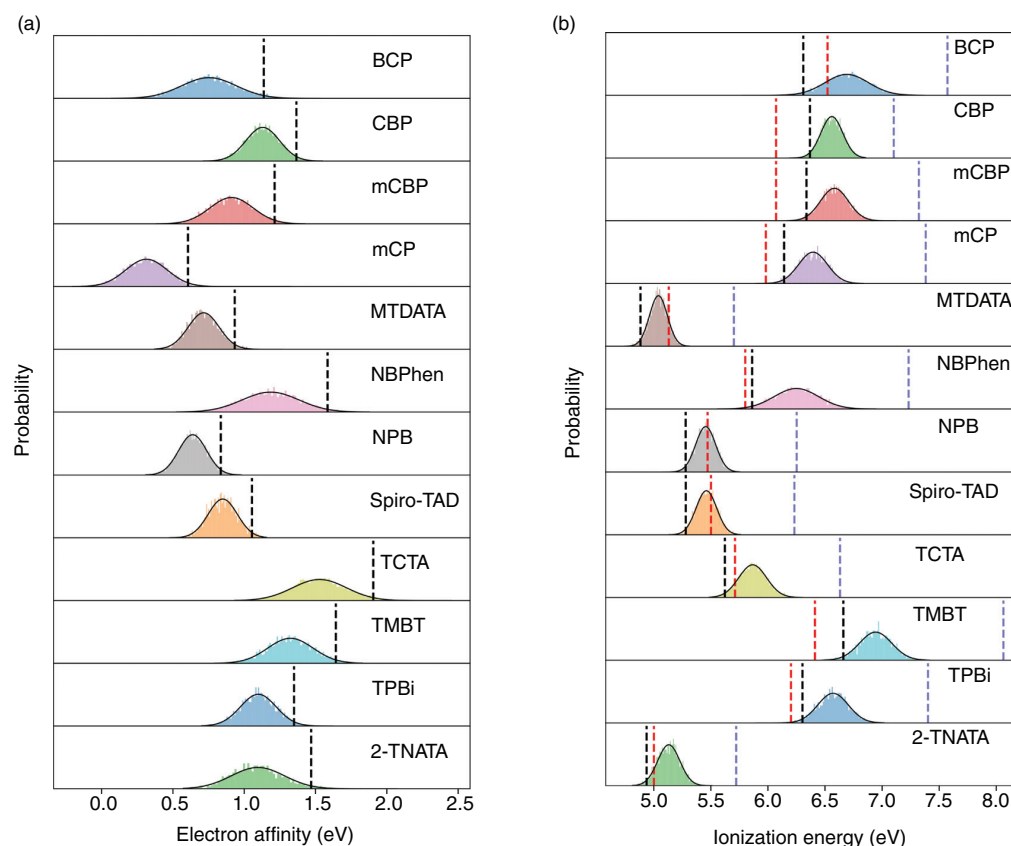
09 January 2025 14:14:36

FIG. 4. The density of states (distribution of site energies) in the amorphous materials for (a) anion, with solid-state electron affinity (EA$_{tot}$) shown by the black dashed lines, and (b) cation, with solid-state ionization energy (IE$_{tot}$) shown by the black dashed lines. Experimental reference lines for ionization energy (IE$_{exp}$) are shown as red dashed lines. Gas-phase ionization energy (IE$_0$) values obtained by M062X/6–311+g(d,p) level of theory are shown using blue dashed lines.

is in the anionic/cationic or neutral state, including the constant internal contribution due to the gas-phase electron affinity/ionization potential, are displayed in Figs. 4(a) and 4(b) for electrons and holes, respectively.

The corresponding energetic disorder (widths of site energy distributions) are summarized in Table II. In amorphous organic materials, the energetic disorder is predominantly electrostatic; such electrostatic interaction originates from the potential exerted on a molecule from its specific environment. Therefore, the disorder is governed by the molecular static multipoles, as well as the positional and conformational order in a given material. On the other hand, the induction contribution stemming from the interaction of microscopic dipoles (the distributions of the electrostatic potential in the ground state are shown in Fig. S2 of the supplementary material) with the localized charge carrier, reduces the energetic disorder.[13,56] The electrostatic and induction contributions for each system, for both electrons and holes, are listed in Table II.

Apart from energy distributions, the long-range electrostatic interactions of a charge with molecular dipoles can lead to spatial *correlations* of site energies.[55,57] To unveil such spatial correlations, we computed these correlations for holes and electrons, which are shown in Fig. S3 of the supplementary material. We found that the hole and electron site energy correlations extend up to 2–3 nm. The correlations exhibit a decay profile with distance, approximately following the r^{-1} signature expected for the random dipolar disorder.[55] Therefore, all of these materials possess a correlated disorder even though their ground state dipole moments are small for a large set of molecules. We now analyze in more detail ionization energies, electron affinities, and the widths of the DOSs, which we consider to be the most important parameters for charge transport.

ELECTRON AFFINITY AND IONIZATION ENERGY

The gas-phase electron affinities (EA$_0$) and ionization energies (IE$_0$) were calculated using density functional theory at the M062X/6–311g(d,p) as well as IP/EA-EOM-DLPNO-CCSD/aug-cc-pVTZ level of theories, as described in the Methods section and in the supplementary material. The comparison of EA$_0$ and IE$_0$ obtained at various levels of theory is shown in Figs. S4–S6 (see also Table S2) of the supplementary material. In inverse photoemission spectroscopy (IPS)

TABLE II. (Top) energetic disorder (σ, eV) for electron transport and electronic affinities (EA, eV) and (bottom) energetic disorder (σ, eV) for hole transport with experimental values (eV) and ionization energies (IE, eV) in the studied amorphous materials, with experimental values (eV) and references, where available. SCLC: space charge–limited current, TSL: thermally stimulated luminescence, UPS: ultraviolet photoelectron spectroscopy, PESA: photoemission spectroscopy in air.

System	$\sigma_{electron}^{sim}$	EA_0	EA_{elec}	EA_{ind}	EA_{tot}
			EA_{sim}		
BCP	0.192	0.39	−0.30	0.66	1.14
CBP	0.118	0.45	0.003	0.68	1.37
mCBP	0.151	0.41	−0.19	0.69	1.21
mCP	0.145	−0.27	−0.22	0.80	0.61
MTDATA	0.109	−0.11	−0.12	0.95	0.93
NBPhen	0.200	1.04	−0.43	0.58	1.58
NPB	0.098	0.12	−0.21	0.73	0.83
Spiro-TAD	0.102	0.29	−0.13	0.69	1.05
TCTA	0.189	0.08	0.01	1.43	1.90
TMBT	0.159	0.98	−0.36	0.70	1.64
TPBi	0.125	0.59	−0.18	0.69	1.35
2-TNATA	0.187	0.16	−0.10	1.04	1.47

System	σ_{hole}^{sim}	σ_{hole}^{exp}		IE_0	IE_{elec}	IE_{ind}	IE_{tot}	IE_{exp}	
					IE_{sim}				
BCP	0.190			7.57	0.29	0.59	6.31	6.52/6.5	PESA/UPS[58–60]
CBP	0.096	0.125/0.10	TSL/SCLC[61]	7.10	−0.05	0.59	6.37	6.07/6.1	PESA/UPS[62–64]
mCBP	0.122	0.131	TSL	7.32	0.09	0.65	6.34	6.07/6.1	PESA/UPS[62]
mCP	0.127	0.140	TSL	7.38	0.21	0.77	6.14	5.98/5.9	PESA/UPS[60]
MTDATA	0.079			5.70	0.12	0.54	4.88	5.13	PESA
NBPhen	0.194	0.167	TSL	7.23	0.43	0.55	5.86	5.8	UPS[65]
NPB	0.087	0.088/0.09	TSL/SCLC[61]	6.25	0.20	0.60	5.28	5.47/5.4	PESA/UPS[58,63]
Spiro-TAD	0.090	0.110/0.09	TSL/SCLC[61]	6.23	0.15	0.62	5.28	5.50	PESA
TCTA	0.122	0.110/0.10	TSL/SCLC[61]	6.63	−0.02	0.79	5.62	5.71/5.7	PESA/UPS[62,66]
TMBT	0.141			8.06	0.35	0.77	6.66	6.41	PESA
TPBi	0.134	0.150	TSL	7.40	0.17	0.66	6.30	6.2	UPS[64]
2-TNATA	0.097	0.10	SCLC[61]	5.72	0.09	0.50	4.94	5.0	UPS[63]

and ultraviolet photoelectron spectroscopy (UPS), the electron affinity and ionization energy are measured as an onset of the spectra. In simulations, to account for the finite width of the density of states (σ), the solid-state electron affinities (EA_{tot}) and ionization energies (IE_{tot}) were shifted by 2σ, such that $EA = \alpha + 2\sigma$ or $IE = \alpha - 2\sigma$, where α represents the mean of the DOS for electrons or holes, respectively. The EA_{tot} and IE_{tot} values are summarized in Table II for each material. Experimental ionization energies are also listed in the table and shown in Fig. 4(b), for comparison. Further to this, the comparison of solid-state IE values to the corresponding experimental values are shown in Fig. 5. The method of obtaining IE values by photoelectron yield spectroscopy in air (PESA) is described in the Methods section, the UPS values are taken from the literature, with references included in Table II. Both gas-phase and solid-state ionization energies are compared to PESA and UPS values in the supplementary material,

shown in Fig. S7. Additionally, the gas-phase and solid-state ionization energies and electron affinities are compared to experimental cyclic voltammetry (CV) data, shown in Fig. S8 of the supplementary material, where the experimental method is also described.

The IE values obtained from the DOS of the various materials are in good agreement with the experimental IE values, as depicted in Fig. 4(b) for the individual systems and Fig. 5 as the total correlation. The computed IE_{tot} values are a combination of the gas-phase IE_0 as well as the electrostatic and induction contributions. This is necessary as the gas-phase IE is for a single isolated molecule and does not account for the solid-state effects required to accurately determine electronic properties. Interestingly, as shown in Fig. S7 of the supplementary material, the linear correlation to experimental solid-state values is already reproduced from the gas-phase simulations, however, with a proportionality coefficient
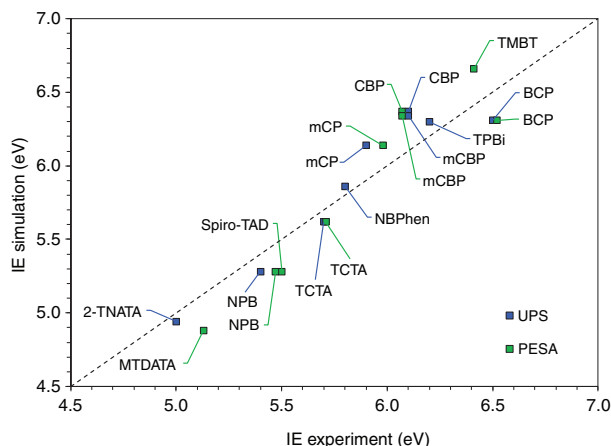
FIG. 5. Simulated solid-state ionization energies (IE$_{tot}$) compared to experimental values obtained by UPS: $R^2 = 0.898$ (blue) and PESA: $R^2 = 0.900$ (green). The linear relationship ($x = y$) is shown by the dashed line.
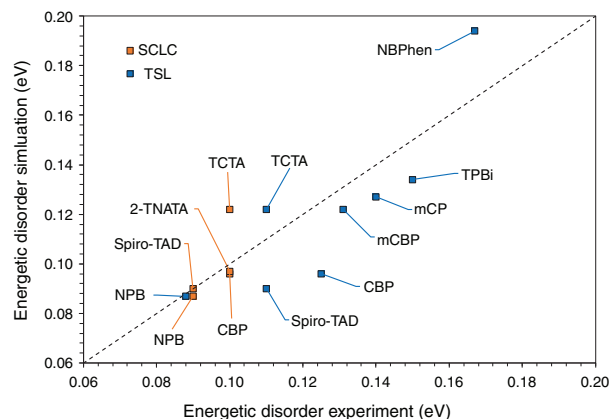

FIG. 6. Simulated and experimental energetic disorder (eV) values for the studied systems. SCLC (orange squares) and TSL (blue squares; $R^2 = 0.736$). The linear relationship ($x = y$) is shown by the black dashed line, highlighting the correlation of experimental and simulated values.

different from unity. The agreement of the computed (IE$_{tot}$) and experimental IE values signifies a reasonable degree of accuracy of the polarizable force fields.

The method deployed in the present work also enables the distinction of different contributions to the EA and IE, e.g., gas-phase, electrostatic, and induction, shown in Table II. For all compounds, the stabilization due to induction (E_{ind}) contributes around 0.5–0.8 eV and 0.6–1.4 eV for holes and electrons, respectively. On the other hand, the electrostatic contribution (E_{elec}) varies from one system to another (0.01–0.4 eV for both holes and electrons) governed by the distribution of molecular dipoles in a given system. A closer scan of the numbers in electrostatic contribution (E_{elec} in Table II) reflects a salient correlation between energetic disorder and electrostatic interactions for molecules such as NBPhen, TMBT, and BCP possessing large charge-dipole interaction. Here, the magnitudes of E_{elec} are almost two times higher than the rest of the materials, as well as the higher σ values, shown for both holes and electrons.

The energetic disorder for hole transport for each material is taken as the width of the DOS in simulations. These values are directly compared in Fig. 6 to experimental values from previously reported space charge–limited current (SCLC) measurements,[61] and/or newly carried out thermally stimulated luminescence (TSL) measurements. Details of the SCLC measurements can be found in Ref. 61, and the TSL measurements are described in the Methods section. The simulations predict a significant variation of the energetic disorder among these materials which features an almost twofold change spanning from $\sigma = 0.09$ eV observed for a weakly disordered NPB, to $\sigma = 0.19$ eV obtained for highly disordered NBPhen. The experimental results demonstrate a remarkably similar trend (Fig. 6), which testifies to the intrinsic nature of the large width of the DOS ($\sigma > 0.1$ eV) observed experimentally in most of these OLED materials, implying the DOS of a chemically pure disordered material rather than being significantly affected by impurity-related traps. The energetic disorder inferred from TSL normally provides the DOS of shallower trapped carriers, which are thermally released and recombine with the more

deeply trapped counter charges. This is because TSL is an electrode-free technique, so the number of electrons and holes in the film is always the same to maintain the material neutrality at any time after the carriers were photogenerated. Once a shallower trapped carrier is released from its trap, it will recombine with its deeper trapped counterpart. Therefore, the latter sort of carriers is expected to already be completely annihilated, and there are simply no carriers left at a temperature relevant to their anticipated release from their deeper states.

The ionization energies of most of the materials measured in this study are less than, or around 6 eV (Table II). Therefore, their hole DOS should not be affected much by extrinsic traps, as the IE values fall within an energy window, inside which organic semiconductors normally do not experience charge trapping.[67] Materials with an ionization energy above 6 eV will exhibit trap-limited hole transport, similarly, an electron affinity lower than 3.6 eV will cause electron trapping to limit electron transport.[67] As the materials in this study have electron affinities significantly less than 3.6 eV (Table II) shown by simulations, the electron transport in these systems is most likely hindered by electron trapping (as oxygen-related traps). Due to this reasoning and taking into account that all samples were exposed to air prior to TSL measurements, which makes relatively deep electron traps unavoidable, our TSL measurements probe the hole DOS in these materials. Although the simulated σ-parameters for holes and electrons (Table II) are not appreciably different, it should be mentioned that TSL measures the "effective DOS" and even a small concentration of shallow extrinsic traps (depending on the trap depth it can even be at trap concentration level of ~0.1%) can give rise to a notable DOS broadening. This has been previously demonstrated by deliberate doping of photoconductive polymers with traps.[68] Since the IE of CBP, mCBP, and TPBi slightly exceeds the trap-free window threshold value of 6 eV, a certain extrinsic hole trapping cannot be excluded here. This can explain why TSL measurements for these materials yield slightly overestimated energetic disorder parameters, compared to the simulated values (Fig. 6).

Finally, we comment on some differences in σ-parameters determined by SCLC and TSL techniques observed for some materials, e.g.,

09 January 2025 14:14:36

151

for CBP. This may be partially due to different film morphologies related to different film deposition techniques used: while films for SCLC measurements were vacuum-deposited, most of the materials for TSL measurements were spin-coated from a solution, except NPB, TCTA, and Spiro-TAD, which were vacuum-deposited. Another likely reason might be due to the fact that the SCLC probes the DOS in a large-carrier-concentration transport regime, for which deep tail states of the DOS (and/or traps) might be filled with carriers during the measurements and therefore, JV-characteristics might be governed mostly by a shallower portion of the DOS. On the other hand, carrier concentration in TSL experiments is significantly smaller (comparable to time-of-flight experiments) and deep tail states can be well probed by this technique.

One can also attempt to relate the observed energetic disorder to molecular dipoles, since lattice models with randomly oriented dipoles of equal magnitude d and lattice spacing a, yield disorder $\sigma \sim d/a$. However, in a realistic morphology, both distances and dipoles can vary from molecule to molecule, which then increases the disorder further. It is evident from the distributions in Fig. S9 that the dipole moments of individual molecules in an amorphous morphology vary significantly from their equilibrium values (see Table S3 of the supplementary material). Such broad distributions of dipole moments are attributed to the presence of one or more soft dihedrals in the organic materials. At finite temperature, rotation around such soft degrees of freedom leads to multiple conformers. In general, systems with a narrow distribution of molecular dipoles in their amorphous morphologies possess small fluctuations of electrostatic multipoles in the amorphous matrix which results in smaller energetic disorders. This conclusion is, however, not universal since large *local* electrostatic

potential variations of TMBT, for example, can result in a sizable disorder despite a zero *molecular* dipole moment. The correlation of average dipole moment and energetic disorder for the 12 systems are shown in Fig. S10 of the supplementary material, for both holes and electrons. Although there is a slightly better correlation for holes compared to electrons, a number of outliers remain for both, implying that it is difficult to predict the trend in sigma, solely from the molecular dipole moment.

CHARGE CARRIER MOBILITY

Charge transport rates were computed using the high temperature limit of classical charge transport theory[47–49] as given by the Marcus rate equation. The master equation can then be solved with kinetic Monte Carlo (KMC), providing the time evolution of the system, giving a randomly generated trajectory of charge carrier movement. This was carried out for one charge carrier (hole or electron) in the presence of an applied electric field ($F = 1 \times 10^4$ V/cm), using a periodic simulation box. Mobilities were extracted as outlined in the Methods section. The extrapolated dependence of mobility on temperature is shown in Fig. S11 and Fig. S12 of the supplementary material, for holes and electrons, respectively. The single-carrier mobilities at room temperature for holes and electrons are summarized in Table III. The experimentally measured mobility and the corresponding experimental techniques used, are also listed for comparison.

Table III and Fig. 7 show the correlation between simulated and experiment mobility. The remarkable agreement of simulation and experiment is particularly evident for hole mobilities. On the other hand, for electron mobilities, a larger deviation is observed between experiment and simulation, where simulated results indicate a

TABLE III. Room temperature hole and electron mobility (cm²/V s), achieved from simulations of the amorphous organic materials, with experimentally achieved mobilities and the corresponding techniques used, references included. TOF: time-of-flight experiment, SCLC: space charge–limited current method.

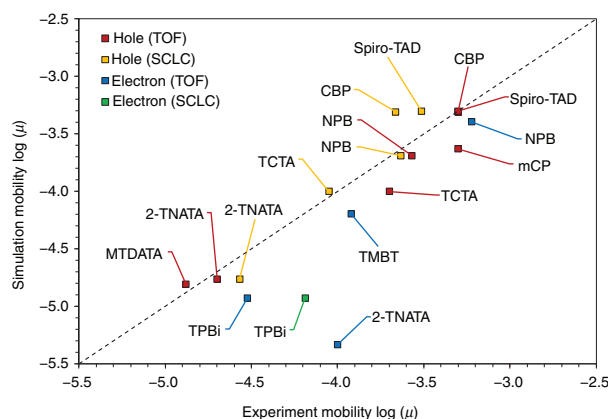| System	$\mu_{hole}^{(sim)}$	$\mu_{hole}^{(exp)}$		$\mu_{electron}^{(sim)}$	$\mu_{electron}^{(exp)}$	
BCP	6.42×10^{-11}	$\cdots$	$\cdots$	6.59×10^{-9}	$\cdots$	$\cdots$
CBP	4.91×10^{-4}	2.2×10^{-4}	SCLC[61]	3.64×10^{-5}	$\cdots$	$\cdots$
		5.0×10^{-4}	TOF[69]			
mCBP	9.00×10^{-4}	$\cdots$	$\cdots$	8.24×10^{-5}	$\cdots$	$\cdots$
mCP	2.35×10^{-4}	5.0×10^{-4}	TOF[70]	1.35×10^{-7}	$\cdots$	$\cdots$
MTDATA	1.56×10^{-5}	1.3×10^{-5}	TOF[71]	8.17×10^{-6}	$\cdots$	$\cdots$
NBPhen	2.41×10^{-11}	$\cdots$	$\cdots$	6.22×10^{-10}	$\cdots$	$\cdots$
NPB	2.04×10^{-4}	2.3×10^{-4}	SCLC[61]	4.04×10^{-4}	$(6–9) \times 10^{-4}$	TOF[58]
		2.7×10^{-4}	TOF[71]			
Spiro-TAD	4.99×10^{-4}	3.1×10^{-4}	SCLC[61]	3.67×10^{-5}	$\cdots$	$\cdots$
		5.0×10^{-4}	TOF[72]			
TCTA	1.00×10^{-4}	8.9×10^{-5}	SCLC[61]	1.61×10^{-9}	$< 10^{-8}$	Ref. 74[a]
		2.0×10^{-4}	TOF[73]			
TMBT	7.47×10^{-6}	$\cdots$	$\cdots$	6.38×10^{-5}	1.2×10^{-4}	TOF[75]
TPBi	1.18×10^{-7}	$\cdots$	$\cdots$	1.18×10^{-5}	6.5×10^{-5}	SCLC[76]
					$(3–8) \times 10^{-5}$	TOF[77]
2-TNATA	1.72×10^{-5}	2.7×10^{-5}	SCLC[61]	4.64×10^{-6}	$(1–3) \times 10^{-4}$	TOF[58]
		$(2–9) \times 10^{-5}$	TOF[58]			

[a]Not measurable by TOF.

FIG. 7. Room temperature hole and electron mobility (μ) values achieved by simulation and compared to experiment values where available. Hole-TOF (red): $R^2 = 0.95$ and hole-SCLC (yellow): $R^2 = 0.94$; electron-TOF (blue): $R^2 = 0.64$ and electron-SCLC (green). The linear relationship ($x = y$) is shown by the black dashed line, highlighting the correlation of experimental and simulated values.

systematic underestimation of experimental measurements. There are several possible explanations to account for these discrepancies. First, due to the much larger energetic disorder for electrons in certain materials (Table II) when compared to holes, the electron mobility will be inherently lower. As a result of the large disorder found in 2-TNATA, the simulated and experimental mobilities show large variation. This may stem from energetic traps in the simulated morphology, which can lead to lower mobility values. To highlight the significant role of energetic disorder on the simulated mobility, a correlation plot is shown in Fig. 8, for both holes and electrons.

Due to different morphologies, the structural and energetic disorder can differ significantly between simulation and experiment. Despite the reasonable agreement for energetic disorder for hole transport, shown in Fig. 6, the experimental systems used for the mobility correlation are a collection of referenced values from various studies, with potentially significant variations in disorder.

It should also be noted that the simulated morphologies for the 12 systems do not account for the presence of carrier traps formed by structural defects or impurities such as water, which are typically unavoidable in reality. However, the inclusion of carrier traps in the simulated morphology would, in fact, lead to larger deviation between simulated and experimental mobilities. As previously stated, hole or electron transport have been shown to become trap-limited in materials with an IE greater than 6 eV or an EA less than 3.6 eV, respectively.[67] Therefore, direct comparison of simulation and experiment mobilities may be difficult when considering low EA and high IE materials.

Finally, the takeaway message here is that the width of the density of states is the key property in determining the mobility (Fig. 8). Hence, accurate predictions of the DOS should be given priority when prescreening OLED hosts. DOS width correlates with some extent with the molecular dipole, but this correlation has too many outliers, e.g., due to conformational freedom or higher order multipoles and therefore, cannot be used as a reliable descriptor for mobility predictions.
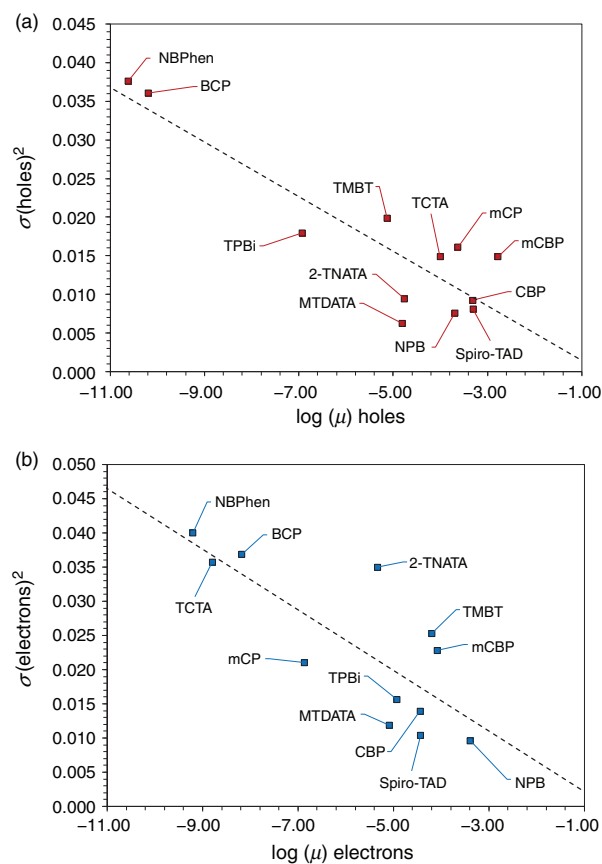
FIG. 8. Correlation of simulated mobility (μ) and energetic disorder (σ) for (a) holes and (b) electrons. The dashed lines are lines of best fit for the corresponding data, to serve as a visual aid.

OUTLOOK

It is clear that a molecular library of OLED hosts would be invaluable, permitting the swift evaluation of new materials. The key question is how accurately and reliable a combination of various simulation techniques can predict relevant material properties, to bring pre-screening a step closer.

For the simulated morphological properties, the T_g comparison showed large variation to experimental values, suggesting that the current approach needs to be improved for accurate evaluation of thermally stable materials. Reliable methods for predicting T_g and accurate atomistic force fields are the key improvements required for more accurate simulation results.

The morphologies used for charge transport simulations revealed that the inaccuracies in T_g predictions had no significant impact on simulated ionization energies. In this respect, PESA measurements and UPS data taken from the literature, as well as cyclic voltammetry measurements, are in an excellent agreement with simulation results, supporting our confidence in the polarizable force fields used for evaluation of the solid-state electrostatic contribution. The situation is

09 January 2025 14:14:36

somewhat different for electron affinities, where using different computational techniques led to large variation of the gas-phase electron affinity values, even at a computationally affordable variation of the coupled cluster implementation. Moreover, there is no clear benchmark possible for the solid-state because of the sparse availability of the inverse photoemission spectroscopy measurements.

Accurate solid-state energetics allowed us to predict the density of states which, when compared to the thermally stimulated luminescence measurements, showed a similar trend. The energetic disorder can be potentially correlated with the distribution of molecular dipoles, but the extent of this will require further investigation to be conclusive.

Finally, the simulated charge carrier mobility showed a remarkable agreement with experimental values, particularly for hole transport where energetic disorder is typically lower. The accurate prediction of energetic disorder is therefore vital, as it has a significant impact on mobility.

Overall, the correlation of simulation and experimental results has been used to validate the accuracy of the force fields and the simulation methods, as an initial step toward building a larger molecular library. The agreement of simulation and experiment for the various parameters, particularly mobility, highlights the predictive capability of the outlined methods and the simulation workflow. The next step is to expand this library with further materials, in an effort to draw structure-property conclusions for effective prescreening.

METHODS

Gas-phase ionization energy and electron affinity

For the isolated molecules, density functional theory (DFT)–based electronic structure methods were used to compute gas-phase ionization energy (IE_0) and electron affinity (EA_0) using the Gaussian09 program.[78] For this, the neutral molecule in the neutral geometry (E_{nN}), as well as the charged molecule in the charged geometry (E_{cC}), are computed. The IE_0 and EA_0 values are then calculated as $E_{cC} - E_{nN}$, where E_{cC} represents the cationic and anionic state, respectively.

The prediction of accurate IEs and EAs remain a challenge in electronic structure theory, primarily due to the self-interaction error[79] (SIE) or localization/delocalization[80] error, inherent to commonly used DFT functionals. In a series of recent reports,[18,81–84] the importance of considering long-range corrected hybrid functionals has been demonstrated, such that the SIEs in DFT description of molecules can be reduced. Therefore, adiabatic IE_0 and EA_0 calculations were performed by employing a range of DFT functionals: PBEPBE, B3LYP, CAM-B3LYP, ωB97X-D, M062X, and LC-ωPBE, combined with the basis set 6–311+g(d,p). The IEs and EAs are compared for each of the 12 organic molecules and each DFT functional, as shown in Fig. S4 of the supplementary material. Different levels of theory are also compared in Fig. S5 and Fig. S6.

It is evident that calculations performed using PBEPBE and B3LYP underestimate IE_0 compared to other functionals, an observation which is attributed to an underestimation of Kohn–Sham eigenvalue by hybrid functionals, leading to significant overscreening of the Coulomb interaction. Overall, the IE_0 is better predicted than the EA_0 for the given molecules. This is clear when comparing the Cam-B3LYP, ωB97X-D, and M062X functionals, as there is greater variation in the EA_0 prediction. The small deviation among these functions, with regard to the IE_0, makes any of the three a suitable choice

(M062X is the chosen functional for comparison to experimental IE and EA values in this study).

Molecular dynamics

DFT methods were then used to accurately parameterize the empirical OPLS-AA force field,[14–16] for the 12 chemically diverse molecules. All Lennard–Jones parameters were taken from this force field in combination with the fudge-factor of 0.5 for 1–4 interactions. Atomic partial charges were computed using the ChelpG[85] scheme for electrostatic potential fitting as implemented in Gaussian09,[78] employing the ground state electrostatic potential determined at the B3LYP/6–311+g(d,p) level of theory.

In order to generate amorphous morphologies, molecular dynamics (MD) simulations were carried out using the GROMACS simulation package.[86,87] The amorphous state was generated by an annealing step, followed by a rapid quenching to lock the molecules in a local energy minimum. This procedure has been previously applied for the preparation of amorphous structures of OLED materials.[61,88] The starting configurations used in the MD simulations were prepared by randomly arranging 3000 molecules in a simulation box using the Packmol program.[89] These initial structures were energy-minimized using the steepest-descent method and annealed from 300–800 K, followed by fast quenching to 300 K. Further equilibration for 2 ns and 1 ns production runs were performed at 300 K. All simulations were performed in the NPT ensemble using a canonical velocity rescaling thermostat,[90] a Berendsen barostat for pressure coupling,[91] and the smooth particle mesh Ewald technique for long-range electrostatic interactions. A time step of 0.005 ps was used to integrate the equations of motion. Non-bonded interactions were computed with a real-space cutoff of 1.3 nm.

To obtain the glass transition temperature of each material, a similar procedure was carried out with a time step of 0.001ps. The material was first equilibrated at 800 K, followed by gradual cooling to 0 K at a rate of 0.1 K/ps. The change in density as the material was cooled was used, in combination with two linear fits (the linear fitting procedure is described in the supplementary material) to extract the intersection point, giving the T_g value.

Density of states

We used MD simulation trajectories to evaluate the site energies of holes and electrons by employing a perturbative scheme. In this approach, the electrostatic and induction energies are added to the gas-phase energies (IE_0 or EA_0), to obtain the total site energy. The electrostatic contribution is calculated with the use of Coulomb sums based on distributed multipoles (obtained from the GDMA program[92]) for neutral and charged molecules in their respective ground states. The polarization contribution is computed using a polarizable force field based on the Thole model[93,94] with isotropic atomic polarizabilities (α_{ai}) on atoms a in molecules i. Aperiodic embedding of a charge method[95] as implemented in the VOTCA[13,43] package, was used for these calculations.

Coupling elements

The transfer integral or coupling elements, $J_{ij} = \langle \phi^i | \hat{H} | \phi^j \rangle$, represent the strength of the coupling of the two frontier orbitals $|\phi^i\rangle$ and $|\phi^j\rangle$ localized on each molecule in the charge transfer complex. It

is highly sensitive to the characteristic features of the frontier orbitals as well as the mutual orientations of the two molecules and follows an exponential decay with distance. The electronic coupling elements shown Fig. S1 of the supplementary material, were computed for each neighboring molecular pair (ij) using a projection method.[96,97] Molecular pairs were added to the neighbor list, with a center-of-mass distance cutoff (between rigid fragments) of 0.7 nm. These calculations were performed at PBEPBE/6–311+g(d,p) level of theory using the Gaussian09[78] and VOTCA[13,43] packages. The frozen core approximation was used with the highest occupied molecular orbitals providing a major contribution to the diabatic states of the dimer.

Reorganization energies

The reorganization energy of the system takes into account the charging and discharging of a molecule. When a charge moves from molecule i to molecule j, there is an intramolecular contribution (λ_{ij}^{int}), due to the internal reorganization of the two molecules and an intermolecular, known as an outersphere contribution (λ_{ij}^{out}), due to the relaxation of the surrounding environment.[13,50] The internal reorganization energy is calculated as $\lambda_{ij}^{int} = (U_i^{nC} - U_i^{nN}) + (U_j^{cN} - U_j^{cC})$, for molecule i and j, where the lowercase represents the neutral (n) or charged (c) molecule and the uppercase represents the neutral (N) or charged (C) geometry. The reorganization energies are summarized for holes and electrons in Table S1 of the supplementary material, for each of the systems. The individual contributions were calculated by DFT using the B3LYP/6–311+g(d,p) level of theory. In the current work, we ignore the outersphere contribution to the reorganization energy, since in the amorphous solids considered here, the Pekar factor is on the order of 0.01,[13] leading to a relatively small contribution to the total reorganization energy.

Mobilities

Mobilities were extracted as $\mu = \langle v \rangle / F$, where $\langle v \rangle$ is the average projection of the carrier velocity in the direction of the field ($F = 1 \times 10^4$ V/cm). The convergence of simulated mobilities with respect to the system size (i.e., a sufficient number of sites for the simulated transport to be nondispersive) due to energetic disorder must be ensured. For this purpose, the critical temperature (within Gaussian disorder model), T_c, at which the transition from dispersive to nondispersive regime takes place, was estimated and is shown in Fig. S11 and Fig. S12 of the supplementary material. The mobilities obtained in the nondispersive regimes are then fitted with an empirical temperature dependence, allowing for extrapolation of the nondispersive charge carrier mobility at room temperature. Details of such calculations can be found elsewhere in Refs. 98 and 99. All charge transport calculations were performed using the VOTCA package.[13,43]

Glass transition temperature: Differential scanning calorimetry (DSC)

For determination of the glass transition temperature (T_g) at Merck KGaA, Darmstadt, Germany, we used differential scanning calorimetry (DSC) analyzing samples of 10–15 mg in DSC 204/1/G Phönix from Netsch. Samples were heated by 5 °C/min up to 370 °C then cooled by 20 °C/min to 0 °C and finally heated again by 20 °C/min to 370 °C, where T_g was determined by the kink in heat flow vs temperature using the temperature corresponding to half the drop in

heat flux. Only for BCP and TMBT, this protocol did not yield a significant kink. TMBT was expected to be the lowest T_g material from simulation, so we tried other protocols to measure T_g. We finally used a 5 mg TMBT sample in DSC Discovery from TA Instruments in nitrogen atmosphere and first heated by 20 °C/min up to 320 °C, then for cooling, quenched the sample by liquid nitrogen and finally heated by 20 °C/min up to 320 °C, where the Tg was observed. Other protocols we tried for TMBT without the cooling quench did not lead to observation of T_g.

Ionization energies: Photoelectron yield spectroscopy in air (PESA)

Photoelectron yield spectroscopy in air (PESA) was performed on 50 nm thick thermally evaporated films at Merck KGaA, Darmstadt, Germany, using the surface analyzer AC-3 from RIKEN KEIKI Co., Ltd. The film is exposed to monochromatic light from a deuterium-lamp, with incident photon energy between 4 and 7 eV (increased in steps of 0.05 eV),[100] while an open counter analyzes the photoelectron yield.[101] The square root of this photoelectron yield is plotted vs energy of the incident photons. The underground is taken as the average horizontal line through the measurement points for low photon energies. The ionization potential is calculated as intersection of the underground and a fit to the onset of the square root of the photoelectron yield.

Due to the energy step size and this fitting procedure, which is done manually, an error bar of roughly ± 0.06 eV must be associated with the obtained ionization energies as we have verified by repeated measurement and evaluation. As compared to UPS measurements of films, PESA has the advantage that the penetration depth of photons of 7 eV is roughly 10 nm, while for UPS, only the top 0.5 nm of the film can contribute, so PESA is measuring bulk properties of the film.

Energetic disorder: TSL technique

TSL is the phenomenon of luminescent emission after removal of excitation (UV light in our case) under conditions of increasing temperature. Our TSL measurements were carried out over a wide temperature range from 5 to 330 K using an optical temperature-regulating helium cryostat. When exciting a sample optically with 313 nm light for typically 3 min at 4.2 K, the charge carriers are generated and populate trapping states. Once the sample is heated up, trapped charge carriers are released and then recombine, producing a luminescence emission. TSL measurements were performed in two different regimes: upon uniform heating at the constant heating rate 0.15 K/s and under the so-called fractional heating regime.[102] In the latter regime, we apply a temperature-cycling program in which a large number of small temperature oscillations are superimposed on a constant heating ramp that allows determining the trap depth with high accuracy. This applies when different groups of traps are not well separated in energy or are continuously distributed, which is of special relevance for disordered organic solids where the intrinsic tail states can act as traps at low temperatures. The details of the TSL measurements have been described elsewhere in Refs. 103–105.

Technically, TSL is a relatively simple technique with a straightforward data analysis. However, it should be noted that the mechanism of TSL in amorphous organic semiconductors with a broad energy distribution of strongly localized states, differs from the

mechanism commonly accepted for crystalline materials with band-type transport where a discrete trapping level model is applicable. A specific feature of amorphous solids is that the localized states within the lower energy part of the intrinsic DOS distribution can give rise to shallow charge trapping at very low temperatures, and as a consequence, TSL can be observed even in materials where the "trap-free limit" has been postulated. Since TSL measurements are normally performed after a long dwell time after photoexcitation, the initial energy distribution of localized carriers is formed after low-temperature energy relaxation of photogenerated carriers within a Gaussian distribution of DOS. Theoretical background for application of TSL for probing the DOS distribution in disordered organic systems has been developed,[105,106] using a variable-range hopping formalism and the concept of thermally stimulated carrier random walk within a positionally and energetically random system of hopping sites. The theory proves that the high temperature wing of the TSL curve in such amorphous materials should be an exact replica of the deeper portion of the DOS distribution[105,106] and yields the effective DOS width. Kadashchuk and co-workers have applied low-temperature fractional TSL to investigate the intrinsic energetic disorder in a variety of important semiconducting polymers, oligomers, and hybrid metalorganic perovskites (see, for instance Refs. [103–109]). A clear advantage of TSL is that it is a purely optical and electrode-free technique. This helps to eliminate interface/contact effects and, most importantly, it allows DOS measurements even in materials with large energy disorder where the charge transport is very dispersive.

SOFTWARE AND INPUT FILES

All simulations were performed with the open-source software package VOTCA.[110] Atomistic and polarizable force fields, VOTCA input files, and analysis scripts are available in the Materials Library git repository, version 1.0.[111]

SUPPLEMENTARY MATERIAL

See the supplementary material for additional material properties, including: reorganisation energies, transfer integrals, comparison of gas phase ionisation energies, and dipole moments. Experimental TSL curves are also shown.

AUTHORS' CONTRIBUTIONS

A.M. and L.P. contributed equally to the work.

ACKNOWLEDGMENTS

DATA AVAILABILITY

The data that support the findings of this study are openly available in https://gitlab.mpcdf.mpg.de/materials, version number 1.0.

REFERENCES

[1] A. Bernanose and P. Vouaux, "Electroluminescence of organic compounds," J. Chim. Phys. **50**, 261–263 (1953).

[2] A. Bernanose, M. Comte, and P. Vouaux, "A new method of emission of light by certain organic compounds," J. Chim. Phys. **50**, 64–68 (1953).

[3] C. W. Tang and S. A. VanSlyke, "Organic electroluminescent diodes," Appl. Phys. Lett. **51**, 913–915 (1987).

[4] P. Friederich et al., "Toward design of novel materials for organic electronics," Adv. Mater. **31**, 1808256 (2019).

[5] P. Kordt et al., "Modeling of organic light emitting diodes: From molecular to device properties," Adv. Funct. Mater. **25**, 1955–1971 (2015).

[6] B. Baumeier, F. May, C. Lennartz, and D. Andrienko, "Challenges for in silico design of organic semiconductors," J. Mater. Chem. **22**, 10971–10976 (2012).

[7] W. Kaiser, J. Popp, M. Rinderle, T. Albes, and A. Gagliardi, "Generalized kinetic Monte Carlo framework for organic electronics," Algorithms **11**, 37 (2018).

[8] H. Uratani et al., "Detailed analysis of charge transport in amorphous organic thin layer by multiscale simulation without any adjustable parameters," Sci. Rep. **6**, 39128 (2016).

[9] S. Kubo and H. Kaji, "Parameter-free multiscale simulation realising quantitative prediction of hole and electron mobilities in organic amorphous system with multiple frontier orbitals," Sci. Rep. **8**, 13462 (2018).

[10] F. Suzuki et al., "Multiscale simulation of charge transport in a host material, N,N′-dicarbazole-3,5-benzene (mCP), for organic light-emitting diodes," J. Mater. Chem. C **3**, 5549–5555 (2015).

[11] F. Suzuki, S. Kubo, T. Fukushima, and H. Kaji, "Effects of structural and energetic disorders on charge transports in crystal and amorphous organic layers," Sci. Rep. **8**, 5203 (2018).

[12] H. Li, Y. Qiu, and L. Duan, "Multi-scale calculation of the electric properties of organic-based devices from the molecular structure," Org. Electron. **33**, 164–171 (2016).

[13] V. Rühle et al., "Microscopic simulations of charge transport in disordered organic semiconductors," J. Chem. Theory Comput. **7**, 3335–3345 (2011).

[14] W. L. Jorgensen and J. Tirado-Rives, "Potential energy functions for atomic-level simulations of water and organic and biomolecular systems," Proc. Natl. Acad. Sci. U.S.A. **102**, 6665–6670 (2005).

[15] W. L. Jorgensen and J. Tirado-Rives, "The OPLS [optimized potentials for liquid simulations] potential functions for proteins, energy minimizations for crystals of cyclic peptides and crambin," J. Am. Chem. Soc. **110**, 1657–1666 (1988).

[16] W. L. Jorgensen, D. S. Maxwell, and J. Tirado-Rives, "Development and testing of the OPLS all-atom force field on conformational energetics and properties of organic liquids," J. Am. Chem. Soc. **118**, 11225–11236 (1996).

[17] X. de Vries, P. Friederich, W. Wenzel, R. Coehoorn, and P. A. Bobbert, "Full quantum treatment of charge dynamics in amorphous molecular semiconductors," Phys. Rev. B **97**, 075203 (2018).

[18] T. Körzdörfer and J.-L. Brédas, "Organic electronic materials: recent advances in the DFT description of the ground and excited states using tuned range-separated hybrid functionals," Acc. Chem. Res. **47**, 3284–3291 (2014).

[19] C. Faber, P. Boulanger, C. Attaccalite, I. Duchemin, and X. Blase, "Excited states properties of organic molecules: From density functional theory to the GW and Bethe–Salpeter Green's function formalisms," Philos. Trans. R. Soc. A **372**, 20130271 (2014).

[20] L. Hedin and S. Lundqvist, "Effects of electron-electron and electron-phonon interactions on the one-electron states of solids," Solid State Phys. **23**, 1–181 (1970).

[21] B. Bagheri, B. Baumeier, and M. Karttunen, "Getting excited: Challenges in quantum-classical studies of excitons in polymeric systems," Phys. Chem. Chem. Phys. **18**, 30297–30304 (2016).

09 January 2025 14:14:36

[22] Y. Jin and W. Yang, "Excitation energies from the single-particle green's function with the GW approximation," J. Phys. Chem. A **123**, 3199–3204 (2019).

[23] G. Tirimbò *et al.*, "Excited-state electronic structure of molecules using many-body Green's functions: Quasiparticles and electron–hole excitations with VOTCA-XTP," J. Chem. Phys. **152**, 114103 (2020).

[24] O. Çaylak and B. Baumeier, "Excited-state geometry optimization of small molecules with many-body Green's functions theory," J. Chem. Theory Comput. **17**, 879–888 (2021).

[25] R. Coehoorn, H. van Eersel, P. Bobbert, and R. Janssen, "Kinetic Monte Carlo study of the sensitivity of OLED efficiency and lifetime to materials parameters," Adv. Funct. Mater. **25**, 2024–2037 (2015).

[26] H. Li and J.-L. Brédas, "Developing molecular-level models for organic field-effect transistors," Natl. Sci. Rev. **8**, nwaa167 (2021).

[27] Y. Yang *et al.*, "Emergent properties of an organic semiconductor driven by its molecular chirality," ACS Nano **11**, 8329–8338 (2017).

[28] F. Symalla *et al.*, "Multiscale simulation of photoluminescence quenching in phosphorescent OLED materials," Adv. Theory Simul. **3**, 1900222 (2020).

[29] S. Lee, H. Kim, and Y. Kim, "Progress in organic semiconducting materials with high thermal stability for organic light-emitting devices," InfoMat **2**, 12123 (2020).

[30] Y. Zhao *et al.*, "Trifluoromethyl-functionalized bathocuproine for polymer solar cells," J. Mater. Chem. C **4**, 4640–4646 (2016).

[31] T. Komino *et al.*, "Electroluminescence from completely horizontally oriented dye molecules," Appl. Phys. Lett. **108**, 241106 (2016).

[32] L. Xiao *et al.*, "Recent progresses on materials for electrophosphorescent organic light-emitting devices," Adv. Mater. **23**, 926–952 (2011).

[33] Y. Kuwabara, H. Ogawa, H. Inada, N. Noma, and Y. Shirota, "Thermally stable multilared organic electroluminescent devices using novel starburst molecules, 4,4′,4″-Tri(N-carbazolyl)triphenylamine (TCTA) and 4,4′,4″-Tris(3-methylphenylphenylamino)triphenylamine (m-MTDATA), as hole-transport materials," Adv. Mater. **6**, 677–679 (1994).

[34] S. Li-Ying *et al.*, "Improving the efficiency of blue organic light-emitting diodes by employing Cs-derivatives as the n-dopant," Acta Phys.-Chim. Sin. **28**, 1497–1501 (2012).

[35] F. Steuber *et al.*, "White light emission from organic LEDs utilizing Spiro compounds with high-temperature stability," Adv. Mater. **12**, 130–133 (2000).

[36] H.-F. Chen *et al.*, "Peripheral modification of 1,3,5-triazine based electron-transporting host materials for sky blue, green, yellow, red, and white electrophosphorescent devices," J. Mater. Chem. **22**, 15620 (2012).

[37] Z. Wang *et al.*, "Phenanthro [9,10-d]imidazole as a new building block for blue light emitting materials," J. Mater. Chem. **21**, 5451 (2011).

[38] K. N. Park, Y.-R. Cho, W. Kim, D.-W. Park, and Y. Choe, "Raman Spectra and current-voltage characteristics of 4,4′,4″-Tris(2-naphthylphenylamino)-triphenylamine thin films," Mol. Cryst. Liq. Cryst. **498**, 183–192 (2009).

[39] S. S. Dalal, D. M. Walters, I. Lyubimov, J. J. de Pablo, and M. D. Ediger, "Tunable molecular orientation and elevated thermal stability of vapor-deposited organic semiconductors," Proc. Natl. Acad. Sci. U.S.A. **112**, 4227–4232 (2015).

[40] D. Yokoyama, Y. Setoguchi, A. Sakaguchi, M. Suzuki, and C. Adachi, "Orientation control of linear-shaped molecules in vacuum-deposited organic amorphous films and its effect on carrier mobilities," Adv. Funct. Mater. **20**, 386–391 (2010).

[41] S. Singh, M. D. Ediger, and J. J. de Pablo, "Ultrastable glasses from in silico vapour deposition," Nat. Mater. **12**, 139–144 (2013).

[42] D. M. Walters, L. Antony, J. J. de Pablo, and M. D. Ediger, "Influence of molecular shape on the thermal stability and molecular orientation of vapor-deposited organic semiconductors," J. Phys. Chem. Lett. **8**, 3380–3386 (2017).

[43] V. Rühle, C. Junghans, A. Lukyanov, K. Kremer, and D. Andrienko, "Versatile object-oriented toolkit for coarse-graining applications," J. Chem. Theory Comput. **5**, 3211–3223 (2009).

[44] J. Xu and B. Chen, "Prediction of glass transition temperatures of OLED materials using topological indices," J. Mol. Model. **12**, 24–33 (2005).

[45] S. Yin, Z. Shuai, and Y. Wang, "A quantitative structure−property relationship study of the glass transition temperature of OLED materials," J. Chem. Inf. Comput. Sci. **43**, 970–977 (2003).

[46] Q. Wu and T. Van Voorhis, "Direct optimization method to study constrained systems within density-functional theory," Phys. Rev. A **72**, 024502 (2005).

[47] R. A. Marcus, "Electron transfer reactions in chemistry: Theory and experiment (Nobel lecture)," Angew. Chem. Int. Ed. Engl. **32**, 1111–1121 (1993).

[48] R. A. Marcus and N. Sutin, "Electron transfers in chemistry and biology," Biophys. Acta **811**, 265–322 (1985).

[49] R. A. Marcus, "Chemical and electrochemical electron-transfer theory," Annu. Rev. Phys. Chem. **15**, 155–196 (1964).

[50] V. May and O. Kühn, *Charge and Energy Transfer Dynamics in Molecular Systems.* (Wiley-VCH: Weinheim, 2011).

[51] V. Cápek, "Generalized master equations and phonon-assisted hopping," Phys. Rev. B **36**, 7442–7447 (1987).

[52] V. Cápek, "Generalized master equations and other theories of the phonon-assisted hopping conduction," Phys. Rev. B **38**, 12983–12987 (1988).

[53] H. Bässler, "Charge transport in disordered organic photoconductors a Monte Carlo simulation study," Phys. Status Solidi B **175**, 15–56 (1993).

[54] W. F. Pasveer *et al.*, "Unified description of charge-carrier mobilities in disordered semiconducting polymers," Phys. Rev. Lett. **94**, 206601 (2005).

[55] S. V. Novikov, D. H. Dunlap, V. M. Kenkre, P. E. Parris, and A. V. Vannikov, "Essential role of correlations in governing charge transport in disordered organic materials," Phys. Rev. Lett. **81**, 4472–4475 (1998).

[56] M. Schrader *et al.*, "Comparative study of microscopic charge dynamics in crystalline acceptor-substituted oligothiophenes," J. Am. Chem. Soc. **134**, 6052–6056 (2012).

[57] S. D. Baranovskii, "Theoretical description of charge transport in disordered organic semiconductors," Phys. Status Solidi B **251**, 487–525 (2014).

[58] S. C. Tse, K. C. Kwok, and S. K. So, "Electron transport in naphthylamine-based organic compounds," Appl. Phys. Lett. **89**, 262102 (2006).

[59] I. G. Hill and A. Kahn, "Organic semiconductor heterointerfaces containing bathocuproine," J. Appl. Phys. **86**, 4515–4519 (1999).

[60] R. J. Holmes *et al.*, "Efficient, deep-blue organic electrophosphorescence by guest charge trapping," Appl. Phys. Lett. **83**, 3818–3820 (2003).

[61] N. B. Kotadiya *et al.*, "Rigorous characterization and predictive modeling of hole transport in amorphous organic semiconductors," Adv. Electron. Mater. **4**, 1800366 (2018).

[62] R. T. White, E. S. Thibau, and Z.-H. Lu, "Interface structure of MoO3 on organic semiconductors," Sci. Rep. **6**, 21109 (2016).

[63] M. T. Greiner *et al.*, "Universal energy-level alignment of molecules on metal oxides," Nat. Mater. **11**, 76–81 (2012).

[64] Z. B. Wang *et al.*, "Controlling carrier accumulation and exciton formation in organic light emitting diodes," Appl. Phys. Lett. **96**, 043303 (2010).

[65] A. Salehi *et al.*, "Highly efficient organic light-emitting diode using a low refractive index electron transport layer," Adv. Opt. Mater. **5**, 1700197 (2017).

[66] B. Dänekamp *et al.*, "Influence of hole transport material ionization energy on the performance of perovskite solar cells," J. Mater. Chem. C **7**, 523–527 (2019).

[67] N. B. Kotadiya, A. Mondal, P. W. M. Blom, D. Andrienko, and G.-J. A. H. Wetzelaer, "A window to trap-free charge transport in organic semiconducting thin films," Nat. Mater. **18**, 1182–1186 (2019).

[68] I. I. Fishchuk, A. K. Kadashchuk, H. Bassler, and D. S. Weiss, "Nondispersive charge-carrier transport in disordered organic materials containing traps," Phys. Rev. B **66**, 205208 (2002).

[69] N. Matsusue, Y. Suzuki, and H. Naito, "Charge carrier transport in neat thin films of phosphorescent iridium complexes," Jpn. J. Appl. Phys. **44**, 3691–3694 (2005).

[70] M.-F. Wu *et al.*, "The quest for high-performance host materials for electrophosphorescent blue dopants," Adv. Funct. Mater. **17**, 1887–1895 (2007).

[71] S. C. Tse, S. W. Tsang, and S. K. So, "Nearly Ohmic injection contacts from PEDOT:PSS to phenylamine compounds with high ionization potentials." in *Organic Light Emitting Materials and Devices X; 63331P: Proceedings of the SPIE Optics + Photonics, San Diego, California, United States,* 2006, edited by Z. H. Kafafi and F. So.

[72] T. P. I. Saragi, T. Spehr, A. Siebert, T. Fuhrmann-Lieker, and J. Salbeck, "Spiro compounds for organic optoelectronics," Chem. Rev. **107**, 1011–1065 (2007).

09 January 2025 14:14:36

[73]S. Noh, C. K. Suman, Y. Hong, and C. Lee, "Carrier conduction mechanism for phosphorescent material doped organic semiconductor," J. Appl. Phys. **105**, 033709 (2009).

[74]J.-W. Kang *et al.*, "Low roll-off of efficiency at high current density in phosphorescent organic light emitting diodes," Appl. Phys. Lett. **90**, 223508 (2007).

[75]H.-F. Chen *et al.*, "1,3,5-Triazine derivatives as new electron transport–type host materials for highly efficient green phosphorescent OLEDs," J. Mater. Chem. **19**, 8112 (2009).

[76]S. H. Rhee *et al.*, "Effect of electron mobility of the electron transport layer on fluorescent organic light-emitting diodes," ECS Solid State Lett. **3**, R19–R22 (2014).

[77]W.-Y. Hung *et al.*, "Employing ambipolar oligofluorene as the charge-generation layer in time-of-flight mobility measurements of organic thin films," Appl. Phys. Lett. **88**, 064102 (2006).

[78]M. J. Frisch *et al.*, *Gaussian 09 Revision D.01*. Gaussian, Inc., Wallingford CT, 2013.

[79]J. P. Perdew and A. Zunger, "Self-interaction correction to density-functional approximations for many-electron systems," Phys. Rev. B **23**, 5048–5079 (1981).

[80]A. Ruzsinszky, J. P. Perdew, G. I. Csonka, O. A. Vydrov, and G. E. Scuseria, "Spurious fractional charge on dissociated atoms: Pervasive and resilient self-interaction error of common density functionals," J. Chem. Phys. **125**, 194112 (2006).

[81]L. Gallandi and T. Körzdörfer, "Long-range corrected DFT meets GW: Vibrationally resolved photoelectron spectra from first principles," J. Chem. Theory Comput. **11**, 5391–5400 (2015).

[82]T. Stein, L. Kronik, and R. Baer, "Reliable prediction of charge transfer excitations in molecular complexes using time-dependent density functional theory," J. Am. Chem. Soc. **131**, 2818–2820 (2009).

[83]R. Baer, E. Livshits, and U. Salzner, "Tuned range-separated hybrids in density functional theory," Annu. Rev. Phys. Chem. **61**, 85–109 (2010).

[84]T. Körzdörfer, J. S. Sears, C. Sutton, and J.-L. Brédas, "Long-range corrected hybrid functionals for π-conjugated systems: Dependence of the range-separation parameter on conjugation length," J. Chem. Phys. **135**, 204107 (2011).

[85]C. M. Breneman and K. B. Wiberg, "Determining atom-centered monopoles from molecular electrostatic potentials. The need for high sampling density in formamide conformational analysis," J. Comput. Chem. **11**, 361–373 (1990).

[86]B. Hess, C. Kutzner, D. van der Spoel, and E. Lindahl, "GROMACS 4: Algorithms for highly efficient, load-balanced, and scalable molecular simulation," J. Chem. Theory Comput. **4**, 435–447 (2008).

[87]S. Pronk *et al.*, "GROMACS 4.5: A high-throughput and highly parallel open source molecular simulation toolkit," Bioinformatics **29**, 845–854 (2013).

[88]T. Neumann, D. Danilov, C. Lennartz, and W. Wenzel, "Modeling disordered morphologies in organic semiconductors," J. Comput. Chem. **34**, 2716–2725 (2013).

[89]L. Martínez, R. Andrade, E. G. Birgin, and J. M. Martínez, "PACKMOL: A package for building initial configurations for molecular dynamics simulations," J. Comput. Chem. **30**, 2157–2164 (2009).

[90]G. Bussi, D. Donadio, and M. Parrinello, "Canonical sampling through velocity rescaling," J. Chem. Phys. **126**, 014101 (2007).

[91]H. J. C. Berendsen, J. P. M. Postma, W. F. van Gunsteren, A. DiNola, and J. R. Haak, "Molecular dynamics with coupling to an external bath," J Chem. Phys. **81**, 3684–3690 (1984).

[92]A. J. Stone, "Distributed multipole analysis: Stability for large basis sets," J. Chem. Theory Comput. **1**, 1128–1132 (2005).

[93]B. T. Thole, "Molecular polarizabilities calculated with a modified dipole interaction," Chem. Phys. **59**, 341–350 (1981).

[94]P. T. van Duijnen and M. Swart, "Molecular and atomic polarizabilities: Thole's model revisited," J. Phys. Chem. A **102**, 2399–2407 (1998).

[95]C. Poelking and D. Andrienko, "Long-range embedding of molecular ions and excitations in a polarizable molecular environment," J. Chem. Theory Comput. **12**, 4516–4523 (2016).

[96]E. F. Valeev, V. Coropceanu, D. A. da Silva Filho, S. Salman, and J.-L. Brédas, "Effect of electronic polarization on charge-transport parameters in molecular organic semiconductors," J. Am. Chem. Soc. **128**, 9882–9886 (2006).

[97]B. Baumeier, J. Kirkpatrick, and D. Andrienko, "Density-functional based determination of intermolecular charge transfer properties for large-scale morphologies," Phys. Chem. Chem. Phys. **12**, 11103–11113 (2010).

[98]A. Lukyanov and D. Andrienko, "Extracting nondispersive charge carrier mobilities of organic semiconductors from simulations of small systems," Phys. Rev. B **82**, 193202 (2010).

[99]P. Kordt, T. Speck, and D. Andrienko, "Finite-size scaling of charge carrier mobility in disordered organic semiconductors," Phys. Rev. B **94**, 014208 (2016).

[100]R. Keiki, "Product description from RIKEN KEIKI for the Photoelectron Sprectrometer in air, surface analyzer model AC-3," https://www.rkiinstruments.com/pdf/AC3.pdf

[101]D. Yamashita, Y. Nakajima, A. Ishizaki, and M. Uda, Photoelectron spectrometer equipped with open counter electronic structures organic materials. J. Surface Analysis **14**, 433–436 (2008).

[102]I. A. Tale, "Trap spectroscopy by the fractional glow technique," Phys. Status Solidi A **66**, 65–75 (1981).

[103]A. Kadashchuk *et al.*, "The origin of thermally stimulated luminescence in neat and molecularly doped charge transport polymer systems," Chem. Phys. **247**, 307–319 (1999).

[104]A. Kadashchuk *et al.*, "Thermally stimulated photoluminescence in poly(2,5-dioctoxy p -phenylene vinylene)," J. Appl. Phys. **91**, 5016–5023 (2002).

[105]A. Kadashchuk *et al.*, "Thermally stimulated photoluminescence in disordered organic materials," Phys. Rev. B **63**, 115205 (2001).

[106]V. I. Arkhipov, E. V. Emelianova, A. Kadashchuk, and H. Bässler, "Hopping model of thermally stimulated photoluminescence in disordered organic materials," Chem. Phys. **266**, 97–108 (2001).

[107]S. A. Patil, U. Scherf, and A. Kadashchuk, "New conjugated ladder polymer containing carbazole moieties," Adv. Funct. Mater. **13**, 609–614 (2003).

[108]A. Fakharuddin *et al.*, "Reduced efficiency roll-off and improved stability of mixed 2D/3D perovskite light emitting diodes by balancing charge injection," Adv. Funct. Mater.. **29**, 1904101 (2019).

[109]A. Stankevych *et al.*, "Density of states of OLED host materials from thermally stimulated luminescence," Phys. Rev. Appl. **15**, 044050 (2021).

[110]VOTCA. https://gitlab.mpcdf.mpg.de/votca (last accessed on 12/07/2020).

[111]The Materials Library git repository, version 1.0, containing atomistic and polarizable force fields, VOTCA input files, and analysis scripts. Materials Library. https://gitlab.mpcdf.mpg.de/materials (last accessed 12/07/2020).

09 January 2025 14:14:36

Supporting Information

Physical properties of OLED host materials

Anirban Mondal [1,#], Leanne Paterson [1,#], Jaeyoung Cho [1,2], Kun-Han Lin [1], Bas van der Zee [1], Gert-Jan A. H. Wetzelaer [1], Andrei Stankevych [3], Alexander Vakhnin [3], Jang-Joo Kim [2], Andrey Kadashchuk [3,4], Paul W. M. Blom [1], Falk May, [5] and Denis Andrienko [1,*]

[1] Max Planck Institute for Polymer Research, Ackermannweg 10, 55128 Mainz, Germany

[2] Department of Materials Science and Engineering and the Center for Organic Light Emitting Diode, Seoul National University, Seoul, 151-744, South Korea

[3] Institute of Physics, Natl. Academy of Sciences of Ukraine, Prospect Nauky 46, 03028 Kyiv, Ukraine

[4] IMEC, Kapeldreef 75, B-3001 Leuven, Belgium

[5] Merck KGaA, 64293 Darmstadt, Germany

[#] these authors contributed equally to the work

[*] E-mail: denis.andrienko@mpip-mainz.mpg.de

System	λ_{holes}	$\lambda_{\text{electrons}}$
BCP	0.41	0.41
CBP	0.13	0.53
mCBP	0.05	0.53
mCP	0.08	0.11
MTDATA	0.45	0.19
NBPhen	0.17	0.27
NPB	0.31	0.17
Spiro-TAD	0.22	0.27
TCTA	0.24	0.15
TMBT	0.13	0.28
TPBi	0.25	0.39
2-TNATA	0.42	0.12

Table S1 Reorganisation energies (λ) for holes and electrons, listed for each of the systems, calculated by DFT using B3LYP/6-311+g(d,p) level of theory
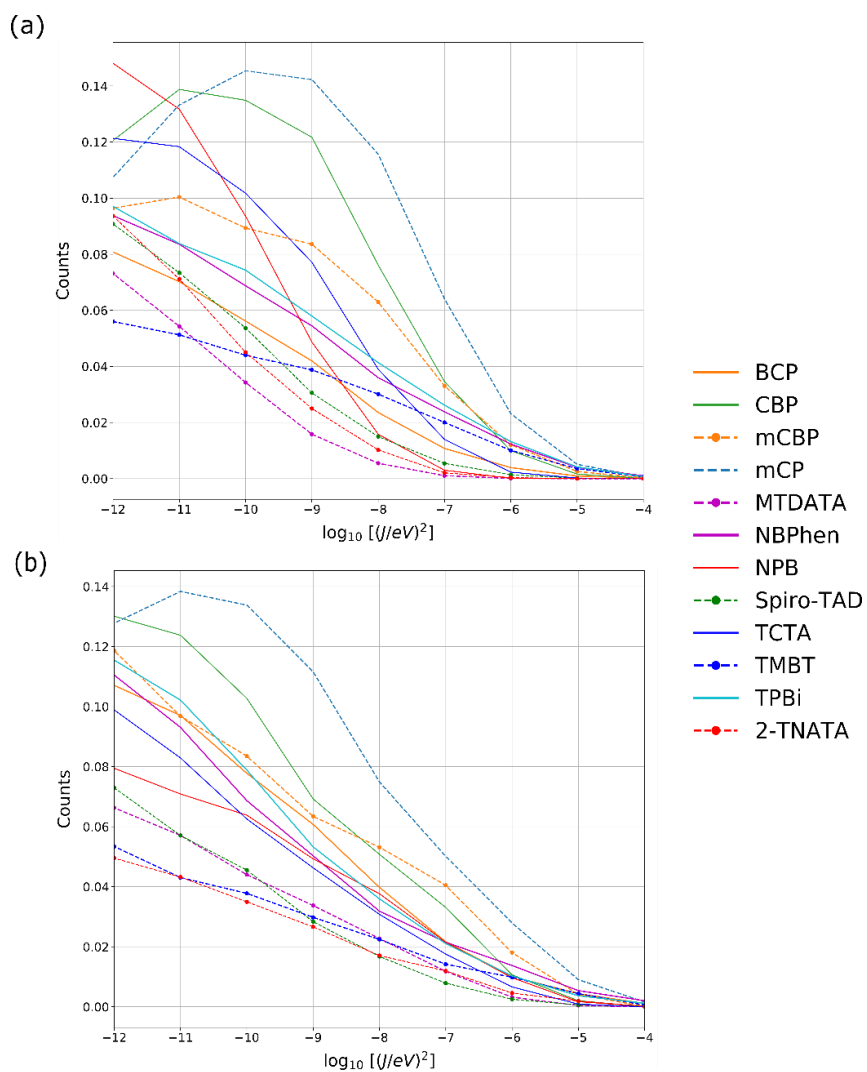
Figure S1 Distributions of the logarithm of the transfer integral J for (a) hole and (b) electron transport constructed from diabatic states based on the whole molecule.
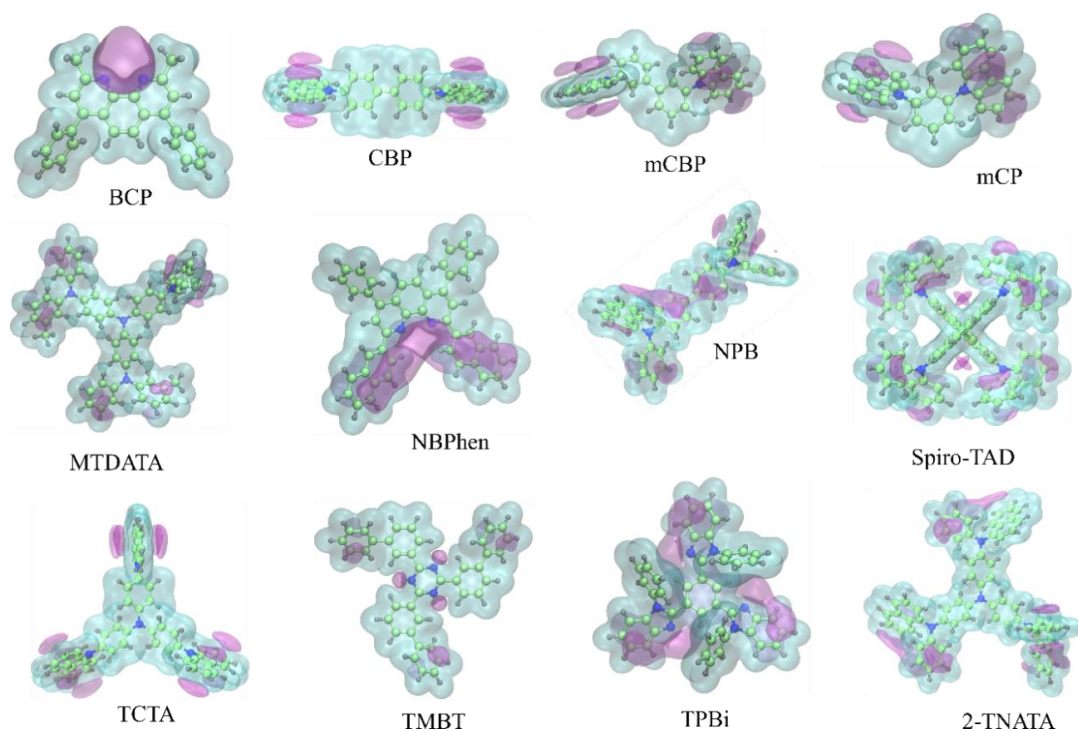
Figure S2 Iso-electrostatic potential surfaces, which are primarily responsible for the solid-state contribution to the ionization energy and the width of the density of states, for the organic semiconductors investigated in this work; BCP, CBP, mCBP, mCP, MTDATA, NBPhen, NPB, TCTA, TMBT, TPBi, Spiro-TAD and 2-TNATA.
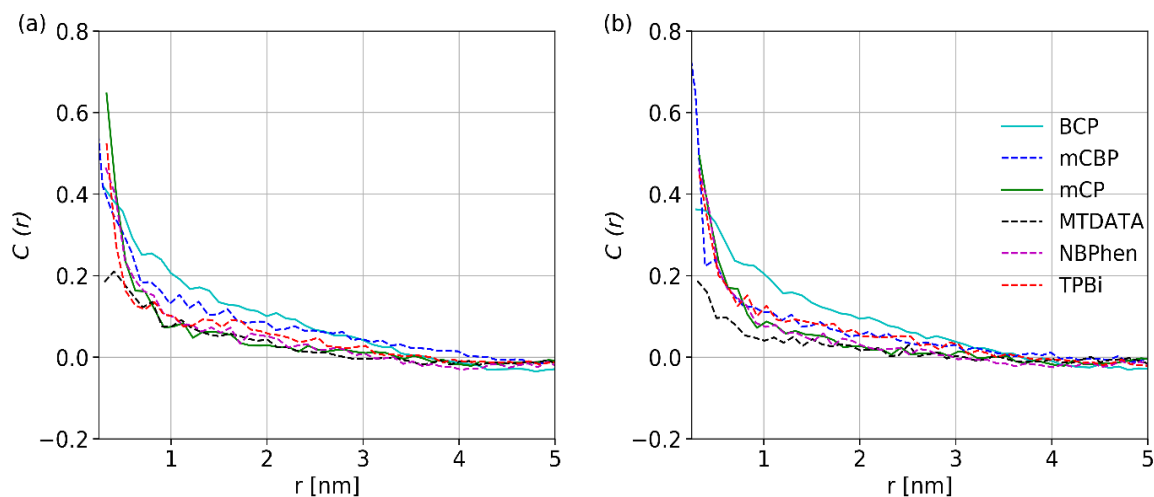
Figure S3 Site energy correlations for (a) holes and (b) electrons as a function of intermolecular distance in the amorphous organic semiconductors.
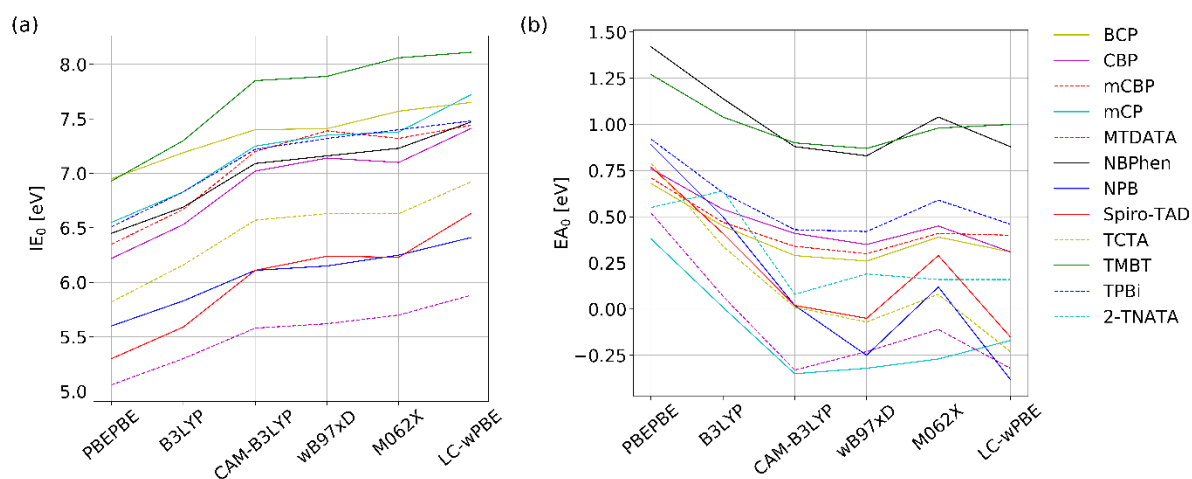
Figure S4 Gas phase (a) ionisation energies (IE_0) and electron affinities (EA_0) of the twelve organic semiconductors, as a function of DFT functionals, with the basis set 6-311+g(d,p).
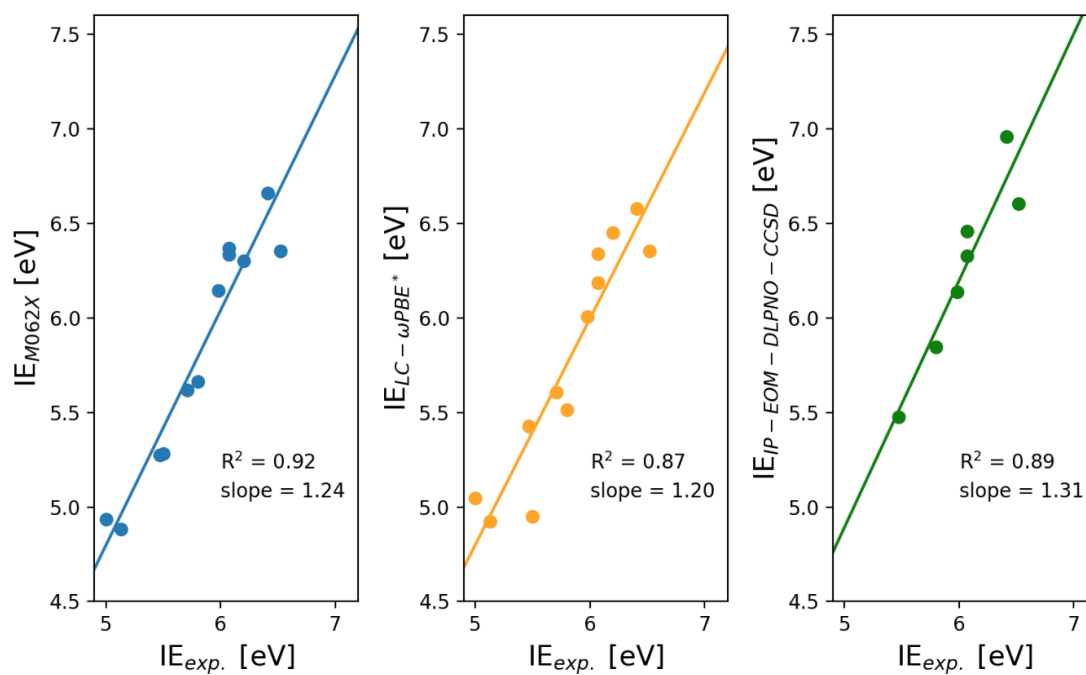
Figure S5 Comparison of experimental ionisation energies (IE_{exp}) and simulated (solid state) ionisation energies (IE_{tot}), with the gas phase (IE_0) obtained from different levels of theory: M062X/6-311+G(d,p), ω-tuned LC-ωPBE(LC-ωPBE*)/may-cc-pVTZ[1] and IP-EOM-DLPNO-CCSD/aug-cc-pVTZ.[2]
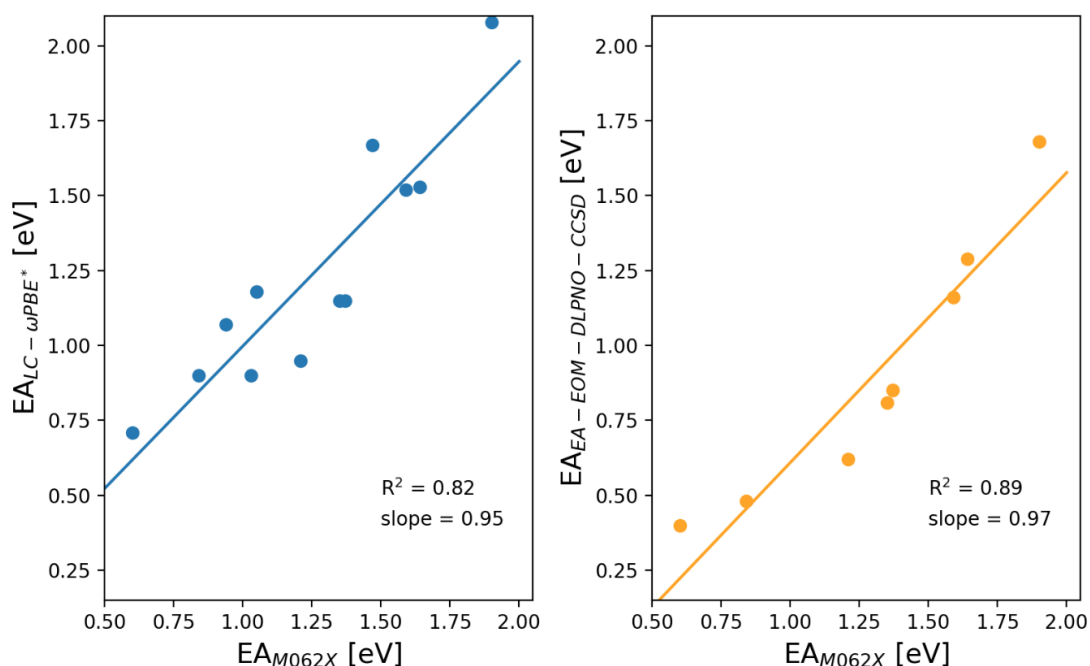
Figure S6 Simulated (solid state) electron affinity (EA_{tot}) with the gas phase (EA_0) obtained from different levels of theory: M06-2X/6-311+G(d,p), ω-tuned LC-ωPBE(LC-ωPBE*)/may-cc-pVTZ[1] and EA-EOM-DLPNO-CCSD/aug-cc-pVTZ.[3] Due to the lack of experimental data, the comparison is made between M062X and other levels of theory.

System	EA₀		IE₀		Optimal ω
	LC-ωPBE*	EA-EOM-DLPNO-CCSD	LC-ωPBE*	IP-EOM-DLPNO-CCSD	
BCP	0.26	NA	7.57	7.82	0.176
CBP	0.23	-0.07	7.07	7.19	0.177
mCBP	0.15	-0.18	7.17	7.31	0.180
mCP	-0.16	-0.47	7.24	7.37	0.180
MTDATA	0.02	NA	5.74	NA	0.141
NBPhen	0.97	0.61	7.08	7.41	0.150
NPB	0.18	-0.24	6.40	6.45	0.175
Spiro-TAD	0.42	NA	5.90	NA	0.125
TCTA	0.26	-0.14	6.62	NA	0.152
TMBT	0.87	0.63	7.98	8.36	0.173
TPBi	0.39	0.05	7.55	NA	0.157
2-TNATA	0.36	NA	5.83	NA	0.150

Table S2 IE_0 and EA_0 (eV) obtained at LC-ωPBE*/may-cc-pVTZ and IP/EA-EOM-DLPNO-CCSD/aug-cc-pVTZ. The optimal ω for each compound is also listed (Bohr^{-1}). Due to the limit of system size, we do not have values for all compounds using EOM-DLPNO-CCSD method (listed as NA).

IE₀/EA₀ Technical details:

To reduce the self-interaction error in DFT, it has been proposed to take ω in range-separated functionals as a parameter for further optimization. The optimization procedure for IE utilizes the fact that minus HOMO of a system equal to its IE in exact density functional theory. The ω that fulfils this criterion is then considered the optimal ω that significantly reduces the self-interaction error. This ω-tuned optimization procedure for IE has been extended to have a balance description for charge-transfer states[4] and HOMO-LUMO gap.[1] This is achieved by introducing the target function (J) to be minimized, defined as

$$J = |IE_N + \epsilon_{N,HOMO}| + |IE_A + \epsilon_{A,HOMO}|$$

where the capital N and A stands for the neutral and anionic states, respectively. Here we followed a protocol similar to that proposed by Brédas *et al.*[1] The anionic and neutral ground state geometries were optimized at the ωB97XD/6-311G(d,p) level. The ω-tuning procedure was performed using LC-ωPBE/may-cc-pVTZ. The optimal ω for each compound is shown in Table S2.

Another way to avoid the self-interaction error in DFT is to adopt a wavefunction-based method. The IP/EA-EOM-DLPNO-CCSD method has shown to be an affordable method for large molecules with a reasonable accuracy.[2,3] We hereby utilized these methods for IE₀/EA₀ computations. For details of the setting, we used aug-cc-pVTZ basis set with AutoAux (or def2/JK in case of convergence issue) and aug-cc-pVTZ/C auxiliary basis set. The Normal PNO scheme was used and the CutPNO Singles is set to 1e-10.
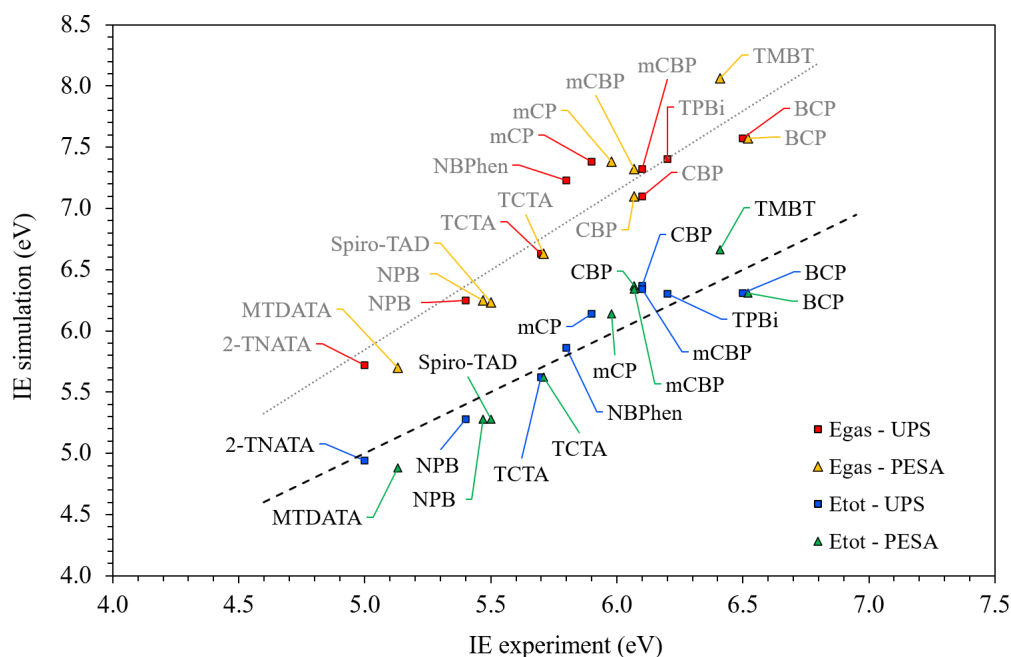
Figure S7 Simulated gas phase ionisation energies (Egas) compared with experimental UPS: red squares (R^2=0.878) & PESA: yellow triangles (R^2=0.925). Simulated solid-state ionisation energies (Etot) compared with experimental UPS: blue squares (R^2=0.898) & PESA: green triangles (R^2=0.900). The linear relationship (x=y) is shown by the black dashed line, highlighting the correlation of experimental and simulated solid state ionisation energies. For comparison, the grey dashed line is used as a visual aid to show the shift of gas phase ionisation energies.

Cyclic Voltammetry (CV) measurements:

For Cyclic Voltammetry measurements at Merck KGaA, Darmstadt, Germany we have used a potentiostat from Metronom µAUTOLAB type III in a three-electrode setup including working-electrode (Au), counter electrode (Pt) and reference-electrode (Ag/AgCl, KCl 3 M). Oxidation was measured in DCM and reduction in THF and tetrabutylammonium hexafluorophosphate (0.11 M) was added as electrolyte. As internal standard we have used ferrocene or decamethylferrocene. Ionisation energies (IE) and electron affinities (EA) were calculated according to the following relationships where Eox and ERed are taken as half-step potential.[5]

$$IE = -4.8 \text{ eV} - Eox \text{ vs. Fc/Fc+}$$

$$EA = -4.8 \text{ eV} - ERed \text{ vs. Fc/Fc+}$$

Errors for single IE measurements are +-0.01eV as we have analysed for repeated measurements for independently prepared solutions of the same material. In case of EA, the lower conductivity of THF as compared to DCM leads to stronger voltage drop in the solution

which broadens the reduction peaks and leads to a larger error of +-0.02eV for EA measurements. These errors are estimated for reversible and well resolvable oxidation/reduction peaks and will increase in case of multiple (overlapping) peaks or if EA or IP are close to the limit of measurable potential range.
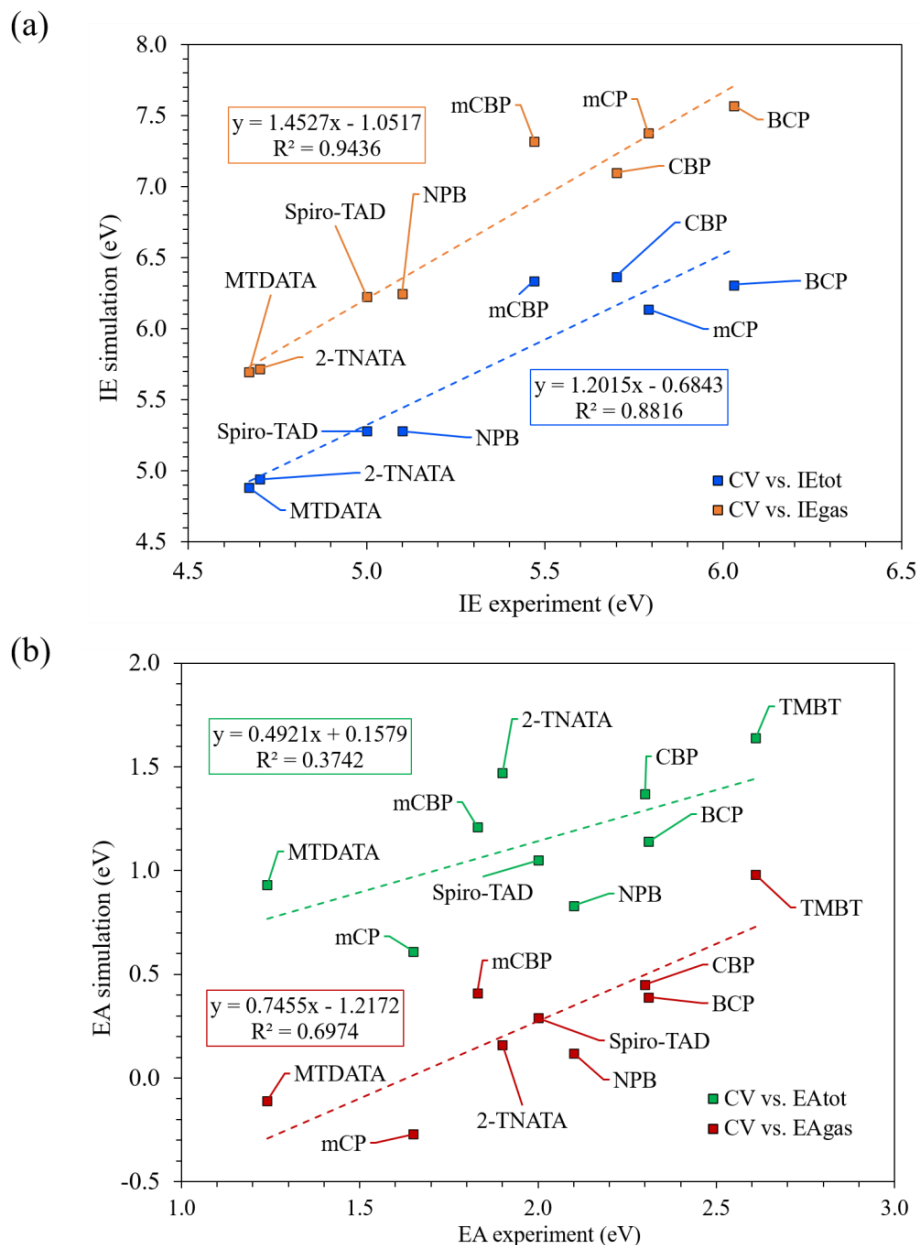
Figure S8 (a) Experimental CV (HOMO) data compared with simulated gas phase ionisation energy (IE_{gas}) orange (R^2=0.9436) and simulated solid state ionisation energy (IE_{tot}) blue (R^2=0.8816). (b) Experimental CV (LUMO) data compared with simulated gas phase electron affinity (EA_{gas}) red (R^2=0.6974) and simulated solid state electron affinity (EA_{tot}) green (R^2=0.3742). The dashed lines are the lines of best fit for the values of matching colour, to serve as a visual aid.
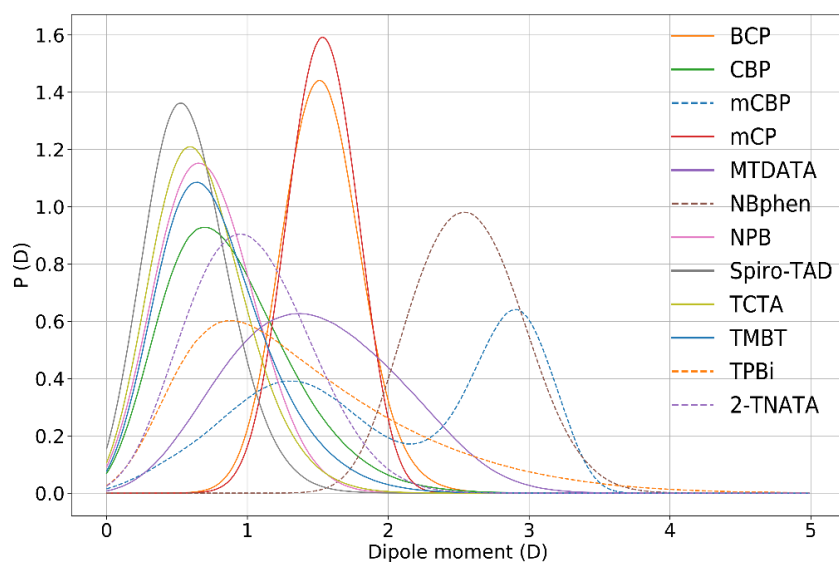
Figure S9 Distribution of molecular dipoles in the amorphous morphology for the twelve organic materials, calculated from MD simulations at 300K, with the partial charges obtained by GDMA.

System	d DFT	<d> MD	std(d) MD
BCP	2.91	1.53	0.24
CBP	0.0001	0.87	0.43
mCBP	0.95	2.03	0.87
mCP	1.27	1.52	0.20
MTDATA	0.79	1.48	0.57
NBPhen	3.43	2.56	0.36
NPB	0.31	0.71	0.30
Spiro-TAD	0.001	0.58	0.26
TCTA	0.01	0.67	0.31
TMBT	0.01	0.77	0.37
TPBi	6.33	1.89	1.86
2-TNATA	0.56	1.02	0.40

Table S3 Dipole moment (d) (Debye) of an isolated molecule obtained from quantum chemical calculations (DFT) using M062X/6-311+g(d,p) level of theory (d DFT). The average dipole moment from molecular dynamics simulations, calculated at 300K, using the partial charges obtained by GDMA[6] (<d> MD) with standard deviation (std(d) MD).
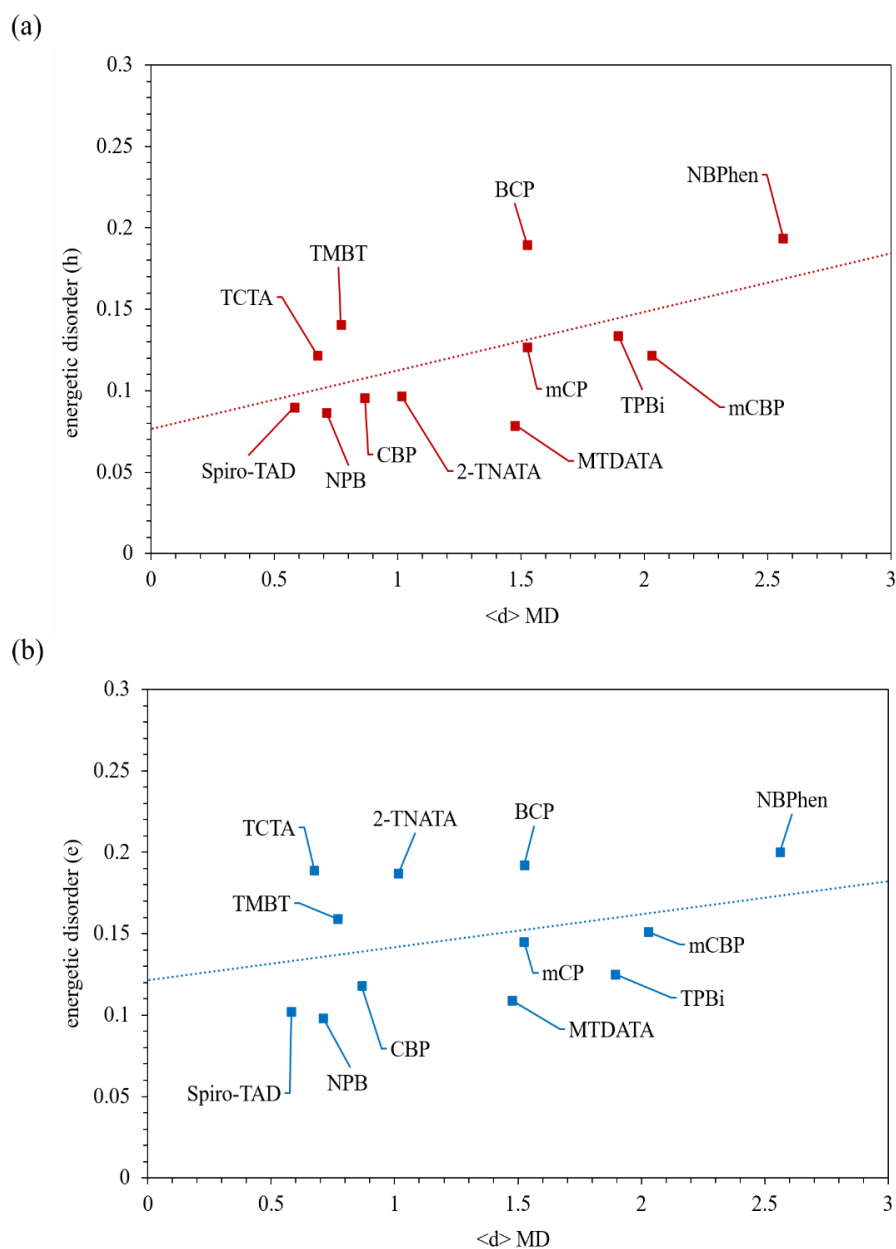
Figure S10 The average dipole moment from molecular dynamics simulations, calculated at 300K, using the partial charges obtained by GDMA ($\langle d \rangle$, MD), plotted against the energetic disorder for the twelve systems, for (a) holes and (b) electrons. The dashed lines are lines of best fit, to serve as a visual aid of the correlation.
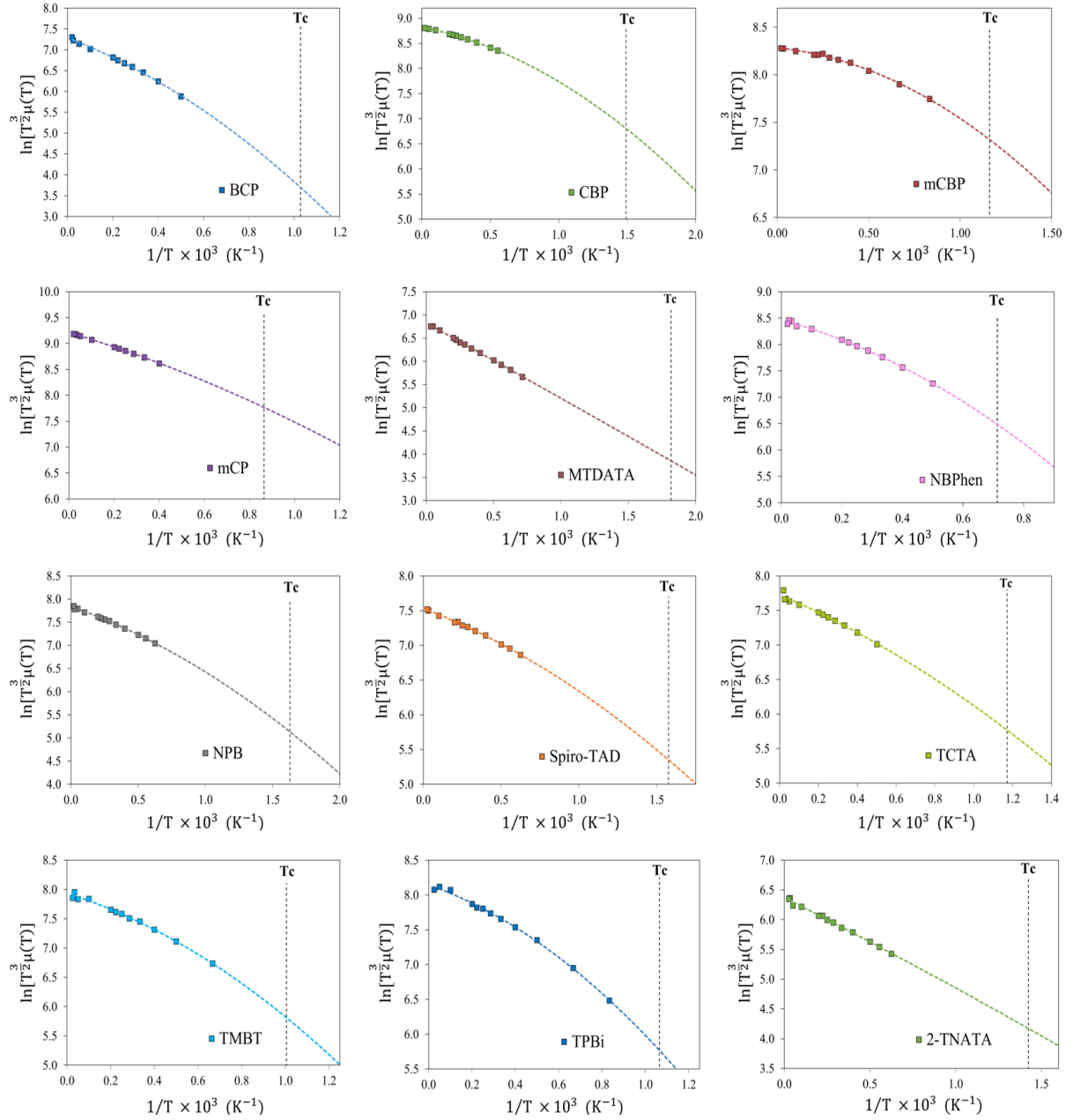
Figure S11 Hole mobility (μ) temperature (T) dependence for the twelve systems, including the estimated critical temperature (within Gaussian Disorder model) Tc, at which the transition from dispersive to nondispersive regime takes place (dashed black line). Calculated for one charge carrier (hole) at a range of high temperatures, with an applied field F = 1x10^4 V/cm. (x-axis: $\frac{1}{T} \times 10^3\ K^{-1}$ & y-axis: $\ln\left[T^{\frac{3}{2}}\mu(T)\right]$) Further information regarding the temperature dependence, explanation of the fitting procedure and extraction of room temperature mobilities can be found here.[7]
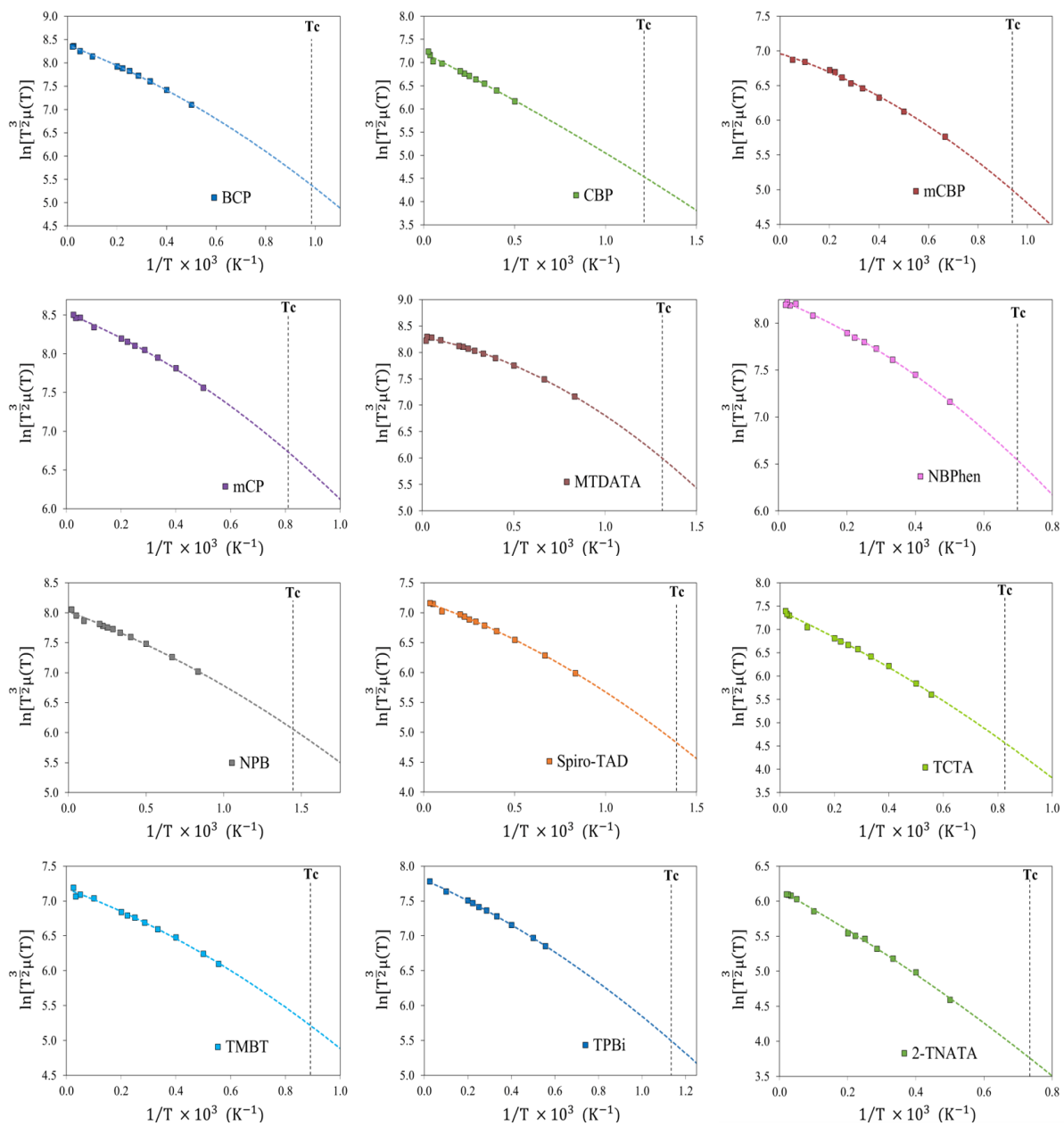
Figure S12 Electron (μ) temperature (T) dependence for the twelve systems, including the estimated critical temperature (within Gaussian Disorder model) Tc, at which the transition from dispersive to nondispersive regime takes place (dashed black line). Calculated for one charge carrier (electron) at a range of high temperatures, with an applied field F = 1x10⁴ V/cm. (x-axis: $\frac{1}{T} \times 10^3\ K^{-1}$ & y-axis: $\ln\left[T^{\frac{3}{2}}\mu(T)\right]$) Further information regarding the temperature dependence, explanation of the fitting procedure and extraction of room temperature mobilities can be found here.[7]

Glass Transition temperature – linear fitting procedure:

To reduce human error and any inaccuracies in choosing the range for linear fitting, we plotted the R^2 value as a function of temperature with a 200 K range (see Figure S13), i.e. [T-200, T] for T$\in$[200, 800]. The valley observed in such a plot characterises the non-linear transition in the density-temperature plot. We define the hill tops (maximum R^2 value) on two opposite sides of the valley as the optimal fitting ranges.
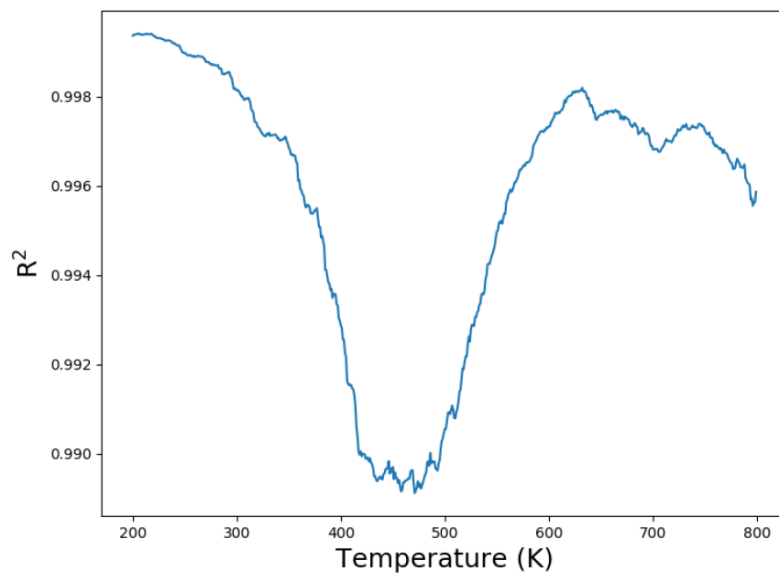
Figure S13 R^2 as a function of temperature with a range of 200K [T-200, T].

Thermally stimulated luminescence (TSL)
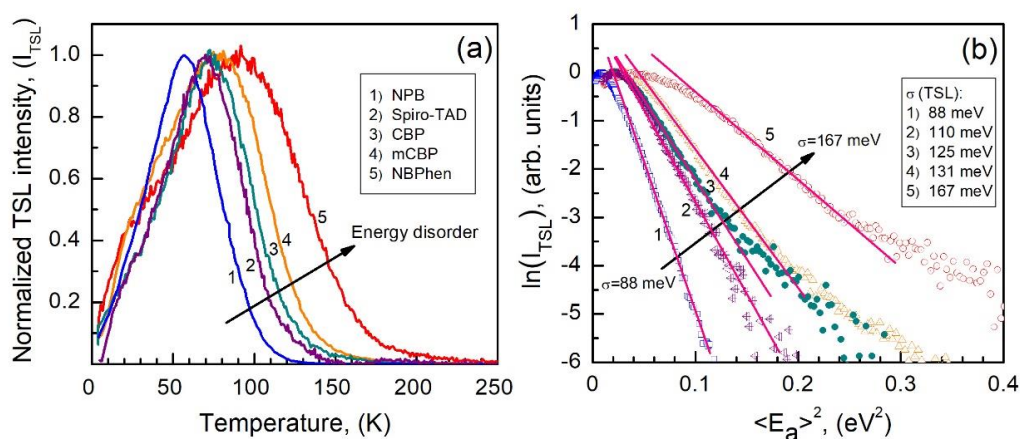
Figure S14(a) Normalized spectrally integrated TSL glow curve measured at the constant heating rate 0.15 K/s after excitation with 313nm-light for 3 min at 4.2 K in NPB, Spiro-TAD, CBP, mCBP, and NBPhen films (curve 1, 2, 3, 4, 5, respectively). (b) "Gaussian" analysis of high temperature wings of the TSL curves shown in (a). The temperature scale was converted to a trap energy scale $\langle Ea \rangle (T)$ using the following empirical calibration relation $\langle Ea \rangle = 0.0032 \times T - 0.091$ (in eV) (see [8] for details) obtained by fractional TSL measurements, and then the high-temperature part of the TSL signal intensity was plotted logarithmically against $\langle Ea \rangle 2$. The slope of the straight lines is a measure of the DOS width, and the extracted σ-parameters for the above materials are listed in the Inset. More details about the TSL data analysis can be found elsewhere.[9]
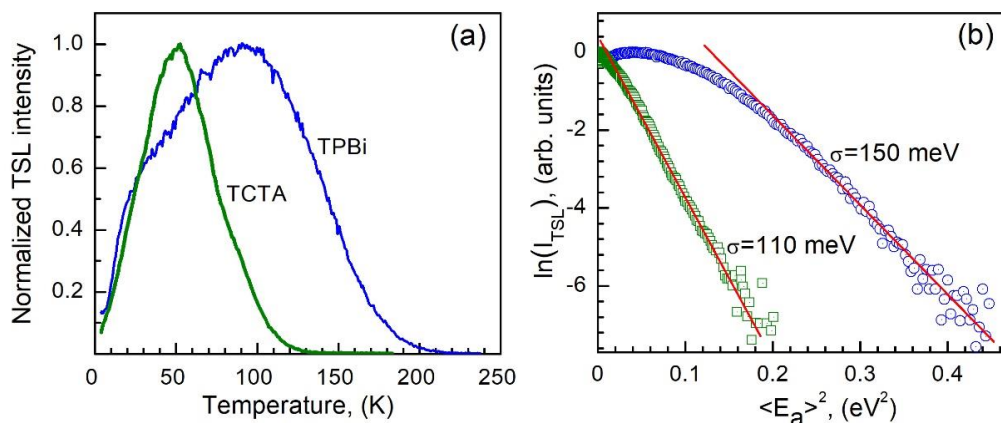
Figure S15 (a) Normalized spectrally integrated TSL glow curve measured at the constant heating rate 0.15 K/s after excitation with 313nm-light for 3 min at 4.2 K in TCTA and TPBi films (curve 1 and 2, respectively). (b) "Gaussian" analysis of high temperature wings of the TSL curves shown in (a), which is done using the same procedure as mentioned in Figure S14(b).
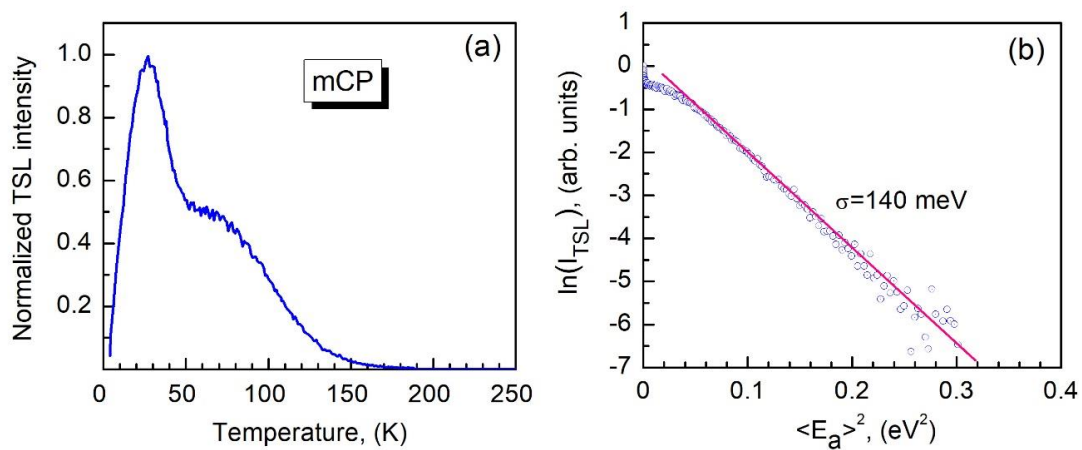
Figure S16 (a) Normalized spectrally integrated TSL glow curve measured after excitation with 313nm-light for 3 min at 4.2 K in a mCP film. (b) "Gaussian" analysis of high temperature wings of the TSL curve shown in (a), which is done using the same procedure as mentioned in Figure S14(b).

References

(1)   Sun, H.; Ryno, S.; Zhong, C.; Ravva, M. K.; Sun, Z.; Körzdörfer, T.; Brédas, J.-L. Ionization Energies, Electron Affinities, and Polarization Energies of Organic Molecular Crystals: Quantitative Estimations from a Polarizable Continuum Model (PCM)-Tuned Range-Separated Density Functional Approach. *J. Chem. Theory Comput.* **2016**, *12* (6), 2906–2916. https://doi.org/10.1021/acs.jctc.6b00225.

(2)   Dutta, A. K.; Saitow, M.; Riplinger, C.; Neese, F.; Izsák, R. A Near-Linear Scaling Equation of Motion Coupled Cluster Method for Ionized States. *The Journal of Chemical Physics* **2018**, *148* (24), 244101. https://doi.org/10.1063/1.5029470.

(3)   Dutta, A. K.; Saitow, M.; Demoulin, B.; Neese, F.; Izsák, R. A Domain-Based Local Pair Natural Orbital Implementation of the Equation of Motion Coupled Cluster Method for Electron Attached States. *J. Chem. Phys.* **2019**, *150* (16), 164123. https://doi.org/10.1063/1.5089637.

(4)   Stein, T.; Kronik, L.; Baer, R. Reliable Prediction of Charge Transfer Excitations in Molecular Complexes Using Time-Dependent Density Functional Theory. *J. Am. Chem. Soc.* **2009**, *131* (8), 2818–2820. https://doi.org/10.1021/ja8087482.

(5)   Dandrade, B.; Datta, S.; Forrest, S.; Djurovich, P.; Polikarpov, E.; Thompson, M. Relationship between the Ionization and Oxidation Potentials of Molecular Organic Semiconductors. *Organic Electronics* **2005**, *6* (1), 11–20. https://doi.org/10.1016/j.orgel.2005.01.002.

(6)   Stone, A. J. Distributed Multipole Analysis: Stability for Large Basis Sets. *J. Chem. Theory Comput.* **2005**, *1* (6), 1128–1132. https://doi.org/10.1021/ct050190+.

(7)   Lukyanov, A.; Andrienko, D. Extracting Nondispersive Charge Carrier Mobilities of Organic Semiconductors from Simulations of Small Systems. *Phys. Rev. B* **2010**, *82* (19), 193202. https://doi.org/10.1103/PhysRevB.82.193202.

(8)   Stankevych, A.; Vakhnin, A.; Andrienko, D.; Paterson, L.; Genoe, J.; Fishchuk, I.; Bässler, H.; Köhler, A.; Kadashchuk, A. Density of States of OLED Host Materials from Thermally Stimulated Luminescence. *Phys. Rev. Applied* **2021**, *15* (4), 044050. https://doi.org/10.1103/PhysRevApplied.15.044050.

(9)   Kadashchuk, A.; Weiss, D. S.; Borsenberger, P. M.; Nešpùrek, S.; Ostapenko, N.; Zaika, V. The Origin of Thermally Stimulated Luminescence in Neat and Molecularly Doped Charge Transport Polymer Systems. *Chemical Physics* **1999**, *247* (2), 307–319. https://doi.org/10.1016/S0301-0104(99)00169-X.

Paper 4: Charge-carrier photogeneration in single-component organic carbazole-based semiconductors via low excitation power triplet-triplet annihilation

Andrei Stankevych[#], Rishabh Saxena[#], Jeannine Grüne, Sebastian Lulei, Andreas Sperlich, Stavros Athanasopoulos, Alexander Vakhnin, Prakhar Sahay, Wolfgang Brütting, Vladimir Dyakonov, Heinz Bässler, Anna Köhler, Andrey Kadashchuk

[#]Authors contributed equally.

Charge-carrier photogeneration in single-component organic carbazole-based semiconductors via low excitation power triplet-triplet annihilation

Andrei Stankevych[1,2,‡] Rishabh Saxena[1,‡] Jeannine Grüne,[3,4] Sebastian Lulei,[3]
Andreas Sperlich,[3] Stavros Athanasopoulos,[5] Alexander Vakhnin,[2] Prakhar Sahay,[6]
Wolfgang Brütting,[6] Vladimir Dyakonov,[3] Heinz Bässler,[7] Anna Köhler,[1,7] and
Andrey Kadashchuk[1,2,*,†]

[1]*Soft Matter Optoelectronics and Bavarian Polymer Institute (BPS), University of Bayreuth, Universitätsstr. 30, 95448 Bayreuth, Germany*

[2]*Institute of Physics, National Academy of Sciences of Ukraine, Prospect Nauky 46, 03028 Kyiv, Ukraine*

[3]*Experimental Physics VI and Würzburg-Dresden Cluster of Excellence ct.qmat, Julius-Maximilians-Universität Würzburg, 97074 Würzburg, Germany*

[4]*Cavendish Laboratory, University of Cambridge, JJ Thomson Avenue, Cambridge CB3 0HE, UK*

[5]*Departamento de Física, Universidad Carlos III de Madrid, Avenida Universidad 30, Leganés, 28911 Madrid, Spain*

[6]*Institute of Physics, University of Augsburg, Universitätsstr. 1, 86159 Augsburg, Germany*

[7]*Bayreuth Institute of Macromolecular Research (BIMF), University of Bayreuth, Universitätsstr. 30, 95448 Bayreuth, Germany*

It is generally believed that intrinsic charge generation via an autoionization mechanism in pristine single-component organic semiconductors is impossible upon photoexcitation within the lowest excited singlet state due to the large exciton binding energy. However, we present measurements of thermally stimulated luminescence, light-induced ESR, and photocurrent in the carbazole-based molecule 3′,5-di(9H-carbazol-9-yl)-[1,1′-biphenyl]-3-carbonitrile (mCBP-CN) films, revealing that charge-carrier pairs are efficiently produced upon excitation near their absorption edges. The photocurrent measurements show a superlinear dependence on the cw-photoexcitation intensity even at very low excitation power (below 1 mW/cm^2), suggesting a bimolecular nature of the charge photogeneration process. The photocurrent measured over a broad temperature range of 5–300 K exhibits a prominent maximum at moderately low temperature around 170 K and rolls off significantly at higher temperatures. This correlates remarkably with the maximum of delayed fluorescence induced by bimolecular triplet-triplet annihilation (TTA), i.e., triplet fusion, in this material. This behavior implies that the photocurrent is governed mainly by the TTA-induced production of geminate pairs and only a little by their subsequent dissociation. Moreover, we find that the field-assisted dissociation probability of photogenerated charge pairs becomes almost temperature-independent at temperatures below 100 K. This can be quantitatively described using a charge dissociation model accounting for the energy disorder and the distribution of geminate-pair radii. The key conclusion of this study is that triplet fusion can promote the energy up-conversion (to 5.42 eV), thereby enabling the autoionization of a high-energy neutral excited state. This serves as the predominant mechanism of intrinsic photogeneration in this single-component heavy-atom-free system. We attribute the effect to efficient intersystem crossing in mCBP-CN, a high triplet energy level (2.71 eV), and very long-lived triplet excitations. A broader implication of this finding is that the so far neglected mechanism of TTA-facilitated charge-carrier generation might be relevant for organic long-persistent luminescence materials, and even for organic photovoltaics and potentially for photocatalytic water splitting processes.

I. INTRODUCTION

Triplet-triplet annihilation (TTA) is a common bimolecular process that can occur in any organic solids

where the high density of spin-triplet excitons and their ability to diffuse facilitate a non-negligible encounter probability during their (long) lifetime. Efficient photon energy up-conversion (UC) enabled by TTA under low excitation intensities is a well-established phenomenon for organic *two-component systems* employing heavy metal organic complexes as triplet sensitizers [1–5]. This implies the population of a singlet excited state via fusion of

*Corresponding author. kadash@iop.kiev.ua
†andriy.kadashchuk@uni-bayreuth.de
‡Authors contributed equally to this work

two lower-energy triplet excitons sensitized by embedded triplet "sensitizers" in a fluorescent "emitter" host material. Because these triplet sensitizers exhibit a high triplet population at room temperature, the TTA-UC in such composite films can occur at continuous-wave (cw)-excitation intensities as low as around 1 mW/cm^2 of noncoherent light. Therefore, such bimolecular energy UC is of interest for various photonic applications [6–8]. It is particularly interesting for organic solar cells, since it potentially enhances the efficiency of photovoltaic devices. The efficiency increase occurs, for example, by utilizing near-infrared photons beyond the band gap of solar cells via their UC to visible light [9] or by limiting triplet-related nonradiative losses [10,11]. The TTA-UC process is also viewed as an alternative or complementary mechanism to thermally activated delayed fluorescence and phosphorescence emitter strategies of utilizing the nonemissive triplets in organic light-emitting diode (OLED) devices [12–14], which may also solve the problem of the "efficiency roll-off" associated with these devices. Moreover, considering the easily tunable excitation and/or emission wavelength and low power excitation, the TTA-UC organic systems can be especially promising for photocatalytic water splitting to produce hydrogen [15], as they could be combined with a variety of photocatalysts that are only photoactive under ultraviolet light or in the short-wavelength region of visible light. In this study, we highlight another intriguing application of TTA as a major mechanism of intrinsic photocurrent (PC) generation in a *single-component*, heavy-atom-free annihilator medium, showing self-TTA. This mechanism has just recently been suggested for the single-component metal-organic complex of platinum(II) octaethylporphyrin (PtOEP) containing a heavy atom [16].

It is generally established that thermally stimulated luminescence (TSL) [17] and light-induced electron spin resonance (LESR) techniques [18,19] are valuable tools for probing trapped charge carriers in organic semiconductors. Of particular relevance is that both are electrode-free techniques that allow the separation of interface or contact effects from intrinsic bulk effects and do not require good charge transport in the material. Moreover, these techniques can be applied at very low temperature, enabling the characterization of even very shallow charge trapping. A lesser-known aspect of their use is that the action spectra of TSL and LESR signals could also provide essential information regarding charge-carrier photogeneration mechanisms in these materials [20,21]. Indeed, the LESR action spectra measured in films of the conjugated polymers of cyano-substituted poly(*p*-phenylene vinylene) (CN-PPV) and poly(2-methoxy,5-(2′-(ethyl-hexyloxy)-*p*-phenylene vinylene) (MEH-PPV) have demonstrated a clear threshold behavior at energies significantly exceeding the energy of the lowest singlet exciton (S_1) transition, which was found to match well with the PC action spectra reported for PPV derivatives [22]. The latter was attributed

to intrinsic bulk charge-carrier photogeneration and the observed energy offset relative to the absorption spectra can provide an estimate for the exciton binding energy.

Similar behavior has been observed for the action spectra of TSL measured for various PPV derivatives [20,23]; namely, the TSL signal drastically increased with increasing excitation photon energy well above the $S_0 \rightarrow S_1$ absorption edge of these polymers. Thus, since TSL in organic semiconductors is believed to arise from the recombination of long-range geminate charge-carrier pairs [17,24,25], the TSL action spectra can be used to assess the carrier photogeneration efficiency in response to excitation photon energy. It is important to note that TSL probes geminate pairs generated predominantly through intrinsic photogeneration. This is because (i) TSL excludes electrode-sensitized charge photogeneration, in contrast to the thermally stimulated current technique [26], and (ii) any geminate pairs generated extrinsically via exciton dissociation at incidental (most likely acceptor-like) impurities, such as oxygen, are expected to recombine nonradiatively at impurity moieties that serve as recombination centers and thus make no contribution to the TSL signal. Despite this, some organic semiconductors, such as ladder-type methyl-substituted poly(phenylene), poly(*N*-vinyl carbazole), and different polyfluorene derivatives, show a surprisingly strong TSL under excitation at the optical absorption edge, with no appreciable dependence of TSL intensity on excitation photon energy above the optical gap [17,24]. This phenomenon has so far remained unresolved.

The present study was motivated by an intriguing recent observation of strong TSL signals under excitation *at the optical absorption edge* in pristine amorphous films of a large set of small-molecule carbazole-based OLED host materials [25,27], implying efficient carrier photoproduction within the lowest excited singlet state in *single-component* materials. This work focuses on 3′,5-di(9*H*-carbazol-9-yl)-[1,1′-biphenyl]-3-carbonitrile (mCBP-CN), a common wide-band-gap host material for blue emitters in OLEDs owing to its high triplet level, which was chosen here as an exemplary material exhibiting a significant phosphorescence emission at low temperatures. For comparison purposes, we also measured the TSL action spectra in a regioregular poly-3-hexylthiophene (rr-P3HT), chosen as a *representative counterexample*, i.e., a well-known nonphosphorescent material [28]. We found that the TSL of rr-P3HT behaves fundamentally differently, featuring a significant energy offset (0.6–0.7 eV) of the onset of its TSL action spectrum with respect to the absorption edge.

To clarify the mechanism of charge photogeneration in neat mCBP-CN films, we undertook a comprehensive study employing a range of techniques, including PL spectroscopy, LESR, PL-detected magnetic resonance (PLDMR), and PC measurements. We demonstrate that a large population of triplet excitons and concomitant

177

efficient TTA-UC occurring even at very low cw-excitation intensities lead to the autoionization of a high-energy neutral excited state. This is the dominant mechanism of geminate-pair generation in this material. In contrast, there is no noticeable population of triplets in rr-P3HT films owing to its very low intersystem crossing (ISC) rate upon excitation within the S_1 excited state. Accordingly, this results in negligible intrinsic charge generation. Hence, charge generation in mCBP-CN films is a bimolecular process, as evidenced by the observed supralinear dependence of the PC upon excitation intensity. Its efficiency exhibits the temperature dependence characteristic of the TTA process, namely peaking at moderately low temperatures and drastically decreasing when approaching room temperature because of progressively enhanced monomolecular triplet quenching by impurities. Concomitantly, the PC is observed only at low temperatures, and exhibits a prominent maximum at 170 K. This maximum is found to be mainly determined by the TTA-induced geminate-pair generation process. In contrast, the temperature dependence of the dissociation probability for the TTA-induced geminate pair is found to play a secondary role. In fact, we find that the field-assisted dissociation probability is surprisingly almost temperature independent at low temperatures $T \le 100$ K, which can be well described within a charge dissociation model by accounting for the presence of energy disorder and longer-distance geminate pairs.

II. EXPERIMENT

A. Materials

mCBP-CN [see Fig. 1(a)] was purchased from Lumtec Corp. and used as received. For spectroscopy measurements, thin films of the mCBP-CN are spin-coated from 20-mg/ml chloroform solutions onto cleaned fused quartz substrates (1000 rpm, 30 s) that typically result in 50-nm-thick layers. Subsequently, the deposited films are dried in an oven at 40 °C for 10 min and then under vacuum for 2 h to remove residual solvent. For photocurrent measurements, mCBP-CN films are vacuum evaporated with a typical thickness of 150 nm. Photodiode devices with evaporated mCBP-CN active layers have a conventional configuration of glass/ITO(90 nm)/poly (3,4-ethylenedioxythiophene):poly(styrenesulfonic acid) (PEDOT:PSS)(25 nm)/mCBP-CN(150 nm)/LiF(0.5 nm)/ Al(100 nm).

B. Optical spectroscopy measurements

Steady-state absorption and PL spectra are measured using a double-beam Shimadzu 2450 UV-VIS spectrophotometer and a Jasco FP-8600 spectrofluorometer equipped with a Xe arc lamp (150 W) as an excitation light source. The spectrofluorometer also allows PL measurements in phosphorescence mode, for which the excitation light is chopped, the detector unit is opened at a delay of 50 ms after excitation, and the signal is acquired for 100 ms. For the 77 K measurements, the sample is immersed in liquid nitrogen. Photoluminescence quantum yield (PLQY) is measured using an integrating sphere coupled to the spectrofluorometer.

Time-resolved PL measurements are made using a setup consisting of a spectrograph coupled to a gated intensified charge-coupled device (ICCD) camera (Andor iStar 334) for acquiring emission spectra with distinct delay and integration time, where samples are excited with a frequency-tripled Nd:YAG laser (Innolas SpitLight 600) with a wavelength of 355 nm (3.5 eV). All experiments are performed with the sample in a temperature-controlled continuous flow helium cryostat (Oxford Instruments OptistatCF).

C. Photocurrent measurements

Stationary PC measurements are conducted in the same temperature-controlled helium cryostat, using excitation from a 1200-W Xe arc lamp coupled to a double-grating monochromator for wavelength selection. The temperature
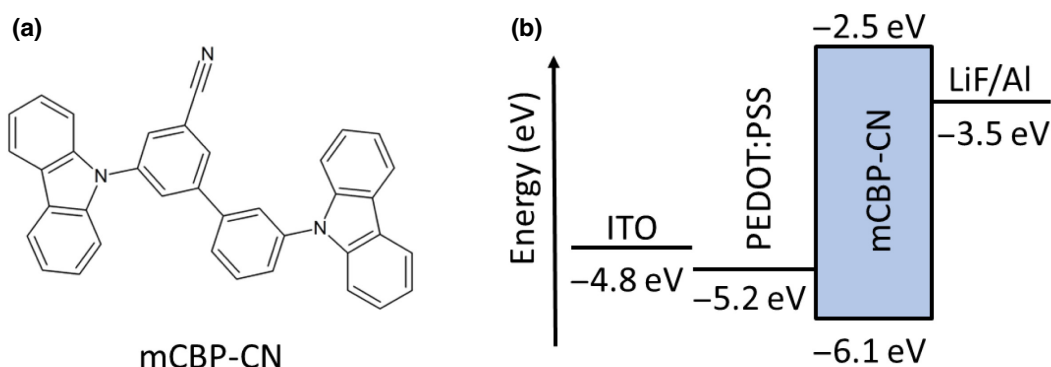
FIG. 1 (a) Molecular structure of mCBP-CN, (b) schematic energy levels diagram of investigated mCBP-CN single-layer photodiode.

dependence of the PC is measured at a weak cw-excitation power (0.54 mW/cm^2) at 355 nm. To measure the excitation intensity dependence of the PC, we employ an appropriate set of neutral density filters. PC action spectra are measured at a reverse bias of -7 V and using a lock-in technique for signal detection. To ensure that the PC has stabilized and is representative, we wait for 15 s after each monochromator advance and take several averages. The PC action spectrum is then corrected to account for the effective absorption spectrum of the mCBP-CN layer embedded in the device [Fig. 1(b)]. We calculate the effective absorption spectrum by using a transfer matrix approach implemented by Burkhard *et al.* [29]. The real and imaginary part of the refractive index, *n* and *k*, were measured for mCBP-CN by Naqvi *et al.* [30] using Sentec SE 850 Spectroscopic Ellipsometry along with SPECTRARAY software for the fitting. For other layer materials, we use the values provided in Ref. [29].

D. Thermally stimulated luminescence measurements

TSL is the phenomenon of light emission arising after the removal of excitation (UV light, in our case) under conditions of increasing temperature. Generally, in the TSL method, the trapping states are first populated by the photogeneration of charge carriers, usually at low temperatures. After terminating the excitation, the trapped charge carriers can be released by heating the sample and the luminescence due to charge recombination is recorded as a function of temperature. TSL measurements are carried out using a homebuilt system over a temperature range from 5 to 300 K using an optical temperature-regulating helium cryostat (see Ref. [27] for more details). More specifically, after cooling to 5 K, the samples are photoexcited, usually for 30 s, with a high-pressure 500-W mercury lamp with an appropriate set of glass optical filters for light selection, or with a UV LED emitting at 274 nm. After that, the samples are kept in the dark at a constant temperature (5 K) during a certain dwell time (typically 15 min) before the TSL heating run begins to allow the long isothermal afterglow (arising due to isothermal recombination of short-range geminate pairs) to decay to a negligible value. Then TSL measurements are started upon heating the sample from 5 to 300 K with a linear heating ramp (at constant heating rate, $\beta = 0.15$ K/s). TSL emission is detected with a cooled photomultiplier tube operated in photon-counting mode, attached to the cryostat window. We also measure the TSL action spectra; namely, the dependence of the integrated TSL intensity, i.e., the area under the TSL glow curve, upon the photon energy of excitation ($E_{h\upsilon}$). Since the TSL intensity may nonlinearly depend on the intensity of the incident light, the photon flux from different emissive lines of the mercury lamp used for TSL excitation is balanced by an appropriate attenuation of the stronger lines. Finally, the spectral range of the TSL emission is

roughly estimated using a set of glass cutoff filters, as demonstrated in Ref. [31].

E. Light-induced ESR and PL-detected magnetic resonance

PLDMR and LESR experiments are carried out with a modified *X*-band spectrometer (Bruker E300) equipped with a continuous-flow helium cryostat (Oxford ESR 900) and a microwave cavity (Bruker ER4104OR, approximately 9.43 GHz) with optical access. Optical excitation is performed with either a 305-nm or 365-nm UV LED through the aperture in the cavity. Generally, PLDMR probes the microwave-induced PL changes at the resonance magnetic field for triplets or charges. For PLDMR, PL is detected with a silicon photodiode (Hamamatsu S2281), using a 355-nm or 409-nm long-pass filter to suppress the excitation light. The PL signal is amplified by a current and/or voltage amplifier (Femto DHPCA-100) and recorded by a lock-in amplifier (Ametek SR 7230), referenced by on-off-modulating the microwaves with a modulation frequency of 517 Hz. The microwaves are generated with a microwave signal generator (Anritsu MG3694C), amplified to 3 W (Microsemi), and guided into the cavity. For LESR spectra and transients, a microwave bridge (Bruker ER 047 MRP) provides microwave power up to 200 mW. An arbitrary waveform generator (Keithley 3390) provides 100-kHz sinusoidal field modulation superimposed onto the main magnetic field, referencing the lock-in amplifier. For transient LESR, the lock-in time constant is set to 100 ms to not influence the detected signal decay times. For LESR studies, a small amount of the mCBP-CN solution is poured into an ESR tube and vacuum dried, leaving a film of mCBP-CN on the tube wall. For PLDMR samples, the same spin-coated films used for optical spectroscopy are used by inserting them into ESR tubes. All ESR tubes are finally sealed under a helium atmosphere.

III. RESULTS

A. Spectroscopic and photocurrent measurements

A basic spectroscopical characterization of mCBP-CN films is shown in Fig. 2. For comparison, Fig. 2 also presents measurements for P3HT, which is chosen as a representative counterexample, i.e., a well-known nonphosphorescent material [28]. The steady-state PL emission spectrum of a mCBP-CN film is depicted by the blue solid curve in Fig. 2(a) and reveals both fluorescence and phosphorescence components clearly seen under cw-excitation at 77 K. The fluorescent component is characterized by a relatively broad structureless band peaking at 405 nm, which is a consequence of the charge transfer (CT)-character of the lowest singlet state of mCBP-CN due to presence of an acceptor

CN group. The latter also results in a slightly lower energy of the singlet state in this material, whose 0–0 transition is very close to the onset of emission at $S_1 = 3.30$ eV, as compared to mCBP films ($S_1 = 3.47$ eV) [33] devoid of such a CN group. The phosphorescence component dominates the delayed emission [blue dashed curve in Fig. 2(a)] measured using the same excitation light. In contrast to the fluorescence, the phosphorescence features a well-resolved vibronic structure of the $T_1 \rightarrow S_0$ emission spectrum with the 0–0 vibrational transition at $T_1 = 2.71$ eV, similar to that observed in mCBP films. As has been demonstrated before [33], such phosphorescence has been attributed to triplet excitation localized on the central biphenyl core in meta-linked carbazole-biphenyl materials, rather than on the carbazole moiety of such molecules, which has also been supported

by quantum chemical calculations [34]. It is noteworthy that the phosphorescence of mCBP-CN films is readily visible even in steady-state PL spectra at 77 K; it appears as additional narrower peaks in the range $\lambda > 450$ nm superimposed on the broad fluorescence band [blue solid curve in Fig. 2(a)], implying a quite efficient ISC process in this material. Using the PLQY value of 11% (at 293 K) we measure in the mCBP-CN films, the ISC rate is estimated as $k_{\mathrm{ISC}} = 1.8 \times 10^8$ s^{-1}, which is higher than the radiative rate of singlet excitations, $k_r^S = 2.1 \times 10^7$ s^{-1}, in this material. The delayed emission also reveals a delayed fluorescence (DF) component identical to the prompt fluorescence with a maximum at 405 nm [Fig. 2(a) dashed blue curve], which originates from the TTA process, as will be shown in the following.
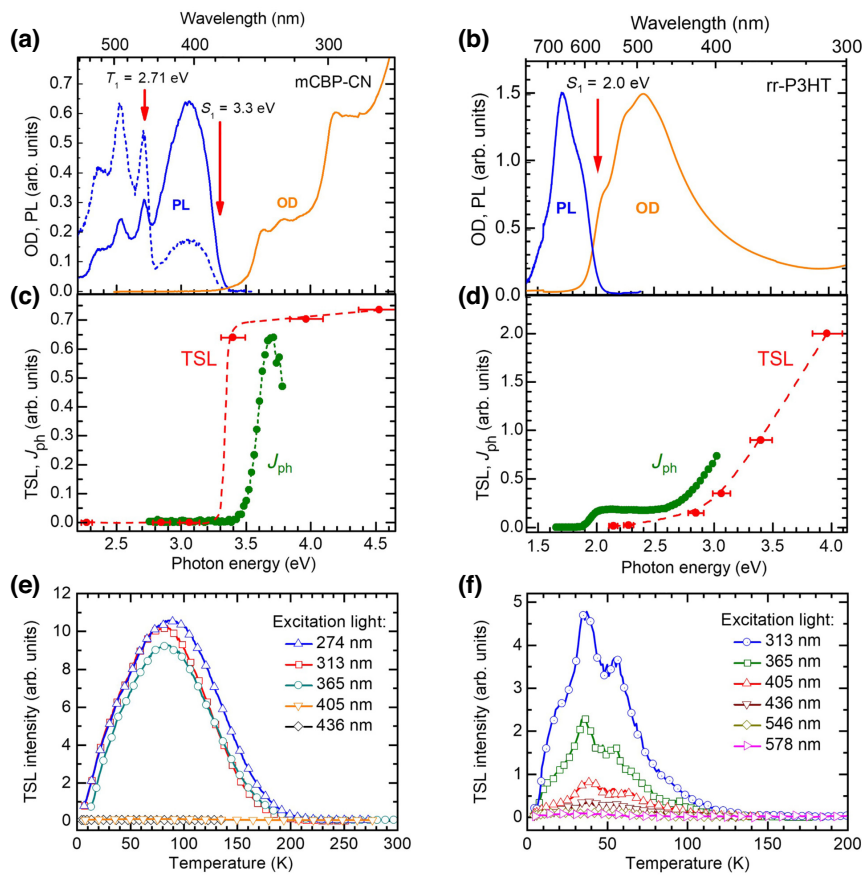
FIG. 2. (a) Absorption (orange solid line) where OD denotes optical density, low-temperature steady-state PL (blue solid line), and delayed emission (blue dashed line) of a mCBP-CN film measured at 77 K with a standard spectrofluorometer using a Xe lamp for excitation. The delayed emission is measured with 50-ms delay time after excitation and an integration time of 100 ms. (b) Absorption (orange solid line) and steady-state PL (blue solid line) measured at 77 K of a rr-P3HT film. (c) Dependence of the integrated TSL intensity upon the photon energy of excitation (red symbols) and PC action spectra (green symbols) of a mCBP-CN film; (d) action spectrum of TSL (red symbols) measured in this work as well as PC (green circles) adopted from Ref. [32] for rr-P3HT film. Dashed lines are a guide to the eye. (e) TSL glow curves of mCBP-CN film and of (f) a rr-P3HT film, both measured after excitation at 5 K with different photon energies of the cw-excitation light (wavelengths of the excitation are indicated in the figure).

As expected, in contrast to the mCBP-CN films, no phosphorescence component is found either in steady-state or delayed emission in rr-P3HT films even at low temperatures, owing to the negligible triplet state population in this system [28]. Figure 2(b) shows absorption spectra and cw-PL for a rr-P3HT film (orange and blue curves, respectively), exhibiting only fluorescence emission.

TSL in disordered organic semiconductors is known to originate from radiative recombination of spatially well separated trapped charge-carrier pairs created during photoexcitation of the sample at a low temperature [24,27]. The measured TSL curve itself is known to map a distribution of charge carriers localized within the lower-energy part of the intrinsic density of states (DOS). This technique allows determination of the width of the DOS σ_{DOS}, which has been found to be 151 meV in mCBP-CN films [27]. Action spectra of TSL (red circles) for mCBP-CN and rr-P3HT films are presented in Figs. 2(c) and 2(d), respectively. The TSL action spectra are obtained by plotting the integrated TSL intensity, calculated as the area under the TSL curves shown in Figs. 2(e) and 2(f), versus the photon excitation energy ($E_{h\nu}$). These action spectra demonstrate the fundamental difference in the TSL behavior between mCBP-CN and rr-P3HT. That is, there is a *significant energy offset* between the absorption edge and the action spectrum of TSL for rr-P3HT [Fig. 2(d)], while, in contrast, TSL intensity in mCBP-CN is virtually independent of $E_{h\nu}$ above the optical gap [Fig. 2(c)]. For rr-P3HT, the onset of the TSL action spectrum [Fig. 2(d)] is approximately 0.6–0.7 eV higher than the lowest singlet exciton state $S_1 = 2.0$ eV, which is in agreement with the exciton binding energy of 0.7 eV determined by Deibel *et al.* [32] from the combined spectrally resolved PC and photoemission measurements. This perfectly agrees with transient absorption measurements [28], showing that in single-layer P3HT devices the charge carriers are generated only from hot excitons and not from relaxed singlet exciton states. It is therefore reasonable to expect a similar offset for the TSL action spectrum. In contrast, the TSL intensity of the mCBP-CN films rises steeply at the optical gap and then appears to be remarkably *independent* of the energy of the excitation photons $E_{h\nu}$ above the optical gap [Figs. 2(c) and 2(e)]. mCBP-CN shows the same TSL signal even at zero excess photon energy of the exciting illumination with 365-nm light, i.e., within the lowest singlet S_1 state.

Figures 2(c) and 2(d) also present the action spectra of the PC (green circles) using photodiodes based on mCBP-CN (measured at 5 K) and rr-P3HT (measured at ambient temperature), respectively. The curves turn out to be similar to the action spectra of TSL. That is, for mCBP-CN, the PC rises sharply at the onset of absorption (some apparent decrease above 3.7 eV is due to absorption of the glass substrate covered with ITO and PEDOT:PSS layers). The PC is measured at a reverse bias of −7 V, which

prevents electrode-sensitized photogeneration of charge carriers [35]. This indicates that the PC in mCBP-CN films is dominated by intrinsic bulk photogeneration, similar to the situation in TSL. In the photodiode made with rr-P3HT, we see a small PC component at the onset of absorption attributed to *extrinsic* dissociation, and the main onset at higher energies congruent with the electrical gap. The latter is the *intrinsic* PC resulting from autoionization that also produces the geminate pairs probed by the TSL signal.

The DF component seen in Fig. 2(a) (dashed blue curve) is spectrally identical to the prompt fluorescence (solid blue curve). This suggests the presence of a mechanism that involves triplet excitons, as demonstrated in the following. To elucidate the role of TTA in photophysical processes in the mCBP-CN films, we employ time-resolved PL measurements with pulsed nanosecond-laser excitation. Figure 3(a) shows the dependence of DF and phosphorescence intensity on variable laser excitation intensity for the mCBP-CN film at 5 K. The emission is recorded with a time delay of 2 ms after the laser excitation pulse at 355 nm (3.5 eV) and the gate width of 2 ms. The plotted emission intensities are obtained by integrating over the wavelength. The actual delayed emission spectra are presented in Fig. S1(a) of the Supplemental Material [36]. The phosphorescence intensity shows almost a square-root increase with increasing excitation laser power ($I_{ph} \sim I_{exc}^m$, where $m = 0.63$), implying that TTA is a dominant mechanism for depletion of the triplet reservoir in the range of laser intensities used in this experiment [37,38]. The DF intensity increases more steeply with increasing laser intensity, revealing an almost doubled exponent [37] with respect to the phosphorescence intensity increase ($m = 1.14$). The latter strongly suggests that DF emission is predominantly caused by TTA processes in this material.

Figure 3(b) presents the temperature dependence of the spectrally integrated phosphorescence intensity, DF intensity, and the PC (green triangles, blue squares, and red circles, respectively) measured from the same mCBP-CN film. As evident from Fig. 3(b), the phosphorescence intensity decreases monotonically with increasing temperature from 5 to 290 K. See Fig. S1(b) of the Supplemental Material [36] for the actual delayed emission spectra. In contrast, the DF detected in the same time slot of the ICCD detector first increases to its maximum intensity at around 110 K and then drops to an almost negligible level at room temperature. Note that the DF reaches its maximum intensity at a temperature T_{max} where the phosphorescence intensity is reduced to 50% of its value at 5 K. It should be emphasized that this type of temperature dependence peaking at an intermediate temperature is *very characteristic of DF* and was previously observed for DF in films of polyfluorene oligomers [39]. It has already been shown using a kinetic equation approach and kinetic Monte Carlo simulations [40] that the observed nonmonotonic temperature dependence of DF is a consequence
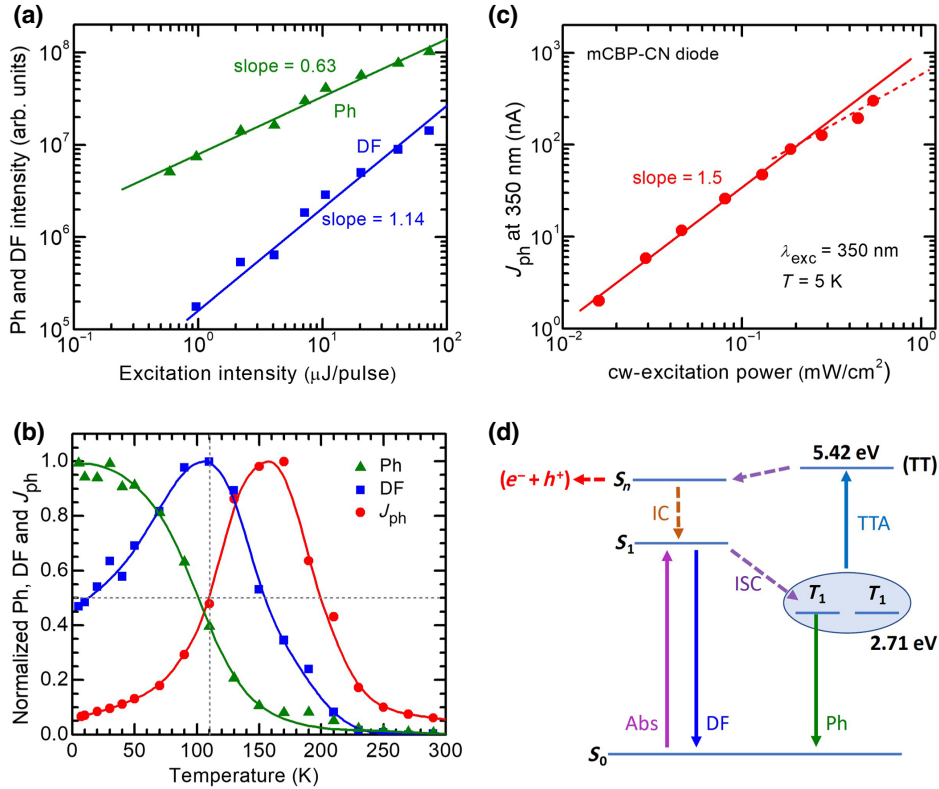
FIG. 3.   Evidence for efficient TTA in mCBP-CN films: (a) dependence of spectrally integrated phosphorescence (Ph) (green triangles) and DF (blue squares) intensity on pulsed nanosecond-laser excitation intensity at 5 K, along with power-law fits to the data (solid line); (b) intensity of spectrally integrated Ph, DF, and PC (J_{ph}) versus temperature (symbols), along with guides to the eye (solid lines); (c) double-logarithmic plot of the PC vs cw-excitation intensity at 350 nm measured at 5 K (red circles). The observed supralinear dependence with slope 1.5 indicated by the red line is principally similar for the diode measured at both short-circuit and reverse bias (-7 V) conditions. (d) Suggested simplified energy diagram for the charge photogeneration process in mCBP-CN films, where IC and ISC denotes internal conversion and intersystem crossing, respectively.

of the temperature-dependent interplay between TTA and monomolecular quenching of the triplet excitations by quenching centers, controlled by thermally activated triplet exciton diffusion. At lower temperature, triplet diffusion causes TTA so that the phosphorescence is reduced and DF can be observed. The yield of this process increases with increasing temperature until the growing diffusion to quenching sites becomes sufficiently significant to reduce the triplet population and hence to curb the TTA process so that the DF falls off.

A similar nonmonotonic temperature dependence is also observed for the photocurrent J_{ph} measured in a mCBP-CN diode at very weak cw-excitation, which correlates with the temperature-dependent DF, although somewhat shifted towards higher temperatures [red circles, Fig. 3(b)]. The $J_{\mathrm{ph}}(T)$ features a clear maximum at a moderately low temperature of around 170 K, followed by a drastic decrease in the PC up to room temperature. This

suggests that the temperature dependence of the photocurrent $J_{\mathrm{ph}}(T)$ is mostly governed by the TTA-UC-induced generation of the higher lying singlet state from which the geminate pairs are then generated, and less by a thermally activated field-assisted dissociation of these TTA-induced geminate pairs into free carriers. Figure 3(c) shows that the PC exhibits the supralinear dependence on cw-excitation power ($J_{\mathrm{ph}} \propto I_{\mathrm{exc}}^m$, where $m = 1.5$) measured in the range $0.016 < I_{\mathrm{exc}} < 0.54$ mW/cm^2, i.e., under very low light fluences, evidencing that carrier photogeneration is a bimolecular process in this system. It is worth mentioning that a similar supralinear dependence with an exponent $m = 1.7$ was recently reported for a TTA-based up-converted fluorescence observed in virtually the same excitation power range $I_{\mathrm{exc}} < 0.4$ mW/cm^2 in poly(styrene) nanoparticles doped with PtOEP and 9,10-diphenylanthracene [41]. Moreover, exponents of 1.47 to 1.57 have been reported for

TTA-induced enhanced PLDMR in nonfullerene acceptors (NFAs) and for TTA up-converted PL in bilayer NFA/rubrene systems, respectively [10,42]. The exact origin of such TTA behavior requires further investigation; however, Izawa and Hiramoto [42] have speculated that the value $m < 2$ may be attributed to some other parallel triplet quenching processes, such as triplet quenching by charge carriers.

The observed bimolecular character of the PC in mCBP-CN films [Fig. 3(c)], as well as the remarkable correlation between temperature dependences of the DF and the $J_{ph}(T)$ [Fig. 3b)], with both reaching a maximum value at moderately low temperatures and rolling off towards room temperatures, implies that the PC is governed by the TTA-UC-induced photogeneration of charge carriers. This mechanism is schematically depicted in Fig. 3(d): owing to the high energy of the lowest triplet state in mCBP-CN, the efficient TTA process can promote the energy UC to 5.42 eV (2.71 eV + 2.71 eV) and thus provides enough excitation energy to overcome the exciton binding energy, enabling autoionization to yield a separated electron (e^-) and hole (h^+) charge-carrier pair.

B. PLDMR and LESR transient measurements

The TTA process in mCBP-CN films can be studied elegantly using PLDMR, as shown in Fig. 4. The principle of PLDMR investigations of triplet excitons and TTA is illustrated in Fig. S8 of the Supplemental Material [36]. Since TTA and the corresponding DF are spin-dependent, resonant microwave irradiation can modulate TTA probabilities and concomitantly the PL intensity. Figure 4 shows a positive (PL enhancing) half-field PLDMR spectrum at 10 K. In order to clarify how this triplet PLDMR signal is related to fluorescence and phosphorescence pathways, we measure it through either a 355-nm long-pass optical filter (transmitting both fluorescence and phosphorescence, red) or with a 380–420-nm bandpass filter (only the fluorescence component is transmitted, blue). Whilst keeping the measurement conditions the same, the bandpass-filtered spectrum (blue) shows a larger PLDMR contrast ($\Delta PL/PL$). The total PL is reduced considerably when the phosphorescence component is blocked with the bandpass filter, while ΔPL changes less, leading to the increased contrast. However, the decisive factor is not the change in contrast, but that PLDMR is detected at all for the fluorescence component. Direct singlet fluorescence is spin-*independent*, while we observe spin-*dependent* fluorescence. This suggests the enhancement of the fluorescence component is related to a spin-dependent process, such as TTA-induced DF. The higher noise level of the bandpass curve (blue) in contrast to the long-pass curve (red) stems from dividing by the reduced PL intensity. Overall, these results testify that the TTA-induced DF process does take place in this material even at 10 K.
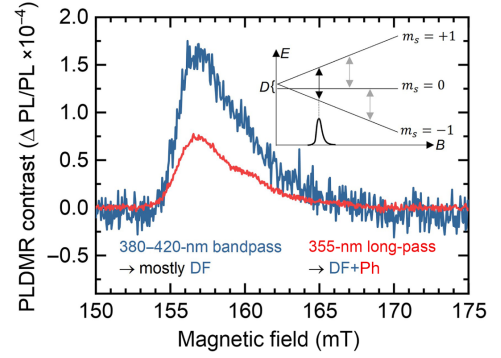
FIG. 4. PLDMR triplet spectra of fluorescence (380–420-nm bandpass filter, blue) and fluorescence plus phosphorescence (overall PL spectrum ≥355 nm, red). The bandpass-filtered DF-based spectrum shows increased PLDMR contrast ($\Delta PL/PL$) in comparison to the long-pass-filtered spectrum that also probes phosphorescence. This is evidence that the PLDMR mostly stems from TTA-UC-induced DF rather than phosphorescence. The inset shows the probed $\Delta m_s = \pm 2$ triplet transition as a black arrow, in contrast to the gray arrows for the $\Delta m_s = \pm 1$ transitions.

To gain a deeper insight into the *formation and recombination dynamics* of the trapped photogenerated charge carriers as well as the *lifetime of triplet excitons* in mCBP-CN films at low temperatures, we apply transient LESR. Since both triplets and charge carriers are paramagnetic excitations, they can be probed by LESR transient measurements, which complement the TSL measurements very well. In contrast to TSL, the ESR technique can potentially be used to estimate the concentration of *trapped charges*, as it results from direct microwave absorption by the paramagnetic species. Another distinguishing feature of LESR and PLDMR techniques is that, unlike TSL, they detect all charge carriers in the film regardless of whether they are generated via intrinsic or extrinsic mechanisms.

Figure 5(a) shows an example of the LESR spectrum of a neat mCBP-CN film at $g = 2$ ($\Delta m_s = \pm 1$, $S = 1/2$, see inset), which is due to photoinduced charge carriers recorded under steady-state 365-nm illumination at 10 K. No "dark" LESR signal is observed prior to illumination, excluding any impurity paramagnetic species. The multiple shoulders and secondary maxima in the low magnetic field region of the observed LESR signal are probably caused by hyperfine interactions of charge carriers with paramagnetic ^{14}N nuclei in mCBP-CN. The shape of this LESR spectrum is also found to depend on microwave power, as demonstrated in Fig. S3 of the Supplemental Material [36]. Another LESR component at $g = 4$ ($\Delta m_s = \pm 2$) is observed in the mCBP-CN film at half-field resonance, as shown in Fig. 5(b), which can only

arise for a total spin of $S > 1$. The position of the half-field signal suggests a high zero-field splitting, i.e., dipolar interaction, supporting the theory of molecular excitons with nearby spins as triplet excitons [43]. The observed LESR triplet spectrum in Fig. 5(b) corresponds to the same transition as the PLDMR spectrum shown in Fig. 4. Since a high zero-field splitting makes the signal in the full field ($\Delta m_s = \pm 1$) very broad, the signal intensity is too low to detect the spectrum in the full field (Fig. S9 of the Supplemental Material [36]). Note, the LESR spectra appear as first derivatives of the microwave absorption signals due to the used magnetic field modulation in contrast to PLDMR. A direct comparison of ESR and PLDMR spectra for charges ($S = 1/2$) and triplets ($S = 1$) is shown in Fig. S10 of the Supplemental Material [36].

This study focuses on the fact that, similar to the TSL, charge-related LESR signals in mCBP-CN films can be observed (i) upon photoexcitation within the S_1 state of this material, and (ii) only when photoexcitation occurs at low temperatures (see Fig. S7 of the Supplemental Material [36]). Moreover, no light-induced ESR signals are observed in neat rr-P3HT films, in agreement with our previous studies [44], indicating negligible charge-carrier photogeneration in rr-P3HT upon excitation within the absorption edge. These observations are perfectly correlated with the TSL excitation behavior for mCBP-CN and rr-P3HT films shown in Fig. 2, implying that the *same trapped charge carriers are responsible for both TSL and LESR phenomena*.

Figure 5(c) shows the temporal evolution of the LESR signal in mCBP-CN film at 10 K, which demonstrates the extremely slow LESR kinetics of both charge accumulation and charge recombination after ceasing the cw illumination. Interestingly, the LESR intensity gradually increases with exposure time, revealing no saturation even after a prolonged 60-min illumination (see Figs. S4–S6 and Note S1 of the Supplemental Material [36]). When the illumination is turned off, the LESR signal at 10 K decreases due to the recombination of charges following the $I_{LESR} \sim -\log(t)$ decay kinetics measured over hours as shown in Fig. 5(e). This kinetic is indicative of dispersive charge recombination due to energy and/or spatial distribution of charge-carrier pairs and perfectly agrees with the isothermal recombination luminescence (IRL) (or long afterglow) decay kinetics $I_{IRL} \sim -t^{-1}$ as depicted in Fig. S2 in the Supplemental Material [36] measured in the long delayed time limit after photoexcitation. This is because the LESR signal is proportional to the carrier concentration $I_{LESR} \sim n$, whereas the IRL intensity is the first derivative of carrier concentration $I_{IRL} \sim -dn/dt$ [45]. At elevated temperatures, the charge accumulation and recombination are accelerated, as expected, as demonstrated by the LESR transients for charges measured at temperatures 10, 50, and 100 K (Fig. S5 of the Supplemental Material [36]). The LESR results thus indicate that (i) the majority of

photogenerated charges in mCBP-CN films under steady-state excitation at 10 K are metastable, originating from long-lived long-range geminate pairs, and (ii) no really fast charge recombination can be seen in these experiments because of the limited time resolution (100 ms) of the present LESR kinetics measurements.

In contrast to the very slow temporal evolution of the LESR signal caused by the recombination of charge carriers in Fig. 5(e), the LESR caused by triplets, as shown in Fig. 5(d), demonstrates fast increase, decrease, and saturation within seconds of switching the illumination on or off. The signal decrease as shown in Fig. 5(f) features exponential decay kinetics with a time constant $\tau = 1.7$ s. This value is comparable to the decay constant of the initial part of the isothermal afterglow measured at a constant temperature $T = 5$ K prior to the TSL heating run (Fig. S2 of the Supplemental Material [36]) and we ascribe it to the lifetime of triplet excitons in mCBP-CN films.

Thus, the PLDMR and LESR experiments demonstrate the abundance of charge carriers and triplet excitons being generated in mCBP-CN films upon photoexcitation within the absorption edge. In this regard, both methods show a high degree of similarity, as shown in Fig. S10 of the Supplemental Material [36].

C. Modeling of geminate-pair dissociation

It is obvious from the striking similarity between the temperature dependences of the DF and the PC [see Fig. 3(b)] that the PC is essentially determined (limited) by the same TTA process that determines the DF. Based on the experimental data presented in Sec. III A and the LESR data of Sec. III B, we suggest that TTA leads to the formation of a higher lying singlet state, $T_1 + T_1 \rightarrow S_n$. Autoionization from this state followed by thermalization leads to the formation of geminate pairs, $S_n \rightarrow (e^- \ldots h^+)$. These geminate pairs may have shorter or longer separation distances r_0 between the respective electron and hole. They will eventually dissociate by thermally activated and field-assisted diffusive hopping into free charges $(e^- \ldots h^+) \rightarrow (e^- + h^+)$. However, it still needs to be clarified to what extent the measured $J_{ph}(T)$ is governed by the TTA-induced geminate-pair generation and to what extent it is governed by the dissociation of these geminate pairs into free carriers. Note that the PC is observed at low temperatures, and the geminate pairs are bound together by their Coulomb energy, which acts as an energy barrier for dissociation. This leads to a more general fundamental question: How does a photogenerated geminate pair dissociate into free carriers at such low temperatures, including liquid-helium temperature?

PC generation is a two-stage process and can therefore be expressed as a product of geminate-pair generation yield, which is a temperature-dependent quantity in the
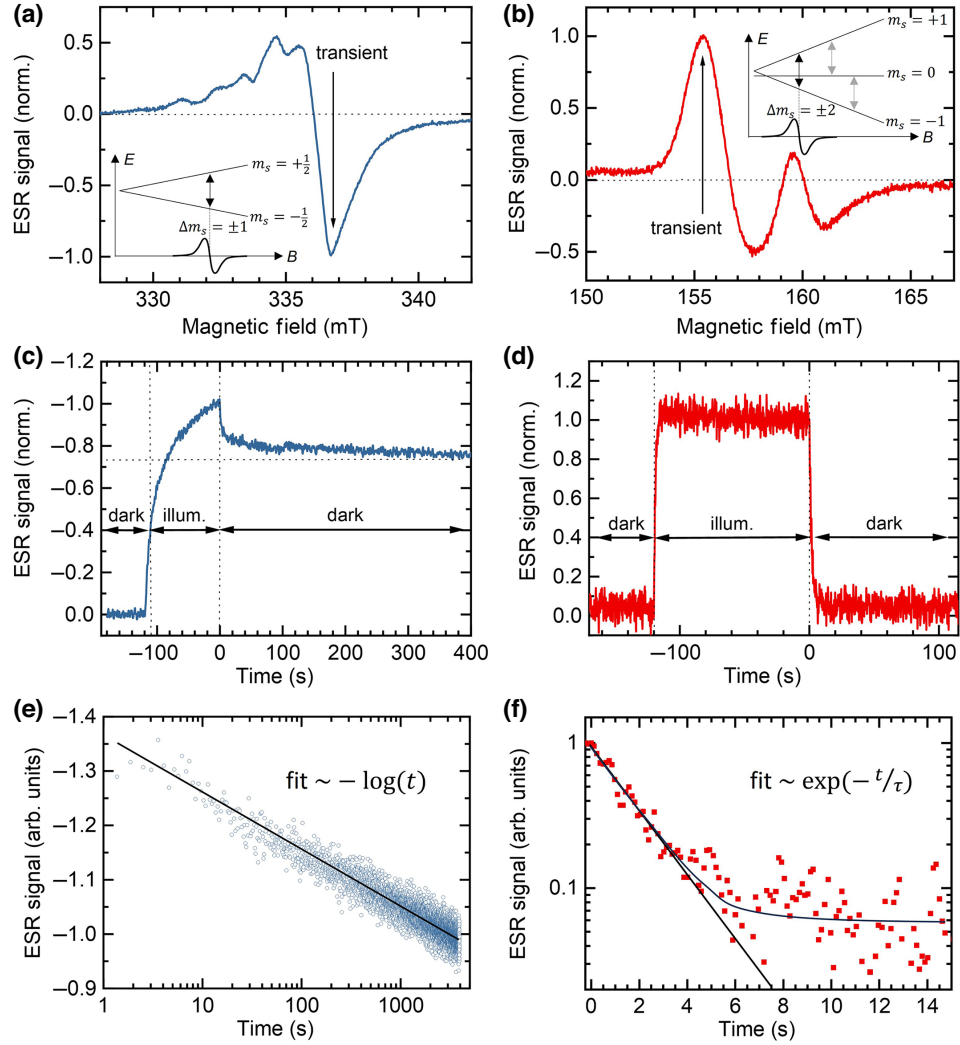
FIG. 5. Light-induced ESR of mCBP-CN under 365-nm excitation at 10 K due to charge carriers [blue lines or symbols in (a),(c),(e)] or triplets [red lines or symbols in (b),(d),(f)]. (a),(b) LESR signal as function of the applied magnetic field. The vertical arrows indicate the signal peaks where transients are measured. The insets show the Zeeman splitting of charge carriers or triplets and the probed $\Delta m_s = \pm 1$ and ± 2 ESR transitions, respectively. (c),(d) Illumination-dependent transient signal evolution. The signals grow upon illumination and decay in the dark with drastically different temporal behaviors. (e),(f) Semilog plots of the signal decays in the dark after terminating the excitation. For charges, a logarithmic time dependence $I_{\text{LESR}} \sim -\log(t)$ is observed. Charges accumulate and decay over hours. For the triplet signal, an exponential decay $I_{\text{LESR}} \sim \exp(-(t/\tau))$ with a time constant $\tau = 1.7$ s is observed.

case of TTA-facilitated autoionization $\Phi(T)$, and the probability of charge-pair dissociation $\eta(T)$ into free carriers. Hence, the entire process can be written as

$$T_1 + T_1 \xrightarrow{\Phi(T)} S_n (e^- \ldots h^+) \xrightarrow{\eta(T)} (e^- + h^+). \quad (1)$$
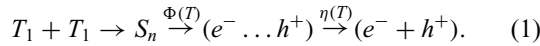
Therefore, comparison of the DF and the PC measurements at various temperatures allows one to decouple the temperature-dependent geminate-pair generation $\Phi(T)$ and dissociation $\eta(T)$. Here we assume that $\Phi(T)$ is proportional to the measured temperature-dependent DF

intensity, as both phenomena are induced by the same TTA process. The temperature dependence of the charge-pair dissociation probability can therefore be evaluated as $\eta(T) \propto J_{\text{ph}}(T)/\Phi(T)$ [cf. Eq. (2) below] using the experimental data from Fig. 3(b) and is presented in Fig. 6(a) (black circles). As one can see, $\eta(T)$ demonstrates a clear nonexponential dependence when plotted in Arrhenius representation for the temperature ranging from 20 to 290 K. This implies that the classical disorder-free Onsager dissociation model is not applicable to amorphous organic semiconductors and should be extended to account for the

disorder that is known to assist the dissociation of photogenerated geminate pairs [46–50]. This is because the stronger the disorder is, the more easily the charge carriers can escape from the Coulomb potential since they are able to hop via localized states below the center of the DOS distribution, thereby requiring significantly less thermal energy. The shortcomings of the classical Onsager dissociation model have recently been solved in an extended model by Rubel *et al.* [46] that also accounts for the hopping motion involved in the dissociation process in a disordered system. Therefore, the dissociation probability $\eta(r_0, \tau, \sigma, T, E)$ is a function of the initial charge separation distance of the geminate pairs r_0, the lifetime of a geminate pair τ, the amount of energetic disorder in the material σ, temperature T, and electric field E. The PC then reads as follows:

$$J_{\text{ph}}(T) \propto \Phi(T)\eta(r_0, \tau, \sigma, T, E). \tag{2}$$

To understand the observed temperature dependence of the dissociation yield $\eta(T)$, we use the analytical hopping model of Rubel *et al.* [46], which reproduces the Onsager and Frenkel field dependences of the dissociation probability as asymptotic cases. The model is based on a rate equation approach in a one-dimensional lattice of hopping sites where one charge is fixed (e.g., the electron) and the countercharge (e.g., the hole) executes a biased random walk in the presence of an external electric field and the Coulomb potential of the fixed charge. The mobile carrier will either recombine with the fixed charge at the origin, with a lifetime τ, or separate over a given distance $L = na$ to become free, where n is the number of lattice sites and a is the lattice constant. The temperature-dependent dissociation probability is

$$\eta(T) = 1 - \frac{\sum_{j=i}^{n-1} \nu_{j,j+1}^{-1} e^{(\varepsilon_j - \varepsilon_1/k_B T)}}{\tau + \sum_{j=1}^{n-1} \nu_{j,j+1}^{-1} e^{(\varepsilon_j - \varepsilon_1/k_B T)}}, \tag{3}$$

where i is the starting site of the mobile carrier ($i = 1$ corresponds to electron and hole being nearest neighbors with distance a), ε_j the site energies, k_B the Boltzmann constant, and $\nu_{j,j+1}$ the Miller-Abrahams hopping rates between nearest-neighbor sites j and $j + 1$, given by

$$\nu_{j,j+1} = \nu_0 e^{-2\gamma a} e^{-((\varepsilon_{j+1} - \varepsilon_j + |\varepsilon_{j+1} - \varepsilon_j|)/2k_B T)}, \tag{4}$$

with ν_0 the attempt-to-hop frequency and γ the inverse localization length. The on-site energies of the jth localized state at position $x_j = aj$,

$$\varepsilon_j = -\frac{q^2}{4\pi\epsilon_r\epsilon_0 x_j} - qEx_j + \varepsilon_j^0, \tag{5}$$

include the Coulomb binding energy, the potential energy drop due to the applied electric field E, and random

Gaussian disorder ε_j^0 with standard deviation σ and mean value zero. q is the charge of the hole and ϵ_r, ϵ_0 the relative and vacuum permittivity, respectively. We have used $\epsilon_r = 3.5$, $\sigma = 0.1$ eV, $a = 1$ nm, $n = 100$, $E = 10^5$ V/cm, $\gamma = 2$ nm^{-1}, $\nu_0 = 10$ ps^{-1}, and computed the dissociation probability by averaging over 10^7 disorder realizations for different electron-hole initial separation distances $r_0 = ia$, where i is the integer number 1, 2, 3, 4, or 5. Note that although the latter option was included in the equation in the original Rubel model, it was not applied to compute the probability for different distances. Thus, the major advance we make using the model described here is that we also account for longer-distance geminate pairs.

In Fig. 6(a), we plot the dissociation probability of geminate electron-hole pairs ($e^- \dots h^+$) normalized to the dissociation probability at 290 K. We use a lifetime for the pair of $\tau = 3 \times 10^4 t_0$, where $t_0 = e^{2\gamma a}/\nu_0$ is the minimum hopping time between isoenergetic sites. This lifetime corresponds to a value of around 164 ns for a minimum hopping time of about 5.5 ps. Importantly, we find that in order to reproduce the non-Arrhenius temperature dependence of the experimental data with a relatively steep activation energy at high temperatures (about 80 meV for $T \geq 150$ K) and nearly zero activation energy at low temperatures we need to include both short-distance pairs with $r_0 = 1$ nm and longer-distance pairs with $r_0 \geq 2$ nm. The short-distance pairs contribute to the high-temperature steep drop of the dissociation yield with decreasing T, while the longer-distance pairs account for the T-independent low-temperature part. Note that in the absence of electric field and energetic disorder, the thermal activation energy for the dissociation of nearest-neighbor pairs would be around 411 meV [Fig. 6(b)]. In the fit to the data presented in Fig. 6(a), approximately 97.0% of the charges are generated at $r_0 = 1$ nm, 2.9% at $r_0 = 2$ nm, and 0.1% at $r_0 = 3$ nm. The individual dissociation yields for $r_0 = 1, 2, 3, 4,$ and 5 nm are shown in the Supplemental Material (Fig. S11) [36]. Satisfactory fits of the experimental data could also be obtained by considering different r_0 ratios, for example, 99.87% of the charges at $r_0 = 1$ nm and 0.13% at $r_0 = 5$ nm, or by considering a longer lifetime $\tau = 3 \times 10^6 t_0$ with 99% of the charges at $r_0 = 1$ nm and 1% at $r_0 = 5$ nm. However, they key common feature is that the vast majority of the geminate electron-hole pairs ($e^- \dots h^+$) following autoionization from S_n are nearest neighbors and the minority are separated by intermediate distances. Figure 6(b) highlights the dramatic influence of disorder in assisting charge separation of short-distance Coulombically bound electron-hole pairs at low temperatures.

Finally, we emphasize that even though the long-distance geminate pairs seem to be only a small fraction of the total number of TTA-generated geminate pairs,
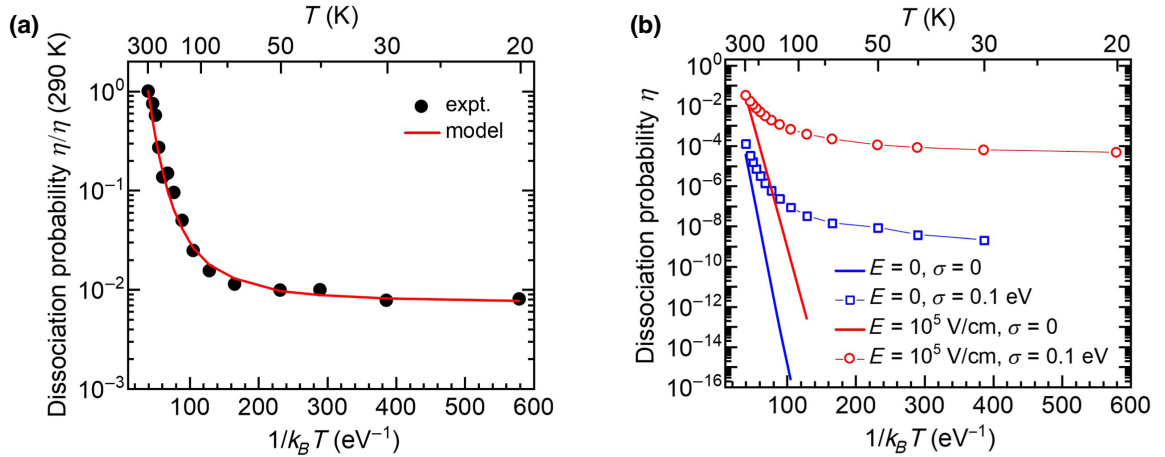
186

FIG. 6. (a) Arrhenius plot of the Onsager probability of charge dissociation extracted from the experimental data of Fig. 3(b) (black circles) and from the analytical hopping model (red curve) with the yield dissociation values normalized to the yield at 290 K. (b) Arrhenius plot of the dissociation probability of a short-distance electron-hole pair ($r_0 = 1$ nm) for a disordered (circles, squares) and a disorder-free (lines) system in the absence of electric field (blue line and squares) and in the presence of an electric field (red line and circles).

their abundance in mCBP-CN films is unambiguously testified by the strong isothermal afterglow (Fig. S2 in the Supplemental Material [36]), the TSL, and the LESR signals observed under photoexcitation at 10 K. The presented LESR kinetics cannot probe the nearest-neighbor charge pairs as their lifetime is shorter than the time resolution of the LESR kinetic measurements (limited by the 100-ms lock-in time constant). Note that any intermediate short-lived pairs can be probed on (sub-)microsecond timescales only with transient LESR upon pulsed nanosecond-laser excitation, as has been demonstrated for bulk hetero-junction photovoltaic systems [51,52]. Furthermore, the ESR signal shape for those close pairs is expected to be broader due to enhanced short-range dipolar interaction in comparison to the spectra presented in Fig. 5(a).

IV. DISCUSSION

We briefly discuss the reason for the occurrence of a pronounced maximum in the DF intensity at a certain temperature [cf. Fig. 3(c), blue curve]. A similar effect has been studied in detail for a series of poly(*p*-phenylene) oligomers [39] and it was found to be a consequence of thermally activated triplet exciton diffusion toward quenching sites in a disordered organic solid. Even in well purified compounds, there may be some residual amount of structural or chemical defects capable of quenching triplet excitons due to their long lifetime. The triplet quenching in the mCBP-CN films is evidenced by the observed drastic decrease of phosphorescence with increasing temperature [Fig. 3(c), green curve], which drops to a negligible level at room temperature. Considering that both the bimolecular TTA and monomolecular triplet quenching

are diffusion-controlled processes, their interplay leads to the situation that the number of TTA events peaks at a certain temperature [40]. Indeed, triplet quenching is negligible at zero temperature and the DF tends to increase with temperature due to the temperature-dependent diffusivity [53] promoting the collision of two triplets until the triplet quenching rate (which also increases with temperature) equals the intrinsic decay rate [39,40]. From that point on, further increases of temperature lead to a progressive decrease in TTA probability, since the triplet population is reduced by quenching, and concomitantly, the DF intensity falls. In between, the DF features a maximum, and the peak temperature is determined by various material parameters—in particular, by the quencher concentration and the energy disorder. The disorder has been shown to reduce triplet diffusivity, resulting in a shift in the DF maximum towards higher temperatures [40].

A key finding of our study is that, similar to the DF intensity, the intrinsic PC in mCBP-CN diodes exhibits a similar prominent maximum at an intermediate temperature followed by a drastic decrease with temperature upon approaching room temperature [Fig. 3(c), red curve]. Such a decrease with temperature is an unusual behavior for a PC in a disordered system. It suggests that the temperature-dependent bimolecular TTA process governs the intrinsic charge-carrier generation and, consequently, the PC in these films. This is further proven by observation of the supralinear dependence of the PC on cw-excitation power [Fig. 3(c)] at very low excitation power (below 1 mW/cm²).

The high-efficiency TTA process observed in mCBP-CN thin films is not self-evident for a single-component

heavy-atom-free system. We attribute this behavior to a combination of several factors. Firstly, the relatively high ISC rate estimated for mCBP-CN films, $k_{ISC} = 1.8 \times 10^8 \, s^{-1}$, is expected in accordance with the El-Sayed rule, since it involves a change of orbital type from a singlet state with a charge-transfer character to a triplet state localized on the biphenyl moiety. Secondly, a relatively low concentration of quenching centers and the high energy of the lowest triplet state ($T_1 = 2.71$ eV) in mCBP-CN gives rise to a very long triplet lifetime, as found by LESR studies [Fig. 5(d)], which is around 2 s, because the nonradiative rate is greatly reduced in accordance with the energy gap law. These factors can provide a large triplet excitation density in this material under steady-state photoexcitation. In contrast to mCBP-CN, rr-P3HT is not a phosphorescent material due to slow ISC from the lowest singlet state to the T_1 state, as confirmed by transient absorption measurements [28], which revealed no measurable triplet formation in rr-P3HT films under excitation at the absorption band edge. Moreover, the low energy of the lowest triplet exciton state $T_1 = 1.55$ eV for rr-P3HT film [28] is expected to enhance the nonradiative decay rate of triplets in this material.

Further, spin-coated mCBP-CN films are typically amorphous and thus quite disordered. The energetic disorder for charge carriers was found to be about 150 meV [27] and it is dominated by the dipolar-disorder contribution. The energy landscape for triplets is naturally less disordered. In the present work, we estimate a triplet exciton DOS width of about $\sigma_{triplet} = 37$ meV based on the Gaussian width of the 0–0 peak in the phosphorescence spectra presented in Fig. 2(a). For details of the Gaussian fit to the 0–0 peak, see Fig. S12 of the Supplemental Material [36]. This width of the DOS likely results from the significant conformational disorder due to the conformational freedom and presence of soft dihedral angles in this organic material [54]. Recent kinetic Monte Carlo simulations by Saxena *et al.* [40] have demonstrated that the energetic disorder is crucial for obtaining a high yield of TTA because it causes filamentary triplet transport in disordered solids; thus, it locally enhances triplet densities and the probability of two triplets encountering each other rather than an impurity.

Another principal finding of this work is that the dissociation probability $\eta(T)$ of photoinduced charge pairs is almost *temperature-independent* at low temperatures in the range up to $T \leq 100$ K [Fig. 6(a)]. This cannot be rationalized by a classical "disorder-free" Onsager model predicting an exponential drop of the geminate-pair dissociation yield with decreasing temperature, as demonstrated in Fig. 6(b) (straight lines). At higher temperatures, $\eta(T)$ reveals some thermally activated behavior featuring an activation energy of around 80 meV. The latter is responsible for the notable shift of the maximum $J_{ph}(T)$ with respect to the temperature of maximal DF intensity

(i.e., maximum of TTA efficiency) [Fig. 3(b)], which proves that the charge dissociation in the range of moderately high temperatures does require extra thermal energy. We demonstrate that the puzzle can be resolved within the charge dissociation model by Rubel *et al.* [46] by accounting for the presence of energetic disorder, which *dramatically facilitates the separation* of charges, particularly at low temperatures [Fig. 6(b)]. Although previous hopping transport theories and relevant computer simulations [46–48] have shown that the disorder greatly weakens the temperature dependence of the geminate-pair dissociation yield under the applied electric field, they have never been applied to describe PCs in such a low-temperature limit approaching liquid helium temperature. It is remarkable that the Rubel model [46] is found to describe the temperature-dependent PC so well across a broad temperature range from 300 down to 5 K [Fig. 6(a)] by considering a distribution of initial charge separation distances of the geminate pairs. This means that the presence of energetic disorder and energy barriers for back charge recombination, which result in substantially long lifetimes of photogenerated geminate charge pairs and slow recombination, must be taken into consideration. Experimental evidence of very slow charge recombination at 10 K is provided by extremely slow LESR and the afterglow decay kinetics presented in Fig. 5(c) and Fig. S2 (in the Supplemental Material [36]), respectively.

V. CONCLUSIONS

In this study, we demonstrate, that similar to the DF, the intrinsic photogeneration of geminate pairs of charge carriers in a single-component mCBP-CN film is dominated by the TTA-induced UC process. Energetically, this is easily feasible due to the high energy of the lowest triplet state in mCBP-CN. As a result, the TTA process can readily promote energy up-conversion to 5.42 eV [Fig. 3(d)], which provides plenty of excess energy to overcome the exciton binding energy, which is known to be within the range of 0.5–1 eV for small molecule semiconductors. The autoionization of the TTA-UC-generated high-energy neutral excited state is the major cause of the charge photogeneration observed in this material.

This photogeneration mechanism requires a high concentration of long-lived triplets that enable a highly efficient TTA process. This is not a trivial issue for a single-component material that does not contain a heavy atom. We attribute the efficient TTA process in mCBP-CN to efficient ISC, a high triplet energy level (2.71 eV), very long-lived triplet excitations (about 2 s) with a low quenching rate, and the presence of energy disorder that locally enhances the triplet densities. The photocurrent measured in an mCBP-CN diode shows an unusual temperature dependence $J_{ph}(T)$: (i) it is observed primarily at low temperatures peaking at around 170 K and rolls off

significantly at higher temperatures, and (ii) $J_{ph}(T)$ shows a striking correlation with the temperature dependence of the delayed fluorescence. We take this temperature dependence to suggest that triplet fusion is a common origin for both processes. This conclusion is affirmed by a supralinear dependence of the PC on excitation intensity observed even at very low excitation power (below 1 mW/cm^2), implying a bimolecular nature of the charge-generation process. Quantitative modeling of the PC using a hopping transport formalism indeed confirms that the temperature-dependent yield of free charges is mainly determined by the TTA process that forms the high-lying singlet state, and not by the dissociation probability from that high-lying singlet state. To obtain the correct temperature dependence, it is essential to account for the energy disorder and a distribution of initial charge separation distances.

We would like to highlight the importance of energy disorder, which actually plays a twofold beneficial role in the above TTA-UC-induced PC generation. The disorder of the triplet exciton states and that of the charge states in mCBP-CN films is found to be around 37 and 150 meV, respectively. First, the disorder of the excitonic state has previously been shown [40] to locally enhance triplet densities. This local enhancement should facilitate the TTA efficiency in mCBP-CN. It is worth noting that, to achieve a desirable shift of maximal TTA efficiency to room temperature, a somewhat larger triplet DOS width of at least 70 meV is required, as well as a triplet quencher density as small as about 10^{17} cm^{-3} [40]. This might be accomplished by proper selection of organic semiconductor materials and improved material purification and/or encapsulation to reduce the concentration of triplet quenchers, e.g., molecular oxygen. Second, in this work we demonstrate that the disorder of a charged state can have a dramatic influence in assisting the charge separation of Coulombically bound electron-hole pairs at low temperatures, [Fig. 6(b)]. Organic perfect single crystals may not exhibit this disorder-assisted dissociation mechanism. We find that the disorder-based dissociation model of Rubel *et al.* [46] describes remarkably well the dissociation yield over the entire broad temperature range 5–300 K [Fig. 6(a)] if one also accounts for the distribution of geminate-pair radii. Our TSL and LESR measurements clearly prove photogeneration of a significant amount of charge pairs with an intrapair separation of several intermolecular distances. Hence, TTA can lead to the formation of a high-lying singlet state and subsequent formation of long-range geminate pairs that separate into free carriers with virtually no activation energy and that provide an intrinsic photocurrent at the onset of absorption even at temperatures as low as 5 K. It also explains the counterintuitive finding that the level of stationary photocurrent in this disordered material at 5 K is almost the same as at room temperature. Finally, we wish to point out that the mechanism of geminate-pair photogeneration through the TTA-UC process discussed in this paper is not exclusive to mCBP-CN; it may be applicable to other organic semiconductors that possess an efficient ISC and a sufficiently high triplet energy level (e.g., carbazole- or triazine-based compounds), the TSL of which we studied previously [24,25].

[1] S. Baluschev, T. Miteva, V. Yakutkin, G. Nelles, A. Yasuda, and G. Wegner, Up-conversion fluorescence: Noncoherent excitation by sunlight, Phys. Rev. Lett. **97**, 143903 (2006).

[2] P. Bharmoria, H. Bildirir, and K. Moth-Poulsen, Triplet–triplet annihilation based near infrared to visible molecular photon upconversion, Chem. Soc. Rev. **49**, 6529 (2020).

[3] T. Schloemer, P. Narayanan, Q. Zhou, E. Belliveau, M. Seitz, and D. N. Congreve, Nanoengineering triplet–triplet annihilation upconversion: From materials to real-world applications, ACS Nano **17**, 3259 (2023).

[4] H. Goudarzi, L. Koutsokeras, A. H. Balawi, C. Sun, G. K. Manolis, N. Gasparini, Y. Peisen, G. Antoniou, S. Athanasopoulos, and C. C. Tselios, Microstructure-driven annihilation effects and dispersive excited state dynamics in solid-state films of a model sensitizer for photon energy up-conversion applications, Chem. Sci. **14**, 2009 (2023).

[5] R. Karpicz, S. Puzinas, V. Gulbinas, A. Vakhnin, A. Kadashchuk, and B. P. Rand, Exciton dynamics in an energy up-converting solid state system based on diphenylanthracene doped with platinum octaethylporphyrin, Chem. Phys. **429**, 57 (2014).

[6] P. C. Chow, S. Gélinas, A. Rao, and R. H. Friend, Quantitative bimolecular recombination in organic photovoltaics through triplet exciton formation, J. Am. Chem. Soc. **136**, 3424 (2014).

[7] C. Gärtner, C. Karnutsch, U. Lemmer, and C. Pflumm, The influence of annihilation processes on the threshold current

density of organic laser diodes, J. Appl. Phys. **101,** 023107 (2007).

[8] D. Stich, F. Späth, H. Kraus, A. Sperlich, V. Dyakonov, and T. Hertel, Triplet–triplet exciton dynamics in single-walled carbon nanotubes, Nat. Photonics **8,** 139 (2014).

[9] T. Dilbeck and K. Hanson, Molecular photon upconversion solar cells using multilayer assemblies: Progress and prospects, J. Phys. Chem. Lett. **9,** 5810 (2018).

[10] L. J. Hart, J. Grüne, W. Liu, T. k. Lau, J. Luke, Y. C. Chin, X. Jiang, H. Zhang, D. J. Sowood, and D. M. Unson, Understanding the role of triplet-triplet annihilation in non-fullerene acceptor organic solar cells, Adv. Energy Mater. **13,** 2301357 (2023).

[11] D. W. Gehrig, I. A. Howard, and F. Laquai, Charge carrier generation followed by triplet state formation, annihilation, and carrier recreation in PBDTTT-C/PC60BM photovoltaic blends, J. Phys. Chem. C **119,** 13509 (2015).

[12] N. A. Kukhta, T. Matulaitis, D. Volyniuk, K. Ivaniuk, P. Turyk, P. Stakhira, J. V. Grazulevicius, and A. P. Monkman, Deep-blue high-efficiency TTA OLED using para-and meta-conjugated cyanotriphenylbenzene and carbazole derivatives as emitter and host, J. Phys. Chem. Lett. **8,** 6199 (2017).

[13] H. Lim, S. J. Woo, Y. H. Ha, Y. H. Kim, and J. J. Kim, Breaking the efficiency limit of deep-blue fluorescent OLEDs based on anthracene derivatives, Adv. Mater. **34,** 2100161 (2022).

[14] J. Grüne, N. Bunzmann, M. Meinecke, V. Dyakonov, and A. Sperlich, Kinetic modeling of transient electroluminescence reveals TTA as an efficiency-limiting process in exciplex-based TADF OLEDs, J. Phys. Chem. C **124,** 25667 (2020).

[15] A. Monguzzi, A. Oertel, D. Braga, A. Riedinger, D. K. Kim, P. N. Knusel, A. Bianchi, M. Mauri, R. Simonutti, and D. J. Norris, Photocatalytic water-splitting enhancement by sub-bandgap photon harvesting, ACS Appl. Mater. Interfaces **9,** 40180 (2017).

[16] G. Antoniou, P. Yuan, L. Koutsokeras, S. Athanasopoulos, D. Fazzi, J. Panidi, D. G. Georgiadou, T. Prodromakis, and P. E. Keivanidis, Low-power supralinear photocurrent generation via excited state fusion in single-component nanostructured organic photodetectors, J. Mater. Chem. C **10,** 7575 (2022).

[17] A. Kadashchuk, Y. Skryshevskii, A. Vakhnin, N. Ostapenko, V. Arkhipov, E. Emelianova, and H. Bässler, Thermally stimulated photoluminescence in disordered organic materials, Phys. Rev. B **63,** 115205 (2001).

[18] C. Carati, L. Bonoldi, and R. Po, Density of trap states in organic photovoltaic materials from LESR studies of carrier recombination kinetics, Phys. Rev. B **84,** 245205 (2011).

[19] J. M. Cho, D. S. Kim, S. Bae, S.-J. Moon, W. S. Shin, D. H. Kim, S. H. Kim, A. Sperlich, S. Väth, and V. Dyakonov, Light-induced electron spin resonance study of galvinoxyl-doped P3HT/PCBM bulk heterojunctions, Org. Electron. **27,** 119 (2015).

[20] A. Kadashchuk, Y. Skryshevski, Y. Piryatinski, A. Vakhnin, E. Emelianova, V. Arkhipov, H. Bässler, and J. Shinar,

Thermally stimulated photoluminescence in poly(2, 5-dioctoxy p-phenylene vinylene), J. Appl. Phys. **91,** 5016 (2002).

[21] S. Kuroda, K. Marumoto, Y. Shimoi, and S. Abe, ESR spectroscopy of polarons in conjugated electroluminescent polymers, Thin Solid Films **393,** 304 (2001).

[22] A. Köhler, D. Dos Santos, D. Beljonne, Z. Shuai, J.-L. Brédas, A. B. Holmes, A. Kraus, K. Müllen, and R. H. Friend, Charge separation in localized and delocalized electronic states in polymeric semiconductors, Nature **392,** 903 (1998).

[23] A. Kadashchuk, V. I. Arkhipov, C.-H. Kim, J. Shinar, D.-W. Lee, Y.-R. Hong, J.-I. Jin, P. Heremans, and H. Bässler, Localized trions in conjugated polymers, Phys. Rev. B **76,** 235205 (2007).

[24] A. Kadashchuk, A. Vakhnin, Y. Skryshevski, V. Arkhipov, E. Emelianova, and H. Bässler, Thermally stimulated luminescence in π-conjugated polymers containing fluorene and spirobifluorene units, Chem. Phys. **291,** 243 (2003).

[25] A. Stankevych, R. Saxena, A. Vakhnin, F. May, N. Kinaret, D. Andrienko, J. Genoe, H. Bässler, A. Köhler, and A. Kadashchuk, Monitoring the charge-carrier-occupied density of states in disordered organic semiconductors under nonequilibrium conditions using thermally stimulated luminescence spectroscopy, Phys. Rev. Appl. **19,** 054007 (2023).

[26] A. Kadashchuk, R. Schmechel, H. von Seggern, U. Scherf, and A. Vakhnin, Charge-carrier trapping in polyfluorene-type conjugated polymers, J. Appl. Phys. **98,** 024101 (2005).

[27] A. Stankevych, A. Vakhnin, D. Andrienko, L. Paterson, J. Genoe, I. Fishchuk, H. Bässler, A. Köhler, and A. Kadashchuk, Density of states of OLED host materials from thermally stimulated luminescence, Phys. Rev. Appl. **15,** 044050 (2021).

[28] J. Guo, H. Ohkita, H. Benten, and S. Ito, Near-IR femtosecond transient absorption spectroscopy of ultrafast polaron and triplet exciton formation in polythiophene films with different regioregularities, J. Am. Chem. Soc. **131,** 16869 (2009).

[29] G. F. Burkhard, E. T. Hoke, and M. D. McGehee, Accounting for interference, scattering, and electrode absorption to make accurate internal quantum efficiency measurements in organic and other thin solar cells, Adv. Mater. **22,** 3293 (2010).

[30] B. A. Naqvi, M. Schmid, E. Crovini, P. Sahay, T. Naujoks, F. Rodella, Z. Zhang, P. Strohriegl, S. Bräse, E. Zysman-Colman, and Wolfgang Brütting, What controls the orientation of TADF emitters?, Front. Chem. **8,** 750 (2020).

[31] S. Nešpůrek, F. Schauer, and A. Kadashchuk, Visible photoluminescence in polysilanes, Monatsh. Chem. **132,** 159 (2001).

[32] C. Deibel, D. Mack, J. Gorenflot, A. Schöll, S. Krause, F. Reinert, D. Rauh, and V. Dyakonov, Energetics of excited states in the conjugated polymer poly(3-hexylthiophene), Phys. Rev. B **81,** 085202 (2010).

[33] S. A. Bagnich, A. Rudnick, P. Schroegel, P. Strohriegl, and A. Köhler, Triplet energies and excimer formation in meta-

and para-linked carbazolebiphenyl matrix materials, Philos. Trans. R. Soc., A **373**, 20140446 (2015).

[34] S. A. Bagnich, S. Athanasopoulos, A. Rudnick, P. Schroegel, I. Bauer, N. C. Greenham, P. Strohriegl, and A. Köhler, Excimer formation by steric twisting in carbazole and triphenylamine-based host materials, J. Phys. Chem. C **119**, 2380 (2015).

[35] S. Barth and H. Bässler, Intrinsic photoconduction in PPV-type conjugated polymers, Phys. Rev. Lett. **79**, 4445 (1997).

[36] See the Supplemental Material at http://link.aps.org/supplemental/10.1103/PhysRevApplied.20.064029 for an explanation for the lack of saturation of the LESR signals with increasing exposure time (Note S1); more results of PL, TSL, LESR, and PLDMR measurements (Figs. S1–S10); calculated charge dissociation yield for different initial electron-hole separation distances (Fig. S11); and for an estimate of the triplet exciton DOS width (Fig. S12).

[37] D. Hertel, H. Bässler, R. Guentner, and U. Scherf, Triplet-triplet annihilation in a poly(fluorene)-derivative, J. Chem. Phys. **115**, 10007 (2001).

[38] V. Jankus, E. W. Snedden, D. W. Bright, V. L. Whittle, J. Williams, and A. Monkman, Energy upconversion via triplet fusion in super yellow PPV films doped with palladium tetraphenyltetrabenzoporphyrin: A comprehensive investigation of exciton dynamics, Adv. Funct. Mater. **23**, 384 (2013).

[39] S. T. Hoffmann, J.-M. Koenen, U. Scherf, I. Bauer, P. Strohriegl, H. Bässler, and A. Köhler, Triplet–triplet annihilation in a series of poly(*p*-phenylene) derivatives, J. Phys. Chem. B **115**, 8417 (2011).

[40] R. Saxena, T. Meier, S. Athanasopoulos, H. Bässler, and A. Köhler, Kinetic Monte Carlo study of triplet-triplet annihilation in conjugated luminescent materials, Phys. Rev. Appl. **14**, 034050 (2020).

[41] S.-Y. Hwang, D. Song, E.-J. Seo, F. Hollmann, Y. You, and J.-B. Park, Triplet–triplet annihilation-based photon-upconversion to broaden the wavelength spectrum for photobiocatalysis, Sci. Rep. **12**, 9397 (2022).

[42] S. Izawa and M. Hiramoto, Efficient solid-state photon upconversion enabled by triplet formation at an organic semiconductor interface, Nat. Photonics **15**, 895 (2021).

[43] S. S. Eaton, K. M. More, B. M. Sawant, and G. R. Eaton, Use of the ESR half-field transition to determine the interspin distance and the orientation of the interspin vector in

systems with two unpaired electrons, J. Am. Chem. Soc. **105**, 6560 (1983).

[44] A. Sperlich, H. Kraus, C. Deibel, H. Blok, J. Schmidt, and V. Dyakonov, Reversible and irreversible interactions of poly(3-hexylthiophene) with oxygen studied by spin-sensitive methods, J. Phys. Chem. B **115**, 13513 (2011).

[45] R. Chen, Methods for kinetic analysis of thermally stimulated processes, J. Mater. Sci. **11**, 1521 (1976).

[46] O. Rubel, S. Baranovskii, W. Stolz, and F. Gebhard, Exact solution for hopping dissociation of geminate electron-hole pairs in a disordered chain, Phys. Rev. Lett. **100**, 196602 (2008).

[47] E. Emelianova, M. Van der Auweraer, and H. Bässler, Hopping approach towards exciton dissociation in conjugated polymers, J. Chem. Phys. **128**, 224709 (2008).

[48] U. Albrecht and H. Bässler, Yield of geminate pair dissociation in an energetically random hopping system, Chem. Phys. Lett. **235**, 389 (1995).

[49] S. Athanasopoulos, H. Bässler, and A. Köhler, Disorder vs delocalization: Which is more advantageous for high-efficiency organic solar cells?, J. Phys. Chem. Lett. **10**, 7107 (2019).

[50] S. Athanasopoulos, F. Schauer, V. Nádaždy, M. Weiß, F. J. Kahle, U. Scherf, H. Bässler, and A. Köhler, What is the binding energy of a charge transfer state in an organic solar cell?, Adv. Energy Mater. **9**, 1900814 (2019).

[51] J. Niklas, S. Beaupre, M. Leclerc, T. Xu, L. Yu, A. Sperlich, V. Dyakonov, and O. G. Poluektov, Photoinduced dynamics of charge separation: From photosynthesis to polymer–fullerene bulk heterojunctions, J. Phys. Chem. B. **119**, 7407 (2015).

[52] J. Behrends, A. Sperlich, A. Schnegg, T. Biskup, C. Teutloff, K. Lips, V. Dyakonov, and R. Bittl, Direct detection of photoinduced charge transfer complexes in polymer fullerene blends, Phys. Rev. B **85**, 125206 (2012).

[53] S. T. Hoffmann, S. Athanasopoulos, D. Beljonne, H. Bässler, and A. Köhler, How do triplets and charges move in disordered organic semiconductors? A Monte Carlo study comprising the equilibrium and nonequilibrium regime, J. Phys. Chem. C. **116**, 16371 (2012).

[54] A. Mondal, L. Paterson, J. Cho, K.-H. Lin, B. van der Zee, G.-J. A. Wetzelaer, A. Stankevych, A. Vakhnin, J.-J. Kim, and A. Kadashchuk, Molecular library of OLED host materials—Evaluating the multiscale simulation workflow, Chem. Phys. Rev. **2**, 031304 (2021).

191

Supplemental Material

Charge-carrier photogeneration in single-component organic carbazole-based semiconductors via low excitation power triplet-triplet annihilation

Andrei Stankevych,[1,2,†] Rishabh Saxena,[1,†] Jeannine Grüne,[3,4] Sebastian Lulei,[3] Andreas Sperlich,[3] Stavros Athanasopoulos,[5] Alexander Vakhnin,[2] Prakhar Sahay,[6] Wolfgang Brütting,[6] Vladimir Dyakonov,[3] Heinz Bässler,[7] Anna Köhler[1,7] and Andrey Kadashchuk [1,2*]

[1] *Soft Matter Optoelectronics and Bavarian Polymer Institute (BPS), University of Bayreuth, Universitätsstr. 30, 95448 Bayreuth, Germany*

[2] *Institute of Physics, National Academy of Sciences of Ukraine, Prospect Nauky 46, 03028 Kyiv, Ukraine*

[3] *Experimental Physics VI and Würzburg-Dresden Cluster of Excellence ct.qmat, Julius-Maximilians - Universität Würzburg , 97074 Würzburg, Germany*

[4] *Cavendish Laboratory, University of Cambridge, JJ Thomson Avenue, Cambridge CB3 0HE, UK*

[5] *Departamento de Física, Universidad Carlos III de Madrid, Avenida Universidad 30, Leganés, 28911 Madrid, Spain*

[6] *Institute of Physics, University of Augsburg, Universitätsstr. 2, 86159 Augsburg, Germany*

[7] *Bayreuth Institute of Macromolecular Research (BIMF), University of Bayreuth, Universitätsstr. 30, 95448 Bayreuth, Germany*

[†] Authors contributed equally to this work

*Corresponding author: kadash@iop.kiev.ua, andriy.kadashchuk@uni-bayreuth.de
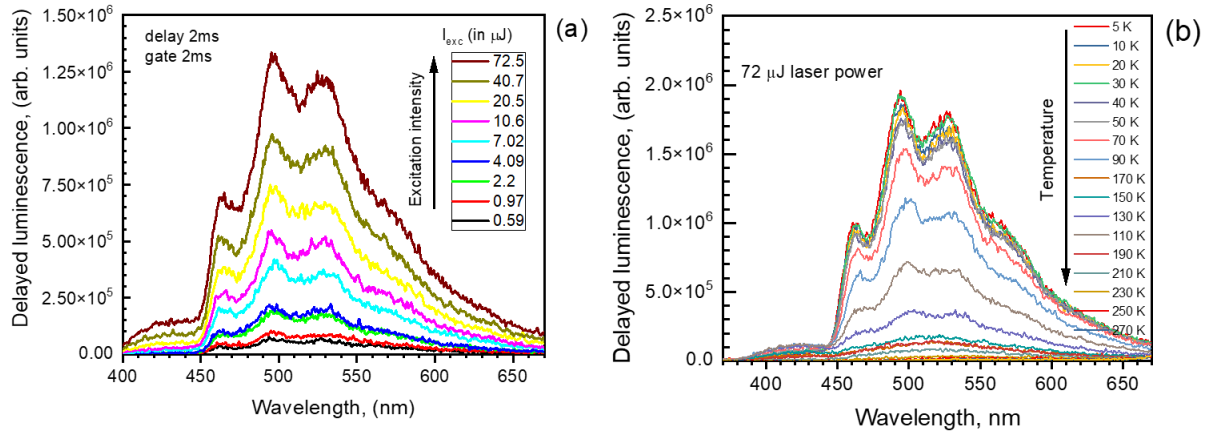
Figure S1: (a) Spectra of phosphorescence (Ph) and delayed fluorescence (DF) measured at 5 K in mCBP-CN films in photodiode device at different excitation intensities with 2 ms delay time after the laser pulse at 355 nm. (b) Ph and DF spectra at different temperatures under the same conditions as (a).
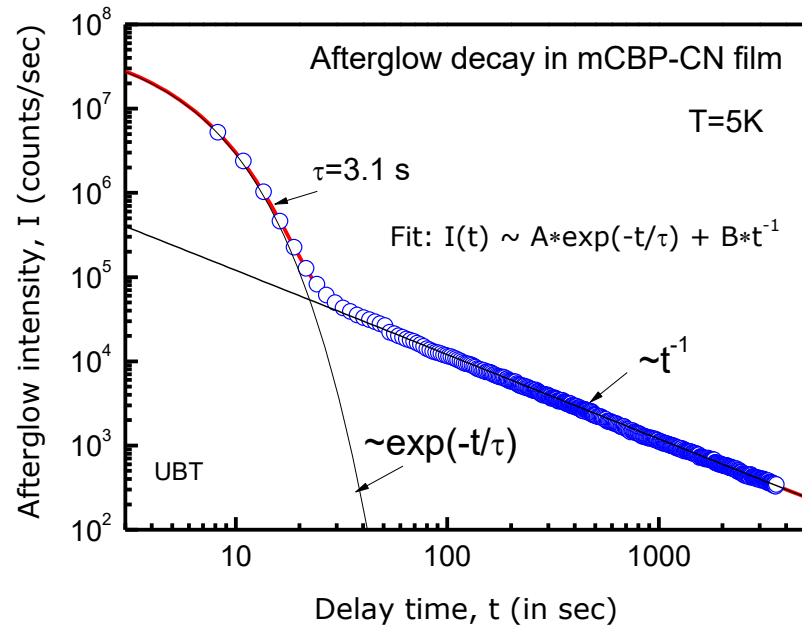
Figure S2: Decay kinetics of the afterglow measured at a constant temperature T=5 K. Note that the afterglow emission at relatively short delay times (<20 s) is dominated by intrinsic phosphorescence, while the emission at large t_{del} is due to recombination of polarons and is directly proportional to the rate of recombination of polarons, $I_{IRL} \sim -dn/dt$. We assume that the recombination is governed by the Miller-Abrahams hopping rate: $\sim\exp(-2r_{ij}/r_0) \times \exp(-e_{ij}/k_BT)$.

2
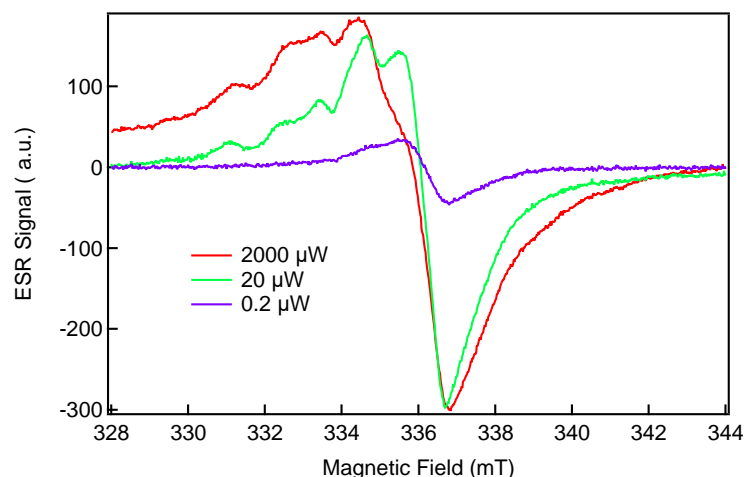
Figure S3: The mCBP-CN LESR signals for charges is a superposition of the individual spectra for positive and negative charges and their spectral contributions cannot be distinguished readily. Spectra recorded at different microwave powers, show drastically different spectral shapes. For low power, a narrow first-derivative Gaussian shape is recorded (blue). At higher powers (green, red), a much broader spectrum is recorded, with multiple shoulders and secondary maxima in the low magnetic field region. The latter features are probably caused by the hyperfine interaction of charge carriers with paramagnetic ^{14}N nitrogen nuclei in mCBP-CN. The observed spectral changes are likely caused by different microwave power saturation behavior for positive / negative charge carriers. Therefore, one kind is observed at low power and saturated at higher powers, while the other kind is not easily saturated and dominates the spectrum at high powers. The assignment of the respective spectral contributions to positive / negative charges is not trivial and beyond the scope of this work.
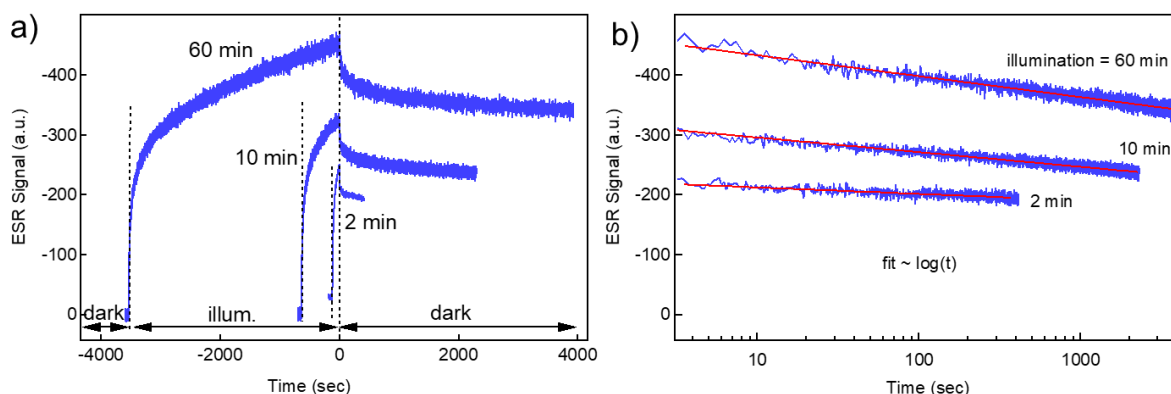
Figure S4: (a) LESR transients for charges under 365 nm excitation at 10 K as also shown in Figure 4c of the main text. For prolonged illumination over 2, 10 or 60 minutes, the charge accumulation does not saturate, but steadily continues. Upon switching off the illumination, the signal decays slowly. (b) A lin-log plot of the signal decay in the dark shows that charge recombination follows a log(time) dependence, irrespective of the previous illumination duration.

3
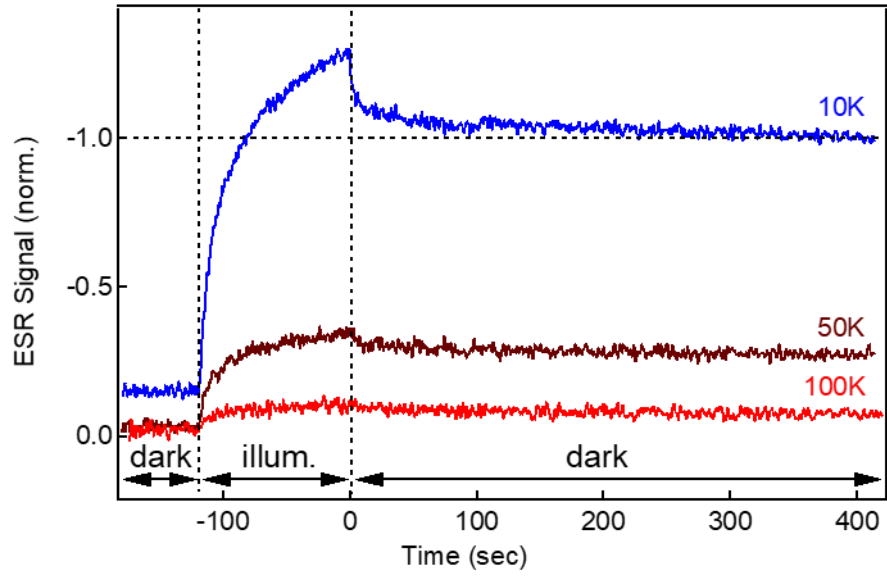
Figure S5: (a) LESR transients for charges under 365 nm excitation at 10, 50 and 100 K as also shown in Figure 4c. The slow accumulation and recombination of charges is accelerated at elevated temperatures.

Note S1. A simplified consideration of the lack of saturation of the LESR signals at 10 K with increasing exposure time (as shown in Fig. S4).

Temporal evolution of the concentration of accumulated trapped charge carriers $n(t)$ at a function of light exposure time (t) is conventionally given as:

$$\frac{\partial n(t)}{\partial t} = aP[N - n(t)] - bPn(t) \tag{S1}$$

N – concentration of traps, a and b – coefficient of charge accumulation and charge release (recombination), respectively. P is the absorbed incident light power. The solution reads as follows

$$n(t) = n_{\infty}[1 - \exp(-At)], \tag{S2}$$

where $n_{\infty} = N/(1 + b/a)$ and $A = P(a + b)$

However, Eq. (S2) is valid only if the incident light is absorbed **homogenously**, i.e., if the film is sufficiently thin. If it is not the case, as it happens for organic layers used in LESR experiments, one has to consider that P is no longer a constant and use $P(L) = P_0\exp(-kL)$, where L is the film thickness. Therefore, in the case of an **inhomogeneous** distribution of the incident light power density over the film thickness, the accumulated number of charges is described by the following relation:

$$n(t) = \int_0^L n_{\infty}[1 - \exp(-P(L)(a + b)t)]dL \tag{S3}$$

4

Note that this simplified consideration neglects the charge diffusion from the illuminated near-surface layer into bulk of the film, which can also contribute to the continued accumulation of charge carriers.
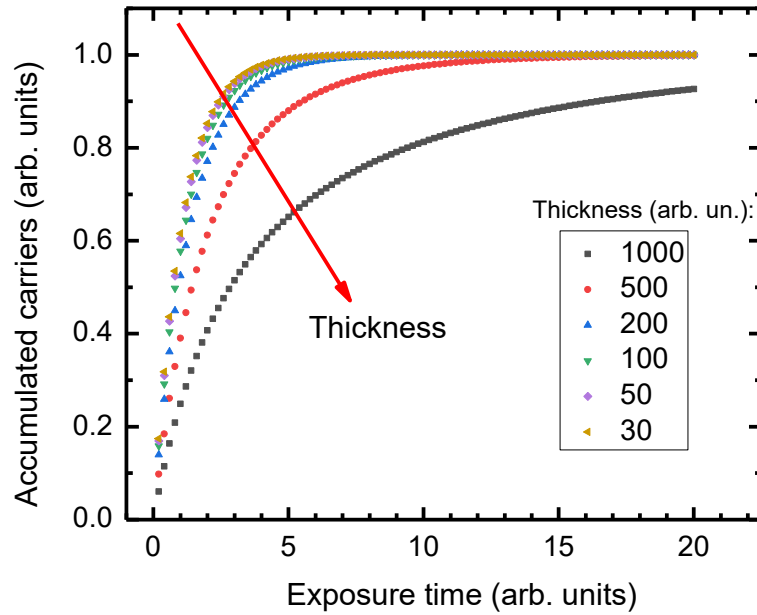
Figure S6: Temporal evolution of the total number of accumulated carriers calculated by Eq.(S3) parametric in film thickness. The results demonstrate that reaching saturation progressively slows down with as film thickness increases.
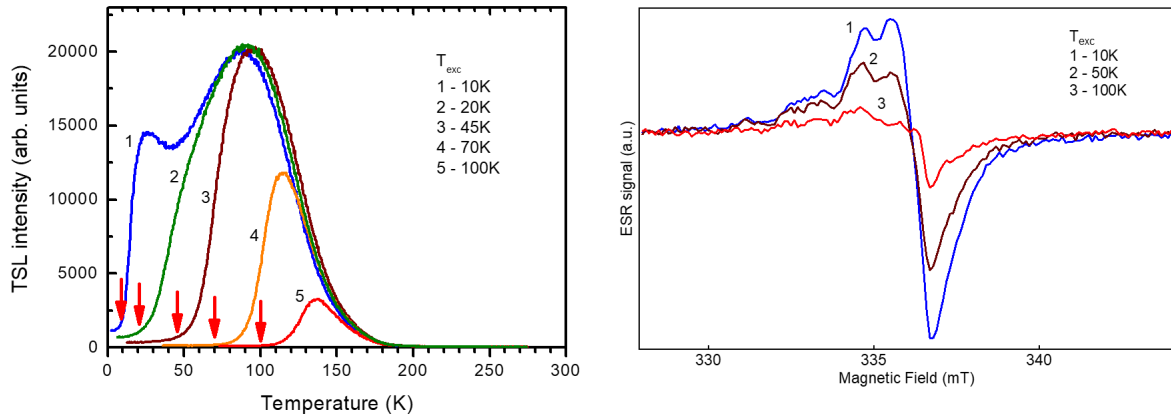
Figure S7. (a) TSL measured for photoexcitation at different temperatures (T_{exc} indicated by arrows). (b) Temperature dependence of LESR in a mCBP-CN film. The sample was illuminated at 10 K, heated to and held at the specified temperature (T_{exc}=50 K or 100 K) for 20 min and subsequently the spectrum was measured after cooling again to 10 K. TSL and LESR reduces in a similar manner with increasing temperature, reflecting thermally assisted release of trapped charge-carriers.

5
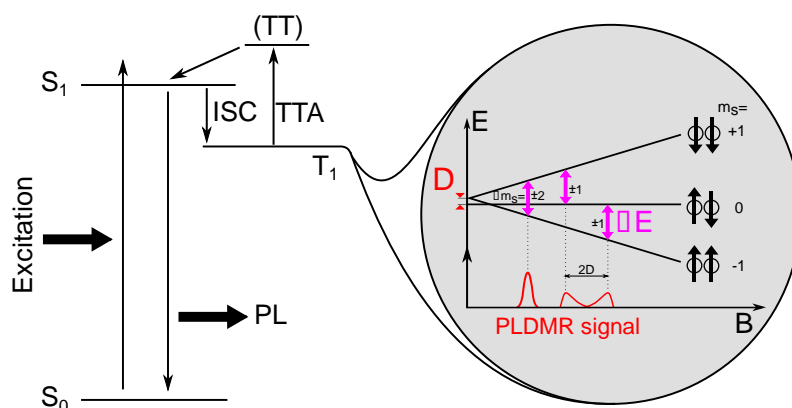
Figure S8: Principle of photoluminescence detected magnetic resonance (PLDMR) to investigate triplet excitons and TTA. Singlet excitation is followed by either direct PL or, alternatively, by intersystem crossing (ISC) to triplet excitons. The accumulation of triplets leads to TTA yielding a higher-energy excited state, denoted here as (TT). Upon relaxation to a singlet excited state, delayed PL is emitted. TTA and the corresponding delayed PL are spin-dependent. Modulation of the Zeeman-split m_s levels by resonant microwave irradiation therefore modulates TTA probabilities and PL intensity. Three possible transitions are observed as PLDMR spectrum, for $\Delta m_s = \pm 1$ and $\Delta m_s = \pm 2$, respectively. The $\Delta m_s = \pm 1$ spectrum is often referred to as "full-field" spectrum, while the $\Delta m_s = \pm 2$ transition is observed at half the magnetic field of the center of the full-field spectrum and is hence referred to as "half-field" spectrum.
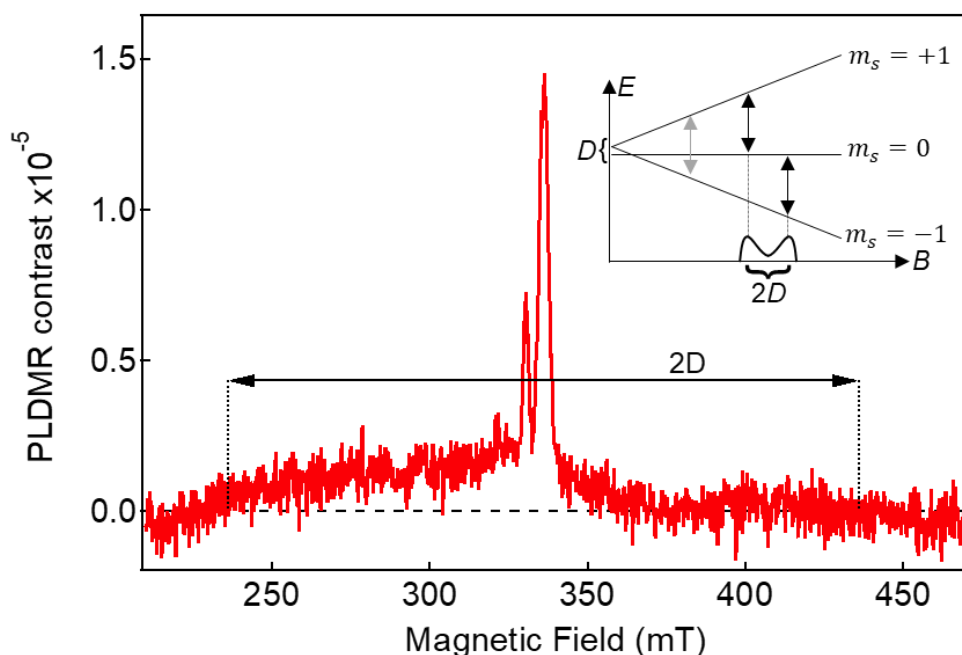
Figure S9: PLDMR spectrum for 365 nm excitation at 10 K. The narrow central peaks are related to charges and are discussed in the respective Figure S10a. A wide spectral component for the $\Delta m_s = \pm 1$ full-field transitions of triplet excitons is buried in the noise floor. The spectral width (2D) of the full-field spectrum cannot be read-off from this data and is instead roughly estimated from the half-field transition presented in Figure 3, 4b and S10a as described by Eaton et al. [43].
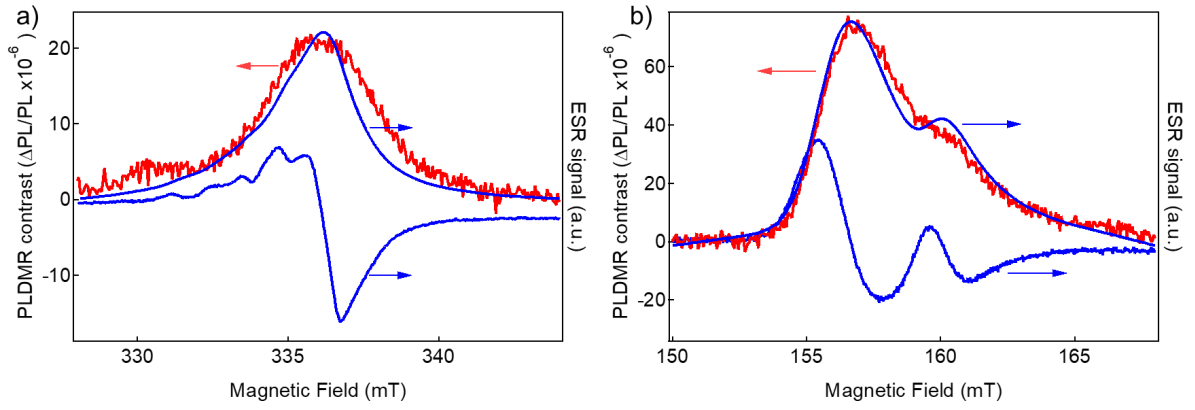
Figure S10. Comparison of the LESR spectra (blue) of charges (a) and the $\Delta m_s = \pm 2$ half-field triplet spectra (b) of Figures 3 and 4 of the main text with the corresponding PLDMR spectra (red). Sample illumination of 365 nm at 10 K. The first-derivative LESR spectra have been integrated to facilitate comparison with the PLDMR spectra. The high similarity of the PLDMR and LESR spectra indicates that the same species are detected by both methods. Some spectral broadening for PLDMR can be ascribed to high microwave powers used for this technique which leads to so-called power broadening. The mechanism that enables PLDMR to detects charge carriers in (a) can be attributed to triplet-charge annihilation [10].
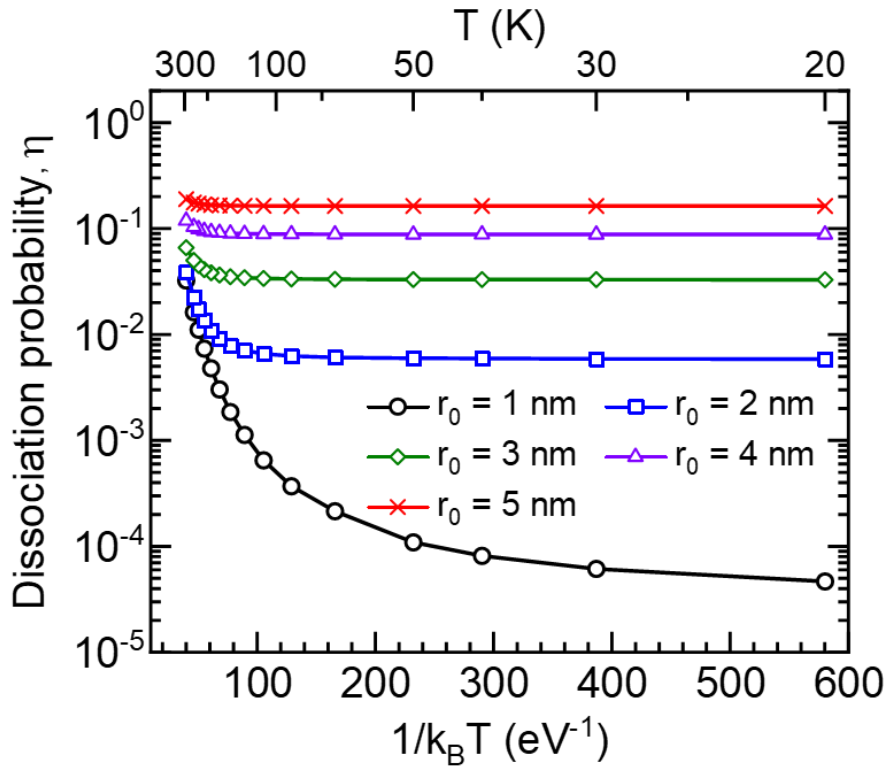
Figure S11: Arrhenius plot of the computed dissociation yield for different initial separation distances r_0 between the electron-hole pairs.

7
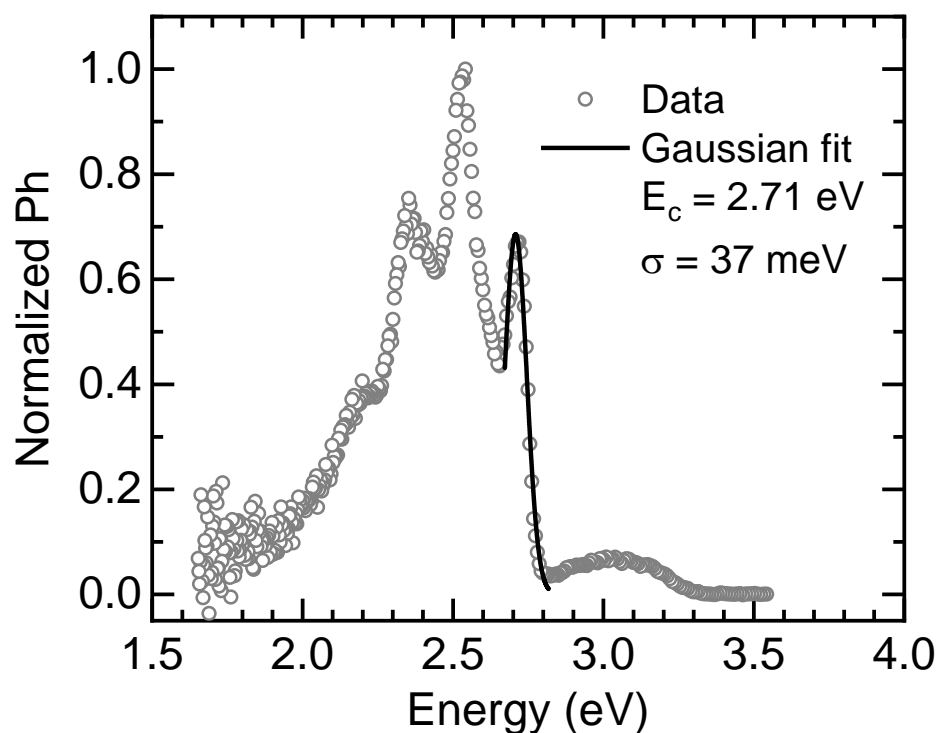
Figure S12: Normalized phosphorescence spectrum of mCBP-CN is depicted (delay = 50 ms, gate width = 100 ms). The black solid line illustrates a Gaussian fit ($A * exp(- (E - E_T)^2/2\sigma^2)$) of the 0-0 peak in the phosphorescence spectrum, performed to estimate the triplet exciton DOS width (σ) in mCBP-CN films. The fitting results are: 0-0 peak energy, $E_T = 2.71 \, eV$ and $\sigma = 37 \, meV$.

References:

[10] L. J. Hart, J. Grüne, W. Liu, T. k. Lau, J. Luke, Y. C. Chin, X. Jiang, H. Zhang, D. J. Sowood, D. M. Unson, J-S. Kim, X. Lu, Y. Zou, F. Gao, A. Sperlich, V. Dyakonov, J. Yuan, and A. J. Gillett, Understanding the Role of Triplet-Triplet Annihilation in Non-Fullerene Acceptor Organic Solar Cells, Adv. Energy Mater., 2301357 (2023).

[43] S. S. Eaton, K. M. More, B. M. Sawant, & G. R. Eaton, Use of the ESR half-field transition to determine the interspin distance and the orientation of the interspin vector in systems with two unpaired electrons, J. Am. Chem. Soc., **105**, 6560-6567 (1983).

8

Acknowledgements

Erklärung und eidesstattliche Versicherung

Hiermit versichere ich an Eides statt, dass ich die vorliegende Arbeit selbstständig verfasst und keine anderen als die von mir angegebenen Quellen und Hilfsmittel verwendet habe.

Weiterhin erkläre ich, dass ich die Hilfe von gewerblichen Promotionsberatern bzw. -vermittlern oder ähnlichen Dienstleistern weder bisher in Anspruch genommen habe, noch künftig in Anspruch nehmen werde.

Zusätzlich erkläre ich hiermit, dass ich keinerlei frühere Promotionsversuche unternommen habe.

Bayreuth, den

Andrei Stankevich